THE UNIVERSITY OF QUEENSLAND

AUSTRALIA

Gradient Coil Design and Acoustic Noise Control in Magnetic Resonance Imaging Systems

Yaohui Wang

Master of Science — Acoustics

Bachelor of Engineering — Environmental

A thesis submitted for the degree of Doctor of Philosophy at

The University of Queensland in 2017

School of Information Technology and Electrical Engineering

Abstract

In magnetic resonance imaging (MRI), three-dimensional linearly varied magnetic field gradients are required in the imaging volume, for the encoding of the spatial information of the imaged object. The gradient magnetic field is generated by gradient coils, whose performance directly affects the final MR image quality. Modern MRI applications demand gradient coils to be designed with higher performance such as a faster slew rate for rapid imaging, and fewer system interactions to ensure distortion-free images.

During MR imaging, the gradient coil current switches quickly and the alternating current under a strong magnetic field generates a large Lorentz force, thus increasing the vibrations and noise in the gradient assembly, and the vibrations can also transmit to other components in the system. Moreover, the gradient magnetic field induces eddy currents on the surrounding conductive materials, resulting in further mechanical vibration. The sound pressure level (SPL) of an MRI scanner very commonly exceeds 100 dB, which may be discomforting to patients. Therefore, an effective acoustic noise control is necessary for the MRI operation.

This thesis attempts to design a novel gradient coil system in an MRI scanner with a particular focus on the investigation of an acoustic noise control scheme. A brief summary of the thesis work is as follows.

(1) Gradient coil design

A conventional cylindrical MRI scanner has a long patient bore, which may make some patients uneasy due to claustrophobia. In order to alleviate this, an asymmetric gradient coil was proposed to accommodate an asymmetric MRI magnet. The coil was designed with a number of features, for example, to enable the installation of the shim tray, the coil was configured with one end connected and the other end separated. The electromagnetic and acoustic performances were also improved compared with a conventional non-connected coil system.

The stream function approach is commonly used in gradient coil design, but an issue with this design is a connection problem between coil loops. To eliminate the field errors due to the coil connections, this thesis proposed a novel spiral coil design scheme, including both transverse coils and a longitudinal coil. The proposed coil design method was not only able to improve the magnetic

performance of the coil, but also could integrate the cooling system into the coil design using hollow wires in the discrete wire space.

Wire spacing is a major engineering problem in gradient coil design. Conventional gradient coils are designed with three primary layers and three shielding layers, and in general, primary transverse coils are located in two layers separated by a very dense wire structure. In this thesis, a novel gradient coil design strategy using a layer-sharing scheme was proposed. This design scheme mutually combined the x and y gradient coil layers, effectively utilizing the unoccupied or sparse coil-layer space. The new method was modelled in the case of an asymmetric head coil design, and enhanced coil performance was achieved when compared with conventional coil configurations.

(2) Analysis and control of acoustic fields in MRI systems

The acoustic fields generated by gradient coils were analysed based on the finite element method (FEM). The FEM model was built using the commercial software ANSYS, and experimentally validated against acoustic measurements in a MRI scanner. The acoustic model has been used to analyse several applications.

In the first acoustic analysis for a split MRI scanner (in the combined MRI-Linear Accelerator (LINAC) system), it was found that the central gap of the split MRI scanner had relatively lower SPL compared with the cylindrical tunnel and the SPL was comparable with a typical scanner counterpart.

In another study, an acoustic damping scheme was investigated, and a support-mounting scheme between the main magnet and the gradient assembly was tested to relocate the acoustic field distribution of the split MRI scanner and adjust the dominant resonance frequency. With a further damping treatment scheme on the inner and outer surfaces of the gradient assembly, the SPL level of the split MRI scanner was significantly reduced, especially at some resonant frequencies.

In addition to hardware designs, a gradient pulse alteration scheme was also proposed to reduce the acoustic noise, by removing the resonant-frequency components from the gradient pulse, based on a resonant-frequency inspection analysis of the scanner structure. The acoustic model confirmed the effectiveness of pulse sequence designs for a noise control scheme without changing or reassembling the hardware components of the MRI system.

The developed FEM model was finally used to investigate the acoustic effects of a warm bore. The simulation indicated that the SPL radiated by the warm bore wall might be higher than the gradient

coil itself if not shielded well. This study suggested that the gradient shielding was critical for acoustic noise reduction. In addition, a proper damping treatment on the warm bore wall would help to further restrain the structure resonance.

It is hoped that the theoretical investigation of the gradient coil design methods and acoustic noise modelling/control schemes in this thesis will aid in the development of a quiet MRI system with high-performance gradient coils.

Declaration by author

This thesis is composed of my original work, and contains no material previously published or written by another person except where due reference has been made in the text. I have clearly stated the contribution by others to jointly-authored works that I have included in my thesis.

I have clearly stated the contribution of others to my thesis as a whole, including statistical assistance, survey design, data analysis, significant technical procedures, professional editorial advice, and any other original research work used or reported in my thesis. The content of my thesis is the result of work I have carried out since the commencement of my research higher degree candidature and does not include a substantial part of work that has been submitted to qualify for the award of any other degree or diploma in any university or other tertiary institution. I have clearly stated which parts of my thesis, if any, have been submitted to qualify for another award.

I acknowledge that an electronic copy of my thesis must be lodged with the University Library and, subject to the policy and procedures of The University of Queensland, the thesis be made available for research and study in accordance with the Copyright Act 1968 unless a period of embargo has been approved by the Dean of the Graduate School.

I acknowledge that copyright of all material contained in my thesis resides with the copyright holder(s) of that material. Where appropriate I have obtained copyright permission from the copyright holder to reproduce material in this thesis.

Publications during candidature

Peer-reviewed journal papers

Y. Wang, F. Liu, E. Weber, F. Tang, J. Jin, Y. Tesiram, and S. Crozier, "Acoustic analysis for a split MRI system using FE method," *Concepts in Magnetic Resonance Part B: Magnetic Resonance Engineering*, vol. 45, pp. 85-96, 2015.

Y. Wang, F. Liu, and S. Crozier, "Simulation study of noise reduction methods for a split MRI system using a finite element method," *Medical Physics*, vol. 42, pp. 7122-7131, 2015.

Y. Wang, F. Liu, Y. Li, F. Tang, and S. Crozier, "Asymmetric gradient coil design for use in a short, open bore magnetic resonance imaging scanner," *Journal of Magnetic Resonance*, vol. 269, pp. 203-212, 2016.

Y. Wang, F. Liu, X. Zhou, and S. Crozier, "Numerical study of the acoustic radiation due to eddy current-cryostat interaction," *Medical Physics*, vol. 44, pp. 2196-2206, 2017.

Y. Wang, F. Liu, X. Zhou, and S. Crozier, "Design of transverse head gradient coils using a layer-sharing scheme," *Journal of Magnetic Resonance*, vol. 278, pp. 88-95, 2017.

Y. Wang, X. Xin, F. Liu and S. Crozier, "Spiral gradient coil design for use in cylindrical MRI systems," *IEEE Transactions on Biomedical Engineering*, DOI:10.1109/TBME.2017.2725962, 2017.

Y. Hu, Q. Wang, X. Hu, X. Zhu, S. Crozier, **Y. Wang** and F. Liu, "A simulation study on the design of gradient coils in MRI for the imaging area above the patient bed," *Measurement Science and Technology*, vol. 28, p. 035402, 2017.

F. Tang, F. Liu, F. Freschi, Y. Li, M. Repetto, L. Giaccone, **Y. Wang** and S. Crozier, "An improved asymmetric gradient coil design for high-resolution MRI head imaging," *Physics in Medicine and Biology*, vol. 61, pp. 8875-8889, 2016.

Y. Hu, Q. Wang, X. Zhu, C. Niu and **Y. Wang**, "Optimization MRI shim coil using second derivative discretised stream function," Concepts in Magnetic Resonance Part B: Magnetic Resonance Engineering, 10.1002/cmr.b.21352, 2017.

Peer-reviewed conference papers

Y. Wang, F. Liu, E. Weber and S. Crozier, "Investigation of acoustic noise reduction method for MRI-LINAC hybrid system", In: *Proceedings of the International Society for Magnetic Resonance in Medicine (ISMRM)*, Toronto, Canada, Jun 2015.

Y. Wang, F. Tang, Y. Li, F. Liu and S. Crozier, "Theoretical investigation of gradient pulse alterations for acoustic noise reduction in an MRI-LINAC system", In: *Proceedings of the International Society for Magnetic Resonance in Medicine (ISMRM)*, Singapore, May 2016.

Publications included in this thesis

Chapter 4

Part 1: Y. Wang, F. Liu, Y. Li, F. Tang, and S. Crozier, "Asymmetric gradient coil design for use in a short, open bore magnetic resonance imaging scanner," *Journal of Magnetic Resonance*, vol. 269, pp. 203-212, 2016.

Contributor	Statement of contribution
Yaohui Wang (Candidate)	Numerical modelling (70%), code implementation (80%), manuscript preparation (100%)
Feng Liu	Manuscript review (80%)
Yu Li	Numerical modelling (30%), manuscript review (10%)
Fangfang Tang	Code implementation (20%)
Stuart Crozier	Manuscript review (10%)

Part 2: Y. Wang, X. Xin, F. Liu and S. Crozier, "Spiral gradient coil design for use in cylindrical MRI systems," *IEEE Transactions on Biomedical Engineering*, DOI:10.1109/TBME.2017.2725962, 2017..

Contributor	Statement of contribution
Yaohui Wang (Candidate)	Numerical modelling (100%), code implementation (100%), manuscript preparation (100%)
Xuegang Xin	Manuscript review (20%)
Feng Liu	Manuscript review (70%)
Stuart Crozier	Manuscript review (10%)

Part 3: Y. Wang, F. Liu, X. Zhou, and S. Crozier, "Design of transverse head gradient coils using a layer-sharing scheme," *Journal of Magnetic Resonance*, vol.278, pp.88-95, 2017.

Contributor	Statement of contribution
Yaohui Wang (Candidate)	Numerical modelling (70%), code implementation (100%), manuscript preparation (100%)
Feng Liu	Numerical modelling (30%), manuscript review (80%)
Xiaorong Zhou	Manuscript review (10%)
Stuart Crozier	Manuscript review (10%)

Chapter 5

Part 1: Y. Wang, F. Liu, E. Weber, F. Tang, J. Jin, Y. Tesiram, and S. Crozier, "Acoustic analysis for a split MRI system using FE method," *Concepts in Magnetic Resonance Part B: Magnetic Resonance Engineering*, vol. 45, pp. 85-96, 2015.

Contributor	Statement of contribution
Yaohui Wang (Candidate)	Numerical modelling (90%), experiment design (100%), experiment implementation (30%), manuscript preparation (100%)
Feng Liu	Manuscript review (75%)
Ewald Weber	Experiment implementation (30%), manuscript review (5%)
Fangfang Tang	Numerical modelling (10%)
Jin Jin	Experiment implementation (20 %), manuscript review (10%)
Yas Tesiram	Experiment implementation (20 %), manuscript review (5%)
Stuart Crozier	Manuscript review (5%)

Part 2: Y. Wang, F. Liu, and S. Crozier, "Simulation study of noise reduction methods for a split MRI system using a finite element method," *Medical Physics*, vol. 42, pp. 7122-7131, 2015.

Contributor	Statement of contribution
Yaohui Wang (Candidate)	Numerical modelling (100%), code implementation (100%), manuscript preparation (100%)
Feng Liu	Manuscript review (90%)
Stuart Crozier	Manuscript review (10%)

Part 3: Y. Wang, F. Tang, Y. Li, F. Liu and S. Crozier, "Theoretical investigation of gradient pulse alterations for acoustic noise reduction in an MRI-LINAC system", In: *Proceedings of the International Society for Magnetic Resonance in Medicine (ISMRM)*, Singapore, May 2016.

Contributor	Statement of contribution
Yaohui Wang (Candidate)	Numerical modelling (100%), code implementation (100%), manuscript preparation (100%)
Fangfang Tang	Manuscript review (5%)
Yu Li	Manuscript review (5%)
Feng Liu	Manuscript review (80%)
Stuart Crozier	Manuscript review (10%)

Part 4: Y. Wang, F. Liu, X. Zhou, and S. Crozier, "A numerical study of the acoustic radiation due to eddy current-cryostat interaction," *Medical Physics*, vol. 44, pp. 2196-2206, 2017.

Contributor	Statement of contribution
Yaohui Wang (Candidate)	Numerical modelling (100%), code implementation (100%), manuscript preparation (100%)
Feng Liu	Manuscript review (80%)
Xiaorong Zhou	Manuscript review (10%)
Stuart Crozier	Manuscript review (10%)

Contributions by others to the thesis

Prof. Feng Liu (Joint principal supervisor), Prof. Stuart Crozier (Principal supervisor), Dr. Fangfang Tang (colleague), Mr. Ewald Weber (colleague) and Dr. Yu Li (colleague) have all made contributions towards generating research ideas, model simulation, experimental validation and manuscript review. The individual contributions are detailed in the previous section. All the work presented in this thesis was drafted entirely by the author. Prior to submission, the thesis was reviewed by all supervisors with corrections being made by the author.

Statement of parts of the thesis submitted to qualify for the award of another degree

None

Acknowledgements

Throughout the research of my PhD, I have received a lot of sincere help from others, which I very much appreciate. Special thanks should go to my supervisors Prof. Feng Liu and Prof. Stuart Crozier for introducing me into such a dynamic research area, namely MRI, and providing me a research environment in which I had the freedom to think and to explore. During my study, Prof. Feng Liu helped me by discussing with me many of my raw ideas and by kindly suggesting lots of workable research approaches. His ongoing encouragement made me confident to research new topics and try new methods. In addition, thanks go to Prof. Feng Liu and Prof. Stuart Crozier for the immeasurable time they spent on editing my manuscript, even at weekends.

Thanks to Dr Fangfang Tang for patient help with my initial research in gradient coil design. Thanks also to Mr Ewald Weber, Dr Jin Jin and Dr Yas Tesiram who helped me with the experimental validation of my first paper; and to Dr Yu Li who helped me with ideas to improve my third paper and also gave me many suggestions regarding my research study. Thanks to Ms Kimberly Nunes and Ms Celia Giumelli who helped me to edit my manuscript.

My thanks also extend to my parents and friends. Their persistent support and care have made me flourish and thrive in my research and my life, and their earnest expectations propel me to keep moving ahead.

The PhD programme was funded by a CSC–UQ (China Scholarship Council–University of Queensland) scholarship and a top up assistance scholarship.

Keywords

MRI, MRI-LINAC, acoustic noise, gradient coil, damping, eddy current, finite element method, finite difference method, discrete wire method, spiral gradient coil

Australian and New Zealand Standard Research Classifications (ANZSRC)

ANZSRC code: 090304, Medical Devices, 80%

ANZSRC code: 090399, Biomedical Engineering not elsewhere classified, 20%

Fields of Research (FoR) Classification

FoR code: 0906, Electrical and Electronic Engineering, 50%

FoR code: 0903, Biomedical Engineering, 50%

Contents

List of figures

List of tables

List of abbreviations used in the thesis

MRI	Magnetic resonance imaging
CT	Computed tomography
SPL	Sound pressure level
LINAC	Linear accelerator
RF	Radio frequency
TR	Repetition time
TE	Echo time
FDM	Finite difference method
BEM	Boundary element method
DSV	Diameter of sphere volume
EPI	Echo planar imaging
PNS	Peripheral neural stimulation
FEM	Finite element method
APDL	ANSYS parametric design language
GUI	Graphical user interface
DOF	Degree of freedom
2D	Two-dimensional
PML	Perfect match layer
LMS	Least mean square
FLD	Free-layer damping
CLD	Constrained-layer damping
ROI	Region of interest
3D	Three-dimensional

Chapter 1

Introduction

Magnetic Resonance Imaging (MRI) is a widely-used non-ionizing, imaging modality in modern medical diagnosis which has advantages with regards to soft-tissue resolution and contrast [1–3]. In recent years, MRI techniques have developed rapidly, especially towards high-field imaging, such as 7 T, 9.4 T or even higher field strengths. MRI technique development requires an associated performance improvement in the system hardware, which mainly includes the main magnet, gradient coil and radio-frequency (RF) coil. In this thesis, improved designs of the gradient coil and a control strategy for the induced acoustic field in MRI systems were investigated.

1.1 From gradient coil design to acoustic noise control

A gradient coil set is an important component in a standard MRI scanner which produces linear gradient magnetic fields that are superimposed over a strong uniform magnetic field. The uniform magnetic field is produced by a main magnet, which aligns with the proton precession direction. The superimposed gradient magnetic field slightly changes the proton precession frequency or phase, thus encoding the spatial information of an imaged object in the frequency associated with a position in space [4]. In general, the magnetic field gradient produced by the gradient coils is required to be as linear as possible, and a well-designed gradient coil should also have low inductance, low resistance, high efficiency, etc. [5]. This is especially pertinent in high-field imaging and fast imaging when all the coils' parameters must be highly optimized. Therefore, novel gradient coil configurations and methods are required to be developed to meet these demands [6, 7].

Gradient technology is faced with a number of technical challenges. For example, since the imaging process is accompanied by the gradient coil current switching on and off, varying Lorentz force is produced on the coil structure, under a strong static magnetic field environment. The varying Lorentz force propels the gradient assembly to vibrate, thus emitting loud acoustic noise [8]. The vibration of the gradient assembly can also transmit to other joint components in the MRI scanner. In addition, the eddy current produced on the surrounding conductive structures may make a significant contribution to the ultimate acoustic field [9, 10]. It is reported that the sound pressure

level (SPL) of the acoustic noise can exceed 130 dB in some scanners [11], which is the pain threshold of normal human hearing [12]. The loud noise emitted during scanning may be unpleasant or cause patient discomfort, and also may damage the patient's auditory system if not well protected [13–16]. Therefore, efficient acoustic noise reduction methods are necessary to be applied to MRI scanners.

The acoustic noise problem in an MRI scanner has a direct relationship with the gradient coil, which includes the vibration of the gradient coil, the vibration transmission from the gradient assembly to other system structures, and also the eddy current induced vibration of the surrounding metal structures [9]. This thesis proposed novel gradient coil design methods and efficient noise control schemes for the development of better, quieter MRI systems.

1.2 Scope of the thesis

This thesis contains three main sections followed by a conclusion. Chapter 2 and Chapter 3 comprise the first section. Chapter 2 firstly gives a brief introduction about the function of gradient coils in MR imaging and the corresponding imaging mechanism; secondly the chapter presents a review of gradient coil design strategies and a comparison of the design methods; and thirdly, the chapter provides a statement about the hardware components of a standard MRI scanner and the existing acoustic noise reduction methods applied to MRI scanners. Chapter 3 is a detailed presentation of the gradient coil design methods used in this thesis and the acoustic modelling process.

Chapter 4 is the gradient coil design section, where three new gradient coil configurations or design methods are presented. The first part is an asymmetric gradient coil design with one end connecting the primary coil to the shielding coil, which is different from the conventional non-connected coil. This asymmetric gradient coil design is for use in a short open bore MRI system. The performance of the connected coil will be compared to that of a system with a non-connected coil. The second part will present a set of spiral gradient coils, including both a transverse gradient coil and a longitudinal coil. The spiral gradient coil design method is based on a discrete wire method, which differs from the commonly used continuous current density-based stream function method. The spiral gradient coil is designed with one single circuit, leaving out the cutting and connecting process required for a conventional coil pattern with separate coil loops. As a comparison, a corresponding transverse gradient coil and a longitudinal gradient coil based on stream function method is designed and performance evaluations of these two kinds of gradient coils will be conducted. In the third part, a novel gradient coil design strategy referred to as a layer-sharing

scheme is proposed. In this scheme, every primary coil layer contains both x and y coils thus avoiding the need to add extra coil layers. A comparison between the novel layer-sharing gradient coil and the conventional layer-separate gradient coil will then be made.

Chapter 5 is the acoustic noise investigation section which is made up of four parts. The first part describes an acoustic analysis of a split MRI scanner, which is the main part of an MRI-LINAC (Linear Accelerator) hybrid system. The model will be experimentally validated and the acoustic noise properties in the split MRI system will be theoretically analysed. Based on the analysis result, the second part will present an acoustic field relocation and a vibration damping scheme to attenuate the loud noise of such a split MRI system. The third part will provide a theoretical investigation of the noise reduction method of the split MRI system by gradient pulse alteration. The second and third parts describe two aspects of the acoustic noise reduction schemes of an MRI system, which are based on the 'hardware' treatment and the 'software' implementation, respectively. In addition, eddy current may also induce acoustic noise, which can be significant if the gradient coil is not well shielded. Based on this, the forth part will be a comparison of the SPLs between the gradient assembly and the warm bore wall followed by a discussion of the engineering solution for acoustic noise due to warm bore wall vibration.

The conclusions will be presented in Chapter 6, along with possible opportunities for future research.

Chapter 2

Literature review

This literature review will start with a brief introduction into the function of gradient coils in MRI. The roles of the three-axis gradient coils in an imaging process will be explained and the ultimate imaging transform will be illustrated. The second part of this chapter will cover gradient coil design methods; the core of gradient coil design is a multi-objective optimization problem [17]. Gradient coil design methods are mainly categorized into the continuous-current density-based method and the discrete wire method, which both have their advantages and disadvantages. The alternating current input in the gradient coil is the origin of the mechanical vibration and acoustic noise. The vibrations in the gradient coil can transmit to other hardware components and the gradient pulse can induce eddy currents on the surrounding metal materials, such as the cryostat and the RF coils [9]. Therefore, for a full understanding of the mechanism of acoustic noise generation and the application of appropriate noise control methods, it is necessary to be familiar with the hardware components of an MRI system. Existing acoustic noise control methods applied to MRI systems will also be briefly introduced.

2.1 General Principles of MRI

In MRI, there is a strong static magnetic field produced by the main magnet, which aligns the protons of the target tissue or organ along the direction of the magnetic field. These protons will precess at a resonance frequency, which is known as the Larmor frequency and expressed as [18, 19]

$$\omega_0 = \gamma B_0 \tag{2-1}$$

where ω_0 is the resonance frequency, γ is the gyromagnetic ratio and B_0 is the magnetic flux density.

The overall magnetization vector of the protons is parallel to the direction of the magnetic field. Usually, the static magnetic field direction is defined as z direction in a Cartesian coordinate system. During imaging, an incoming electromagnetic wave produced by an RF assembly which meets the resonance frequency will excite the protons. Then the overall magnetization direction of the protons when excited by the electromagnetic wave will deviate from the original direction. After the

electromagnetic wave excitation terminates, the protons will relax and the overall magnetization direction will return slightly to the original direction. The release of the overall magnetization vector will induce an electric signal in the RF receiver. The process is shown in Fig. 2-1. However, for the imaging of the target tissue or organ, if the spatial information is not encoded, the signal received theoretically will be a single-frequency signal. Thus, the signal source, namely the protons, will not be distinguished and the tissue structure will not be imaged. Therefore, a gradient magnetic field generation device is introduced to spatially encode the tissue information.

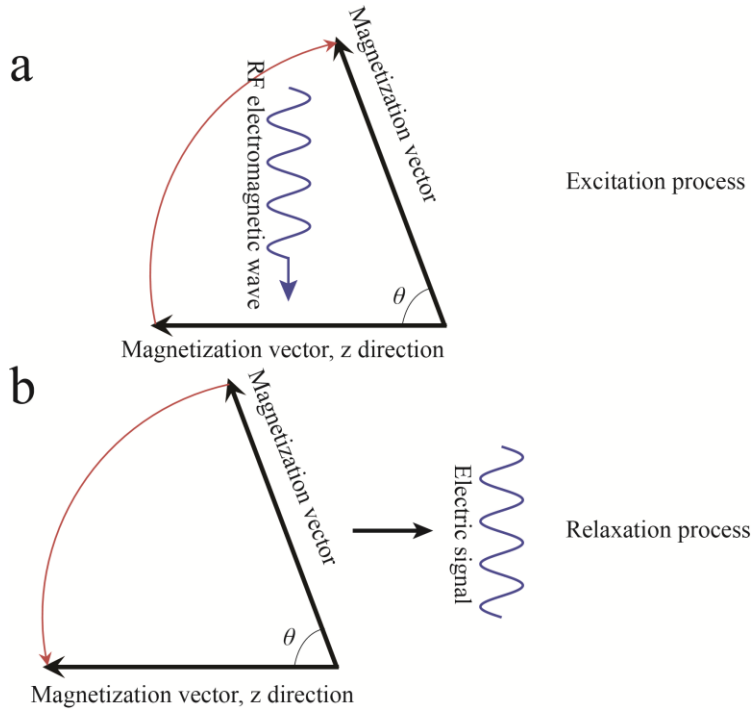

Fig. 2-1 Excitation and relaxation process in MRI: (a) during the excitation process, the magnetization vector is shifted to be deviated from the z direction with an angle θ (defined as flip angle in MRI) by an incoming RF electromagnetic wave produced by an RF transmitter coil and (b) when the RF excitation is terminated, the excited protons are relaxed to the z direction and an electric signal is collected by an RF receiver coil.

The gradient magnetic field in an MRI system is produced by a gradient assembly which contains an x gradient coil, a y gradient coil and a z gradient coil and the corresponding field gradient is $\partial Bz/\partial x$, $\partial Bz/\partial y$ or $\partial Bz/\partial z$, respectively. The gradient magnetic field is superimposed over the strong static magnetic field. Thus, the target space will have a different magnetic field strength. As stated above, the precession frequencies of the protons are proportional to the magnetic field strength. Thus, when the gradient coils are switched on, the protons in different positions in the target tissue will precess at different frequencies and the spatial information of the protons will be distinguished. The mechanisms of gradient coil utilization in MRI can be summarized as follows.

At the start of the imaging process, an RF electromagnetic wave is transmitted by an RF coil. Meanwhile, a gradient coil will be switched on for the slice selection. For axial-plane imaging, the z gradient coil will be switched on, and the x gradient coil will be switched on for sagittal-plane imaging, and the y gradient coil will be switched on for coronal-plane imaging. Whereas the oblique imaging, there will be a combination of the three-axis gradient coils. Take the axial-plane imaging as an example. When the z gradient coil is switched on, the magnetic field along the axial direction will be linearly varied and the precession frequency will also be linearly varied. The tuned narrow-band electromagnetic field will be absorbed by a slice of the target tissue. It is the protons on that slice that are excited. The overall magnetization vector of the protons on the slice will shift to be deviated from the original magnetization direction.

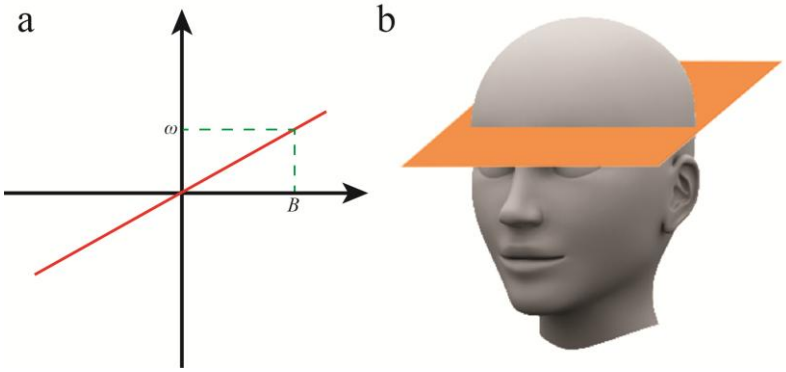

Fig. 2-2 Slice selection in MRI. When the z gradient coil is switched on, an RF electromagnetic wave with frequency ω will excite the slice residing at an axial position with magnetic flux density B, as is shown in (a) and the slice selection diagram is shown in (b).

After the slice selection, a frequency-encoded gradient coil will be switched on. For instance, for the x gradient coil, the gradient strength is denoted by G_x. Thus, in the x direction, the precession frequency of the protons on the slice will be linearly varied along the x direction, as is shown by the ω direction in Fig. 2-3. If only the x gradient coil is switched on, there will be frequency encoding only in the x direction. All the protons on this slice precess at the same phase. However, for the imaging, a y-direction gradient magnetic field is also applied, which is used to produce a phase encoding (see the φ direction in Fig. 2-3). Assuming the y gradient strength is G_y, a phase shift will be created as

$$\varphi = \gamma G_x y t = (\gamma G_x t) y \tag{2-2}$$

and the frequency encoding by the x gradient coil is expressed as

$$\omega = \gamma G_y x = (\gamma G_y) x \tag{2-3}$$

The frequency and phase information from the MRI signal corresponds to the k-space of the two-dimensional (2D) Fourier transform of an image. That is, the data in the MRI is in the frequency domain.

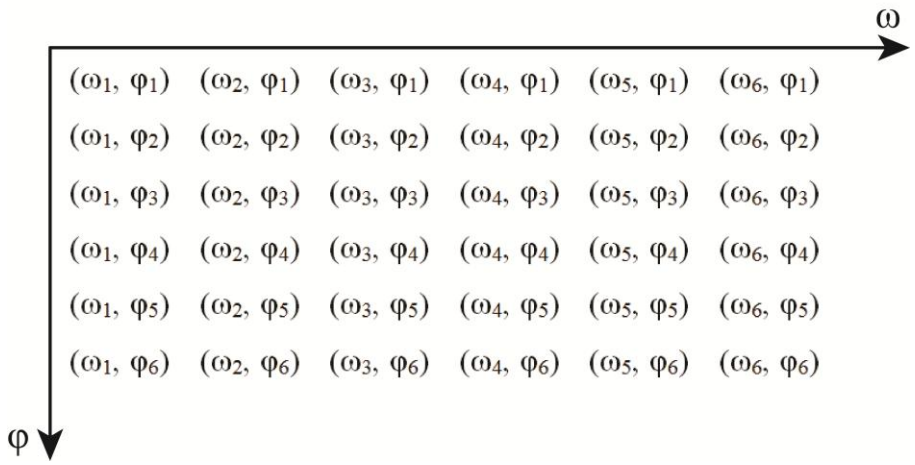

Fig. 2-3 Frequency encoding and phase encoding on a selected slice.

An example of a k-space data from MRI is shown in Fig. 2-4 (a). In k-space, the module, direction and amplitude of the vector from a k-space point to the k-space centre are the frequency, phase and brightness of a 2D image, respectively. By performing a 2D inverse Fourier transform, the 2D tissue-structure image can be easily recovered (see Fig. 2-4 (b)).

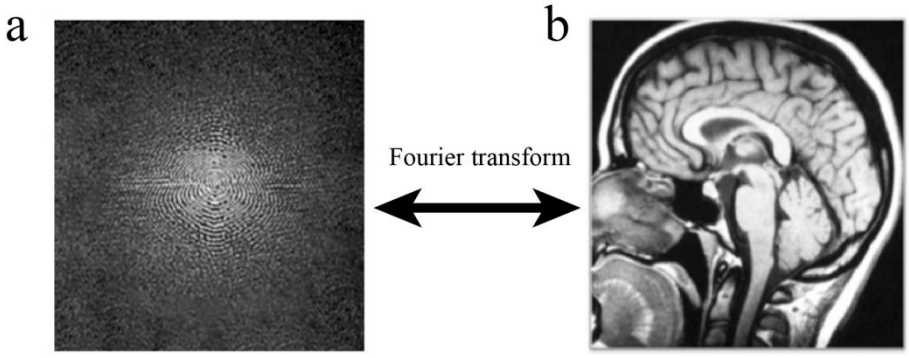

Fig. 2-4 A Fourier transform from a k-space to an image: (a) the raw k-space data from the MRI and (b) tissue-structure image by inverse Fourier transform from the k-space data.

2.2 MRI hardware

A standard MRI scanner is generally composed of three main hardware components: the main magnet, the gradient assembly and the RF assembly. The gradient coil itself, the gradient coil induced eddy current and the mechanical transmission of gradient assembly vibration are known to be important acoustic noise sources in an MRI scanner [9]. Thus, treating only a single noise source

may be not sufficient to achieve an overall noise level reduction. Therefore, it is necessary to be clear about the basic structure of an MRI scanner, namely the basic hardware components. The following section will first introduce the three main components of a standard MRI scanner, and then review existing acoustic noise control methods.

2.2.1 Main magnet

For the main magnet, there are three types of magnets used in practice: permanent magnet, room-temperature magnet and superconducting magnet [18]. A permanent magnet has a simple configuration and a low cost. It also has a weak stray magnetic field for which it is easy to construct shielding. However, the magnetic field uniformity in the imaging area is not as good as for the electric coil and the maximum magnetic field strength that can be reached by a permanent magnet is limited. In addition, variations in surrounding temperature may significantly influence magnetic field performance.

In comparison, the room-temperature magnet and superconducting magnet are both electrically powered. The magnetic field profile and intensity are related to the coil distribution and current strength. Thus, the anticipated magnetic field can be realized by a combination of electric coils and appropriate current input. The room-temperature magnet is easier to fabricate and maintain than the superconducting magnet, but produces much more heat due to the resistance of the conductor, which largely restricts the efficiency of the coil. Whereas, the superconducting magnet coils are immersed in a liquid helium vessel, which is controlled at a temperature not higher than 4.2 K [63]. At such an extremely low temperature, the magnet coil wire is superconductive with zero resistance, that is, there will be no heat produced if the coil is kept well cooled and in such a superconductive state. Due to zero resistance, the superconductive magnet can be packaged with more coil loops with higher current strength compared with the room-temperature magnet. Therefore, the superconductive magnet is capable of providing higher magnetic field intensity than the room-temperature magnet, which makes them popular in MRI systems. Many standard MRI scanners in clinical and research applications currently use superconductive magnets.

Fig. 2-5 shows an illustration of a superconductive magnet. It includes a cryostat to maintain the temperature of the magnet device, a helium vessel to contain the liquid helium, numerous magnet coils immersed in the liquid helium to produce a strong magnetic field, a steel structure to which to fasten the magnet coils (not shown in the figure) etc. The cryostat consists of a warm bore wall, a primary cold shield and a secondary cold shield. And in general, the shim coils are also used to

correct the magnetic field uniformity. The uniform magnetic field in an MRI scanner is commonly defined as the B_0 field.

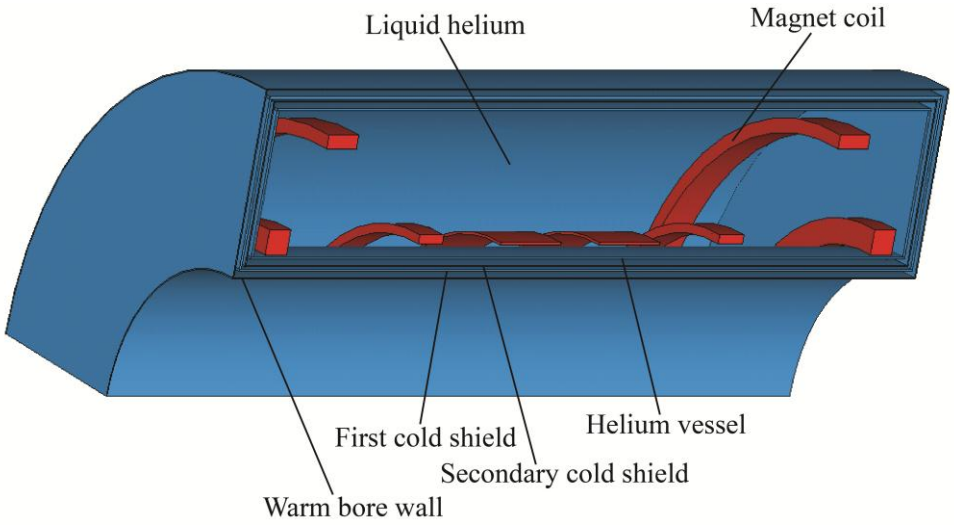

Fig. 2-5 Illustration of a superconductive magnet.

The strong static magnetic field provided by the main magnet influences the Lorentz force on an energized gradient coil by an expression

$$\boldsymbol{F} = I\boldsymbol{L} \times \boldsymbol{B} \tag{2-4}$$

It can be seen that the perpendicular component of the magnetic field relative to the current direction is proportional to the Lorentz force. The alternating Lorentz force will induce alternating displacement of the structures, thus causing structure vibration. A stronger static magnetic field has the potential to trigger a larger vibration of the gradient coil, thus potentially creating a louder acoustic noise [64]. Furthermore, the eddy current on the warm bore wall will also cause it to vibrate and emit noise. In the gaps between the warm bore wall and primary cold shield, the primary cold shield and secondary cold shield, and the secondary cold shield and liquid helium vessel, is a vacuum. Although there are unavoidable eddy currents induced on the primary cold shield and secondary cold shield, there is no acoustic noise radiation.

2.2.2 Gradient assembly

In a gradient assembly, there are three gradient coils, called the x, y and z coils. Fig. 2-6 shows a set of actively shielded gradient coils (here the actively shielding gradient coil is a coil pattern containing both the primary coil and shielding coil). The red and blue colours of the gradient coils indicate where the current flows in clockwise and anti-clockwise. The three-axis gradient coils are fixed by epoxy resin in an encapsulated gradient assembly, as is shown in Fig. 2-7. In an integrated

gradient assembly, there are also cooling devices and a shim tray installed. The hard epoxy resin largely impedes the vibration of the gradient coils, which avoids torsion and deformation of the gradient coils under strong Lorentz force, and also attenuates the SPL. The SPL radiated by the gradient assembly can be further attenuated if the epoxy resin is made stiffer.

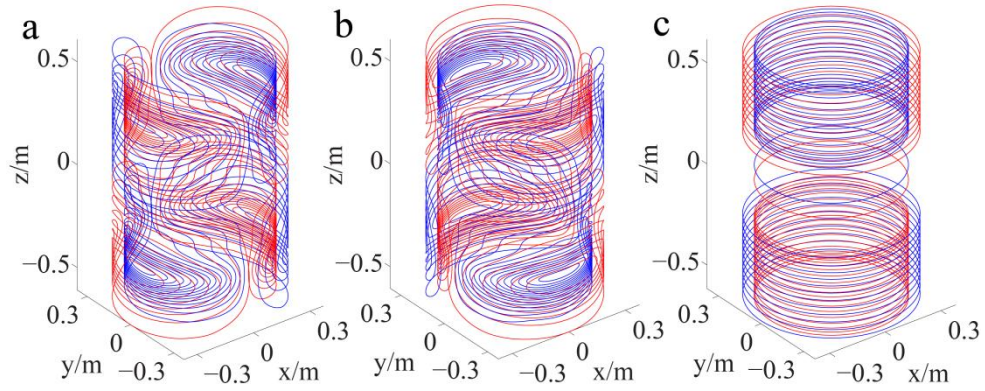

Fig. 2-6 Actively shielded gradient coils used in an MRI scanner: (a) x gradient coil, (b) y gradient coil and (c) z gradient coil. The red and blue colours indicate the direction in which the current flows.

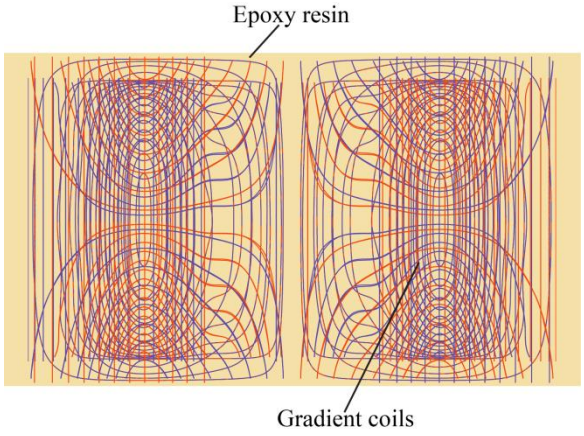

Fig. 2-7 Illustration of the three-axis gradient coils fixed in the epoxy resin.

In an MRI scanner, the gradient assembly is mounted on the warm bore. The vibration in the gradient assembly will transmit to the main magnet through the contact parts. The mechanical transmission adds more acoustic noise sources into the MRI system besides the gradient assembly. Moreover, the mechanical vibration transmitted from the gradient assembly can trigger fluctuations in the static magnetic field to some extent [65]. However, there are also other MRI systems which directly mount the gradient assembly to the floor [9, 66]. This design will increase the length of the MRI scanner, which may aggravate the claustrophobia of some patients.

Apart from the direct Lorentz force acting on the gradient coils, the alternating current also induces eddy currents on the surrounding conductive structures, resulting in non-negligible acoustic noise sources. Therefore, although the gradient coil is the main acoustic noise source of the MRI system, the additional noise sources make the acoustic problem more complex. It is reported that if the gradient coil is not well-shielded, the eddy current induced structure vibration may even become the main contributor to the overall acoustic field [9].

2.2.3 RF assembly

In the MR imaging process, the protons in the imaging target are continually absorbing and releasing electromagnetic wave signals. These electromagnetic wave signals are transmitted and received via the RF assembly. The RF coil in the RF assembly is designed to produce a uniform magnetic field in an imaging area called the B_1 field, which is perpendicular to the direction of the main magnetic field. The RF wave is a narrow-band signal, which excites a slice of target tissue during every emission. The uniformity of the B_1 field significantly influences the accuracy of the slice selection and the ultimate imaging quality.

The RF coil comprises a series of resistors and capacitors, which form oscillating circuits. These oscillating circuits play a role like an antenna to transmit or receive signals. The RF coil shape can be roughly divided into two categories: surface coil and volume coil [18]. The surface coil consists of a single loop or multi-loops. Compared to the volume coil, the surface coil is usually smaller and is placed on the imaging target. Thus, the surface coil usually has a high signal to noise ratio (SNR). However, the magnetic field performance of this kind of coil is not very uniform, so it is mainly used as the receiving coil. For the volume coil, both the Helmholtz coil and saddle coil can be used, but the most commonly used is the birdcage coil. The birdcage coil has the advantage of producing a more uniform B_1 field in a larger area as compared to the surface coil. Furthermore, the birdcage coil can be either used as the transmitting coil or the receiving coil. An illustration of these two types of coils is found in Fig. 2-8.

The operating frequency of the RF coil is in a range much higher than the audible sound frequency range of 20–20000 Hz, so the RF coil itself does not emit audible acoustic noise during imaging. However, the alternating current of the gradient coils will produce eddy currents on the conductive materials of the RF coil. Similar to the cryostat, the eddy current induced vibration of the RF assembly will also contribute to the overall acoustic field.

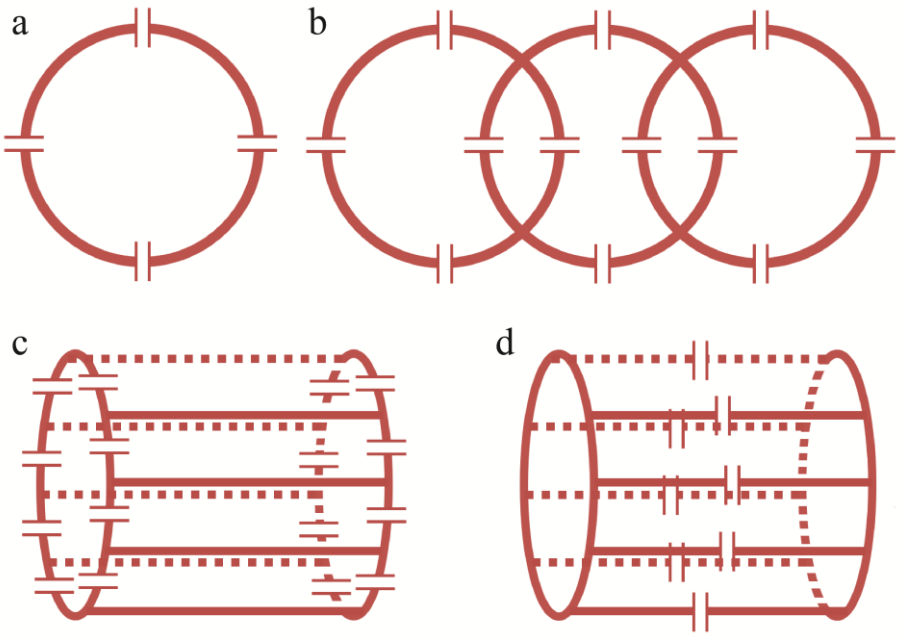

Fig. 2-8 Illustration of the RF coils: (a) single-loop surface coil, (b) multi-loop surface coil, (c) high-pass birdcage volume coil and (d) low-pass birdcage volume coil.

2.3 Gradient coils – function and design

This section will introduce gradient coil design methods and an evaluation of coil performance.

2.3.1 Gradient coil design methods

Gradient coil design methods can generally be divided into two categories: continuous-current density-based methods and discrete wire-based methods. The classic target field method is a type of continuous-current density-based method that was proposed based on the Fourier-space analytical expression of the current densities [20-22]. These current densities were intended to produce a specified magnetic field over an imaging volume surface. This method was initially to create gradient coils on an infinite coil cylinder; and for those cases with a limited length, an additional apodization technique was used to design a practical solution with a specific loss of gradient linearity [23-30]. The constraint conditions applied to the target functions made the mathematical problem ill conditioned; therefore, a smoothing function [18] or coil design parameter optimization (such as inductance minimization or power loss minimization) [23-26] had to be added to guarantee convergence. In general, the analytical solution-based target field method is inflexible and has difficulties in coping with the coil design in complex conditions (such as the case with a very small length-to-diameter ratio).

In practice, the continuous-current density-based method is usually combined with other numerical algorithms such as the boundary element method (BEM) [6, 31-33] or the finite difference method (FDM) [34-36]. These numerical methods produce continuous current density profiles that can be used to obtain a coil-winding pattern with the aid of a stream function. The winding patterns are realized by equally contouring the current density stream function [37, 38].

In contrast to the aforementioned current density-based methods, the discrete wire-based methods directly adjust current loops or segments to produce the required magnetic field gradients. For longitudinal coils, the designated coil geometry is a circular loop, thus the aim of this method is to arrange the positions of each current loop [39, 40] to produce a specified gradient along the axial direction. For the transverse gradient coil, it is relatively less straightforward to determine the winding pattern, because of the complexity of the coil shape. Nevertheless, the basic shape of the transverse gradient coil is mostly predictable [41, 42], varying from quasi-rectangular to quasi-circular. Therefore, one could find some mathematical descriptor to adjust the wire pattern to produce the target magnetic field.

A comparison between the continuous-current density-based method and the discrete wire method is illustrated in Fig. 2-9. Due to the coil symmetry, only a quarter of the coil is plotted. Although the design constraints of these two coils were set to be identical, the coil patterns are different. Since the discrete wire method is based on shape functions, the designed coil seems smoother than the continuous-current density-based method. However, the continuous-current density-based method has a fast computing speed. There are also many other differences for these two methods, which will be elaborated in the next chapter.

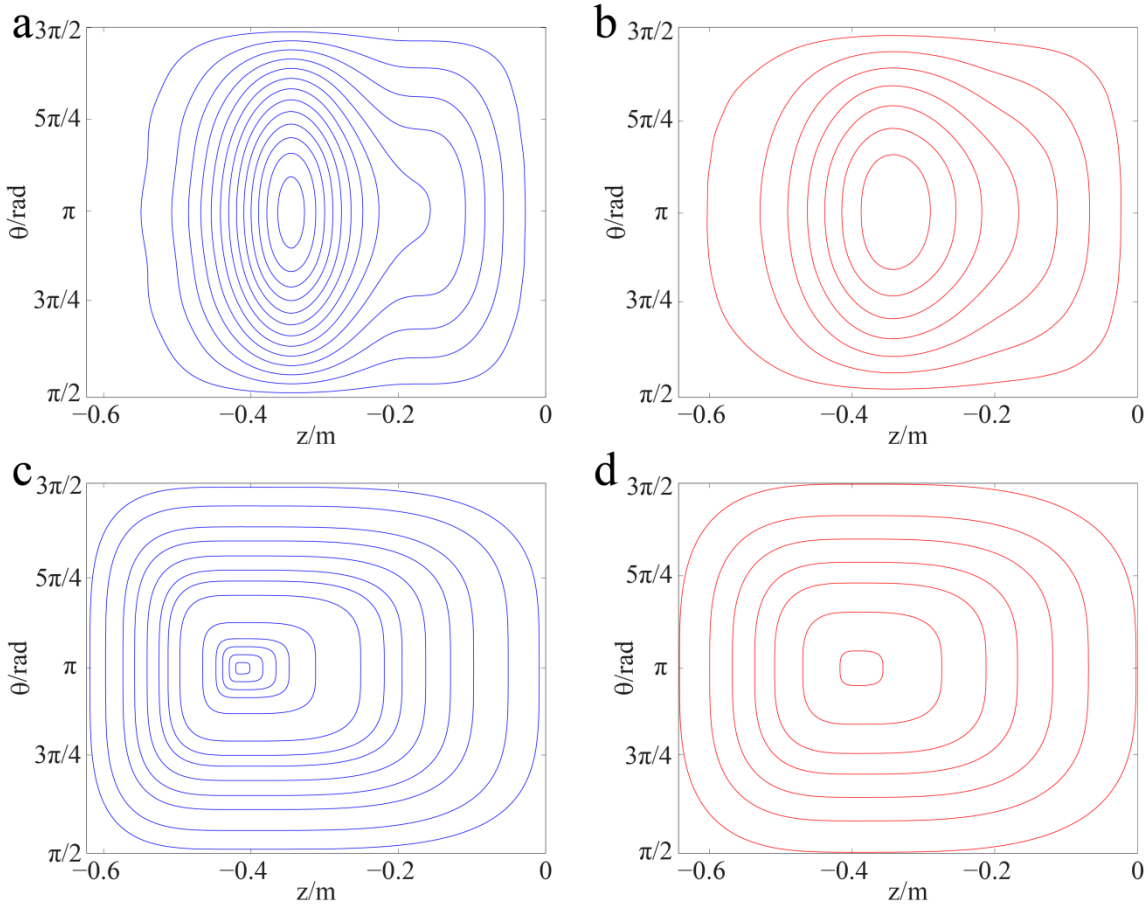

Fig. 2-9 2D gradient coil patterns: (a) and (b) are gradient coil design by continuous-current density-based method where (a) is the primary coil and (b) is the shielding coil, respectively; (c) and (d) are gradient coil design by discrete wire method where (c) is the primary coil and (d) is the shielding coil, respectively. Only a quarter of the coil is shown.

2.3.2 Gradient coil performance optimization

In the optimization of gradient coil design, there are many factors that are related to the coil's performance [17]. In terms of the electromagnetic characteristics, a gradient coil with high performance should have high efficiency, low inductance, low power dissipation, good magnetic shielding, and a uniform gradient magnetic field in the imaging area, which is called the diameter of sphere volume (DSV) [5]. For example, fast imaging techniques like Echo Planar Imaging (EPI) [43] require gradient current that switches on and off quickly, where the gradient coil should have a low inductance [21, 44]. The small and densely wound gradient coils, such as those applied for MR microscopy, potentially have a large resistance if the efficiency increases, whereas the gradient coil design usually minimizes power dissipation [45, 46]. Asymmetric gradient coils under the main magnetic field may arouse a balance problem, so the net torque mitigation should be taken into consideration [47, 48]. The eddy current induced secondary magnetic field in the DSV may result in imaging artefacts, therefore, magnetic field shielding or eddy current control during coil design is

necessary [49-51]. The loud acoustic noise during MRI scanning may make the patient feel very uneasy [13, 15, 52], thus the quiet gradient coil design was proposed [53-56]. The peripheral neural stimulation (PNS) may trigger discomfort for the patient, so during the gradient coil design, the E-field is usually controlled to reduce any induced currents in the patient [57].

Commonly used optimization strategies for gradient coil design include minimization of stored magnetic energy, minimization of power dissipation, induced eddy current control etc. [6, 17, 58]. Apart from the global optimization strategy, local focuses on the maximum current density distribution [59, 60], maximum temperature distribution [61], wire spacing [62] and so on, are also very important. Local high current density in one spot may be hazardous and has the potential to be burned down in the gradient assembly, and wires that are not adequately spaced will cause fabrication problems and also promote increases in current density.

In this thesis, both the continuous-current density-based gradient coil design method and the discrete wire-based gradient coil design method will be applied to investigate coil design. Furthermore, the continuous-current density-based gradient coil design will be combined with a finite difference method. The details of these two methods will be presented in the next chapter.

2.4 Acoustic noise in MRI – sources and reduction techniques

From the first investigation of the acoustic noise of MRI scanners in 1989 [67], many noise reduction methods have been proposed. These methods can be divided into three categories: passive methods, active methods and pulse alterations.

Passive methods are the most frequently used methods for MRI acoustic noise control. A simple and efficient scheme to employ is to use hearing protection measures, namely isolating the auditory system from the acoustic noise, for example, wearing earplugs, earmuffs or even a helmet [68]. Applying an appropriately designed acoustic liner to the gradient assembly can also significantly attenuate the noise level [69]. Some scanners use a vacuum device to block the airborne noise propagating to the patients' ears [66, 70]. Mounting the gradient assembly independently on the floor [9, 66] or reducing the eddy currents [10, 35] can restrain the vibration of some structures, such as the cryostat or RF coils, thus reducing the SPL. Rib stiffeners can help reinforce the gradient assembly, so the response amplitude will be reduced [71]. By mounting supports between the gradient assembly and the main magnet, the mechanical resonance modes of the MRI system can be adjusted, thereby reducing the loud regions of the acoustic field [72]. Using damping materials on the connecting parts between the main magnet and the gradient assembly can attenuate

the vibration transmission [73, 74]. There is also sound-insulating treatment on the RF assembly to barrier the acoustic noise propagating to the scanning subject [75]. The typical feature for the passive methods is that they can reduce the high-frequency noise to some extent, just like low-pass filters. However, for most conditions, they are incapable of achieving significant low-frequency noise attenuation.

The basic principle of active noise control is to use an equal-amplitude, anti-phase noise (namely a secondary noise) to counteract the original noise (namely the primary noise). Sensitive feedback systems should be designed to adjust the secondary noise signal. This method can create a quiet region in space and is mainly used in headphones [76-80]. In addition, actuators can be mounted on the gradient assembly. These actuators can produce counteractive force to restrain the vibration of the gradient assembly and thus reduce the noise [81]. There are also active gradient coil designs to create reverse Lorentz force in order to balance the vibration of the gradient assembly [82, 83]. The active signal cancellation method is only efficient on low-frequency noise, because low-frequency noise has low modal density and long wavelengths. However, all the components of the active noise control device should be MRI compatible, otherwise the metal components in the device may be harmful to the gradient linearity. This restricts the active noise reduction methods to apply to MRI scanners.

For pulse alterations, using sinusoidal components to replace the original linear rise and fall parts can largely reduce the high-frequency components of the gradient pulses. Since low-frequency excitation on the gradient coils has weak sound radiation capability [84, 85], this kind of "soft" pulse can significantly reduce the noise level [84, 86]. In addition, a trapezoidal signal can be regarded as the convolution of two rectangular signals. By changing the width of one rectangular signal, the zero points in the frequency domain can be altered. This method can remove the resonant frequency component in the pulse and then reduce the noise [87]. It is also reported that the can parameters such as the repetition time (TR) and echo time (TE) can help reduce the noise [88]. Changing the gradient pulse shape or parameters may often be a good method to reduce the noise level, but it may also affect the image quality or increase the scanning time.

A brief classification chart of the acoustic noise reduction methods applied to MRI scanners is shown in Fig. 2-10 including possible drawbacks of the respective categories of methods.

In addition to the acoustic noise control methods mentioned above, there are also a noise reduction methods reported in regard to the coil design [56, 89, 90]. However, this method is only possible for

a simplified coil model, because it is difficult to find acoustic analytical solutions for complex gradient assemblies.

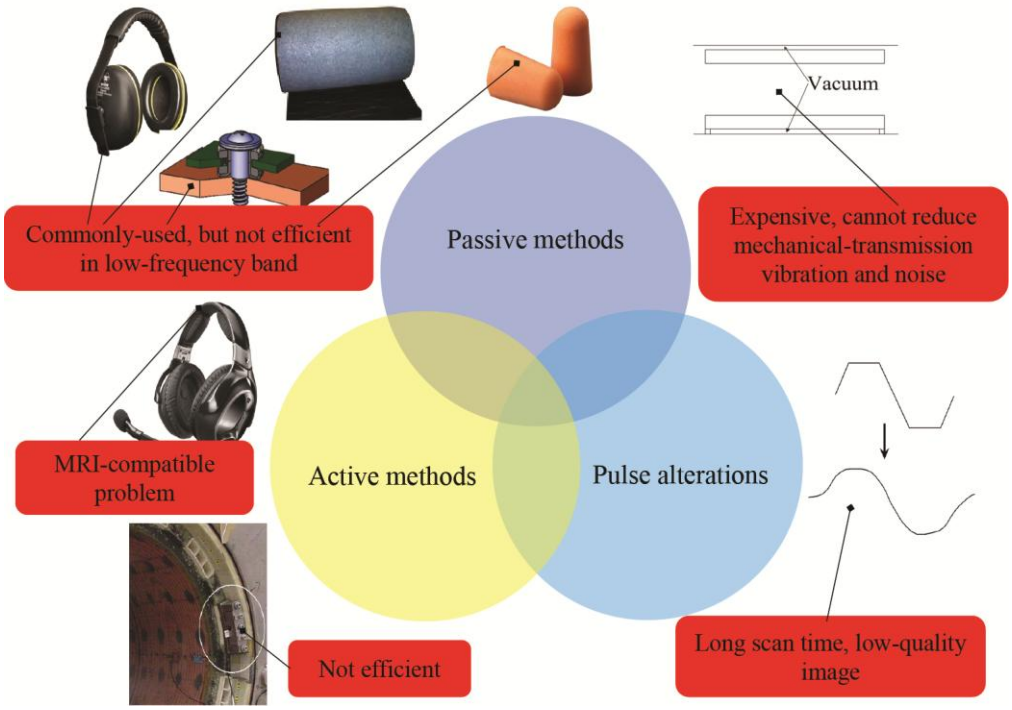

Fig. 2-10 Classification chart of the acoustic noise reduction methods applied to MRI scanners.

Chapter 3

Gradient coil design methods and acoustic modelling of MRI scanners

This chapter will elaborate on gradient coil design methods used in the thesis and the acoustic modelling of MRI scanners.

For the gradient coil design, a finite difference method is used for the meshing of the coil layers. The corresponding current density in a finite difference grid is expressed by the finite difference form of the stream function. The coil performance parameters, such as the storage energy and power dissipation, can also be expressed by the finite difference form of the stream function. The finite difference expression of the coil performance parameters can be easily integrated into the coil design for optimization. Another method for gradient coil design used in this thesis is the discrete wire method. This method applies a shape function to represent the coil loops, which makes it possible to directly control the coil wire shape, spacing and positions. This method will be initially applied to design gradient coils for use in cylindrical MRI systems in this thesis. It is important to note that this method can also be easily implemented into gradient coil designs in planar MRI systems.

For the acoustic modelling, the Finite Element Method (FEM)-based commercial package ANSYS Mechanical APDL was used [91]. This package contains an acoustic analysis module and a mechanical vibration analysis module. These two modules can be coupled during the modelling process, which enables the transfer of the complex mechanical vibrations of the solid structures to acoustic waves in the fluid media, air. Thus, the acoustic modelling actually includes modelling of the mechanical structure and modelling of the fluid media. The APDL, which is an abbreviation of ANSYS parametric design language, makes all the modelling process realized by command flow. Compared to a graphical user interface (GUI), the APDL is much more flexible and efficient in modelling, especially in regard to parameter alterations, which makes it convenient for model modification and optimization.

The following section is divided into two parts to give the details of the gradient coil design methods used in this thesis and then the acoustic modelling process.

3.1 Gradient coil design methods

There are two main kinds of gradient coil design methods used in this thesis. One is the continuous-current density-based finite difference method and the other is the discrete wire method. In the following section, the continuous-current density-based finite difference method is simply called the finite difference method.

3.1.1 Finite difference method for gradient coil design

The target field approach is commonly used for gradient coil design [20] and this method was formulated in a finite-difference framework in this thesis [34] and is briefly summarized here. For cylindrical gradient coils, based on the Bio-Savart law, the z component of the magnetic flux density can be derived as [34]

$$B_z(x,y,z)=\frac{\mu_0}{4\pi}\int_0^{2\pi}\int_{-0.5L_p}^{0.5L_p}\frac{-J_\theta^{(p)}Q}{\left[S^2+Q^2+\left(z-z_p\right)^2\right]^{1.5}}R_p\mathrm{d}\theta\mathrm{d}z_p + \frac{\mu_0}{4\pi}\int_0^{2\pi}\int_{-0.5L_s}^{0.5L_s}\frac{-J_\theta^{(s)}Q}{\left[S^2+Q^2+(z-z_s)^2\right]^{1.5}}R_s\mathrm{d}\theta\mathrm{d}z_s \tag{3-1}$$

Here the current densities are expressed in the cylindrical coordinate system with μ_0 the permeability, J the surface current density, the θ subscript representing the circumferential component of the current density, R the radius of the coil, L the length of the coil, and (p) and (s) representing the primary coil and shielding coil, respectively. The intermediate terms S and Q are

$$\begin{aligned} S&=-x\sin\theta+y\cos\theta \\ Q&=x\cos\theta+y\sin\theta-R \end{aligned} \tag{3-2}$$

Generally, there are requirements to control one or more coil performance parameters during the gradient coil design, for example, power dissipation, magnetic energy etc.

The power dissipation P for the coil design optimization [6, 32, 90, 92] is given as

$$P=\frac{\rho}{h}\int_0^{2\pi}\int_{-0.5L_\mathrm{p}}^{0.5L_\mathrm{p}}\left(\left|J_\theta^{(\mathrm{p})}(\theta,z_\mathrm{p})\right|^2+\left|J_\mathrm{z}^{(\mathrm{p})}(\theta,z_\mathrm{p})\right|^2\right)R_\mathrm{p}\mathrm{d}\theta\mathrm{d}z_\mathrm{p} + \frac{\rho}{h}\int_0^{2\pi}\int_{-0.5L_\mathrm{s}}^{0.5L_\mathrm{s}}\left(\left|J_\theta^{(\mathrm{s})}(\theta,z_\mathrm{s})\right|^2+\left|J_\mathrm{z}^{(\mathrm{s})}(\theta,z_\mathrm{s})\right|^2\right)R_\mathrm{s}\mathrm{d}\theta\mathrm{d}z_\mathrm{s} \tag{3-3}$$

and the magnetic energy W is expressed as

$$W=\frac{\mu_0}{8\pi}\int_0^{2\pi}\int_{-0.5L_\mathrm{p}}^{0.5L_\mathrm{p}}\int_0^{2\pi}\int_{-0.5L_\mathrm{p}}^{0.5L_\mathrm{p}}\frac{\left(J_\theta^{(\mathrm{p})}(\theta,z_\mathrm{p}),J_{z_\mathrm{p}}^{(\mathrm{p})}(\theta,z_\mathrm{p})\right)\cdot\left(J_{\theta'}^{(\mathrm{p})}(\theta',z_\mathrm{p}'),J_{z_\mathrm{p}'}^{(\mathrm{p})}(\theta',z_\mathrm{p}')\right)}{\sqrt{\left|2R_\mathrm{p}^2-2R_\mathrm{p}^2\cos(\theta-\theta')+(z_\mathrm{p}-z_\mathrm{p}')^2\right|}}R_\mathrm{p}^2\mathrm{d}\theta\mathrm{d}z_\mathrm{p}\mathrm{d}\theta'\mathrm{d}z_\mathrm{p}' + \frac{\mu_0}{8\pi}\int_0^{2\pi}\int_{-0.5L_\mathrm{s}}^{0.5L_\mathrm{s}}\int_0^{2\pi}\int_{-0.5L_\mathrm{s}}^{0.5L_\mathrm{s}}\frac{\left(J_\theta^{(\mathrm{s})}(\theta,z_\mathrm{s}),J_{z_\mathrm{s}}^{(\mathrm{s})}(\theta,z_\mathrm{s})\right)\cdot\left(J_{\theta'}^{(\mathrm{s})}(\theta',z_\mathrm{s}'),J_{z_\mathrm{s}'}^{(\mathrm{s})}(\theta',z_\mathrm{s}')\right)}{\sqrt{\left|2R_\mathrm{s}^2-2R_\mathrm{s}^2\cos(\theta-\theta')+(z_\mathrm{s}-z_\mathrm{s}')^2\right|}}R_\mathrm{s}^2\mathrm{d}\theta\mathrm{d}z_\mathrm{s}\mathrm{d}\theta'\mathrm{d}z_\mathrm{s}' \tag{3-4}$$

Here ρ is the resistivity of the coil fabrication material, h is the thickness of the coil layer and the subscript z of J represents the longitudinal component of the surface current density.

For the shielding effect control of an actively shielded gradient coil, there are two strategies used in this thesis. The typical control method is to minimize the magnetic flux density on the cryostat, namely stray field control. The newly proposed secondary magnetic field control method, which is produced by the cryostat, is also used in this thesis. For an actively shielded gradient coil, the expression of the stray field is the same as for Eq. (3-1), where the difference is the calculated target point. The former is to calculate the magnetic field on the surface of the DSV, and the latter is to calculate the magnetic field on the surface of the cryostat.

For the secondary magnetic field control strategy, the eddy current on the cryostat needs to be calculated. If a sinusoidal current with angular frequency ω is used as the input on the gradient coil, the derived eddy current expression is as follows [93]

$$\frac{J(r(\theta_\mathrm{c},z_\mathrm{c}),\omega)}{\sigma}+\mathrm{i}\omega\frac{\mu_0}{4\pi}\int_0^{2\pi}\int_{-0.5L_\mathrm{c}}^{0.5L_\mathrm{c}}\frac{J^{(\mathrm{c})}\left(r(\theta',z_\mathrm{c}'),\omega\right)}{\left|r(\theta_\mathrm{c},z_\mathrm{c})-r(\theta',z_\mathrm{c}')\right|}R_\mathrm{c}\mathrm{d}\theta'\,\mathrm{d}z_\mathrm{c}' + \mathrm{i}\omega\frac{\mu_0}{4\pi}\left[\int_0^{2\pi}\int_{-0.5L_\mathrm{p}}^{0.5L_\mathrm{p}}\frac{J^{(\mathrm{p})}\left(r(\theta,z_\mathrm{p}),\omega\right)}{\left|r(\theta_\mathrm{c},z_\mathrm{c})-r(\theta,z_\mathrm{p})\right|}R_\mathrm{p}\mathrm{d}\theta\,\mathrm{d}z_\mathrm{p}+\int_0^{2\pi}\int_{-0.5L_\mathrm{s}}^{0.5L_\mathrm{s}}\frac{J^{(\mathrm{s})}(r(\theta,z_\mathrm{s}),\omega)}{|r(\theta_\mathrm{c},z_\mathrm{c})-r(\theta,z_\mathrm{s})|}R_\mathrm{s}\mathrm{d}\theta\,\mathrm{d}z_\mathrm{s}\right]=0 \tag{3-5}$$

where $r(\theta, z)$ is the cylindrical coordinate of the current density and the subscript c represents the warm bore wall. The eddy current on the warm bore wall was considered for the gradient coil design [50, 94, 95], where the induced secondary magnetic field on the surface defined by DSV was

constrained (measured as a percentage of the target field). The shielding effect was defined as the shielding ratio [96], which is a ratio of the secondary magnetic field strength over the DSV dividing the primary magnetic field strength.

The stream function, ψ, was used here to obtain the wire contours. The relationship between the current density and the stream function is given by Eq. (3-6) [97]

$$\begin{aligned} J_\theta &= \frac{\partial \psi}{\partial z} \\ J_z &= -\frac{\partial \psi}{R \partial \theta} \end{aligned} \tag{3-6}$$

The core of the finite difference method was to perform the difference operation on Eq. (3-6) and then integrate the difference computation into the above expressions. Fig. 3-4 shows an illustration of the difference process.

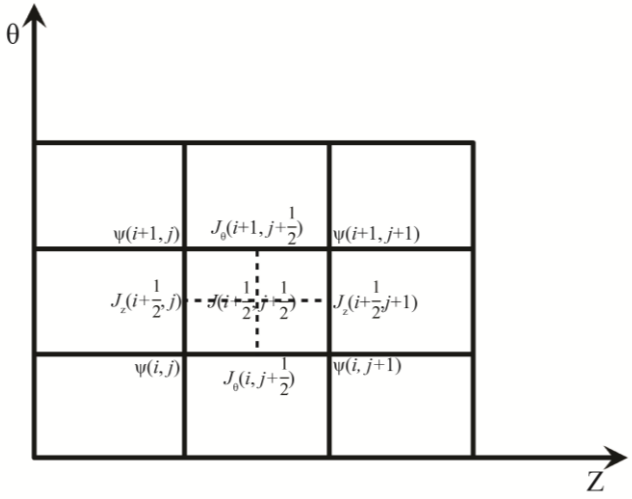

Fig. 3-1 Discretization in a finite difference compuation for the gradient coil design.

The difference computations of the current densities are expressed as follows

$$\begin{aligned} J_\theta\left(i, j+\frac{1}{2}\right) &= \frac{\psi(i,j+1)-\psi(i,j)}{\Delta z} \\ J_\theta\left(i+1, j+\frac{1}{2}\right) &= \frac{\psi(i+1,j+1)-\psi(i+1,j)}{\Delta z} \end{aligned} \tag{3-7}$$

$$\begin{aligned} J_z\left(i+\frac{1}{2}, j\right) &= -\frac{\psi(i+1,j)-\psi(i,j)}{R\Delta\theta} \\ J_z\left(i+\frac{1}{2}, j+1\right) &= -\frac{\psi(i+1,j+1)-\psi(i,j+1)}{R\Delta\theta} \end{aligned} \tag{3-8}$$

As mentioned above, the integral functions Eq. (3-1) and Eqs. (3-3)–(3-5) were calculated by the sum of the finite difference grids. The current density at the centre of the grid was used to represent the discrete value of the whole grid. A mean-value operation for the current density was conducted as

$$\begin{aligned} J_\theta\left(i+\frac{1}{2},j+\frac{1}{2}\right)&=\frac{1}{2}\left[J_\theta\left(i,j+\frac{1}{2}\right)+J_\theta\left(i+1,j+\frac{1}{2}\right)\right] \\ J_z\left(i+\frac{1}{2},j+\frac{1}{2}\right)&=\frac{1}{2}\left[J_z\left(i+\frac{1}{2},j\right)+J_z\left(i+\frac{1}{2},j+1\right)\right] \end{aligned} \tag{3-9}$$

Thus, the continuous current density was discretized and expressed by the surrounding stream function.

There are many approaches to constrain the field deviation, such as the maximum field error on the surface of the DSV, the maximum local gradient error through the DSV, the least mean square (LMS) error on surface of the DSV etc [98]. Taking the LMS error as an example, the whole design process was reduced to

$$\text{Min}\{\lambda_1\mathbf{P}+\lambda_2\mathbf{W}\} \tag{3-10}$$

subject to

$$\begin{aligned} &\frac{\text{norm}\left(B_z^{\text{DSV}}\text{-}B_z^{\text{target}}\right)}{\text{norm}\left(B_z^{\text{target}}\right)}<\varepsilon_1 \\ &\text{norm}\left(B_z^{\text{cryostat}}\right)<B_z^{\text{shield}} \end{aligned} \tag{3-11}$$

or

$$\begin{aligned} &\frac{\text{norm}\left(B_z^{\text{DSV}}\text{-}B_z^{\text{target}}\right)}{\text{norm}\left(B_z^{\text{target}}\right)}<\varepsilon_1 \\ &\frac{\text{norm}\left(\gamma B_z^{\text{target}}+B_z^{\text{eddy}}\right)}{\text{norm}\left(\gamma B_z^{\text{target}}\right)}<\varepsilon_2 \end{aligned} \tag{3-12}$$

where **P** is the matrix calculated from Eq. (3-3) by finite difference of the differential equations and discrete sum of the integral equations, **W** is the matrix calculated from Eq. (3-4) by the same method, λ_1 and λ_2 are the weighting factors, B_z^{DSV} is the magnetic field on the surface defined DSV, B_z^{target} is the target field, B_z^{cryostat} is the magnetic field on the cryostat, B_z^{shield} is the shielding error, B_z^{eddy} is the magnetic field produced by the eddy current, γ is the shielding ratio, and ε_1 and ε_2

are the field errors. Eq. (3-11) is the stray field control strategy for the shielding and Eq. (3-12) is the secondary magnetic field control strategy.

3.1.2 Discrete wire method for gradient coil design

The discrete wire method in this thesis is initially used to design spiral gradient coils. Certainly, the proposed spiral gradient coil design method can be easily transformed into a conventional separate-loop coil design (see head gradient coil design in section 4.3). The following gives a detailed review of this method.

In the cylindrical MRI system, when a transverse gradient coil is unwrapped from a cylinder, the current paths look similar to a set of ellipses, in what is often called a "fingerprint" pattern. Therefore, a quasi-elliptic geometry may be a good approximation of the transverse gradient coil loop. As a variation, a shape butted by two half quasi-elliptic curves was proposed to represent the basic geometry of the transverse gradient coil loop [42] to maximize the optimization space. The expression of such a quasi-elliptic curve is given in Eq. (3-13), where Y_0 and Z_0 are the semi-major axis and semi-minor axis lengths, respectively, with the power p being usually equal to or larger than 1.

$$\frac{|y|^p}{Y_0^2}+\frac{|z|^p}{Z_0^2}=1, \qquad p\geq 1 \tag{3-13}$$

To make a spiral connection between the coil loops, a quasi-conical base was imagined, and the coil curve was first wound around the surface of the base, and then a mathematical transform was applied to map the curve to the coil cylinder. Fig. 3-2 presents such a spiral curve on a quasi-conical base. The three view drawings are shown. It is easy to see that by using this winding scheme the designed gradient coil is always a multi-loop. Here, we assume that the cross-section of the quasi-conical base at the bottom, which is of a quasi-elliptic geometry, extends from $-y_1$ to y_1 and z_1 to z_2 on a plane, and the height of the quasi-conical base extends from 0 to h. The vertex of the quasi-conical base is located at $(0, z_0, h)$. Note that z_0 is not definite at the centre. Here the oblique base is just an example to illustrate a common case.

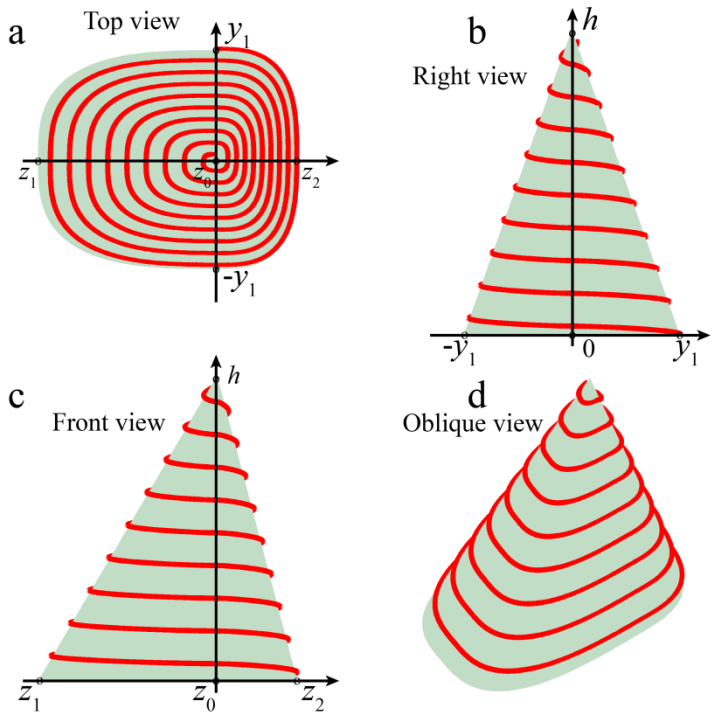

Fig. 3-2 Illustration of a quasi-conical base on which a spiral curve is wound for a transverse gradient coil design. The three view drawings are shown with (a) a top view, (b) a right view, and (c) a front view. An oblique view is also plotted in (d).

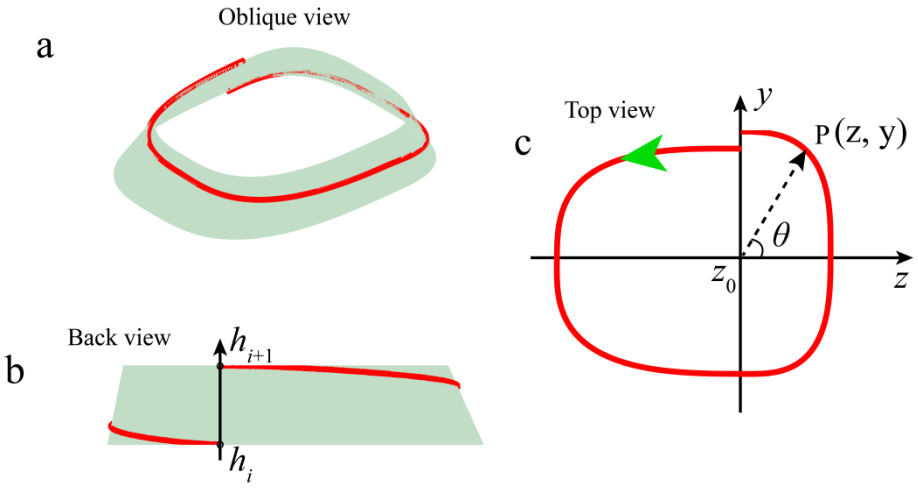

Fig. 3-3 A spiral quasi-elliptical curve for a transverse gradient coil design, (a) oblique view of a single spiral quasi-elliptic loop on a quasi-conical base, (b) back view of the spiral loop, and (c) top view of the spiral loop.

A single spiral loop is extracted from Fig. 3-2 and shown on a section of the quasi-conical base in Fig. 3-3. Here, the spanning height of this spiral loop is assumed to be from h_i to h_{i+1} — as marked in the back view in Fig. 3-3 (b) — and the parametric coordinate for the spiral angle is θ, shown in the top view in Fig. 3-3 (c), where the spiral direction is also pointed out (see the arrow direction.

Note the spiral direction is from 2π to 0). According to these assumptions, the coordinate of a point P in the spiral loop is:

$$\begin{aligned} y&=\frac{h_i+(h_{i+1}-h_i)\frac{\theta}{2\pi}}{h}y_1\cos^{\frac{2}{p}}(\theta) \\ z&=z_0+\frac{h_i+(h_{i+1}-h_i)\frac{\theta}{2\pi}}{h}(z_2-z_0)\sin^{\frac{2}{p}}(\theta) \end{aligned} \qquad 0\le\theta<\frac{\pi}{2} \tag{3-14}$$

$$\begin{aligned} y&=-\frac{h_i+(h_{i+1}-h_i)\frac{\theta}{2\pi}}{h}y_1\cos^{\frac{2}{p}}(\theta) \\ z&=z_0+\frac{h_i+(h_{i+1}-h_i)\frac{\theta}{2\pi}}{h}(z_2-z_0)\sin^{\frac{2}{p}}(\theta) \end{aligned} \qquad \frac{\pi}{2}\le\theta<\pi \tag{3-15}$$

$$\begin{aligned} y&=-\frac{h_i+(h_{i+1}-h_i)\frac{\theta}{2\pi}}{h}y_1\cos^{\frac{2}{p}}(\theta) \\ z&=z_0-\frac{h_i+(h_{i+1}-h_i)\frac{\theta}{2\pi}}{h}(z_0-z_1)\sin^{\frac{2}{p}}(\theta) \end{aligned} \qquad \pi\le\theta<\frac{3\pi}{2} \tag{3-16}$$

$$\begin{aligned} y&=\frac{h_i+(h_{i+1}-h_i)\frac{\theta}{2\pi}}{h}y_1\cos^{\frac{2}{p}}(\theta) \\ z&=z_0-\frac{h_i+(h_{i+1}-h_i)\frac{\theta}{2\pi}}{h}(z_0-z_1)\sin^{\frac{2}{p}}(\theta) \end{aligned} \qquad \frac{3\pi}{2}\le\theta\le2\pi \tag{3-17}$$

If the radius of the coil cylinder is a, then the transformed coordinate from the quasi-conical base to the coil cylinder is:

$$\begin{aligned} x_c&=a\cos\left(\frac{y}{a}\right) \\ y_c&=a\sin\left(\frac{y}{a}\right) \\ z_c&=z \end{aligned} \tag{3-18}$$

The coordinate (x_c,y_c,z_c) given above is a point in the quarter ($-\pi/2<\varphi<\pi/2$, $z>0$) of the x-gradient coil. Here, φ is the angle of the gradient coil in a cylindrical coordinate system. For the other quarters of the x-gradient coil or y-gradient coil, the expressions are similar, but with a change in the corresponding coordinate variables.

In the design, the spiral transverse gradient coil pattern is optimized by adjusting the following variables, (a) the centre of the spiral loops, which is controlled by the value of z_0, (b) the power p of the butted quasi-elliptic curve, (c) the height positions of the start and end points of the spiral loops, and (d) the current strength. The total height h of the quasi-conical base can be specified arbitrarily

in our theory and the loop quantities of the spiral coil are pre-set, and can be adjusted in different trials to determine an optimal coil design.

The basic geometry of the spiral longitudinal gradient coil designed in this work stemmed from the structure of a solenoid. Fig. 3-4 shows such a spiral structure on a cylindrical surface, where (a) displays an oblique view of such a structure and (b) is the front view. Its unwrapping geometry on the cylindrical surface, as is illustrated in Fig. 3-4 (c), are straight lines with every straight line spanning a spiral circular cycle. A single unwrapping spiral loop is plotted in Fig. 3-4 (d). Here, we assume that it stretches from z_i to z_{i+1} along the z direction. Thus, the z coordinate of a point P in the spiral loop is:

$$z=z_{i+1}-(z_{i+1}-z_i)\frac{\theta}{2\pi} \tag{3-19}$$

If the radius of the coil cylinder is a, then the three-axis coordinate of the point P in a Cartesian coordinate system is:

$$\begin{aligned} x_c&=a\cos(\theta)\\ y_c&=a\sin(\theta)\\ z_c&=z \end{aligned} \tag{3-20}$$

The strategy in the spiral longitudinal gradient coil design is to optimize the following variables: (a) the positions of the start and end points of the spiral loops, and (b) the current strength. Similar to the spiral transverse gradient coil design, the number of loops of the spiral longitudinal coil is pre-set, which can be adjusted in different trials to determine an optimal coil design.

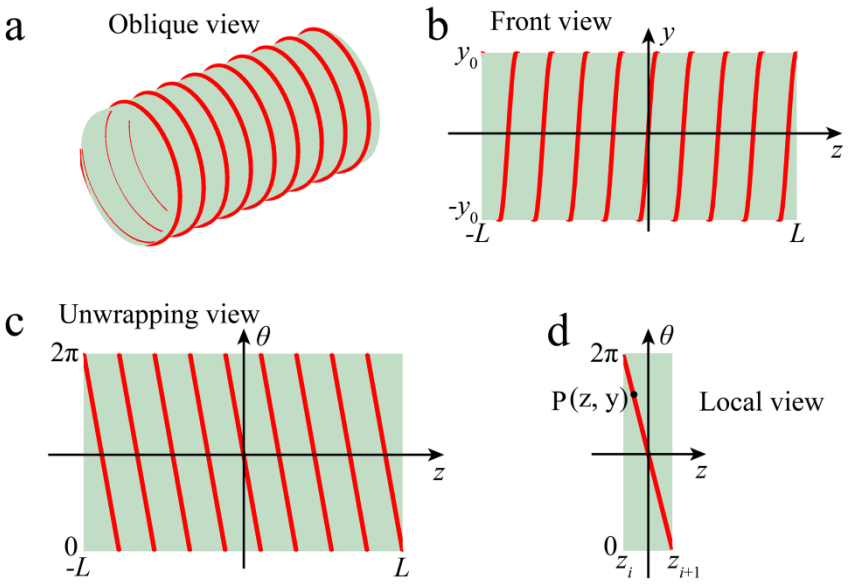

Fig. 3-4 Illustration of a spiral structure on a cylindrical surface for a longitudinal gradient coil design, (a) oblique view of the spiral structure, (b) front view of the spiral structure, (c) unwrapping view of the spiral structure, and (d) local view of the unwrapping spiral structure with a single loop.

The Biot-Savart law for a curve integral was used in the magnetic field calculation of the spiral coil, see Eq. (3-21):

$$B(\boldsymbol{r}) = \frac{\mu_0}{4\pi}\int \frac{I\mathrm{d}\boldsymbol{l}\times(\boldsymbol{r}-\boldsymbol{l})}{|\boldsymbol{r}-\boldsymbol{l}|^3} \tag{3-21}$$

where μ_0 is the vacuum permeability, I is the current, $\boldsymbol{l}$ is the current segment vector and $\boldsymbol{r}$ is the space point.

For a numerical computation, the integral was expressed approximately as the sum of a series of discrete wire segments, as given below:

$$\begin{gathered} l_x = a\cos\varphi_2 - a\cos\varphi_1 \\ l_y = a\sin\varphi_2 - a\sin\varphi_1 \\ r = \sqrt{\left(x' - a\cos\frac{\varphi_1+\varphi_2}{2}\right)^2 + \left(y' - a\sin\frac{\varphi_1+\varphi_2}{2}\right)^2 + \left(z' - \frac{z_1+z_2}{2}\right)^2} \\ B_z(x',y',z') = \sum \frac{\mu_0}{4\pi} I \frac{\left(y' - a\sin\frac{\varphi_1+\varphi_2}{2}\right) l_x - \left(x' - a\cos\frac{\varphi_1+\varphi_2}{2}\right) l_y}{r^3} \end{gathered} \tag{3-22}$$

where (x',y',z') is a spatial point coordinate, l_x and l_y are the x- and y- direction vector components of the discrete wire segment, respectively, and φ_1 and φ_2 are the circumferential coordinates of wire segment endpoints in a cylindrical coordinate system. Only the z component of the magnetic field was considered for the gradient coil design.

The target in this design is to minimize the function:

$$f = \mathrm{norm}\left(B_z^{\mathrm{DSV}} - B_z^{\mathrm{Target}}\right) + \lambda \cdot \mathrm{norm}\left(B_z^{\mathrm{Shield}}\right) \tag{3-23}$$

subject to:

$$\frac{\max\left|B_z^{\mathrm{DSV}} - B_z^{\mathrm{Target}}\right|}{\max\left|B_z^{\mathrm{Target}}\right|} < \varepsilon \tag{3-24}$$

$$\max\left|B_z^{\mathrm{Shield}}\right| < B_z^{\mathrm{Constraint}} \tag{3-25}$$

In addition, the wire spacing for the transverse gradient coil design is controlled by:

$$|h_{i+1} - h_i| \geq \Delta h \tag{3-26}$$

For the longitudinal gradient coil design, the wire spacing is controlled by:

$$|z_{i+1} - z_i| \geq \Delta z \tag{3-27}$$

where B_z^{DSV} is the calculated field on the DSV surface, B_z^{Target} is the target magnetic field defined as $G_x \cdot x$ (G_x is the magnetic field gradient of the x gradient coil), B_z^{Shield} is the magnetic field on the magnet warm bore wall, λ is the weighting factor, ε is the non-uniformity error of the magnetic field gradient, $B_z^{\mathrm{Constraint}}$ is the permitted maximum magnetic field on the magnet warm bore wall, Δh is the designated minimum height difference (see Fig. 3-2 and Fig. 3-3), and Δz is the designated minimum distance of the adjacent coils along the z direction. The weighting factor was used to balance the design between the target field error inside the imaging area and the stray field.

3.2 Acoustic modelling of MRI scanner

The FEM package ANSYS Mechanical APDL is used to calculate the acoustic field produced by gradient coil switching, which numerically solves the mechanical vibration and acoustic wave equation. For the mechanical vibration, the dynamic behaviour of the structure can be described by the following equation [99]:

$$M\ddot{\xi} + C\dot{\xi} + K\xi = F \tag{3-28}$$

where **M**, **C** and **K** are matrices referred to respectively as the mass, damping and stiffness; **F** is the force matrix; and ξ is the mechanical displacement. In a homogeneous non-viscous fluid medium, the acoustic wave propagation is governed by the following equation [100]:

$$\nabla^2 p = \frac{1}{c^2}\ddot{p} \tag{3-29}$$

where ∇^2 is the Laplace operator; c is the speed of sound in the fluid and p is the acoustic pressure. Also, the acoustic pressure and the fluid particle speed have the following relationship [101]:

$$\rho \frac{\partial \boldsymbol{v}}{\partial t} = -\nabla p \tag{3-30}$$

where ρ is the fluid density; $\boldsymbol{v}$ is fluid particle speed; t is the time; ∇ is the gradient operator; and p is the acoustic pressure. At the interface, the structure speed and the fluid particle speed are identical [100]:

$$\boldsymbol{v} = \dot{\xi} \tag{3-31}$$

Thus, the structure and the fluid are coupled and the structural vibration radiates sound to the fluid.

As with finite element modelling, the basic procedure is (a) element type selecting, (b) entity modelling, (c) attribute assigning, (d) meshing, (e) load and boundary condition applying, (f) solving, and (g) post-processing. All the operations can be realized via command flow in ANSYS Mechanical APDL. For specific commands, refer to ANSYS Help and also *http://www.ansys.stuba.sk/html/c-index.htm*.

The entity is the physical structure of the modelled object. For the acoustic analysis, it also contains the fluid space, which normally indicates air. However, before entity modelling, it is necessary to select the element type. The APDL command for the operation is *et*. The element type used for the mechanical structure of the MRI scanner was *SOLID 185*, which is an eight-node brick element and every node has three displacement degrees of freedom (DOF). This element type is suitable for three-dimensional (3D) modelling of solid structures. It supports not only hexahedral mesh, but also prismatic mesh and tetrahedral mesh. For the air modelling, two element types were used, namely *FLUID 30* and *FLUID 130*, both of which are 3D element types. *FLUID 30* is an eight-node element used for the 3D simulation of the air space in and around the MRI scanner and *FLUID 130*

is a four-node element used to simulate the absorptive layer of the air space. This assumes that the MRI scanner is located in a free space with no acoustic wave coming back, so as to accurately investigate the acoustic characteristics of only the MRI scanner itself. The *FLUID 30* element supports hexahedral, prismatic and tetrahedral meshes, like the *SOLID 185*, and correspondingly, the *FLUID 130* also supports triangular area to match *FLUID 30*. There are also two types of *FLUID 30* used for the acoustic simulation. One is with KEYOPT (2)=1, with DOFs which are three-direction displacements and pressure. However, if KEYOPT (2)=0, the DOF of *FLUID 30* will be only pressure. Some element types require input of real constants when modelling. For instance, *FLUID 30* needs a reference pressure and *FLUID 130* should assign a radius of the absorptive layer, but it is not necessary for *SOLID 185* to set real constants. After the element type selection, modelling of the solid structure or fluid can begin.

Fig. 3-5 shows the acoustic model entity of an MRI scanner using finite element modelling, where (a) is the mechanical entity and (b) is the whole model entity including the mechanical entity and fluid space. The mechanical entity consists of main magnet coils, warm bore wall, primary cold shield, secondary cold shield, liquid helium vessel, gradient coils, epoxy resin and bolts between the gradient assembly and the cryostat. The surrounding air is simulated as a sphere. Due to the symmetry of the scanner structure, only a quarter of the whole model is simulated.

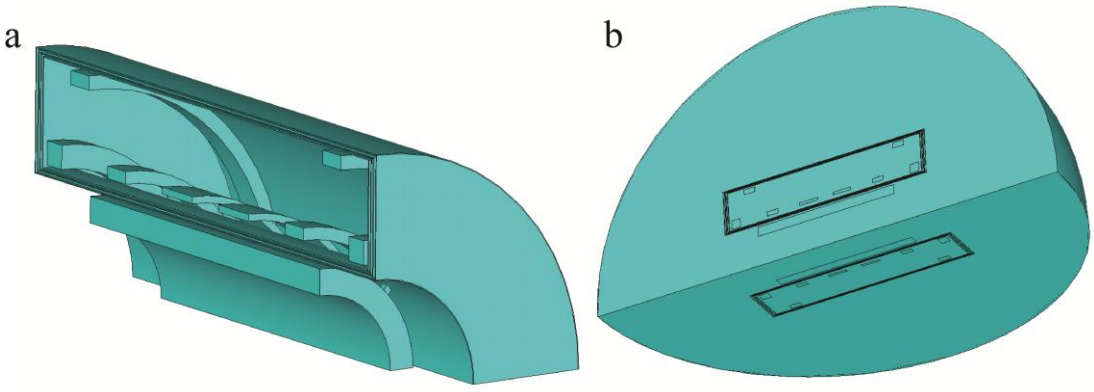

Fig. 3-5 Acoustic model entity of an MRI scanner: (a) mechanical entity and (b) whole model entity including the mechanical entity and fluid space.

The attribute assigning process is to give physical meaning to the model entity. For example, the warm bore wall of the cryostat is made of steel. In the acoustic analysis, the warm bore wall will vibrate due to the mechanical transmission of the gradient assembly and induced eddy current, thus radiating an acoustic field. Here the mechanical property of steel is necessary for the model. However, if the case is not an acoustic problem or a mechanical problem, for instance an electrical problem, then the electrical property should be input for the calculation.

In the acoustic model of the MRI scanner, the physical properties of the components are based on the structure materials [72]. For example, the gradient coils are made of copper, so the input parameters for the mechanical properties of gradient coils are copper's Young's modulus, Poisson's ratio and density. Sometimes, the damping ratio is also an important parameter for vibration analysis. The ANSYS Mechanical APDL command for assigning an attribute to a volume entity is *vatt*. However, if the model entity is area, it will be *aatt* and if it is a line entity, it will be *latt*.

After attribute assigning, the next step and also the most important step is to mesh the model entity. The mesh quality has an important influence on the ultimate result and the efficiency of the solution. Generally, if the region needs special attention or is a crucial contact part it may require a small-size mesh, but if the region is not of interest or not critical for the result, it is not necessary for it to be densely meshed. The mesh shapes should be identical to the supported shapes of the selected element type. Taking the acoustic model of an MRI scanner as an example, *FLUID 30* supports hexahedral, prismatic and tetrahedral meshes, but if there are pyramidal shapes during the meshing, the calculated result may be inaccurate.

The operation *free meshing* is commonly used during model meshing. Although it is easy to implement, it does not always work well. The region of interest may have low-quality mesh, especially for the model details, giving rise to results not as accurate as expected. Sometimes when the meshing conditions are very complex, *free meshing* may be aborted.

To achieve a high-quality meshing, reasonable dividing up of the entity model or subordinate meshing is helpful. If the entity model is a volume, the subordinate meshing indicates that the areas or lines attached to the volume should be meshed first. Most often, these two measures are combined. By dividing the original irregular entity model into regular entities, some regions of the model can be specially meshed. The *volume sweep* meshing can be accompanied by the dividing and subordinate meshing, which is capable of meshing the entity into hexahedral grids. Because the element type *FLUID 30* is designed to be eight-node, the advantage of the hexahedral grids for a 3D acoustic model is calculation-efficient with a small node quantity and the result accuracy can also be improved.

It is not necessary to assign the attributes before meshing. It is possible to mesh the entity model first and then modify the finite element attribute using the ANSYS command *emodif*. This command can modify the finite element type, real constant or material property. By changing the fluid type *FLUID 30* with KEYOPT (2)=0 at the finite element not attached to the mechanical structure to type *FLUID 30* with KEYOPT (2)=1, the element DOFs transform from three-direction

displacements and pressure to pressure only. This can significantly improve the computing speed.

Fig. 3-6 shows a meshed acoustic model of an MRI scanner. The meshing process combined the entity cutting, *volume sweep* meshing and *emodif* operation. All the meshed finite element grids were hexahedral shapes, which had smaller element and node quantities compared with tetrahedral grids, thus largely boosting the computing speed and reducing memory storage.

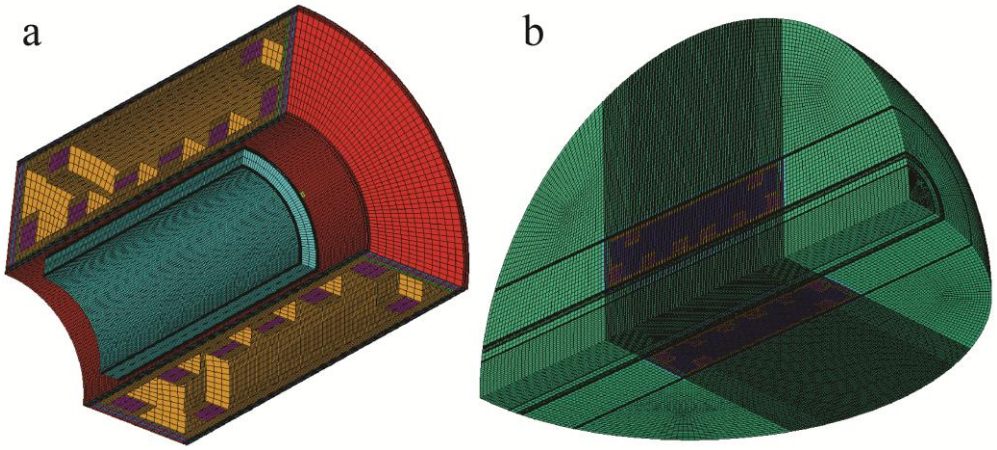

Fig. 3-6 Meshed acoustic model of an MRI scanner: (a) mechanical model and (b) acoustic model including the fluid space.

After meshing but before solving in the acoustic modelling process of an MRI scanner, there are several other procedures that need to be implemented. The acoustic model of an MRI scanner contains both mechanical structures and fluid space and the interfaces of these two different kinds of substances must be coupled to ensure that the mechanical vibration can transmit to the fluid space, thus radiating acoustic waves. By selecting the exterior finite element nodes of the mechanical model and the surrounding fluid elements, and then applying *sf, all*, and *fsi*, the mechanical structure and the fluid space will be coupled in the acoustic model. Some constraint conditions must be applied to simulate the numerical model of the mechanical structures. For example, the displacements of scanner edges were restricted to be zero, representing the fact that the mechanical structures are fixed but not suspended. After that, the Lorentz force was loaded on the gradient coil. For the air space, an infinite boundary was applied on the surface of the sphere volume via the command *esurf*. The surface therefore was set as a perfect match layer (PML) with no acoustic wave reflection.

That is the acoustic model nearly established. As mentioned above, only a quarter of the whole model was established due to the symmetry of the scanner structure. It is important to note that the transverse gradient coils are 1/4 symmetry for their mechanical structures. ASNSYS gives a

command *dsym* to realize the symmetric or asymmetric operation on the finite element model. The operating consequence is equal to applying the symmetric or asymmetric boundary constraint conditions. An illustration of the mechanical-acoustic coupling, displacement boundary conditions applied and symmetric or asymmetric boundary conditions applied is shown in Fig. 3-7. Note that the symmetric or asymmetric boundary condition that was applied to the air nodes with only one DOF pressure is invalid for the calculation, which has no influence on the ultimate result. The valid boundary condition that applies is on the mechanical nodes, which controls their displacement DOFs.

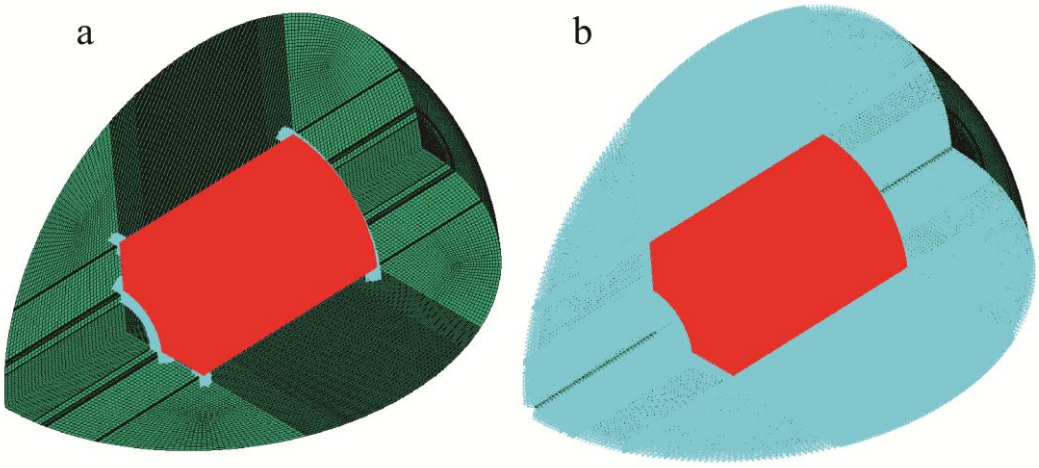

Fig. 3-7 Load options of an MRI scanner acoustic model: (a) mechanical-acoustic coupling and displacement boundary conditions applying and (b) symmetric or asymmetric boundary condition applying on the model edges.

After the model is established, the next procedure is to set the solving method, namely the analysis type. Commonly used analysis types for an acoustic analysis are modal analysis, harmonic analysis and transient analysis. A modal analysis is usually used to detect the natural frequencies of mechanical structures, participation factor, mode shapes [102] etc. For acoustic noise control of a mechanical system, the natural frequencies or resonance frequencies are dominant within the overall SPL. Therefore, by taking measures that target the natural frequencies, the acoustic control effect will be significant. Aside from a modal analysis, a harmonic analysis can also help to detect the dominant natural frequencies. A harmonic analysis can pinpoint the frequencies which radiate high SPL. If the frequency step is small enough in a harmonic analysis, the resonant frequency bands can be accurately determined. However, the direct goal of a harmonic analysis is to investigate the single-frequency response of a system. The calculated result is the steady-state response of a single-frequency excitation input, which has no relationship to the transient inputting excitation form. Thus, it can be used to explore the intrinsic properties of a system, regardless of the real excitation. Whereas, a transient analysis uses the discrete point input of a realistic excitation,

which mimics the response process of a specific excitation form. If the dynamic process of acoustic wave propagation is expected, a transient analysis should be selected. However, a transient analysis is usually time consuming. If the model is much complex with a number of elements and nodes, the transient analysis will be much slower.

After the model solving, the data of the model solutions will be saved in a result file. For different physical circumstances, the saved formats of the result data are different. For example, for a mechanical analysis, including the acoustic analysis, the result data is saved in an *.rst* file. However, for an electromagnetic analysis, the format of the result file is *.rmg*. For a thermal analysis, the result file is in the format of *.rth*. The post-processing procedure is used to collect the calculation results. In an analysis, the default set is to save all the calculation data during the solving including the intermediate process and the ultimate result. Thus, the result file is usually very large, especially when the model contains a large number of elements and nodes. Nevertheless, to save space it is possible to compress the final file via the commands *outpr* and *outres*. These commands can be set to save the full results or only part of the calculated results. It is also possible to make further mathematic calculations on the result data, for example, changing the sound pressure distribution to SPL distribution in an acoustic analysis. It is necessary to mention that the post processing includes two forms, general post processing with command */post1* and time-history post processing with command */post26*. The general post processing checks the calculation results of each load step individually. By comparison, the time-history post processing summarises all of the time-step or frequency-step results. The data result can be read via the command **vread* and written into a text file according to the specified format via the command **vwrite*.

The above description gives an overview of the basic modelling procedure and key ANSYS Mechanical APDL commands. However, for a complete command flow, there are a range of commands and operators and a syntax to follow and every command operation has many options. These commands can complete all the work from job establishment to data collection of post processing. All the acoustic modellings of the MRI scanner in this thesis were realized using APDL to complete acoustic calculations and acoustic control optimization.

Chapter 4

Gradient coil design for MRI scanners

This chapter presents the gradient coil design for MRI scanners. Three parts are included in total, which are based on the contents of the papers below. To make the work fit well with the thesis structure, some minor modifications were made.

Y. Wang, F. Liu, Y. Li, F. Tang, and S. Crozier, "Asymmetric gradient coil design for use in a short, open bore magnetic resonance imaging scanner," *Journal of Magnetic Resonance*, vol. 269, pp. 203-212, 2016.

Y. Wang, X. Xin, F. Liu and S. Crozier, "Spiral gradient coil design for use in cylindrical MRI systems," *IEEE Transactions on Biomedical Engineering*, DOI:10.1109/TBME.2017.2725962, 2017.

Y. Wang, F. Liu, X. Zhou, and S. Crozier, "Design of transverse head gradient coils using a layer-sharing scheme," *Journal of Magnetic Resonance*, vol.278, pp.88-95, 2017.

4.1 Asymmetric gradient coil design for use in a short, open bore magnetic resonance imaging scanner

4.1.1 Introduction

A conventional long-bore cylindrical whole-body MRI scanner is claustrophobic for some patients, thus making them uncomfortable during scanning. One method to make the scanner more open is to enlarge the diameter of the bore. However, this will increase the cost of the magnet and influence the uniformity of the magnetic field. Another method is to move the region of interest (ROI) towards one end of the main magnet [103]. An asymmetric gradient coil design is focused on this to overcome the claustrophobia problem and is paired with an asymmetric magnet design concept [104, 105].

With the development of MRI techniques, the gradient field must be strong and pulsed quickly to enable rapid imaging [43, 106]. However, fast, strong gradient switching can induce significant acoustic noise, making some patients uncomfortable [15, 107]. These issues can be attenuated to some extent by an appropriate coil design scheme, low inductance, low eddy current loss, low acoustic noise level, and so on.

Recent developments in gradient coil design methods allow for the design of arbitrary geometries [22, 32, 46, 108, 109] that provides many possibilities for improving the gradient coil performance. For example, the ultra-short gradient coil was designed with three-dimensional (3D) geometry for ultra-short cylindrical MRI systems, where the length of the gradient coil can be controlled throughout the design process [110]. However, compared with standard long gradient coil sets, the short, layered gradient coils (both having the same ROIs, design methods, border conditions and similar coil patterns, and so on) tend to have a dense coil pattern. The gradient field generating arcs (x, y coils) are competing for space with the return wires, making some wire-wire distances too narrow to manufacture. In addition, thermal heating can be a problem and the inductance may be higher. Coils with two ends connected were proposed to allow the current flow from the primary surface to the shielding surface [32, 111]. Under the same design parameters, this method can relax the current distribution to some extent compared with the conventional non-connected primary and shielding coils, because some return path wires are laid on the connected surface. However, this design has a higher complexity in terms of the mechanical design. Apart from considering the electromagnetic performance of the gradient coil design, the amount of noise generated by the coil also needs to be considered in the design process to improve patient comfort for seriously ill or anxious patients [13-16, 112].

In this work, we propose a novel asymmetric gradient coil design pattern matching an asymmetric magnet design concept [104]. The primary and shielding surfaces of the gradient coil were connected at one end, but separated at the other, to allow for the installation of the cooling device and shim tray, which also provided more space for the coil wire distribution. An equivalent magnetization current method was applied to the design of the gradient coil [32]. For the acoustic analysis, the finite element method (FEM) was used, and the gradient coil was inserted into epoxy resin. The electromagnetic performance and acoustic radiation intensity of the designed asymmetric gradient coil were compared with a non-connected asymmetric gradient coil. Its acoustic characteristics were also compared with a conventional symmetric gradient coil.

4.1.2 Methods

4.1.2.1 Asymmetric MRI scanner configuration

Based on an asymmetric magnet design concept [104], an asymmetric gradient coil was designed for the short MRI magnet, where the ROI was located near one end of the gradient coil. Fig. 4-1 shows an asymmetric scanner whose ROI is near the end of the scanner and a symmetric counterpart with the ROI at the centre of the scanner, which is also plotted for comparison. When doing chest imaging for a normal adult patient in a symmetric scanner, the patient's head will sit in the cylindrical tunnel of the scanner. In contrast, in an asymmetric scanner, the patient's head will sit at the edge of the scanner, thus potentially reducing the patient's discomfort and claustrophobia. In addition, as Fig. 4-1 shows, this design may have advantages for interventional imaging.

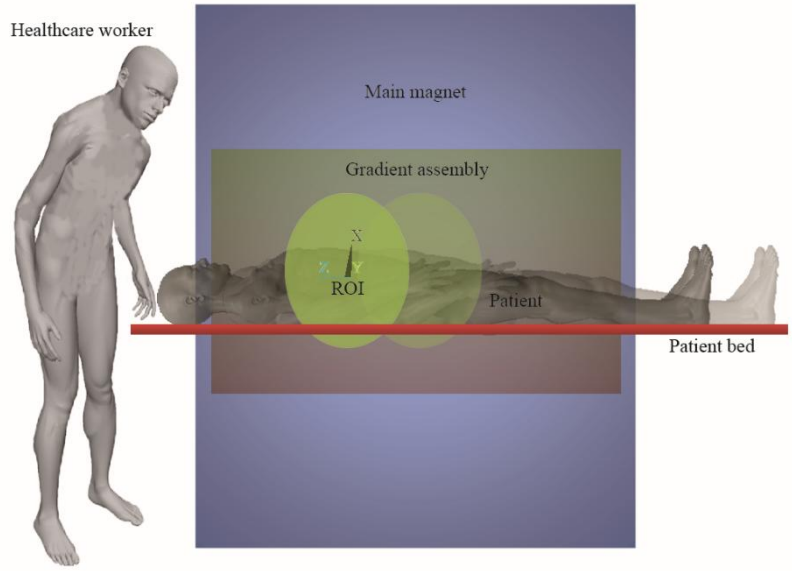

Fig. 4-1 Asymmetric MRI scanner ROI located near one end. Asymmetric counterpart (including the ROI and patient) is plotted in a light colour for comparison.

4.1.2.2 Gradient coil design

The gradient coil design was implemented using our recently-developed equivalent magnetization current method [32, 33]. An asymmetric x coil, whose primary current surface and shielding current surface were connected at one end, but separate at the other end (defined as a connected coil in this work), was designed to provide more dimensions for the spatial distribution of the current density. For the comparison of the coil performance, a corresponding layered asymmetric x coil (defined as a non-connected coil) was designed. The design strategy for both coils was a combination of conventional short (with high current density at both ends) and 3D short (with reduced current density at both ends) with a shift of ROI towards the patient end and an extended length at the other

end. The target field and current density surfaces used in the coil design are plotted in Fig. 4-2 (a) and (b) and the ROI designed here was 500 ×500 ×400 mm (x×y×z). The coil and cryostat sizes are shown in Fig. 4-2 (c) and a diagram of the designed coil layers is illustrated in Fig. 4-2 (d). All the gradient coils designed here had a target gradient strength of 30 mT/m and the maximum field error in the ROI was constrained to ±5% when the coils were designed. The shielding ratios [96] were controlled to be 2% during the design process and the parameters of the cryostat used for the eddy current control are listed in Table 4-1.

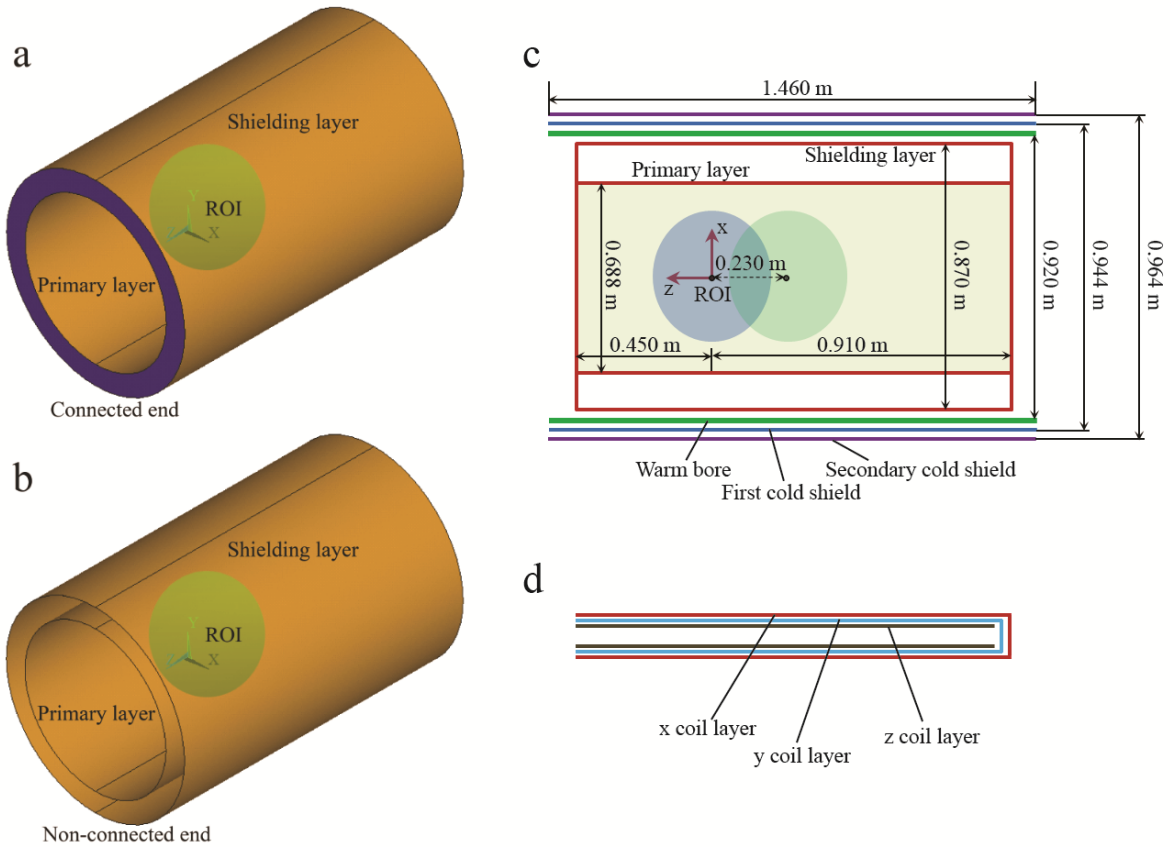

Fig. 4-2 Asymmetric gradient coil configurations, (a) current density surface of the connected coil, (b) current density surface of the non-connected coil, (c) dimensions of the designed x coils and the cryostat and, (d) diagram of the coil layers in a gradient assembly. The ROI shift size is 0.23 m.

Table 4-1 Parameters of the cryostat used for the eddy current control during the coil design process

	Length (m)	Radius (m)	Thickness (mm)	Conductivity (S/m)
Warm bore	1.460	0.460	6	1.1×10^{6}
First cold shield	1.460	0.472	3	3.8×10^{7}
Secondary cold shield	1.460	0.482	3	1.2×10^{9}

4.1.2.3 Acoustic analysis

With respect to the acoustic radiation intensity, a simple mechanical analysis can be used to explain the advantage of the designed coil. Eq. (4-1) is a Navier's equation [113], where $\boldsymbol{f}_{\mathrm{v}}$ is volume force, $\mathbf{B}$ is derivative matrix, $\boldsymbol{\sigma}$ is stress and ρ is density and $\boldsymbol{\varepsilon}$ is displacement. If a torque is applied at the ends of the gradient assembly, it is expected from the Navier's equation that the radial displacement will be influenced. Fig. 4-3 (a) and (b) show a torque diagram at the connected end of the designed coil in a gradient assembly. Taking a cell of the gradient assembly for a spatial stress and strain analysis [114], as shown in Fig. 4-3 (c) and (d), the radial strain will be attenuated owing to a tangential stress. Eq. (4-2) is a derived expression based on the cell stress state analysis, where Δ is attenuated distance from the principal stress direction, E is the Young's modulus, v is the Poisson's ratio, τ_{xz} is the shear stress and l is the edge length of the cell. From Eq. (4-2), increasing the shear stress τ_{xz} can better restrain the displacement of the principal direction. Based on the above analysis, it can be predicted that the torque at the end of the gradient coil can attenuate the vibration amplitude of the radial direction, thus reducing the noise level in the cylindrical tunnel of the gradient assembly.

$$\begin{cases} \boldsymbol{f}_{\mathrm{v}}+\mathbf{B}^{\mathrm{T}}\boldsymbol{\sigma}=\rho\ddot{\boldsymbol{\varepsilon}} \\ \mathbf{B}=\begin{bmatrix} \dfrac{\partial}{\partial r} & 0 & 0 & 0 & \dfrac{\partial}{\partial z} & \dfrac{1}{r}\dfrac{\partial}{\partial \theta} \\ 0 & \dfrac{1}{r}\dfrac{\partial}{\partial \theta} & 0 & \dfrac{\partial}{\partial z} & 0 & \dfrac{\partial}{\partial r} \\ 0 & 0 & \dfrac{\partial}{\partial z} & \dfrac{1}{r}\dfrac{\partial}{\partial \theta} & \dfrac{\partial}{\partial r} & 0 \end{bmatrix} \\ \sigma=\begin{bmatrix} \sigma_{\mathrm{rr}} & \sigma_{\mathrm{r\theta}} & \sigma_{\mathrm{rz}} \\ \sigma_{\mathrm{\theta r}} & \sigma_{\mathrm{\theta\theta}} & \sigma_{\mathrm{\theta z}} \\ \sigma_{\mathrm{zr}} & \sigma_{\mathrm{z\theta}} & \sigma_{\mathrm{zz}} \end{bmatrix} \end{cases} \tag{4-1}$$

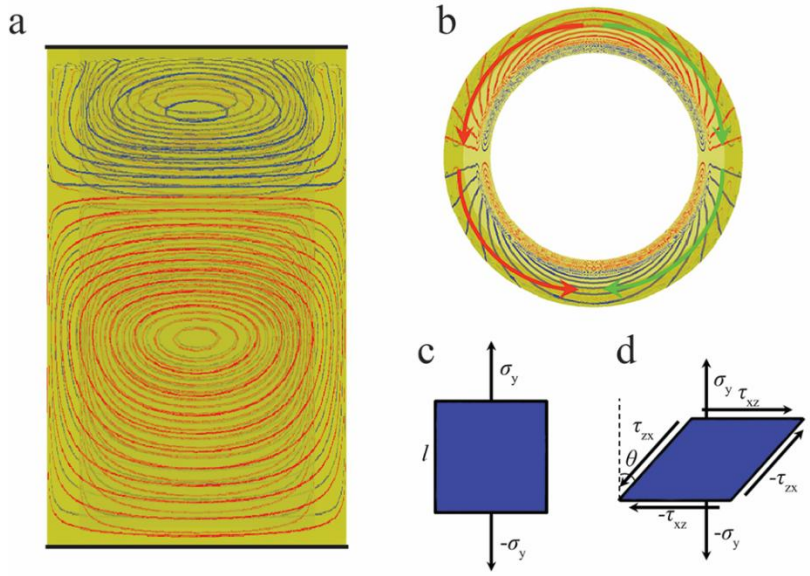

Fig. 4-3 Mechanical diagram of the connected coil, (a) connected coil in an assembly, (b) torque direction at the connected end of the designed coil, (c) two-dimensional (2D) stress state analysis without shear stress and, (d) 2D stress state analysis with shear stress, where l is the edge length of the cell, σ_y is the principal stress, τ_{xz} is the shear stress and θ is the torsion angle due to the shear stress. A coil example was illustrated to introduce the torque analysis.

$$\Delta = \left(1 - \frac{E}{\sqrt{E^2 + 4(1+v)^2 \tau_{xz}^2}} \right) l \tag{4-2}$$

For the acoustic noise analysis of the gradient coil, a three-dimensional (3D) model was established. The gradient assembly was simulated as an epoxy resin cylinder surrounded by air, the ends of which were fixed [115]. Fig. 4-4 (a) is a 3D finite element (FE) model, where the gradient assembly was placed in free space with an infinite boundary (no acoustic wave reflection). The infinite boundary was modelled using the Fluid 130 element type in the ANSYS element type library, which was applied on the outer surface of the air sphere. The size of the gradient assembly is displayed in Fig. 4-4 (b) and the mechanical and acoustic parameters used in the simulation are listed in Table 4-2. The temperature-caused material property variation was not considered in the simulation. For the model establishment, the element size was controlled to be less than 1/6 of the smallest wave acoustic wave length [116]. Harmonic analysis was used here from 100 Hz to 3000 Hz. The sinusoidal peak current used to energize the coil was the coil design current, producing a gradient strength 30 mT/m. Apart from the acoustic comparison between the connected asymmetric gradient coil and the non-connected gradient coil, a conventional symmetric gradient coil was also designed to compare the acoustic differences between the asymmetric coil pattern and symmetric

coil pattern. As with the asymmetric coils, the symmetric coil also produces a 30-mT/m gradient strength. For the Lorentz force calculation, an asymmetric 3 T static magnetic field and a symmetric 3 T static magnetic field were designed to pair the asymmetric gradient coils and the symmetric gradient coil.

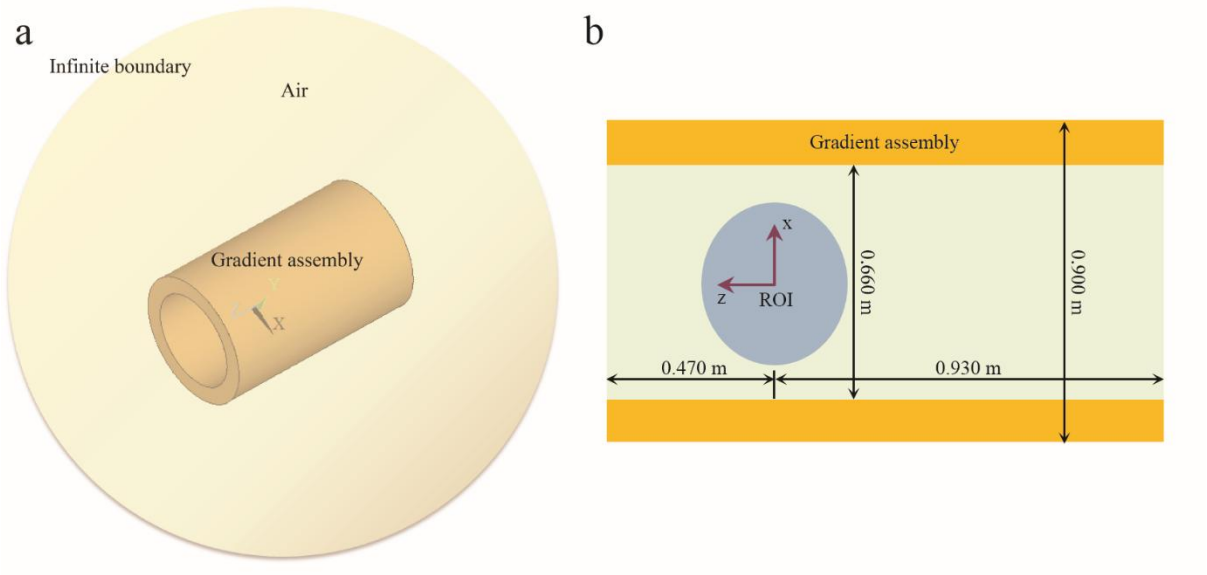

Fig. 4-4 3D FE model for the acoustic analysis of the gradient coil, (a) gradient assembly surrounded by air and (b) dimensions of the gradient assembly.

Table 4-2 Mechanical and acoustic parameters for the simulation of the gradient assembly

Item	E (Gpa)	μ	ρ (kg/m^3)	c (m/s)
Gradient assembly (epoxy resin)	15.7	0.30	1835	
Surrounding air			1.225	340

E, μ and ρ are the Young's modulus, Poisson's ratio and density of the simplified gradient assembly. c is the acoustic speed.

4.1.3 Results

4.1.3.1 Coil performance evaluation

Fig. 4-5 shows the designed asymmetric gradient coil wire contours. The connected coil and non-connected coil are plotted in Fig. 4-5 (a) and (b) respectively. It can be seen from Fig. 4-5 that the wire distribution of the connected coil is slightly looser than the non-connected coil owing to the connected end — this can alleviate the heating problem to some extent [117].

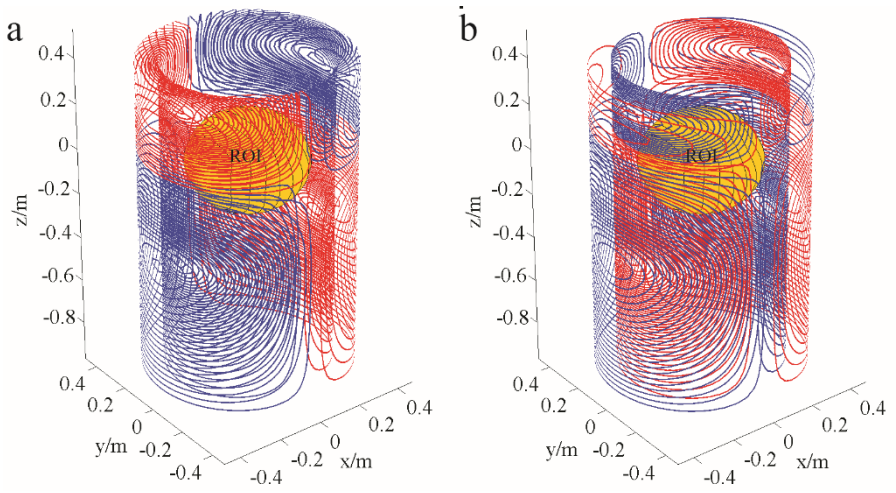

Fig. 4-5 Asymmetric gradient coil wire contours, (a) connected coil and (b) non-connected coil.

Fig. 4-6 is the z-component magnetic field distribution map of the connected coil and non-connected coil, whereby (a) and (b) are the magnetic field distributions of the connected coil and non-connected coil, respectively, on the cutting plane y=0. Comparing Fig. 4-6 (a) and (b), these two coils have nearly identical magnetic field distributions. However, small differences can be appreciated, especially at the peripheral magnetic fields outside the ROIs, where the z-component magnetic field of the non-connected coil is slightly higher than the connected coil. Fig. 4-7 (a) and (b) show the equipotential contours of the z-component magnetic field produced by the inputting current of the coils on the plane y=0, where the ROIs of the connected coil and non-connected coil were plotted. The lines in the ROIs of the two coils are approximately straight, which indicates uniform gradient magnetic fields. Outside the ROIs, the magnetic field uniformities of the two coils drop quickly and their stray fields show some differences. Fig. 4-7 (c) and (d) illustrate the equipotential contours of the z-component magnetic field produced by the eddy current on the cryostat. Also, uniform gradient magnetic fields were formed. The calculation of the magnetic field error on the ROI surface considering the eddy current induced field shows 4.49% and 4.55% deviations from the target field for the connected coil and non-connected coil respectively.

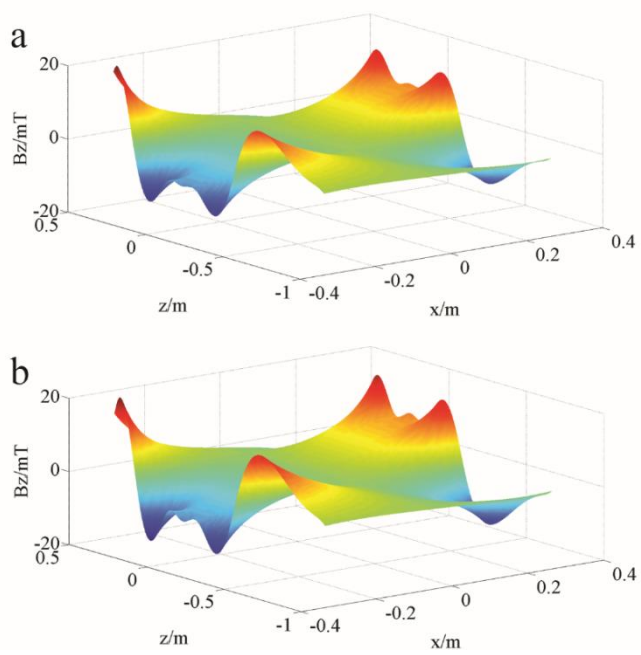

Fig. 4-6 Z-component magnetic field distributions of the asymmetric gradient coils on the cutting plane y=0, (a) connected coil, (b) non-connected coil.

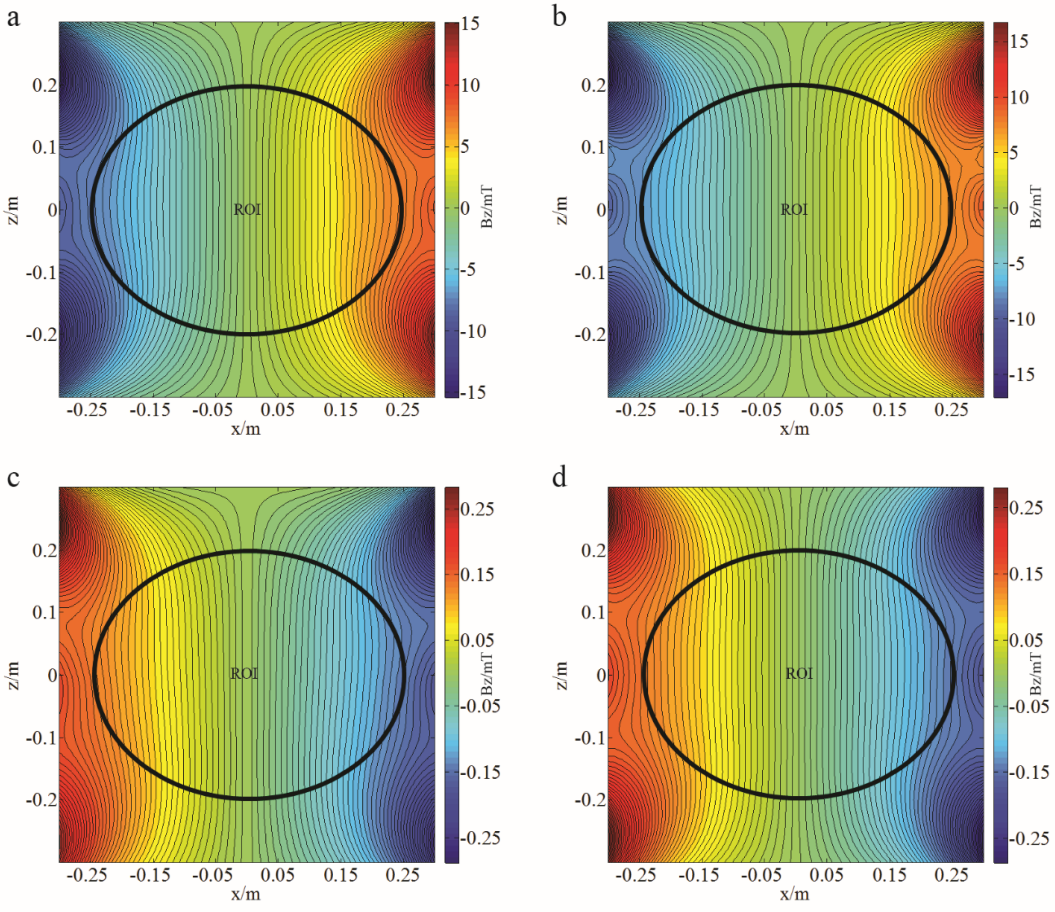

Fig. 4-7 Equipotential contours of the z-component magnetic field on the cutting plane y=0, (a) directly-produced magnetic field of the inputting current on the connected coil, (b) directly-produced magnetic field of the inputting

current on the non-connected coil, (c) induced magnetic field of the connected coil on the cryostat and, (d) induced magnetic field of the non-connected coil on the cryostat.

Minimum wire gaps are illustrated for both the connected coil and non-connected coil, as shown in Fig. 4-8. Because of the asymmetric properties of the gradient coils, the wires are concentrated towards one end together with the ROI. Minimum-gap wires occur at the ends of the primary coils for the two coils. This may become a problem for the fabrication and heating. However, the connected coil can alleviate the wire gap problem to some extent if both kinds of coils have a dense wire distribution, because the connected end provides another space for the wire laying. For the designed coils, the connected coil has a minimum wire gap 6.8 mm, while the non-connected coil has a minimum wire gap 4.7 mm. The comparative advantage of the connected coil may alleviate the heating problem and reduce the coil inductance.

For further comparison of the designed coils, some essential electromagnetic performances of the designed gradient coils and a symmetric coil are listed in Table 4-3. The two asymmetric coils both have 168 wire turns. For a target gradient magnetic field strength of 30 mT/m, the connected coil is operated with a current of 323.5 A, while the non-connected coil has a current input of 328.1 A. Thus, the connected coil has a comparatively higher efficiency than the non-connected coil. In addition, the inductance and resistance of the connected coil are both smaller than the non-connected coil, where the smaller inductance can make a high slew rate and the smaller resistance can reduce a power loss. An integrated parameter figure of merit, which is used to evaluate the overall performance of the gradient coil, also indicates the advantage of the connected coil. When compared with a symmetric coil, the electromagnetic performances of the asymmetric coil do not always show an advantage, although the efficiencies are a little higher. The torques of the asymmetric coils and a symmetric coil were calculated under a 3 T homogeneous static magnetic field. As listed in Table 4-4, the asymmetric coils have larger torques than the symmetric coil on the y because of their asymmetric properties.

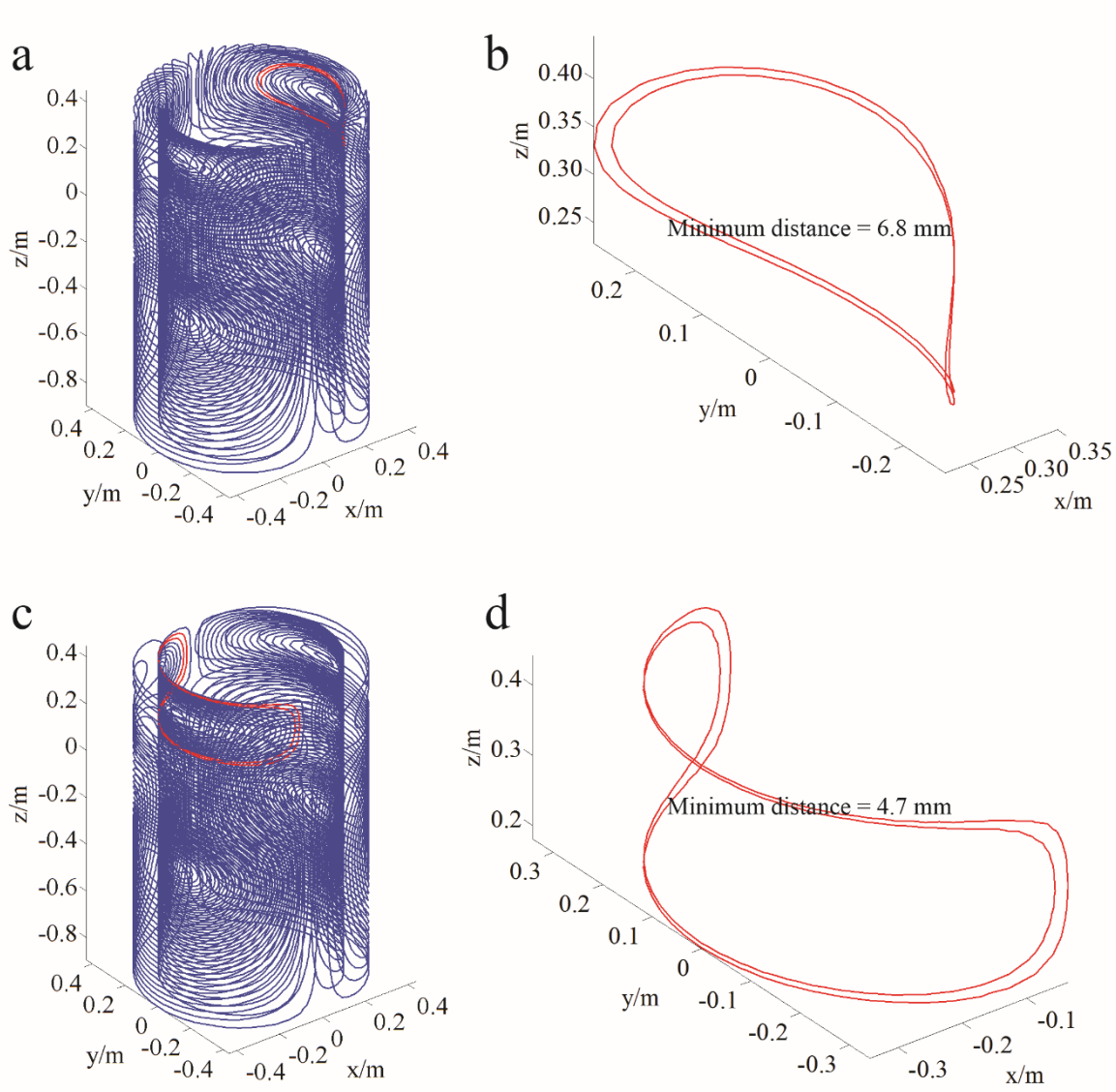

Fig. 4-8 Minimum wire gaps for the asymmetric gradient coil designs, (a) minimum-gap wires shown in the connected coil, (b) minimum-gap wires of the connected coil, (c) minimum-gap wires shown in the non-connected coil and, (d) minimum-gap wires of the non-connected coil.

Table 4-3 Electromagnetic performances of the connected coil, non-connected coil and a symmetric coil

	Maximum current (A)	Efficiency (mT/m/A)	Inductance (μH)	Resistance (mΩ)	Figure of merit ($T^2/m^2/A^2/H$)
Connected coil	323.5	0.093	1014.2	449.2	8.48×10^{-6}
Non-connected coil	328.1	0.091	1073.5	459.7	7.79×10^{-6}
Symmetric coil	387.7055	0.077	631.1	354.4	9.49×10^{-6}

Table 4-4 Torques of the connected coil, non-connected coil and a symmetric coil

	Tx (N·m)	Ty (N·m)	Tz (N·m)
Connected coil	0.5172	423.9	0
Non-connected coil	0.6365	209.2	0
Symmetric coil	0.2640	0.0399	0

4.1.3.2 Acoustic radiation intensity evaluation

The designed static magnetic fields used for the Lorentz force calculation are shown in Fig. 4-9, where Fig. 4-9 (a) and (b) display the longitudinal (z) component and radial (r) component of the asymmetric static magnetic field, and Fig. 4-9 (c) and (d) display the longitudinal (z) component and radial (r) component of the symmetric static magnetic field. Note that the designed static magnetic fields are axi-symmetric with respect to the z axis. The illustrations of the static magnetic fields around the gradient coils are plotted in Fig. 4-9 (e) and (f), where the connected asymmetric gradient coil under the asymmetric 3 T static magnetic field was taken as an example. The calculated Lorentz force was mapped on the gradient assembly.

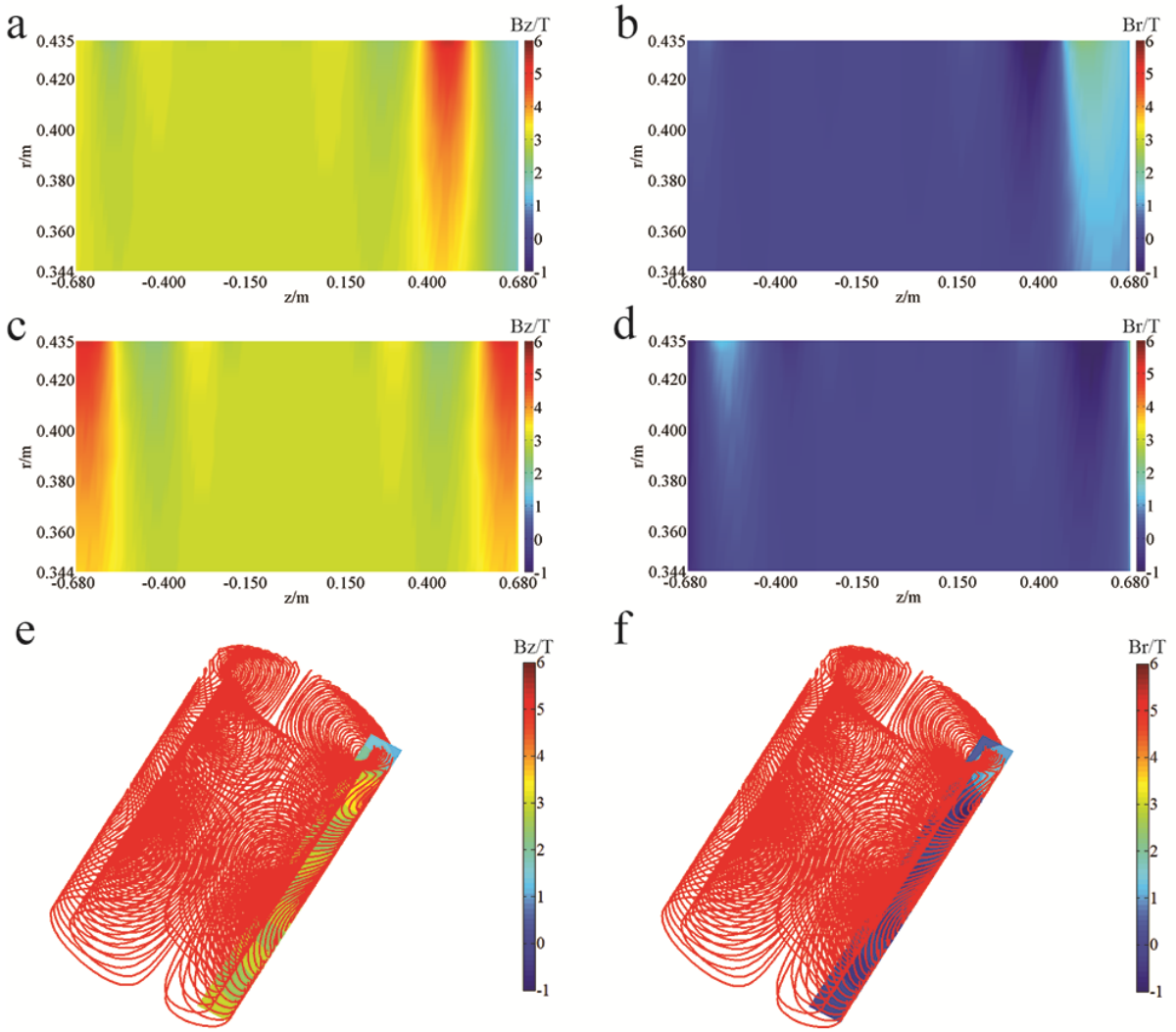

Fig. 4-9 Static magnetic fields for the Lorentz force calculation (target field in the ROI is 3 T), (a) longitudical z component of the asymmetric static magnetic field, (b) radial r component of the asymmetric static magnetic field, (c) longitudical z component of the symmetric static magnetic field, (d) radial r component of the symmetric static magnetic field, (e) connected coil under longitudical z component of the asymmetric static magnetic field and, (f) connnected coil under radial r component of the asymmetric static magnetic field. The designed static magntic fields are axisymmetric with respect to the z axis.

A modal analysis was conducted on the gradient assembly before the acoustic investigation. The mode frequencies and their corresponding mode paticipation factors between 100 Hz to 3000 Hz were indentified. The main bending vibration modes and their participation factors on six degrees of freedom are listed in Table 4-5. These modes have a paticipation factor larger than five in the X or Y displacement direction. Obvously, a gradient pulse containing much energy at these frequencies may cause large bending vibration in the gradient assembly.

Table 4-5 The main bending vibration modes of the gradient assembly and their corresponding participation factors

Frequency (Hz)	Participation factor					
	X	**Y**	**Z**	**Rot-X**	**Rot-Y**	**Rot-Z**
463.9	-0.2285	24.0180	-0.1043e-3	-0.5282e-2	0.1614e-3	0.1256e-4
464.4	24.0190	0.2286	-0.4381e-3	0.1033e-3	0.2176e-2	-0.5339e-4
1296.6	-0.5003e-1	7.8332	0.9168e-2	-0.1932	-0.9095e-3	-0.1366e-4
1318.5	-8.0528	-0.5728e-1	-0.1260e-1	0.4295e-2	-0.2178e-1	-0.1414e-3
2066.6	-0.4030e-1	-5.0534	0.1334e-2	0.1658	0.1942e-2	0.1157e-3

Note: the mode frequencies with participation factors larger than 5 in the X or Y displacment direction are listed.

Fig. 4-10 illustrates the displacements of the connected coil and non-connected coil in the gradient assemblies by a sinusoidal maximum current input (see Table 4-1) with a frequency of 464 Hz around a main bending mode of the gradient assembly. Obviously, the large-displacement regions of the non-connected coil are restrained by using a connected coil design that will attenuate the radiated acoustic field from the assembly surface. Fig. 4-11 shows the sound pressure level (SPL) comparison between the connected and non-connected coils. Also, the SPL of the conventional symmetric coil was plotted to characterize the acoustic differences of the new asymmetric coil and conventional symmetric coil designs. The SPL for a frequency was the averaged result in the cylindrical tunnel [72]. Fig. 4-11 (a) is the SPL comparison from 100 Hz to 3000 Hz. Fig. 4-11 (b), (c) and (d) are partial plots of Fig. 4-10 (a) that show only the frequencies from 1500 Hz to 2500 Hz, 500 Hz to 1000 Hz, and 1000 Hz to 1500 Hz, to clearly reveal the SPL differences between the connected and non-connected coils. Fig. 4-11 (a) shows that the connected coil has an SPL reduction compared to the non-connected coil for nearly the whole frequency band; this is further partially illustrated in Fig. 4-11 (b) and (c). This is more significant in a higher frequency band than a low frequency band. Although this SPL difference is not considerable — around 2.2 dB at some frequencies — this SPL reduction indicates that the connected coil will radiate a lower sound intensity compared with the non-connected coil with the same pulse pattern. However, there is a small frequency band around 1350 Hz where the SPL of the connected coil is higher than that of the non-connected coil. That may be because the Lorentz force distribution of the connected coil was near the peaks of the mode shape (or most forces were applied near the peak of the mode shape) around that frequency; this could easily cause resonance. However, if most forces were applied near the zero displacement points of the mode shape around that frequency, the resonance would be difficult to induce. As with the SPL comparison between the asymmetric coils and the symmetric coil, the SPL difference has a close relationship with the frequency. For frequencies lower than 300 Hz, the SPLs of the asymmetric coils are always lower than that of the symmetric coil. In the frequency band 2200-2550 Hz, the asymmetric coils are much quieter than the symmetric coil,

where the SPL difference is considerable. In other frequency bands, the SPLs of the asymmetric coil and symmetric coils fluctuate up and down with small differences.

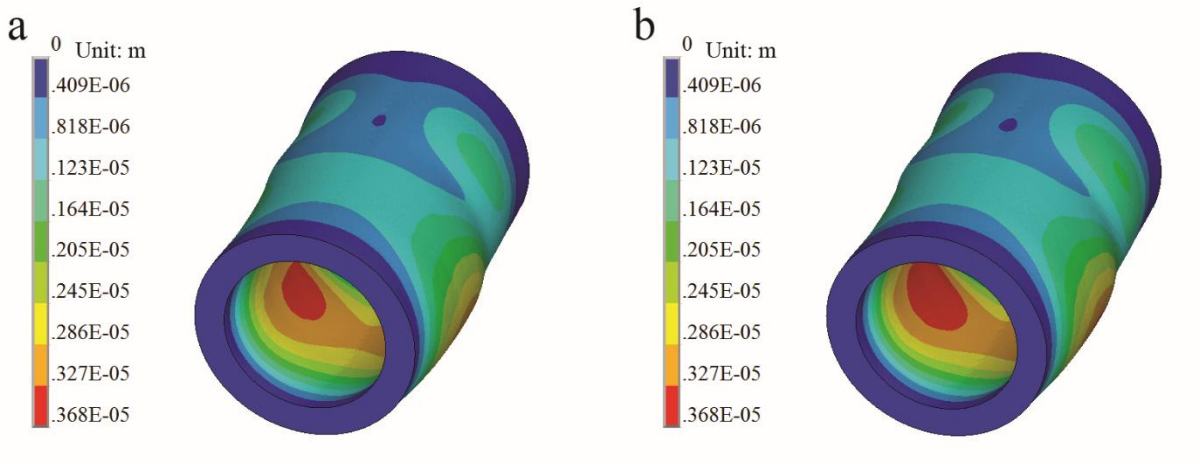

Fig. 4-10 The displacement illustrations of the designed coils in the gradient assemblies under a sinusoidal current input at 464 Hz, (a) connected coil and (b) non-connected coil.

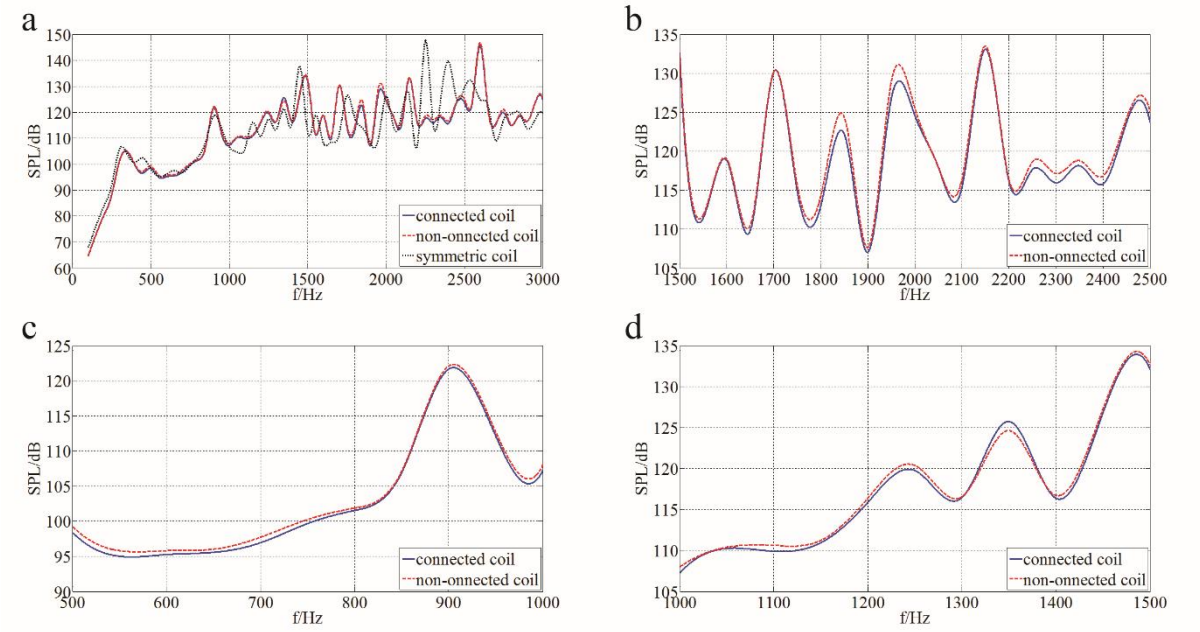

Fig. 4-11 Acoustic radiation intensity comparisons of the connected and the non-connected coils, (a) SPL comparison from 100 Hz to 3000 Hz, and also a comparison with a symmetric coil, (b) SPL comparison from 1500 Hz to 2500 Hz, (c) SPL comparison from 500 Hz to 1000 Hz and, (d) SPL comparison from 1000 Hz to 1500 Hz.

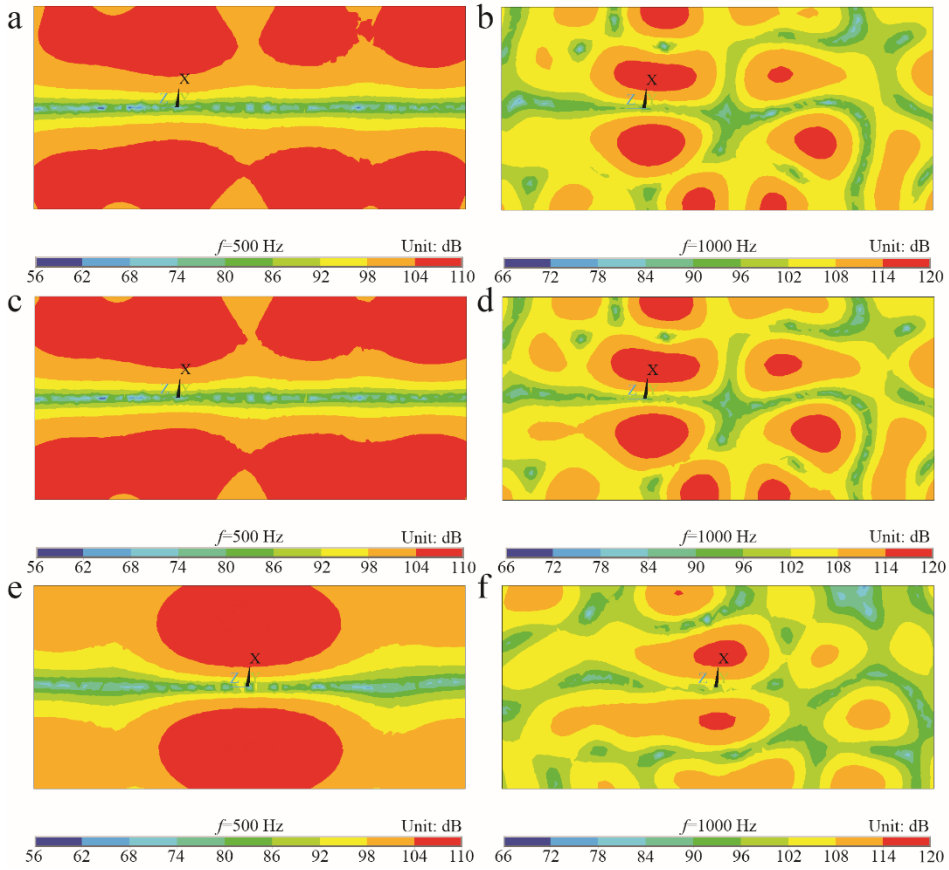

Fig. 4-12 Acoustic field distribution on the cutting plane y=0 of the cylindrical tunnel, (a) acoustic field distribution of the connected coil at 500 Hz, (b) acoustic field distribution of the connected coil at 1000 Hz, (c) acoustic field distribution of the non-connected coil at 500 Hz, (d) acoustic field distribution of the non-connected coil at 1000 Hz, (e) acoustic field distribution of the conventional symmetric coil at 500 Hz and, (f) acoustic field distribution of the conventional symmetric coil at 1000 Hz.

Fig. 4-12 shows the acoustic field distributions on the cutting plane y=0 of the cylindrical tunnel in the gradient assembly. Fig. 4-12 (a), (c) and (e) are the acoustic field comparisons of the connected coil, non-connected coil and conventional symmetric coil respectively, at 500 Hz; and Fig. 4-12 (b), (d) and (f) are the acoustic field comparisons of the connected, non-connected and conventional symmetric coils, respectively, at 1000 Hz. Similar acoustic field distributions can be observed from the comparison between the connected coil and non-connected coil. However, the connected coil has smaller loud areas than the non-connected coil, thus resulting in a lower average SPL. For the acoustic field comparison between the asymmetric coils and the symmetric coil, the loud areas of symmetric coil tend to concentrate in the central part of the cylindrical tunnel, while the central part of the asymmetric coil is relatively quieter.

4.1.4 Conclusions

A novel asymmetric gradient coil pattern was proposed in this work for a cylindrical short-bore asymmetric MRI scanner. The coil was designed with one end connected, which gave more space for the coil wire placement and also made it possible to mount shim trays and to access them from the other end. This design increased the wire gap and improved the electromagnetic performances of the coil compared to a non-connected coil and also had a lower acoustic radiation. The new coil design pattern had a higher efficiency, lower inductance and resistance than the corresponding non-connected coil. Using an overall parameter figure of merit to evaluate the proposed coil pattern, it also behaved better than the non-connected coil. According to the acoustic analysis, the proposed coil pattern had an SPL reduction at most frequencies compared with the non-connected coil pattern. It is noted that the finding is based on our FEM model with simplifying approximations, such as the lack of discrete wires or detailed structural components. Future work will be conducted to include the fabrication of the coil and experimental measurement of its performance.

4.2 Spiral gradient coil design for use in cylindrical MRI systems

4.2.1 Introduction

Gradient coil design methods can generally be divided into two categories, the continuous-current density-based method and the discrete wire-based method, as is mentioned in section 2.2.1. The continuous-current density-based method is always combined with the stream function, and the coil pattern is realized by contouring the stream function. Compared with the discrete wire-based method, the stream function-based method is very efficient in finding solutions. The discrete wire-based method directly adjusts the wire structures in the real geometrical space, with all the magnetic fields generated from the entire wire structure.

However, in the stream function-based methods, the discretization of the continuous current densities into wire contours will introduce system errors that are difficult to reduce by a directional adjustment of the discrete wires [40]. Moreover, the physical connection between the coil contours will also produce additional field errors, affecting the ultimate coil performance. In this paper, we propose a new method that can avoid the cutting and reconnecting process, thus eliminating the above winding errors. Using the new gradient-coil design method, a whole set of spiral gradient coils (including an x-gradient coil and a z-gradient coil) was optimized and evaluated against a conventional stream function-based method.

4.2.2 Method

A shielded-gradient coil design strategy is given in this section. The gradient coil dimensions and design parameters are listed in Table 4-6. An x-gradient coil and a z-gradient coil were designed in this work.

Table 4-6 Coil dimensions and design parameters

Item	*R* (m)	*L* (m)
x primary coil	0.320	1.246
x shielding coil	0.370	1.286
z primary coil	0.330	1.246
z shielding coil	0.380	1.286
DSV (diameter)	0.5 m	
Gradient strength	45 mT/m	

R is the coil radius and *L* is the coil length

The optimization target and constraint for the spiral gradient coil design can be found in section 3.1.2. In comparison, x-gradient and a z-gradient coils based on the stream function method were also designed with the same dimensions and design parameters. As with the stream function-based method, the root mean square (RMS) error relative to the target field was controlled not larger than 5% and the RMS of the shielding field was controlled not larger than 4 Gauss (1 Gauss=0.0001 T) in a cylinder with radius 0.430 m and length 1.460 m for the x-gradient coil design. For the z-gradient coil design, the maximum absolute error relative to the target field was controlled not larger than 5% and the maximum absolute shielding field was controlled not larger than 10 Gauss at a cylinder with radius 0.430 m and length 1.460 m.

4.2.3 Result

4.2.3.1 x-gradient coil

Fig. 4-13 (a–b) shows an x-gradient coil design based on the stream function method. The coil pattern was contoured from the current density stream function to obtain an engineering realization by discrete wires. For the coil configuration, the primary coil (Fig. 4-13 (a)) contains 152 loops and the shielding coil (Fig. 4-13 (b)) contains 84 loops. The operating current is 596.24 A. During fabrication, these separate loops should be connected to form a continuous current path. The connected coil is shown in Fig. 4-13 (c–d).

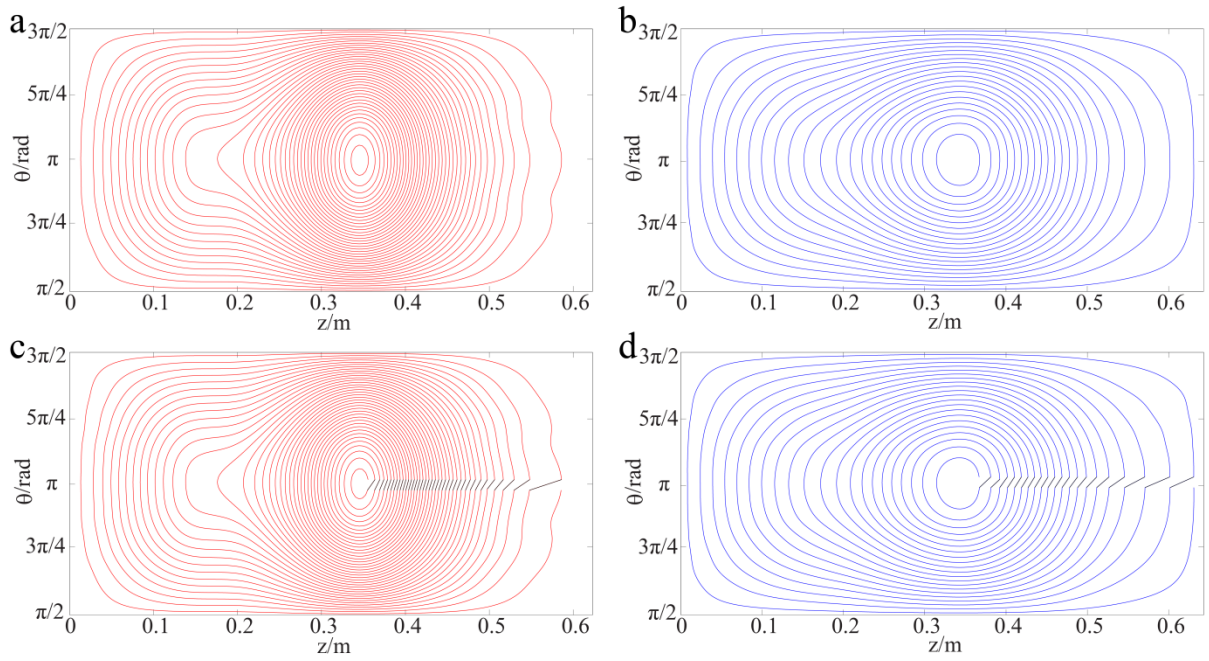

Fig. 4-13 Conventional x-gradient coil design based on stream function method, (a) unconnected primary coil, (b) unconnected shielding coil, (c) connected primary coil and, (d) connected shielding coil. Only a quarter is shown due to coil symmetry. The connection sections from the unconnected coil to the connected coil are shown in black (see (c) and (d)).

Fig. 4-14 shows the magnetic field distribution of the x-gradient coil design based on the stream function method. The magnetic field distributions on the cutting planes y=0 and z=0 are given, and also the magnetic field distribution outside the gradient coil is plotted for a review of the shielding effect. Fig. 4-14 (a–c) are the magnetic field distributions calculated from the current densities during the gradient coil design, and Fig. 4-14 (d–f) are the magnetic field distributions calculated from the connected gradient coil wires (see Fig. 4-13 (c–d)). The 5% magnetic field error is marked. Comparing Fig. 4-14 (a–c) and Fig. 4-14 (d–f), it is evident that the magnetic field error can be introduced during the contouring and connecting process. The direct influence is that the DSV shrinks from about 50 cm to approximately 45 cm. In addition, the shielding effect slightly decreases (see Fig. 4-14 (c) and Fig. 4-14 (f)).

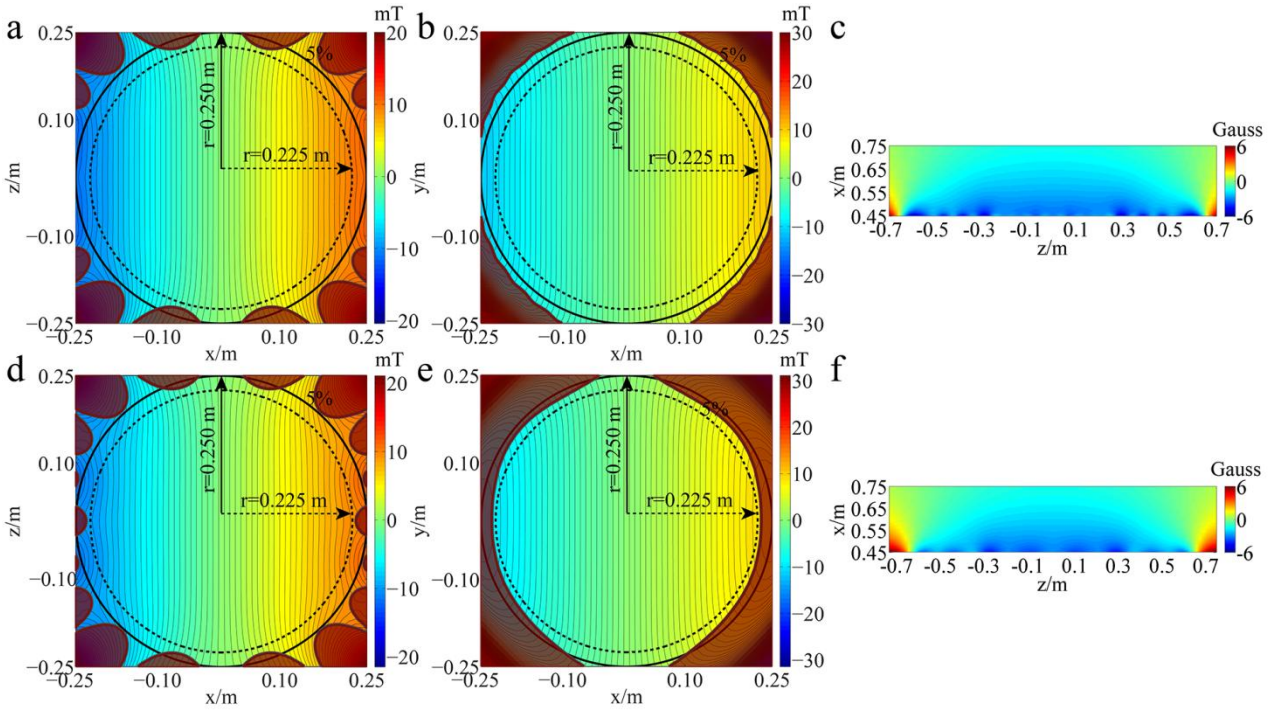

Fig. 4-14 Magnetic field distributions of the x-gradient coil design using a stream function-based method. (a-c) are magnetic field distributions calculated by current densities during the gradient coil design and (d-f) are magnetic field distributions calculated by connected gradient coil wires. Specifically, (a) and (d) are the magnetic field distributions on the plane y=0, (b) and (e) are the magnetic field distributions on the plane z=0 and (c) and (f) are the magnetic field distributions outside the gradient coil. The 5% field error was marked where inside the marks means that the field error was within 5%.

Fig. 4-15 shows the designed spiral x-gradient coil pattern, where (a) is the primary coil and (b) is the shielding coil. Each quarter of the spiral gradient coil consists of a single wire. The current directions of the primary coil and the shielding coil are marked.

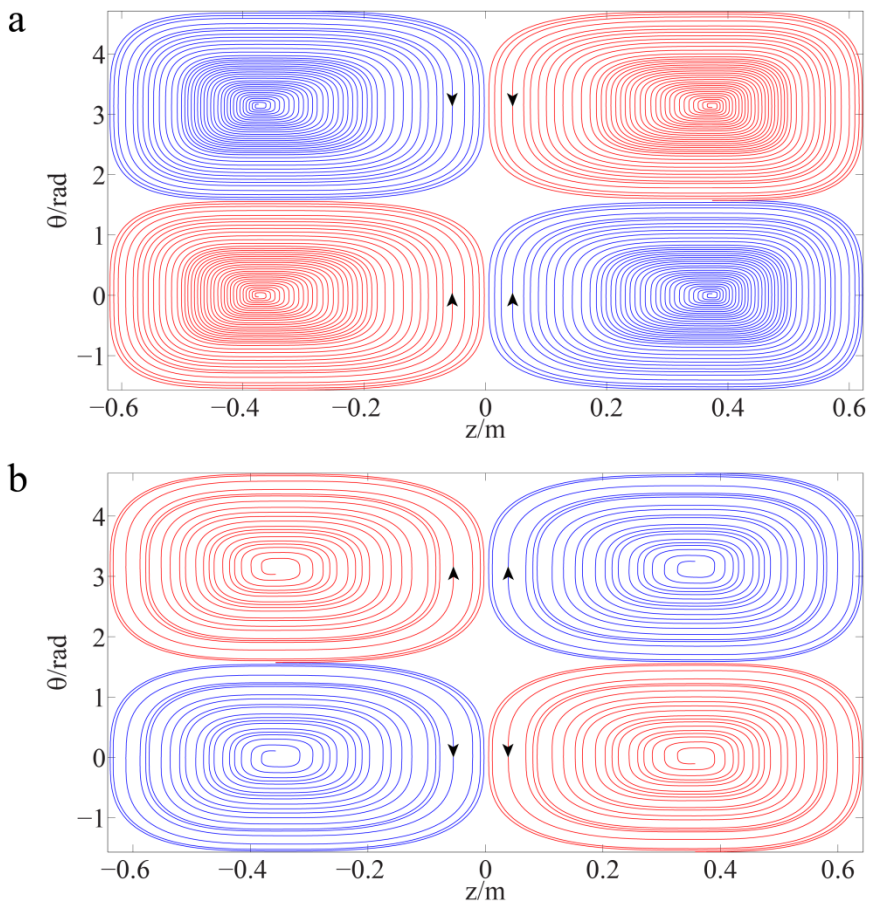

Fig. 4-15 Spiral x-gradient coil design based on discrete wire method, (a) primary coil and, (b) shielding coil. The current directions were marked by arrows.

In total, the primary coil has 148 spiral loops and the shielding coil 80 spiral loops. The optimized operating current is 595.87 A, which is slightly lower than that (596.24 A) of the conventional stream function-based gradient coil design. Comparing Fig. 4-13 (c) and Fig. 4-15 (a), the sparser wire distribution of the spiral coil is clearly observable. The minimum wire spacing of the spiral coil is 5 mm, while the minimum wire spacing of the conventional coil is only 3.3 mm. The small wire spacing of the conventional coil may cause a heating problem and also a fabrication difficulty.

Fig. 4-16 shows the magnetic field distributions of the spiral x-gradient coil design. Similarly, the magnetic field distributions inside the gradient coil on the planes y=0 and z=0 are given and also the magnetic field distribution outside the gradient coil is plotted. By comparing the conventional-stream function-based gradient coil and the spiral-gradient coil designs, both can achieve a DSV of about 45 cm with a magnetic field gradient non-uniformity error around 5%. Also, both of them have a good shielding effect (the leaking magnetic field strength of the spiral gradient coil design is slightly higher than that of the conventional stream function-based gradient coil design, see Fig. 4-

16 (c) and Fig. 4-14 (f)). In Fig. 4-16 (c), the field shows some asymmetry along the z direction, which is because the spiral gradient coil has slight asymmetry in structure.

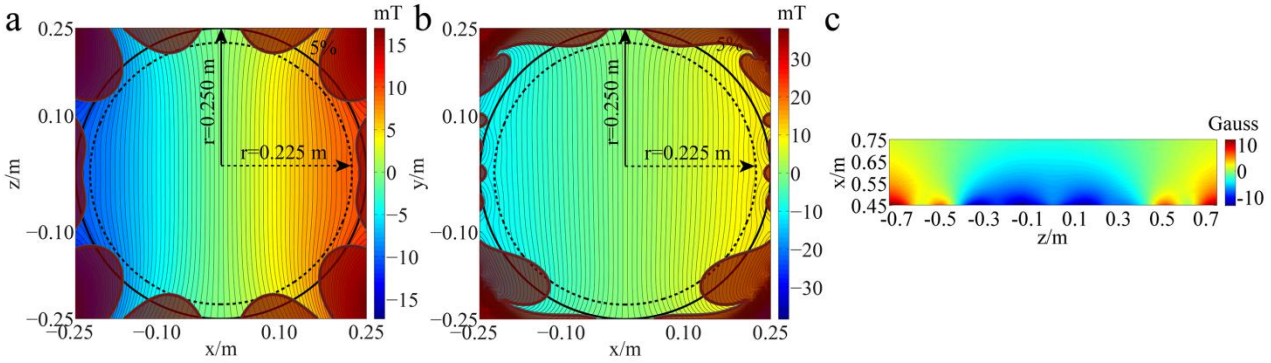

Fig. 4-16 Magnetic field distribution of the spiral x-gradient coil design using discrete wire method, (a) magnetic field distribution on the plane *y*=0, (b) magnetic field distribution on the plane *z*=0 and, (c) magnetic field distribution outside the gradient coil. The 5% field error was marked where inside the marks means that the field error was within 5%.

The coil performances of the conventional-stream function-based-gradient coil design and the spiral x-gradient coil design are listed in Table 4-7. The inductances and resistances of these two gradient coils were calculated using FastHenry [118], with a uniform rectangular wire cross-section 3 mm x 3 mm. The coil performances of the conventional gradient coil design are calculated from the final connected coil. It can be seen that the efficiency of the spiral gradient coil is similar to or actually slightly higher than that of the conventional gradient coil. The maximum magnetic field error of the conventional gradient coil is 9.51% over a DSV of 50 cm, while the spiral gradient coil is 8.56%. Over a DSV of 45 cm, the maximum magnetic field error of the conventional gradient coil is 4.50%, compared to the spiral gradient coil 6.00%. As for the inductance and resistance, the spiral gradient coil has a significant advantage compared with the conventional gradient coil. The inductance of the spiral gradient coil is 1925.7 μH, with a 20.9% reduction compared to the conventional gradient coil 2433.1 μH, and the resistance of the spiral gradient coil is 608.1 mΩ, with a 10.5% reduction compared with the conventional gradient coil of 679.8 mΩ. The overall coil performance (Figure of Merit (FoM), defined as η^2/L, where η is the coil efficiency and L is the inductance) of the spiral gradient coil is 2.962×10^{-6} $T^2/m^2/A^2/H$, which increases by 26.5%, compared with the conventional gradient coil 2.341×10^{-6} $T^2/m^2/A^2/H$.

Table 4-7 Performances of the conventional x gradient coil and the spiral gradient coil

Parameters	Conventional coil	Spiral coil
Loop number (n, primary/shielding)	152/84	148/80
Current amplitude (A)	596.24	595.87
Efficiency (mT/m/A)	0.07547	0.07552
Maximum field error (%, DSV=50 cm)	9.51	8.56
Maximum field error (%, DSV=45 cm)	4.50	6.00
Inductance (μH)	2433.1	1925.7
Resistance (mΩ)	679.8	608.1
Figure of merit ($T^2/m^2/A^2/H$)	2.341×10^{-6}	2.962×10^{-6}
Minimum wire spacing (mm)	3.3	5.0

Note: The inductance and resistance of the two coils were calculated using FastHenry, by assuming a uniform rectangular wire cross-section of 3 × 3 mm.

Fig. 4-17 shows the three-dimensional (3D) plot of the conventional-stream function-based x-gradient coil design (the separate wire loops were connected) and a spiral x-gradient coil design. Because every loop of the spiral gradient coil design has an accurate quasi-elliptic mathematical expression, the loop geometry looks much smoother than the conventional-stream function-based gradient coil design. In addition, the sparser wire distributions of the spiral gradient coil are also visible in the comparison. Apart from the aforementioned coil cooling advantage (less local heating problem), the spiral gradient coil is more easily fabricated than the conventional gradient coil.

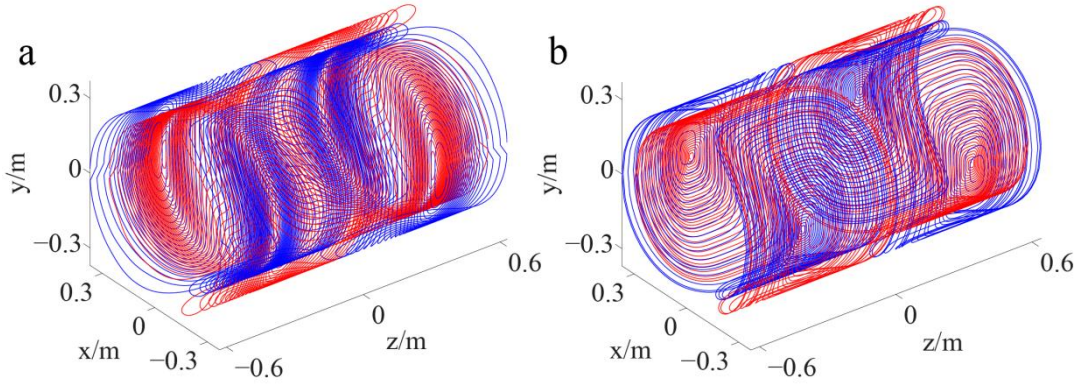

Fig. 4-17 3D plot of the conventional stream function-based x-gradient coil design and the spiral x-gradient coil, (a) conventional gradient coil and, (b) spiral gradient coil.

4.2.3.2 z-gradient coil

Fig. 4-18 (a–b) shows a z-gradient coil design based on the stream-function method. The discrete wire coil pattern was created by contouring the current density-stream function. The coil contains 76 primary loops (Fig. 4-18 (a)) and 50 shielding loops (Fig. 4-18 (b)), with an operating current of 590.97 A. The connected coil pattern is shown in Fig. 4-18 (c–d).

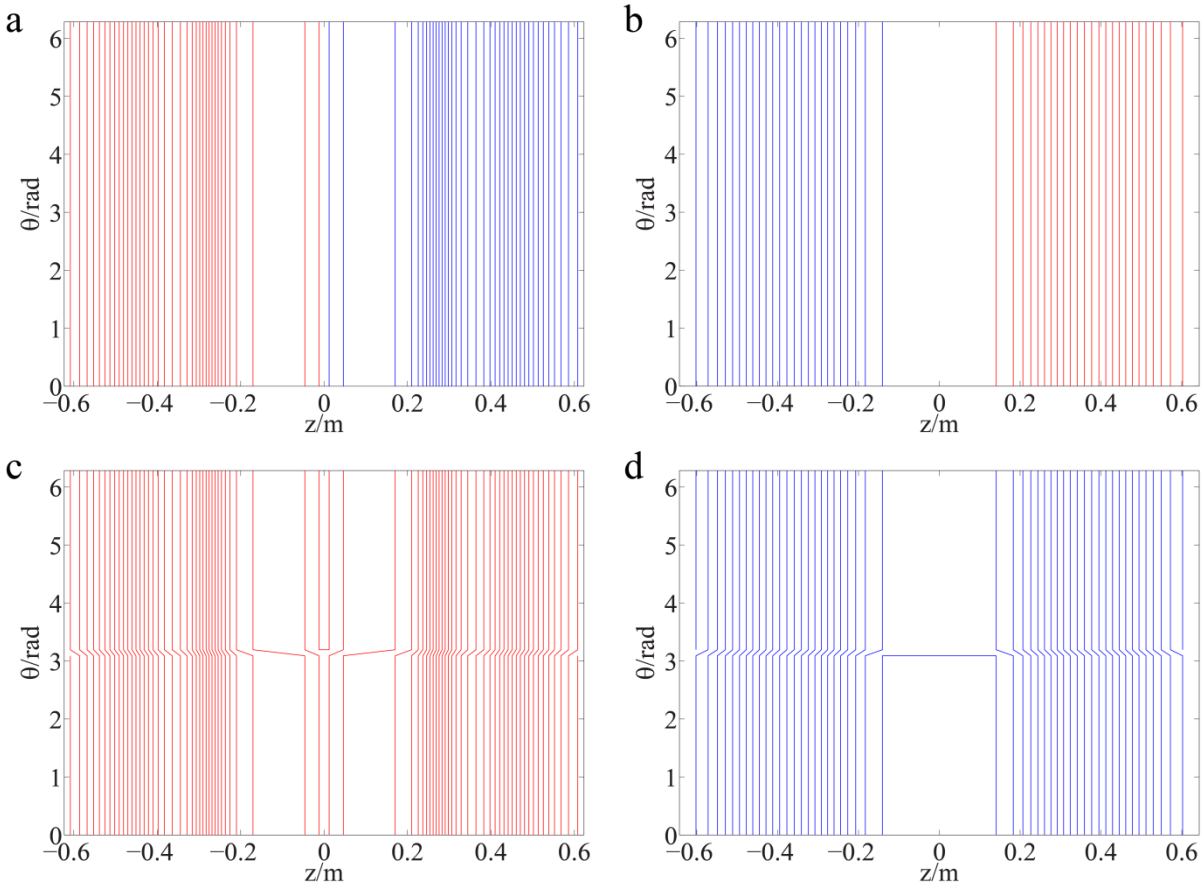

Fig. 4-18 Conventional z-gradient coil design based on the stream function method, (a) an unconnected primary coil, (b) an unconnected shielding coil, (c) a connected primary coil and, (d) connected shielding coil.

Fig. 4-19 shows the magnetic field distribution of the z-gradient coil design based on the stream function method. Similar to the x-gradient coil, the magnetic field distributions on the cutting planes x=0 and y=0, and also the magnetic field distribution outside the gradient coil, are given. The magnetic field distributions calculated from the current densities during the gradient coil design are shown in Fig. 4-19 (a–c), and the magnetic field distributions calculated from the connected gradient coil wires (see Fig. 4-19 (c–d)) are shown in Fig. 4-19 (d–f) for comparison. The 5% deviation from the target field is marked on the magnetic field profile. It is obvious that by comparing Fig. 4-19 (a–b) and Fig. 4-19 (d–e), that the non-uniform regions in the gradient coil cylinder are enlarged, which results in a smaller DSV than the initial design. The 5% deviation

curve corresponds to a DSV of approximately 45 cm. In addition, the maximum shielding magnetic field strength also slightly increases by comparing Fig. 4-19 (c) and Fig. 4-19 (f).

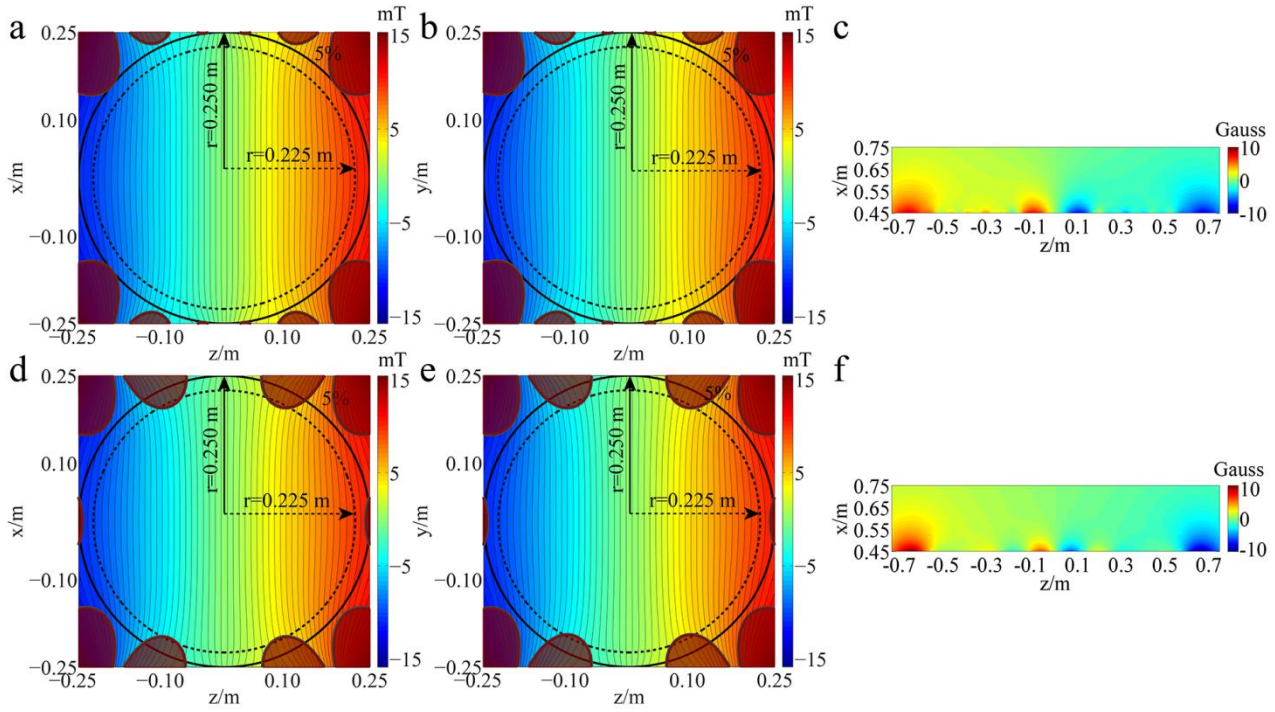

Fig. 4-19 Magnetic field distributions of the z-gradient coil design using a stream function-based method. (a-c) are magnetic field distributions calculated by current densities during the gradient coil design and (d-f) are magnetic field distributions calculated by connected gradient coil wires. Specifically, (a) and (d) are the magnetic field distributions on the plane y=0, (b) and (e) are the magnetic field distributions on the plane x=0 and (c) and (f) are the magnetic field distributions outside the gradient coil. The 5% field error was marked where inside the marks means that the field error was within 5%.

Fig. 4-20 shows the designed spiral z-gradient coil pattern with (a) the primary coil and, (b) the shielding coil, where the length of the optimized spiral z-gradient coil slightly exceeds the initial setting length. Because the coil wire of the spiral z-gradient coil is continuous, for the unwrapping plot, the ending point of a straight line is merely the starting point of the next one. The current directions of the primary coil and the shielding coil are marked. For the spiral z-gradient coil design, the operating current is 590.97 A, which is identical to that of the conventional design. However, the spiral z-gradient coil has fewer coil loops compared with the conventional design. The minimum wire spacing of the conventional coil is 7.1 mm, while the minimum wire spacing of the spiral coil is 10.0 mm.

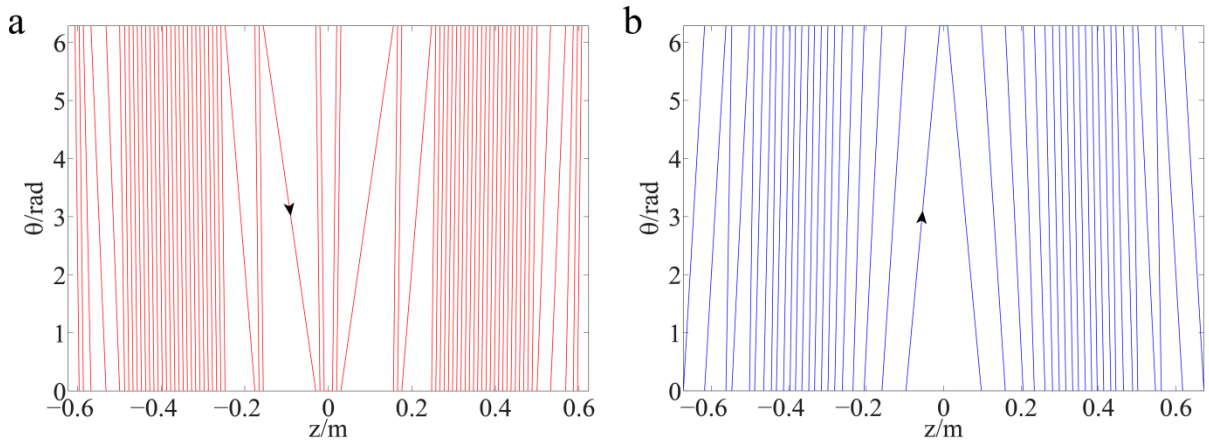

Fig. 4-20 Spiral z-gradient coil design based on the discrete wire method (a) primary coil and, (b) shielding coil. The red and blue colours show where the currents flow in different directions.

Fig. 4-21 shows the magnetic field distributions of the spiral z-gradient coil design. Similarly, both the magnetic fields around the DSV and the shielding regions are plotted. By comparison with the conventional z gradient coil design, the spiral z-gradient coil has a more uniform gradient magnetic field over a larger DSV, and also the shield effect is improved.

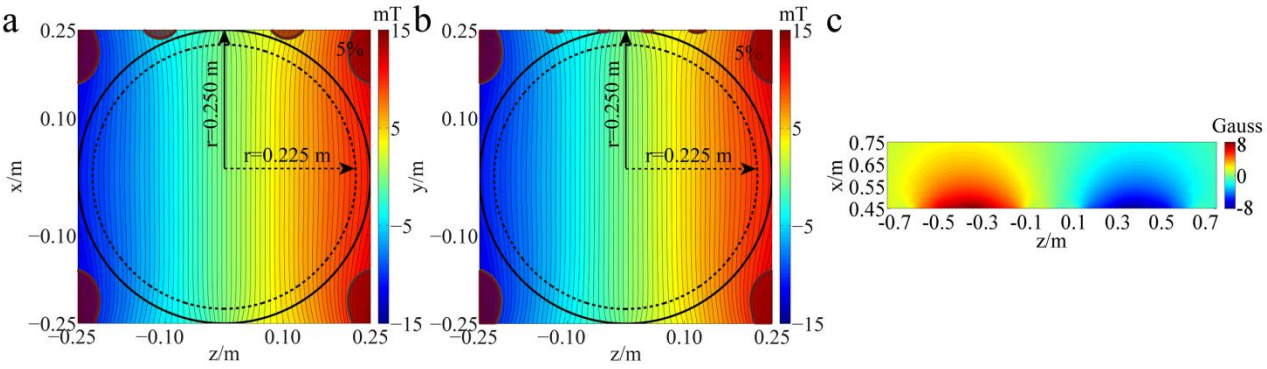

Fig. 4-21 Magnetic field distribution of the spiral z-gradient coil design using the discrete wire method, (a) the magnetic field distribution on the plane *y*=0, (b) the magnetic field distribution on the plane *z*=0 and, (c) the magnetic field distribution outside the gradient coil.

The coil performances of the conventional z-gradient coil design and the spiral z-gradient coil design are listed in Table 4-8. Similarly to the x-gradient coil, the inductances and resistances of these two gradient coils were calculated using FastHenry [118] with a uniform rectangular wire cross section 3 mm × 3 mm. The maximum magnetic field error of the conventional gradient coil is 9.00% over a DSV 50 cm and 6.22% over a DSV 45 cm, while the spiral gradient coil has a 5% magnetic field error over a 50 cm DSV. In addition, the spiral z-gradient coil also has an obvious advantage in the inductance and resistance compared with the conventional z-gradient coil. The inductance of the spiral z-gradient coil is 1999.1 μH compared with the conventional gradient coil's

2353.5 μH, with a 15.1% reduction, and the resistance of the spiral gradient coil is 489.5 mΩ compared with the conventional gradient coil 524.9 mΩ with a 6.7% reduction. The overall coil performance FoM of the spiral gradient coil is 2.901×10^{-6} $T^2/m^2/A^2/H$, while the conventional gradient coil is 2.464×10^{-6} $T^2/m^2/A^2/H$, which increases by 17.7%.

Table 4-8 Performances of the conventional z-gradient coil and the spiral z-gradient coil

Parameters	Conventional coil	Spiral coil
Loop number (n, primary/shielding)	76/50	72/46
Current amplitude (A)	590.97	590.97
Efficiency (mT/m/A)	0.07615	0.07615
Maximum field error (%, DSV=50 cm)	9.00	5.00
Maximum field error (%, DSV=45 cm)	6.22	2.73
Inductance (μH)	2353.5	1999.1
Resistance (mΩ)	524.9	489.5
Figure of merit ($T^2/m^2/A^2/H$)	2.464×10^{-6}	2.901×10^{-6}
Minimum wire spacing (mm)	7.1	10.0

Note: The inductance and resistance of the two coils were calculated using FastHenry, by assuming a uniform rectangular wire cross section 3 x 3 mm.

Fig. 4-22 shows the 3D plot of the conventional z-gradient coil design (the separate wire loops were connected) and spiral z-gradient coil design. Because the cutting and connecting process is avoided in the spiral coil design, the coil loop has a smooth jump from one to the next. For the spiral design, it is easy to implement a cooling pipe directly into the wire by making the wire hollow. This will save precious space in an MRI system; it is possible to produce a better cooling effect compared to the conventional cooling design. In addition, the spiral z-gradient coil is also sparser than the corresponding conventional coil, but with the same efficiency; thus, the heating problem is reduced compared to the conventional coil.

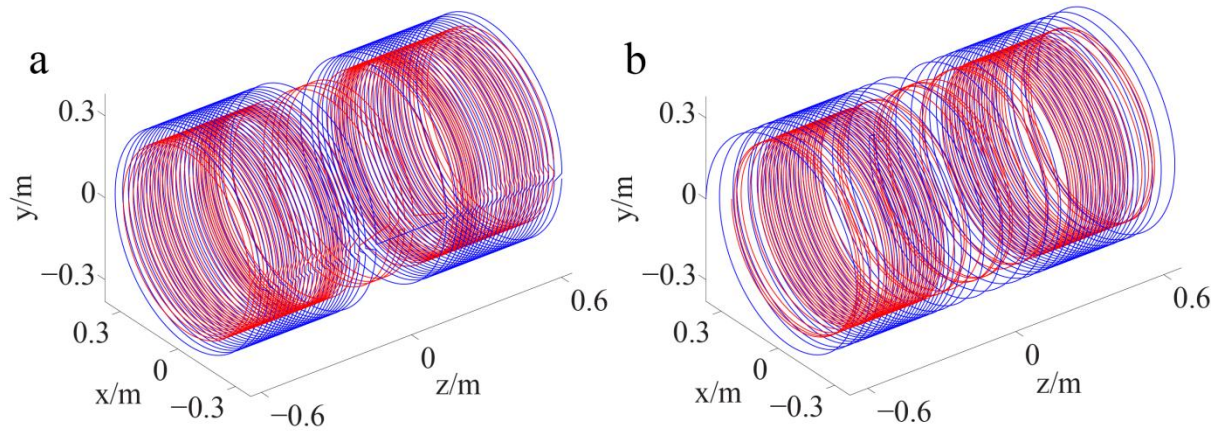

Fig. 4-22 3D plot of the conventional z-gradient coil design and the spiral gradient coil, (a) conventional z-gradient coil and (b) spiral z-gradient coil.

4.2.4 Conclusion

The spiral gradient coil design method proposed in this work used a butted quasi-elliptic geometry to generate the transverse gradient coil loop configuration and a helical geometry to generate the longitudinal gradient coil loop configuration. Compared with the commonly-used stream function-based gradient coil design method, the proposed method avoids the design errors associated with the discretization of continuous current density and wire connections. In addition, the proposed method is flexible in terms of adjusting the wire shape and distribution, especially the wire spacing.

By adjusting and optimizing the loop geometry parameters, the proposed method can design a spiral gradient coil with high performance. The numerical calculation shows that, for the x-gradient coil, the inductance and resistance of the gradient coil were reduced by 20.9% and 10.5% respectively when using the spiral design, compared with the conventional stream function-based gradient coil design. The overall coil performance FoM was increased by 26.5%; for the z-gradient coil, the inductance and resistance of the gradient coil were reduced by 15.1% and 6.7%, respectively, when using the spiral design, compared with the conventional stream function-based gradient coil design. The overall coil performance FoM was increased by 17.7%. Moreover, the spiral wire loops are smoother and the wire distributions are sparser than the conventional stream function-based gradient coil design and should therefore be easier to fabricate.

4.3 Design of transverse head gradient coils using a layer-sharing scheme

4.3.1 Introduction

Some recent developments in gradient coil design include multilayer coils which were proposed to spread the coil tracks out onto more coil layers [45]. For a given coil efficiency, this method can produce a smaller resistance compared with an actively-shielded two-layer coil, resulting in potentially improved thermal performance. 3D gradient coils have been proposed and connect the primary coil layer and the shielding coil layer, allowing the current flow directly from the primary coil to the shielding coil [72, 102, 110, 112, 119]. Under the same constraints as a layered coil, a 3D coil is able to increase the wire spacing and reduce the coil inductance and local heating problems [60, 102, 120]. However, both the multilayer and 3D designs can be challenging to fabricate.

In this work, a novel gradient coil configuration was proposed with the focus on improving the electromagnetic performance of the transverse coils. This new design employs a layer-sharing scheme, with some sections of the x primary layer distributed to the y coil and *vice versa*. Compared to existing gradient coil configurations/designs, the key advantage of the proposed method lies in its higher efficiency in delivering the required magnetic field inside the imaging region (DSV), without requiring any extra construction complexity. This advantage can be used to improve other coil properties, such as reducing inductance, resistance, and so on. Numerical simulations on asymmetric head coil designs using this method [7, 121, 122] were carried out and the coil performances were compared with corresponding conventional coils.

4.3.2 Method

4.3.2.1 Layer-sharing scheme for transverse head coil design

The proposed work is focused on the improvement of transverse head coils. Fig. 4-23 shows an example of the transverse coils, where (a) and (b) are the actively-shielded x and y coils respectively. In general, the coil cylinder is divided into two half-cylinders and every half-cylinder has an appropriate fingerprint for the primary coil and shielding coil, respectively. As shown in Fig. 4-23, there are two gaps between the half-cylinders as marked by the angle θ in Fig. 4-23 (c) and (d), where the wire patterns have a low density. These are essentially the return paths, and they do not constructively contribute to the gradient field formation in the DSV. In comparison, the wire tracks distributed at the centre of the coil in Fig. 4-23 (a) and (b) are much denser and these constructively contribute to the gradient field formation in the DSV.

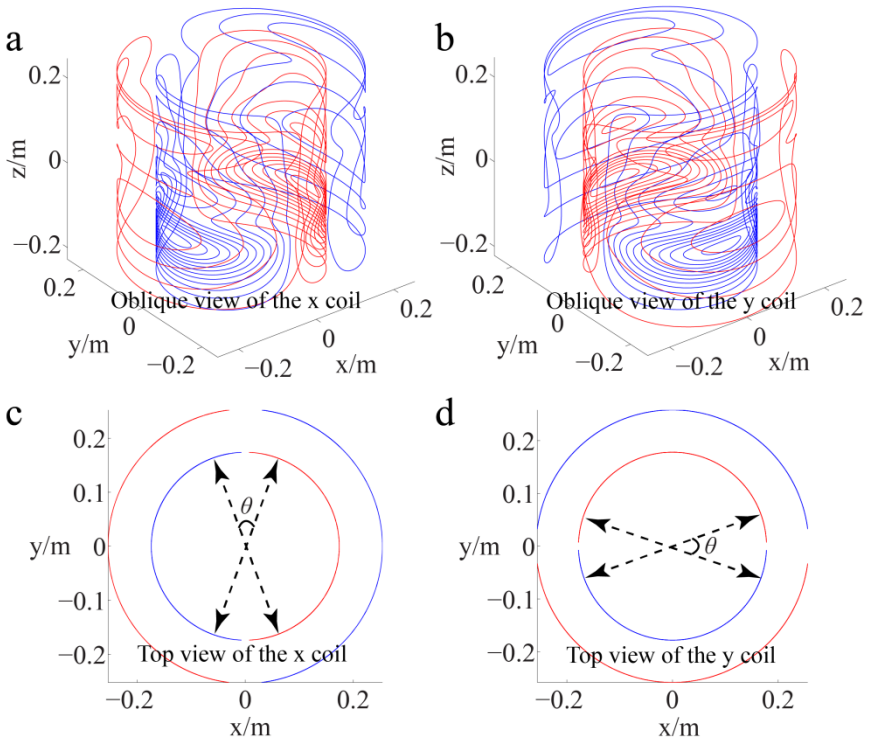

Fig. 4-23 Conventional actively-shielded asymmetric head gradient coil pattern: (a-b) x and y coils respectively, and (c-d) top views of the x and y coils.

Based on the above observations, we proposed a novel coil design by a layer-sharing scheme. As shown in Fig. 4-24, (a) and (b) are the cross sections of the original x primary coil and y primary coil respectively. For our design, the section of the x primary coil (marked as θ) that provides a weak B_z magnetic field contribution is allocated to y gradient coil. Here the angle θ is defined as the coil sharing angle. Similarly, the section of the y primary coil (marked as θ) that provides only a weak B_z magnetic field contribution is allocated to the x gradient coil design. Here we define the remaining part of the original primary coil as primary coil 1 and the supplementary part from the other transverse coil as primary coil 2. Fig. 4-24 (c) and (d) display the layouts of the novel x and y primary coils.

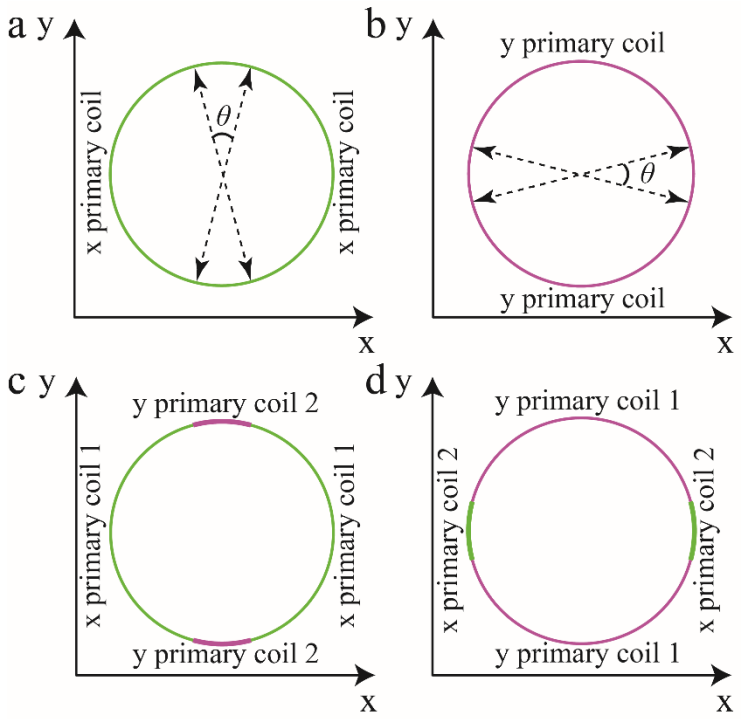

Fig. 4-24 Novel transverse gradient coils design by a layer sharing scheme: (a) conventional x primary coil, (b) conventional y primary coil, (c) novel x primary coil and (d) novel y primary coil. For the novel gradient coil design, each primary coil layer includes sections of both the x primary coil and y primary coil.

4.3.2.2 Coil design using the discrete wire method

The discrete wire method [41, 42] was used for the asymmetric head gradient coil design and the quasi-elliptic geometry was used to approximate the coil contours. For the loop optimization, a quasi-conical geometry base was applied. The deformed geometry may restrict the possible solution space compared with commonly-used stream function methods. Nevertheless, here our main focus is to take advantage of the fact that the discrete wire method can easily handle the wire spacing, thus reducing the local heating problems. It is noted that, in conventional continuous-current density-based methods, the final coil pattern is formed by contouring the stream function, which can involve discretization errors. In comparison, the discrete wire method directly controls the wire pattern, without any potential discretization error in the mapping between stream function and wire contours.

Fig. 4-25 shows the structure of the base. The function of the basic geometry is

$$\frac{|y|^p}{A^2}+\frac{|z|^p}{B^2}=1, \qquad p\geq 1 \tag{4-3}$$

In which, $A=\frac{\pi}{2}a$ and where a is the radius of the coil cylinder. Here the cylinder is assumed to be unwrapped as a plane. When $z > z_0$, $B=0.5L_a - z_0$ and when $z < z_0$, $B= 0.5L_a + z_0$. The centre of the basic geometry is z_0 and L_a is the coil length. The coil coordinates can be expressed as

$$\begin{aligned} x_c &= a\cos\left(\frac{y}{a}\right) \\ y_c &= a\sin\left(\frac{y}{a}\right) \\ z_c &= z \end{aligned} \tag{4-4}$$

For the other half of the head coil, y is replaced with $y + \pi$.

The height of the geometry base is defined as H. Assuming that the vertical coordinate of the coil contour is h_i, correspondingly, A_i is $h_i/H{\cdot}A$ and B_i is $h_i/H{\cdot}B$.

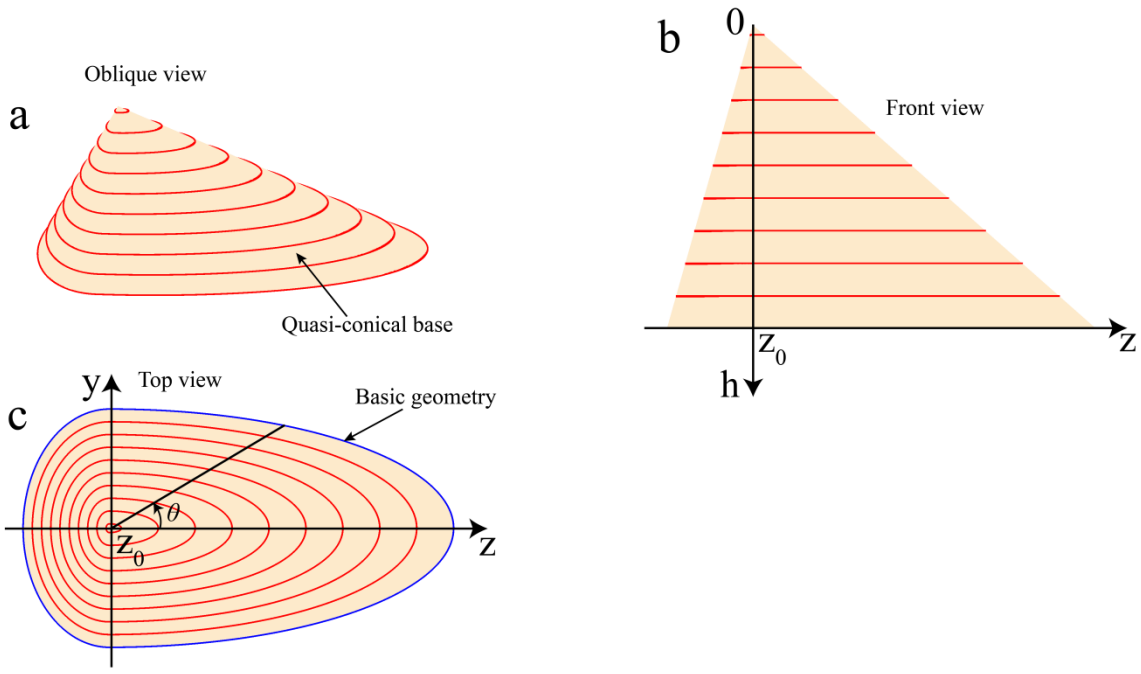

Fig. 4-25 Illustration of the quasi-conical base where the coil contour are wound on: (a) oblique view, (b) front view and (c) top view.

During the optimization, the loop positions were mapped onto the coil cylinder. The integral expression of the Biot-Savart law below was used in the magnetic field calculation [18]

$$B(\boldsymbol{r}) = \frac{\mu_0}{4\pi}\int \frac{I\mathrm{d}\boldsymbol{l}\times(\boldsymbol{r}-\boldsymbol{l})}{|\boldsymbol{r}-\boldsymbol{l}|^3} \tag{4-5}$$

where μ_0 is the vacuum permeability, I is the current, $\boldsymbol{l}$ is the current circuit and $\boldsymbol{r}$ is the magnetic field point.

The target for the optimization is to minimize the function

$$f=\text{norm}\left(B_z^{\text{DSV}}-B_z^{\text{Target}}\right)+\lambda\cdot\text{norm}\left(B_z^{\text{Shield}}\right) \tag{4-6}$$

with the wire spacing being controlled by

$$|h_{i+1}-h_i|\geq\Delta h \tag{4-7}$$

where B_z^{DSV} is the z-component magnetic field over the DSV surface, B_z^{Target} is the defined target magnetic field, B_z^{Shield} is the magnetic field on the cryostat, λ is the weighting factor, h is the vertical height on the quasi-conical base and Δh is the height difference between the neighbouring contours.

The optimization parameters for the discrete wire method include geometry shape (see Fig. 3(c)) p [42, 123], z_0 position (see Fig. 4-25 (c)), h positions (see Fig. 4-25 (b)) and current I.

Both asymmetric x and y head coils were designed in this paper. In the simulated results presented below, the target gradient strength was 45 mT/m with a DSV 24 cm; the DSV was shifted 7 cm away from the centre. The coil dimensions are summarized in Table 4-9.

Table 4-9 Dimensions for the asymmetric head gradient coil design

Item	r (m)	l (m)
x primary coil	0.174	0.5
x shielding coil	0.254	0.5
y primary coil	0.178	0.5
y shielding coil	0.258	0.5
Warm bore wall	0.486	1.46

Note: r is the coil radius and *l* is the coil length. The warm bore wall was used for the shielding effect control.

The function *fmincon* in Matlab was used for the optimization and the maximum iteration step 50 was selected for both the conventional coil design and novel coil design to ensure that the optimization solution converges well. For the initial solution, p was 4, z_0 was $-0.25L_a$, h_i was an equal-spaced array from 0.3 m to 10 m and I was 500 A.

4.3.3 Results

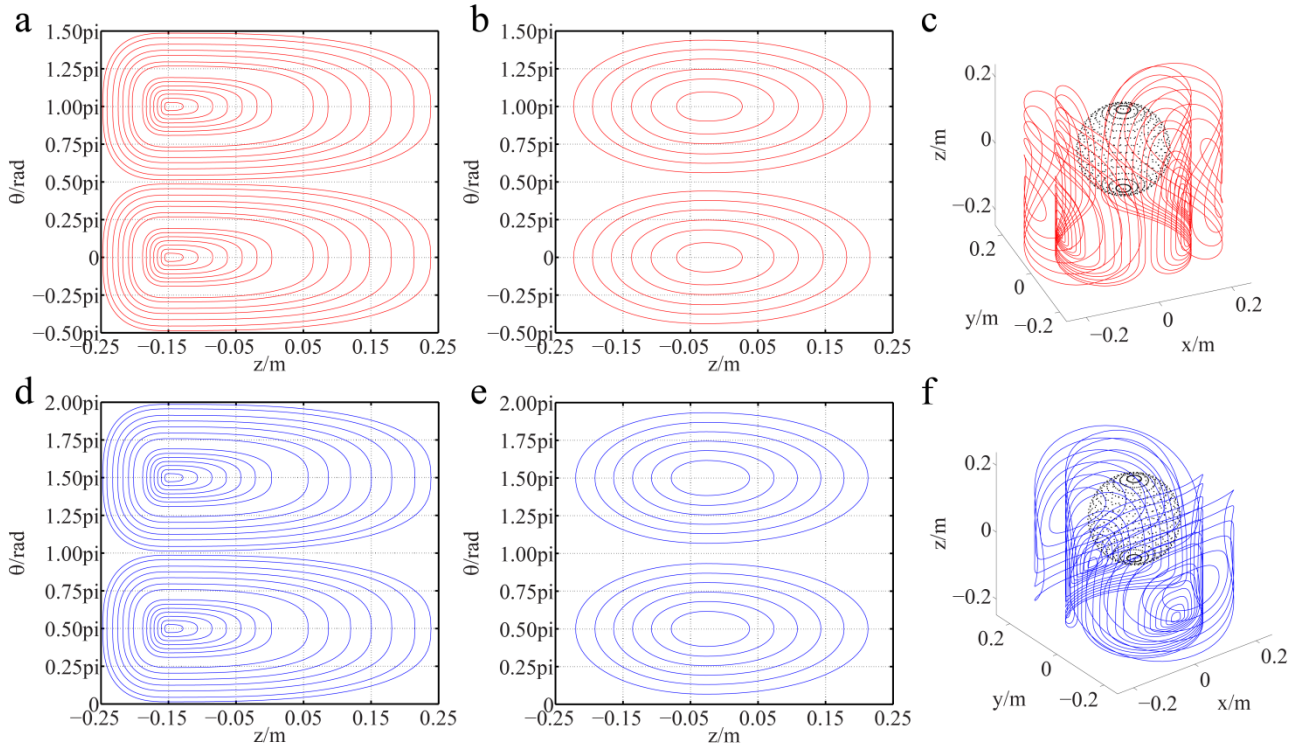

Fig. 4-26 Conventional asymmetric head gradient coils: (a) x primary coil, (b) x shielding coil, (c) 3D x coil, (d) y primary coil, (e) y shielding coil and (f) 3D y coil. DSV is shown in the 3D plot.

Using the design parameters shown in Table 4-9, a set of transverse asymmetric head gradient coils were designed with the conventional approach and the results are presented in Fig. 4-26. Specifically, Fig. 4-26 (a) and (d) show the primary layers, with (b) and (e) being the shielding layers. The weighting factor λ in this work was set as 0.2 and the total height of the geometry base H was 10 m. The DSV was shifted toward the z+ direction by 7 cm. Thus, the distance from the coil cylinder end to the DSV edge is 6 cm based on the coil design dimension. The x and y coil have similar coil patterns, but reside in different layers. Fig. 4-26 (c) and (f) are the plots of the 3D coil patterns.

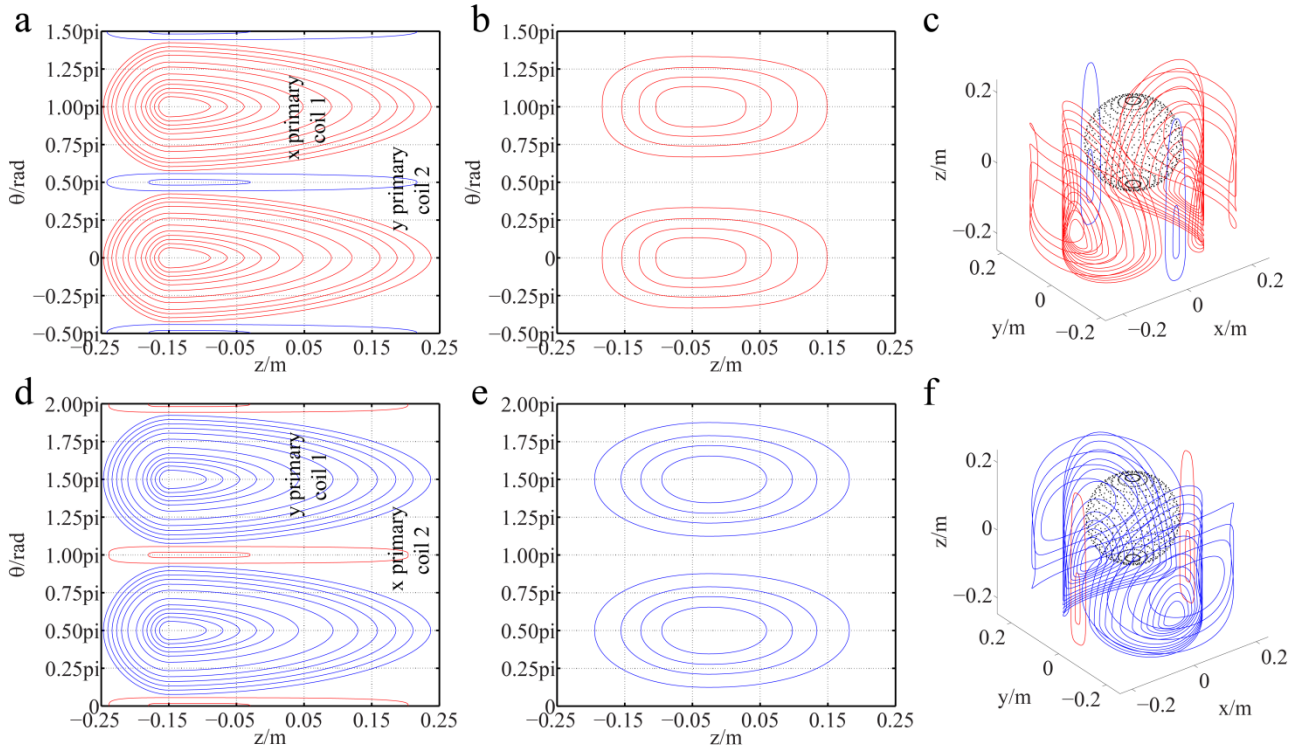

Fig. 4-27 Novel asymmetric head gradient coils, (a) x primary coil 1 and y primary coil 2, (b) x shielding coil, (c) 3D coil (including x primary coil 1, y primary coil 2 and x shielding coil), (d) y primary coil 1 and x primary coil 2, (e) y shielding coil and (f) 3D coil (including y primary coil 1, x primary coil 2 and y shielding coil). DSV is shown in the 3D plot. Note that the x primary coil 1 and y primary coil 2 reside at the same coil layer, and the same is to the y primary coil 1 and x primary coil 2.

Using the new strategy proposed in this work, a set of transverse asymmetric head coils was designed and the results are shown in Fig. 4-27. Here the coil sharing angle θ is 22.5^{o} (π/8 radian). The 22.5 degree was chosen, based on our simulation studies. A smaller number will result in a densely localized wire distribution on the small coil, and larger number will induce a further gradient nonlinearity inside the DSV. For each transverse coil, there are two primary coils (coils 1 and 2) and one shielding coil. The x primary coil 1 and y primary coil 2 are plotted together (see Fig. 4-27 (a)), as are the y primary coil 1 and x primary coil 2 (see Fig. 4-27 (d)). Considering the 3D coil pattern (Fig. 4-27 (c) and (f)), the primary coil 2 is located on the central part of the primary coil 1 for both the x and y coils, which accompanies the primary coil 1 to make magnetic field contribution in imaging area. The x primary coil 1 contains 12 loops and 2 loops in x primary coil 2, while, for comparison, the conventional x primary coil has 16 loops. For the shielding coils, the novel x coil has 4 loops, while the conventional x shielding coil has 6 loops. The same conditions are applied to the y coils.

The optimized parameters of the conventional coils and novel coils are listed in Table 4-10.

Table 4-10 The optimized coil pattern parameters

Conventional x coil	**Primary coil**	**Height h_i (m)**	**1**	**2**	**3**	**4**	**5**	**6**	**7**	**8**
			0.540	1.089	1.638	2.187	2.736	3.284	3.833	5.366
		Height h_i (m)	**9**	**10**	**11**	**12**	**13**	**14**		
			5.916	6.766	7.451	8.259	9.102	9.720		
		Loop center z_0 (m)	-0.150	**Power p**	2.858					
	Shielding coil	**Height h_i (m)**	**1**	**2**	**3**	**4**	**5**	**6**		
			1.943	3.644	4.943	6.283	7.536	8.789		
		Loop center z_0 (m)	-0.027	**Power p**	2.161	**Current (A)**	508.902			
Conventional y coil	**Primary coil**	**Height h_i (m)**	**1**	**2**	**3**	**4**	**5**	**6**	**7**	**8**
			0.534	1.070	1.607	2.143	2.680	3.216	3.821	5.169
		Height h_i (m)	**9**	**10**	**11**	**12**	**13**	**14**		
			5.919	6.743	7.513	8.267	9.123	9.717		
		Loop center z_0 (m)	-0.150	**Power p**	2.767					
	Shielding coil	**Height h_i (m)**	**1**	**2**	**3**	**4**	**5**	**6**		
			2.321	3.629	4.881	6.139	7.377	8.659		
		Loop center z_0 (m)	-0.027	**Power p**	2.100	**Current (A)**	529.987			
Novel x coil	**Primary coil 1**	**Height h_i (m)**	**1**	**2**	**3**	**4**	**5**	**6**	**7**	**8**
			1.526	2.154	2.781	3.409	4.081	4.961	6.004	6.770
		Height h_i (m)	**9**	**10**	**11**	**12**	**Primary coil 2**	**Height h_i (m)**	**1**	**2**
			7.803	8.431	9.059	9.686			3.004	8.853
		Loop center z_0 (m)	-0.150	**Power p**	1.793			**Power p**	2.605	
	Shielding coil	**Height h_i (m)**	**1**	**2**	**3**	**4**				
			2.660	3.914	5.194	6.650				
		Loop center z_0 (m)	-0.051	**Power p**	3.583	**Current (A)**	509.390			
Novel y coil	**Primary coil 1**	**Height h_i (m)**	**1**	**2**	**3**	**4**	**5**	**6**	**7**	**8**
			1.389	2.004	2.617	3.242	3.874	4.801	6.078	6.994
		Height	**9**	**10**	**11**	**12**	**Primary**	**Height**	**1**	**2**

		h_i (m)	7.719	8.397	9.033	9.684	**coil 2**	**h_i (m)**	3.004	9.166
		Loop center z_0 (m)	-0.150	**Power *p***	1.879			**Power *p***	2.524	
	Shielding coil	**Height**	**1**	**2**	**3**	**4**				
		h_i (m)	3.099	4.479	5.788	7.528				
		Loop center z_0 (m)	-0.026	**Power *p***	2.110	**Current (A)**	529.999			

Table 4-11 lists the coil performance of the new design as well as the conventional design. For the sake of comparison, the current of the proposed gradient coil was adjusted to be similar to that in the conventional design by choosing appropriate numbers of coil windings. To approximate the practical coil fabrication, a minimum 1 mm gap was set between wire tracks, the maximum coil track width was set to be 2 cm and the coil track thickness was assumed to be 3 mm [124]. Coil resistances and inductances were computed using FastHenry [118]. Both the self-inductances and mutual-inductances including the primary coils and shielding coils were considered for the coil inductance calculation. From Table 4-10, it can be seen that the proposed coil design has lower inductances with 59.49 μH and 58.00 μH for the x and y coils respectively, while the corresponding values of the conventional design are 61.21 μH and 61.27 μH. For the resistances, the proposed coil design has 13.06 mΩ and 12.56 mΩ compared to conventional design with 15.75 mΩ and 15.23 mΩ for the x and y coils respectively. An overall performance measure, the figure-of-merit, was also used for the coil comparison. This figure-of-merit was defined as η^2/L [32], where η is the coil efficiency and L is the inductance. The figure of merit of the proposed coil design is 1.3106×10^{-4} $T^2/m^2/A^2/H$ and 1.2428×10^{-4} $T^2/m^2/A^2/H$ for the x and y coils respectively; these are higher than those of the conventional coils with 1.2767×10^{-4} $T^2/m^2/A^2/H$ and 1.1764×10^{-4} $T^2/m^2/A^2/H$. The performance improvement with the figure-of-merit is 2.66 % and 5.64 % for the x and y coils respectively. Another important performance parameter, η^2/R [61], is also commonly used in gradient coil performance evaluation, where R is the resistance. For the proposed coil design, the η^2/R is 5.9701×10^{-7} and 5.7389×10^{-7} for the x and y coils respectively; for the conventional coils, it is 4.9616×10^{-7} and 4.7328×10^{-7}. The respective performance improvements with η^2/R are 20.32 % and 21.26 %. The minimum wire spacings for both the conventional coils and novel coils are all larger than 5 mm. The novel coil patterns have a lower wire density than the conventional coils.

Table 4-11 Performances of the conventional asymmetric head gradient coils and the novel asymmetric head gradient coils

Parameters	Conventional x coil	Conventional y coil	Novel x coil	Novel y coil
Loop number (n, primary/shielding)	28/12	28/12	24+4/8	24+4/8
Current amplitude (A)	508.9	530.0	509.4	530.0
Efficiency (mT/m/A)	0.0884	0.0849	0.0883	0.0849
Inductance (μH)	61.21	61.27	59.49	58.00
Resistance (mΩ)	15.75	15.23	13.06	12.56
Magnetic energy (J)	7.93	8.61	7.72	8.15
Power dissipation (kW)	4.08	4.28	3.39	3.53
Figure of merit ($T^2/m^2/A^2/H$)	1.2767×10^{-4}	1.1764×10^{-4}	1.3106×10^{-4}	1.2428×10^{-4}
η^2/R ($T^2/m^2/A^2/\Omega$)	4.9616×10^{-7}	4.7328×10^{-7}	5.9701×10^{-7}	5.7389×10^{-7}
Minimum wire spacing (mm)	5.5	5.4	6.3	6.1

Note: The inductance and resistance were calculated by FastHenry by setting the coil track with a minimum gap 1 mm and maximum width 2 cm, and the coil thickness was set as 3 mm. The magnetic energy and power dissipation were calculated by $1/2I^2L$ and I^2R respectively.

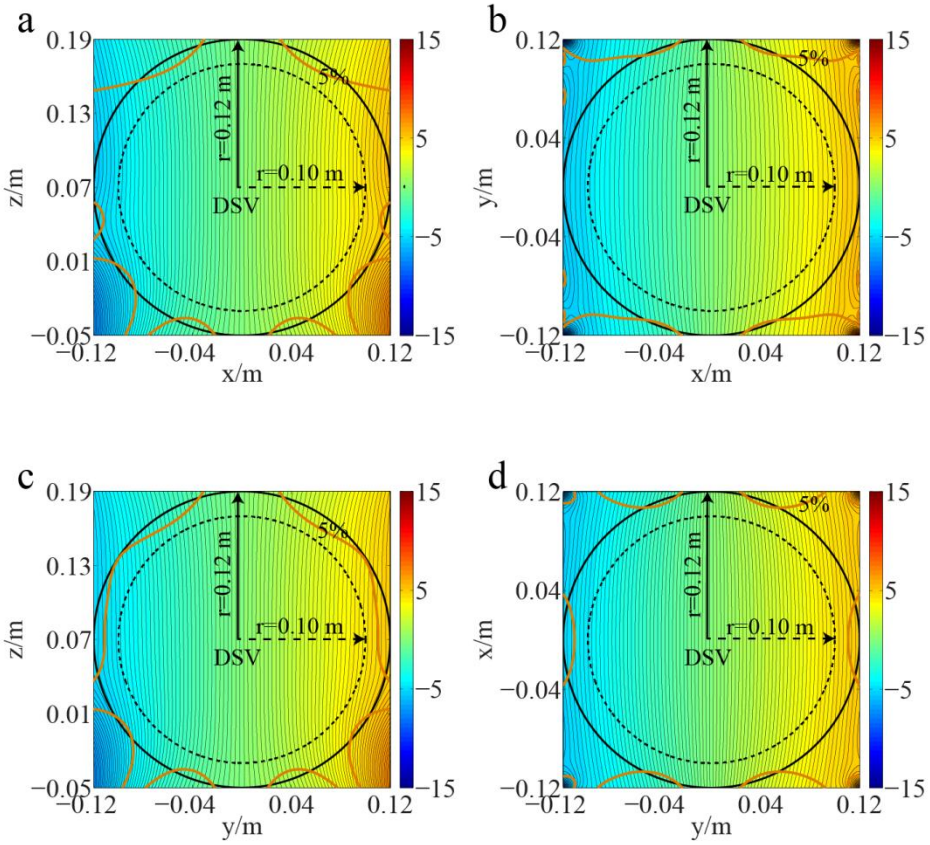

Fig. 4-28 B_z field distributions produced by the conventional asymmetric head gradient coils: (a) magnetic field distribution of the conventional x coil at xz section, (b) magnetic field distribution of the conventional x coil at xy

section, (c) magnetic field distribution of the conventional y coil at yz section and (d) magnetic field distribution of the conventional y coil at yx section. The 24 cm DSV (radius 0.12 m), 20 cm DSV (radius 0.10 m) and 5% magnetic field deviation lines are marked.

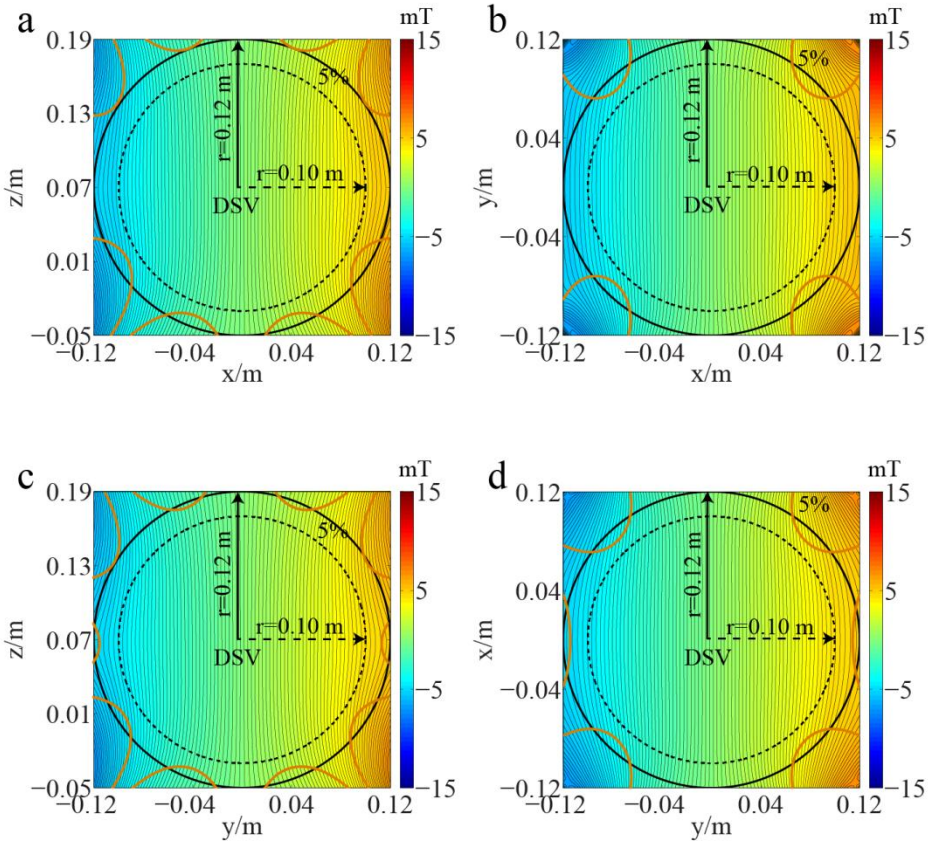

Fig. 4-29 B_z field distributions produced by the novel asymmetric head gradient coils: (a) magnetic field distribution of the novel x coil at xz section, (b) magnetic field distribution of the novel x coil at xy section, (c) magnetic field distribution of the novel y coil at yz section and (d) magnetic field distribution of the novel y coil at yx section. The 24 cm DSV (radius 0.12 m), 20 cm DSV (radius 0.10 m) and 5% magnetic field deviation line were marked.

The B_z distributions in and around the imaging area for the conventional design are illustrated in Fig. 4-28 with the distributions of counterpart novel design being illustrated in Fig. 4-29. The gradient magnetic field non-uniformity evaluation used for the coil designs is expressed as [6, 98]

$$\frac{\max\left|B_z^{DSV}-B_z^{target}\right|}{\max\left|B_z^{target}\right|} \tag{4-8}$$

In a DSV with 24 cm, the gradient magnetic field non-uniformities of the conventional coils are 6.33 % and 6.41 % for the x and y coils respectively, while for the novel coils, they are 7.26 % and

7.07 %. For a smaller sized DSV (20 cm), the conventional coils have gradient magnetic field non-uniformities 4.14 % and 4.74 % for the x and y coils respectively, compared to 4.40 % and 4.04 % for the novel coils.

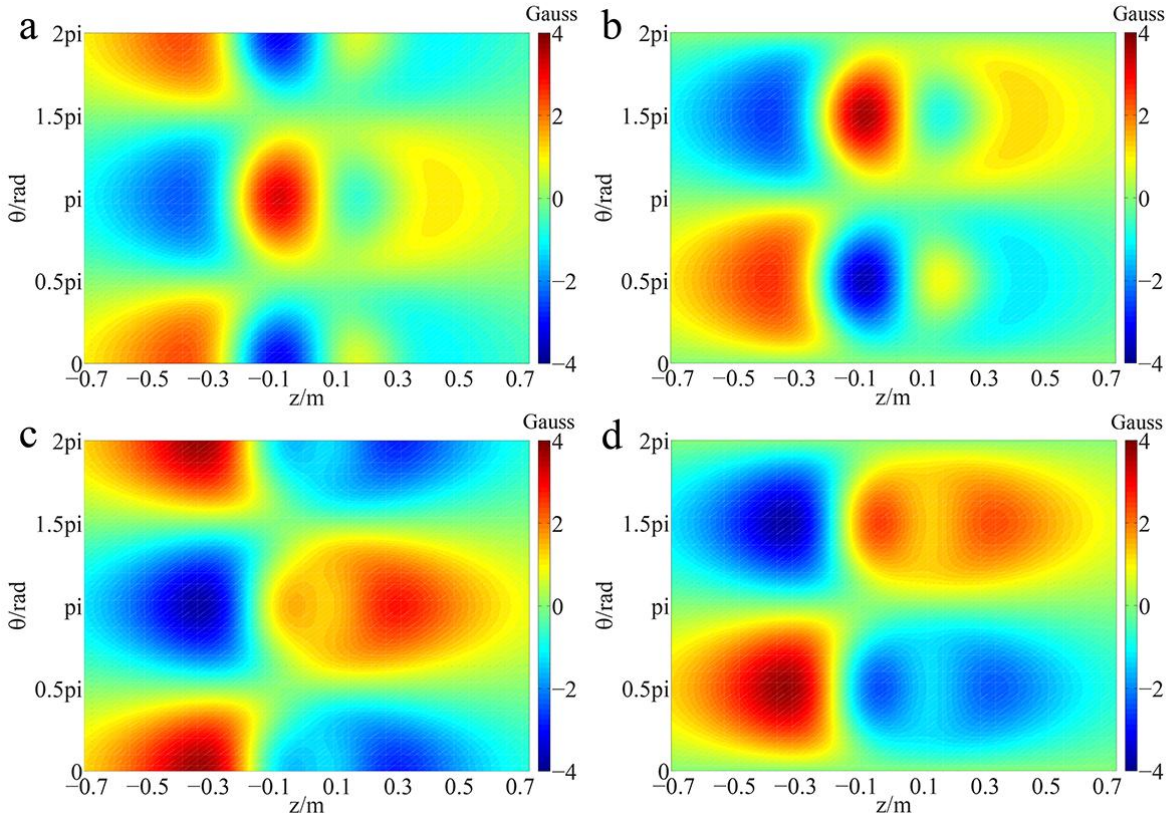

Fig. 4-30 B_z magnetic field distributions on the cryostat with the conventional asymmetric head gradient coils design and novel head gradient coils design: (a) conventional x coil, (b) conventional y coil, (c) novel x coil and (d) novel y coil.

The z components of the magnetic field distributions on the cryostat for the conventional coil design ((a) and (b)) and the novel coil design ((c) and (d)) are illustrated in Fig. 4-30. For the case of producing a targeted maximum dB/dz=45 mT/m, the peak magnetic field strengths on the cryostat for the conventional coil design are 3.22 Gauss and 3.64 Gauss for the x and y coils respectively. For the novel coil design, the maximum magnetic field strengths on the cryostat are 3.74 Gauss and 3.78 Gauss.

It is acknowledged that the gradient coils are designed with the focus on the magnetic fields [42, 123] (here both field over the DSV and stray field), thus some system parameters such as inductance or resistance are not explicitly controlled and could be sub-optimal. To ensure sufficient wire spacing in the discrete wire-based design procedure, the field errors (and stray fields) for the proposed coils are slightly worse than those of the conventional ones.

When fabricating a gradient coil, the separate loops should be connected to allow current flowing through. Fig. 4-31 illustrates a connection pattern of the novel x gradient coil, as an example. Only a half is shown due to symmetry. The connections among the coil layers were at the end of the coil furthest from the DSV. Fig. 4-31 (a) shows the connecting configuration of the three coil layers and Fig. 4-31 (b) shows the local view of the connections at the coil end, where the connecting wires are shown as dash lines. The connections are not expected to have any obvious influence on gradient performance.

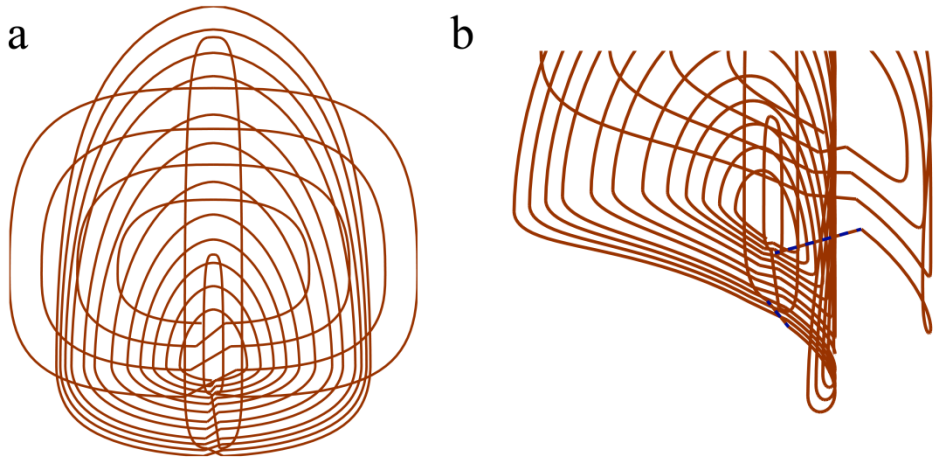

Fig. 4-31 Connection configuration of the novel x gradient coil, (a) integrated connection of the three coil layers and (b) local view of the connecting part. The connecting wires between the different coil layers were marked. Due to the symmetry, only a half-coil is shown here.

4.3.4 Conclusion

A novel transverse asymmetric head gradient coil design was proposed in this work. By applying a layer-sharing scheme, the regions which do not constructively contribute to the gradient magnetic field in a transverse gradient coil were supplemented to the other one, and *vice versa*. In the new design, each transverse coil layer contains both the x and y coils. There are two primary coil layers and one shielding layer in each complete transverse coil. Compared with a conventional design, the new design has smaller magnetic energy. For similar efficiencies, the new design has a lower inductance and resistance compared with conventional designs. The overall performances evaluated by η^2/L are improved by 2.66 % and 5.64 % for the x and y coils, respectively, and for η^2/R, the improvements are 20.32 % and 21.26 %, respectively.

Chapter 5

Acoustic noise investigation for MRI scanners

This chapter presents the acoustic investigation for MRI scanners during PhD candidature. It encompasses four parts in total. The contents of these four parts are based on the papers below. Some minor modifications were made to enhance the fluency of the context structure.

Y. Wang, F. Liu, E. Weber, F. Tang, J. Jin, Y. Tesiram, and S. Crozier, "Acoustic analysis for a split MRI system using FE method," *Concepts in Magnetic Resonance Part B: Magnetic Resonance Engineering*, vol. 45, pp. 85-96, 2015.

Y. Wang, F. Liu, and S. Crozier, "Simulation study of noise reduction methods for a split MRI system using a finite element method," *Medical Physics*, vol. 42, pp. 7122-7131, 2015.

Y. Wang, F. Tang, Y. Li, F. Liu and S. Crozier, "Theoretical investigation of gradient pulse alterations for acoustic noise reduction in an MRI-LINAC system", In: *Proceedings of the International Society for Magnetic Resonance in Medicine (ISMRM)*, Singapore, May 2016.

Y. Wang, F. Liu, X. Zhou, and S. Crozier, "Numerical study of the acoustic radiation due to eddy current-cryostat interaction," *Medical Physics*, vol. 44, pp. 2196-2206, 2017.

5.1 Acoustic analysis for a split MRI system using FE method

5.1.1 Introduction

It is reported that the loud noise during MRI operation potentially could cause damage to both the patient's hearing and the hearing of any health workers near the system [15, 16, 52]. The noise can reach 120-138 dB in some scanners [11, 52], which is around or higher than the pain threshold of human hearing [12]. MRI is continually moving towards scanners operating at higher magnetic fields, however this results in even higher noise levels [14, 81, 125].

Many studies have been conducted on the characteristics of the acoustic noise generated by MRI systems. It is well-known that the acoustic field of a MRI scanner varies spatially and is dependent

on the types of sequences used [8, 67, 69, 126-128]. The correlation between gradient magnetic field fluctuations and the acoustic noise has also been investigated [65]. It is commonly recognized that the most of the noise is generated by the gradient coils [8, 56, 65, 67, 69, 101, 115, 126-134]. In order to theoretically analyse the vibration and radiated acoustic noise of a MRI scanner, a number of gradient models have been built. These models can be divided into two groups, namely analytical models and numerical models. In many cases, analytical models have proven to be more efficient [56, 101, 129] as the model parameters can be easily adjusted to simulate different conditions. These models, however, are based on simplified cases, which are less useful in coping with the complex structures found in realistic designs. In numerical models, the Finite Element (FE) and the Boundary Element (BE) methods have been used [130, 131]. In some cases, cylindrical gradient coil models have been implemented to fully describe the vibrational modes and corresponding natural frequencies [115, 132-134] of the system.

MRI is increasingly being integrated with other medical devices, such as Linear Accelerator (LINAC), in order to facilitate image-guided therapies. The development of these hybrid systems is not a trivial engineering task. For example, in the case of a MRI-LINAC gradient coil system, the LINAC needs to be accommodated somehow. One solution is to design the gradient coil with a large central gap [96, 135-137] where the patient can reside or the LINAC can be mounted. However this configuration may alter the vibration and acoustic characteristics of the system. Although there are many acoustic models for conventional gradient coils, the acoustic characteristics of split MRI gradient coils, to the authors' best knowledge, have never been reported.

In this work, a 3-dimensional (3D) Finite Element Method (FEM) model of a split MRI system and a traditional MRI system design will be developed. The modelling procedure and modelling method will be validated by comparing an experimental measurement in a conventional MRI scanner and its corresponding simulated results. Then, a comparison of the acoustic characteristics and acoustic field distributions of the split MRI system and a traditional MRI system design will be conducted. Finally, some potential noise reduction schemes will be discussed for future MRI-LINAC system designs.

5.1.2 Methods

5.1.2.1 FEM acoustic model of a conventional MRI scanner

Fig. 5-1 displays the simplified 2-dimensional (2D) structure of a MRI scanner [130]. The acoustic model is established here for a Bruker BioSpec 94/30 USR scanner. The geometric characteristics of the gradient coils and magnet are presented in Table 5-1. Since the exact size of the cryostat is

not available, it has been estimated based on the size of the main magnet. The gradient coils were reversely designed based on the specifications and approximate knowledge of the coil geometry [138].

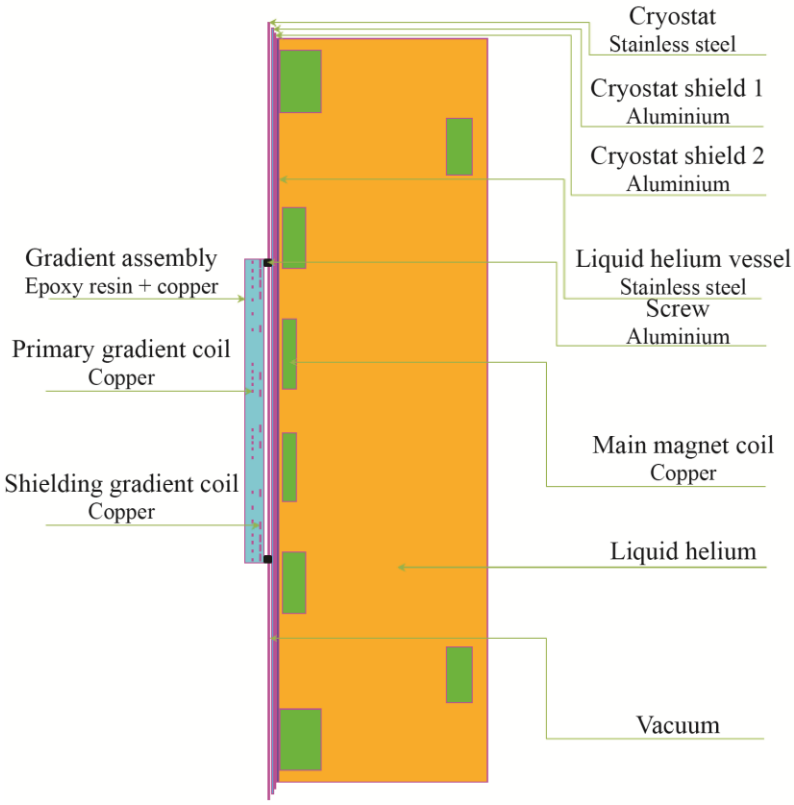

Fig. 5-1 Simplified structure of a conventional MRI scanner. The acoustic model presented here is based on this structure.

Table 5-1 Measured size parameters of the Bruker 9.4 T scanner

Item (unit: m)	Inner diameter	Outer diameter	Length
Small gradient assembly	0.114	0.198	0.513
Larger gradient assembly	0.200	0.302	0.814
Main magnet	0.342	1.706	2.08

We note that there are two sets of gradient assemblies in the scanner. The larger one is used to scan large animals when the small one is absent, and the smaller one is used to scan small animals. For acoustic analysis, a 3D MRI scanner model was built including both gradient assemblies. The connected screws between these structures were simulated as aluminium blocks. The thickness of the coil tracks was set to be 2.5 mm.

The MRI scanner was assumed to be located in a free space. Normally, the surrounding air sphere radius is required to be no less than $R = r + 0.2\lambda_{max}$, where r is the radius of the vibrating object and λ_{max} is the largest acoustic wavelength. Considering the frequency feature of the commonly-used gradient pulses, harmonic analysis method with frequency ranging from 100 Hz to 3000 Hz was applied. The structure and the adjacent air were fully coupled, which means there is identical speed at the interfaces, thus the structure vibration can be transmitted to be acoustic disturbance. As a general rule, it is suggested that the mesh size should be less than 1/6 of the smallest wavelength in acoustic analysis [139]. The largest side of the FE hexahedrons was controlled according to this criterion. Infinite acoustic boundary condition was applied on the outer surface of the surrounding air, implying that the acoustic wave was totally absorbed here with no reflection [139]. The cryostat was set to be simply supported [116]. Since the load distribution of the different coils has symmetric or anti-symmetric features, 1/8 model can be used to simulate the scanner as a whole. The corresponding boundary conditions are displayed in Table 5-2.

Table 5-2 Structural symmetric and anti-symmetric boundary conditions

Plane	x coil	y coil	z coil
x=0	s	s	s
y=0	s	s	s
z=0	s	s	a

Symmetric boundary conditions are represented by 's' and anti-symmetric boundary conditions are represented by 'a'. In a structural analysis, if using U to indicate the displacement, for plane x=0, symmetry indicates Ux=0 and anti-symmetry indicates Uy & Uz=0; for plane y=0, symmetry indicates Uy=0 and anti-symmetry indicates Ux & Uz=0; for plane z=0, symmetry indicates Uz=0 and anti-symmetry indicates Ux & Uy=0.

Fig. 5-2 shows the acoustic modelling process of the conventional MRI scanner. The FEM program used in this work is the commercial ANSYS package. The FEM package is used to calculate the acoustic field produced by gradient coil switching, which numerically solves the mechanical vibration and acoustic wave equation. The dynamic behaviour of the structure can be referred to section 3.1.

The current peak value in this study was $I = 45$ A (15 percent of the maximum current, which is 300 A) which was applied on the x coils of the smaller gradient assembly and the main magnetic flux density was $B = 9.4$ T. The forces on the coil tracks were calculated based on its FE meshes (hexahedrons) and then distributed on the corresponding eight nodes uniformly.

5.1.2.2 Experimental validation of the acoustic model

The experiment was conducted in the scanner mentioned in Section 5.1.2.1. The acoustic noise was measured using a MRI-compatible piezoelectric transducer. Before the experiment, the transmission gain between the sound pressure measurement and the corresponding voltage was calculated using a HHB Circle 3 loudspeaker and an IC 1592 - Pro sound level meter. In the experiment, the transducer was mounted as an extension to the supplied animal bed (i.e. only the transducer was positioned in the desired position in the gradient coil). The position of the transducer was adjusted by moving the animal bed. The transducer was connected to a personal computer through a long screened cable. Both the transducer and cable were MRI-compatible. Fig. 5-3 shows the experimental platform of microphone calibration and acoustic measurement.

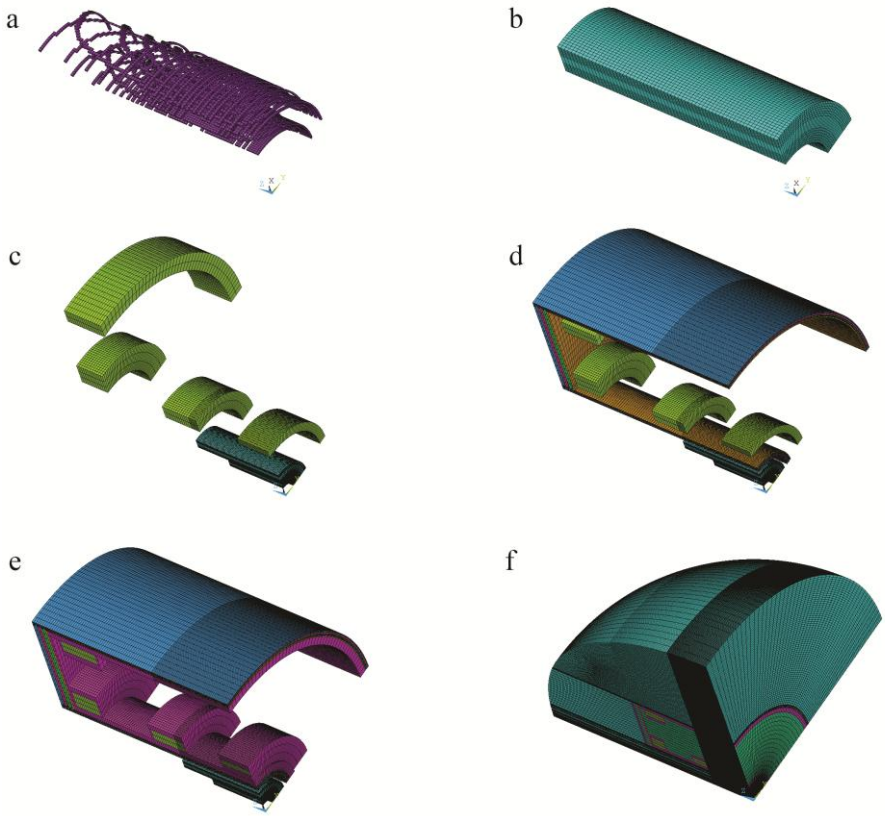

Fig. 5-2 Acoustic model of the conventional MRI system. (a-f) shows the process of modelling of the scanner. Only one eighth of the whole model is established here. (a) Gradient coils, (b) gradient assembly, (c) gradient assembly and main magnet coils, (d) gradient assembly, main magnet coils and cryostat, (e) whole scanner and (f) acoustic model.

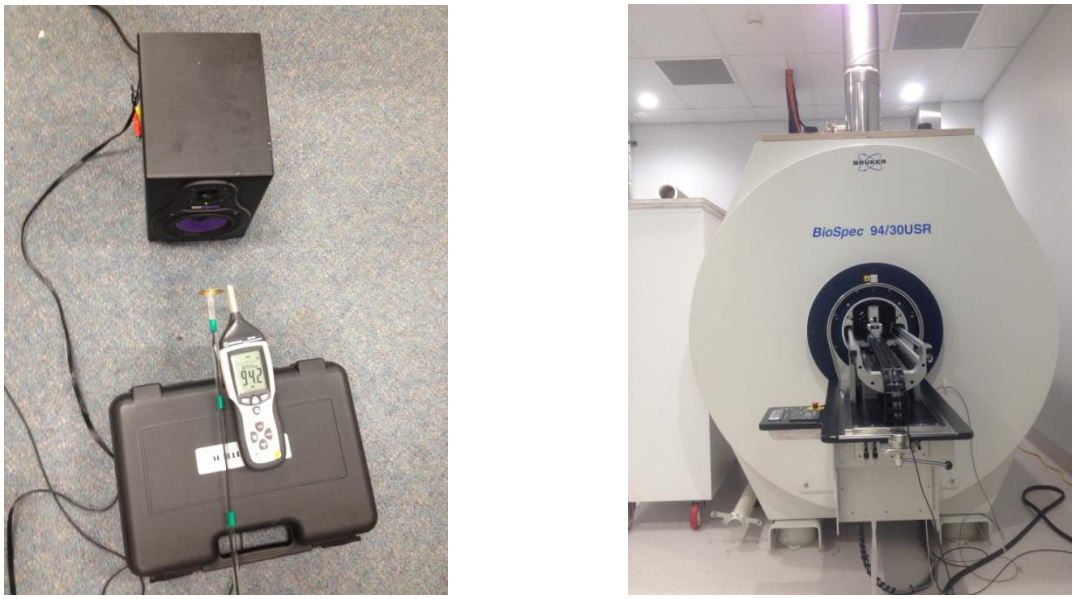

(a) (b)

Fig. 5-3 Experimental platform of the microphone calibration and acoustic measurement. (a) Microphone calibration and (b) acoustic measurement.

The experimental validation considers the acoustic field distribution. A 1-kHz gradient pulse with peak current value 45 A was used to excite the x coils of the smaller gradient assembly. There were 11 sampling points with 5-cm interval along the longitudinal axis of the smaller gradient assembly. The sound pressure level (SPL) distribution of the experimental results was compared with the simulated results.

5.1.2.3 Acoustic simulation of a split MRI system and its typical counterpart

After validation, a split MRI scanner model and a traditional scanner design were established using the same acoustic modelling procedures, with the same material properties used in the conventional scanner model. Herein the MRI scanner of the MRI-LINAC system was referred to as “split MRI system” and the traditional scanner design was referred to as “typical system”. The acoustic models consist of a gradient assembly, cryostat and main magnet. The connected screws were also simulated as aluminium blocks. For the acoustic analysis of the split MRI scanner, it is not applicable to use anti-symmetric or boundary condition on the plane z=0. This is because in a conventional typical cylindrical system, there exists a middle plane, z=0, which can be treated as an anti-symmetric boundary condition for the z coils (the Lorentz force on the coils is anti-symmetric with respect to this plane) and symmetric boundary condition for the transverse coils. For the split system, however, the central gap will not support such boundary conditions. In numerical simulations, if symmetric or anti-symmetric boundary conditions are available, DOFs can be set to

be zero. For example, in a mechanical analysis, if the structure is symmetric on plane z=0, the displacement DOF z is zero on this plane. While for the anti-symmetric case, the displacement component x and y are zero. However, in the air (central gap), only one DOF (pressure) exists. The symmetric or anti-symmetric boundary conditions cannot be embodied by applying constraints on this DOF (for the embodiment of the symmetric and anti-symmetric boundary conditions, please see Table 5-2). Therefore, here a quarter of the split MRI scanner acoustic model was established. For comparison, the typical MRI scanner acoustic model was also simulated as a quarter. Fig. 5-4 shows the acoustic models of the split MRI system and its typical counterpart. The simulated scanner sizes are listed in Table 5-3. Harmonic analysis was used to investigate the acoustic characteristics of the two systems. The magnetic flux density of the main magnet was B=1 T and the gradient intensity was G=20 mT/m for both the split system and its typical counterpart.

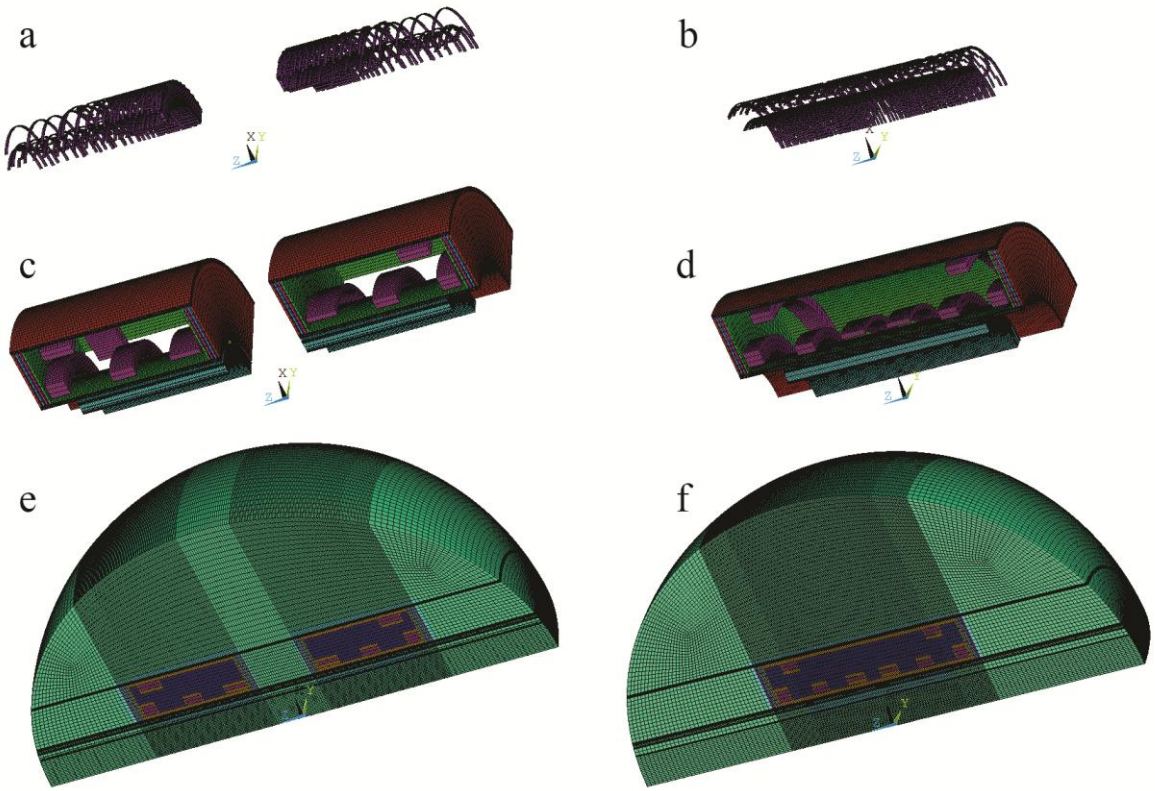

Fig. 5-4 Acoustic models of the split MRI system and its typical counterpart. Only one quarter of the whole model was established here. (a) Split gradient coils, (b) typical gradient coils, (c) split MRI system, (d) typical MRI system, (e) acoustic model of the split MRI system and (f) acoustic model of the typical MRI system. The area between the two cylindrical tunnels of the split gradient assembly (see Fig. 4 (c)) is defined as the central gap.

Table 5-3 Size parameters of the simulated split MRI system and its typical counterpart

	Item (unit: m)	Inner radius	Outer radius	Length
Split MRI system	Gap			0.500
	Gradient assembly	0.310	0.407	0.927[a]
	Cryostat (Outer layer)	0.427	0.430	
	Cryostat (Shield 1)	0.435	0.441	
	Cryostat (Shield 2)	0.444	0.447	
	Liquid helium vessel	0.452	0.456	
	Main magnet (Including the cryostat and the liquid helium vessel)	0.427	0.927	1.143[a]
Typical MRI system	Gradient assembly	0.310	0.407	1.414
	Cryostat (Outer layer)	0.427	0.430	
	Cryostat (Shield 1)	0.435	0.441	
	Cryostat (Shield 2)	0.444	0.447	
	Liquid helium vessel	0.452	0.456	
	Main magnet (Including the cryostat and the liquid helium vessel)	0.427	0.927	2.000

[a] The length is half of the split system not including the central gap.

5.1.3 Results and Discussion

5.1.3.1 Experimental validation

The experimental results are plotted in Fig. 5-5. It shows the SPL distribution along the longitudinal axis of the smaller gradient assembly. The experimental results are indicated by a red line and the simulated results are indicated by a blue line. *d* is the distance from the testing point to the isocentre. Only half of the acoustic field distribution is calculated. The other half is processed using symmetry. It is clear to see that these two curves have a consistent pattern, that is, the middle part has slightly higher SPL and the part far away from the isocentre has lower SPL values.

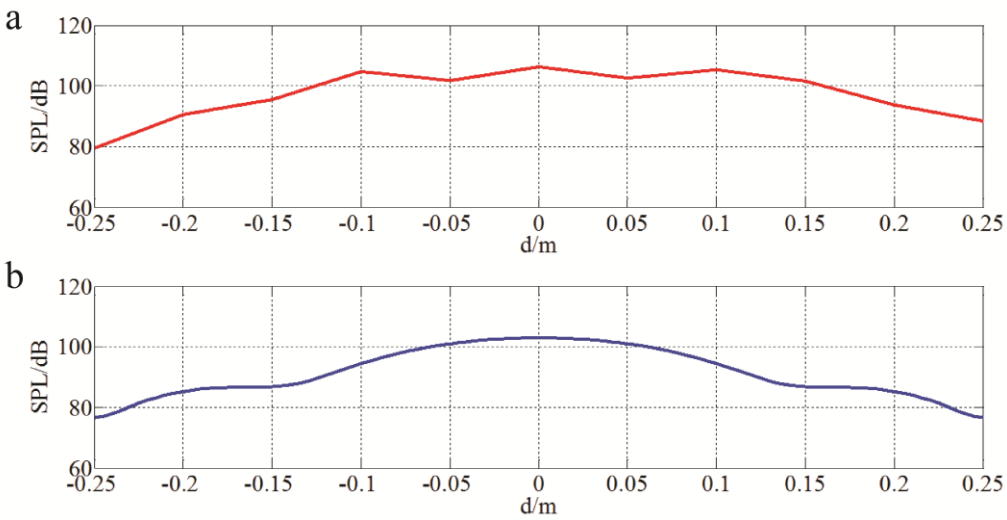

Fig. 5-5 The SPL distribution along the longitudinal axis of the smaller gradient assembly. Here a 1-kHz sinusoidal gradient pulse was used to energize the x coils. (a) represents the experimental results and (b) represents the simulated results.

Based on the above comparison, it can be concluded that, within the limitations of the assumptions made in the model, the amplitude and trend of the simulated results generally match those of the experimental results.

5.1.3.2 Results and comparison of the acoustic simulations of the two different MRI systems

In the harmonic analysis of the split MRI acoustic model, 59 frequency responses were calculated with a 50-Hz interval from 100 Hz to 3000 Hz. Since the structure is symmetric about the plane z=0, the acoustic field distribution is also symmetric. In order to clearly observe the general pattern of the frequency responses and reduce the influence of positions on the acoustic intensity, the SPLs of several uniformly-spaced sampled points along the axis of $z \geq 0$ part of the central gap were plotted in Fig. 5-6. Fig. 5-6 (a-c) are the frequency responses of the x, y and z coils, respectively. The dominant resonant frequencies were circled. Since the x and y coils have the same structures except that the y coils are smaller than the x coils, their frequency responses are basically similar. For the z coils, the frequency responses at the gap centre are significantly lower than at other positions. Since the z coils are anti-symmetric about the plane z=0 as far as the current direction is concerned, the Lorentz force on the z coils is also anti-symmetric. The acoustic field distribution creates a relatively quiet region at the gap centre. That is why there is a curve significantly lower than the others in Fig. 5-6 (c).

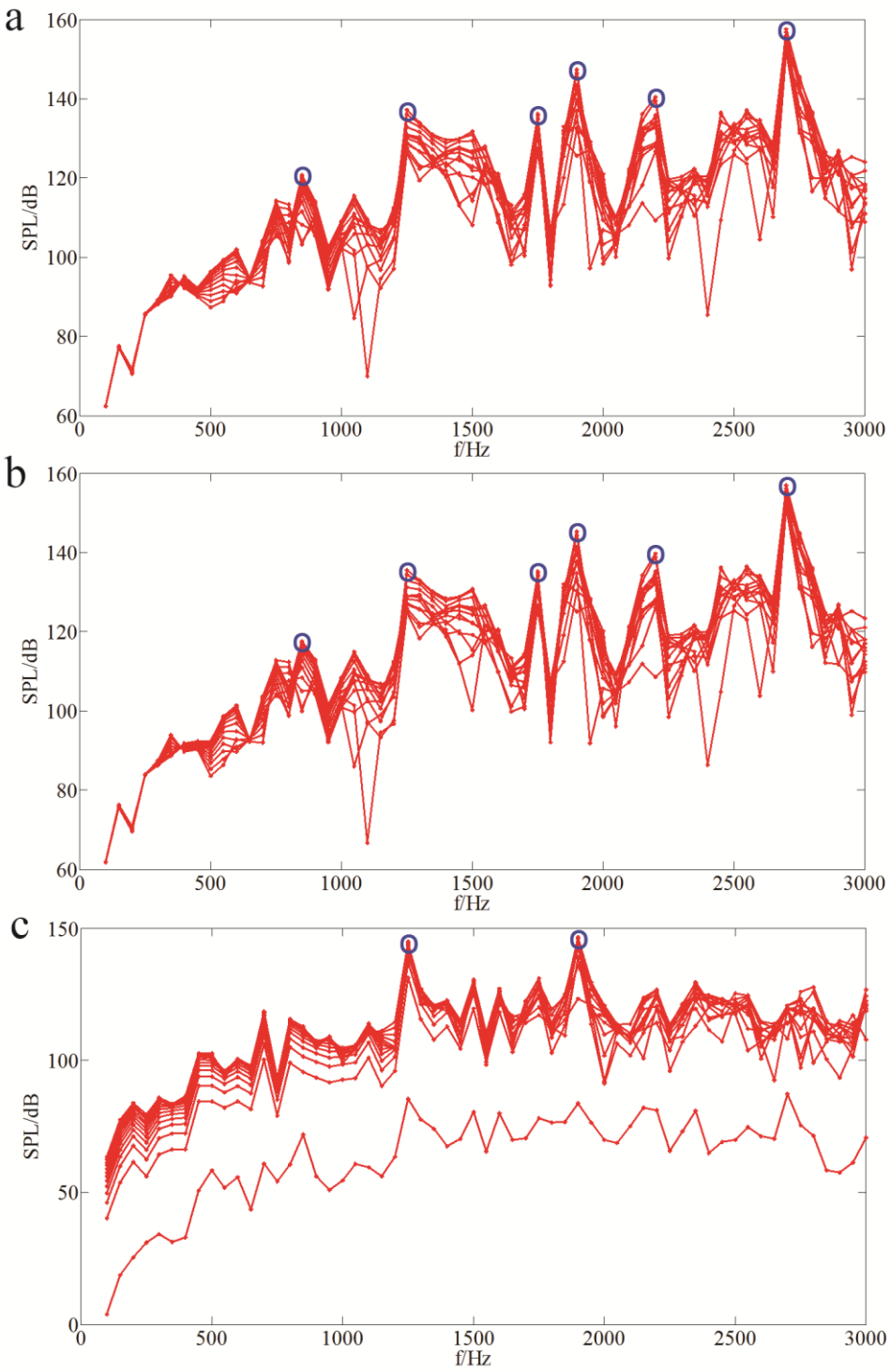

Fig. 5-6 Acoustic frequency responses of the split MRI system. (a) Frequency responses of the x coils; (b) frequency responses of the y coils; (c) frequency responses of the z coils. The SPLs of 13 uniformly sampled points along the axis of $z \geq 0$ part of the central gap are plotted for x, y, and z coils. The dominant resonant frequencies are marked by blue circles.

From the harmonic analysis, it can also be seen that the frequency response of the z coils is flatter and relatively lower for most frequencies than the x and y coils as a whole. For the x, y and z coils together, the low and medium-frequency (no higher than 1200 Hz here) acoustic responses are

distinctly weaker than those at high frequencies (higher than 1200 Hz). It is reported that, using sinusoidal ramps, "soft" gradient pulses can be designed individually to available delays. These "soft" pulses are band-limited to low frequencies, which can considerably reduce the noise level [84, 86]. It has also been reported that by varying the width of the trapezoidal pulse and keeping the ramps constant, it is possible to suppress a selected frequency and its higher harmonics [87]. Therefore, these studies indicate that, incorporating more low and medium-frequency components in the gradient pulses might be an effective way to reduce the noise level [84, 86, 87].

The acoustic field distribution investigation can also provide some potential noise reduction solutions. Figs. 5-7 and 5-8 show the acoustic field distributions of the split and typical systems respectively. Three frequencies (1200, 1300 and 1400 Hz) were analysed. The regions between the two black lines in Fig. 5-7 (a-f) denote the central gap and the regions above and below the lines are the cylindrical tunnels of the split gradient system. It can be seen that the sound energies mainly concentrate in the cylindrical tunnels for the split system. In comparison, the central gap is relatively quieter. However, as shown in Fig. 5-8, the sound energies in its central part are not weaker than those at the cylindrical ends. The intense sound energy areas alternate in the cylindrical tunnel of the typical system and are relatively more uniformly distributed than those of the split system.

Fig. 5-9 shows the average SPLs of all the 59 evenly-spaced frequencies from 100 Hz to 3000 Hz in the central gap (SPLs 1), the cylindrical tunnels (SPLs 2) of the split MRI system and the average SPLs in the cylindrical tunnel (SPLs 3) of its typical counterpart. Fig. 5-9 (a) and Fig. 5-9 (b) are the average SPLs when the x or z coils were energized respectively. From the comparison, as for the x coils, the SPLs 2 are higher than SPLs 1 at nearly all the frequencies except for frequencies 400 Hz, 450 Hz, 500 Hz, 550 Hz, 850 Hz and 1450 Hz. As for the z coils, similar observation is made except for frequency 1600 Hz. The largest difference for the x coils occurs at frequency 1800 Hz, where the SPL 2 is 23.7 dB higher than SPL 1. For the z coils, the largest difference occurs at frequency 1200 Hz, where the SPL 2 is 24.2 dB higher than SPL 1. From the above analysis, it can be concluded that the central gap in the split system is much quieter than in the cylindrical tunnels is because the acoustic waves are reflected on the inner surfaces of the split gradient assembly and also at the open ends of these two cylinder walls. In the acoustic environment of the central gap, there exist some field cancelation effects in the central gap region. When compared, the acoustic waves superimposed in the cylindrical tunnels, and thus the acoustic pressure in the typical cylindrical tunnels is usually higher.

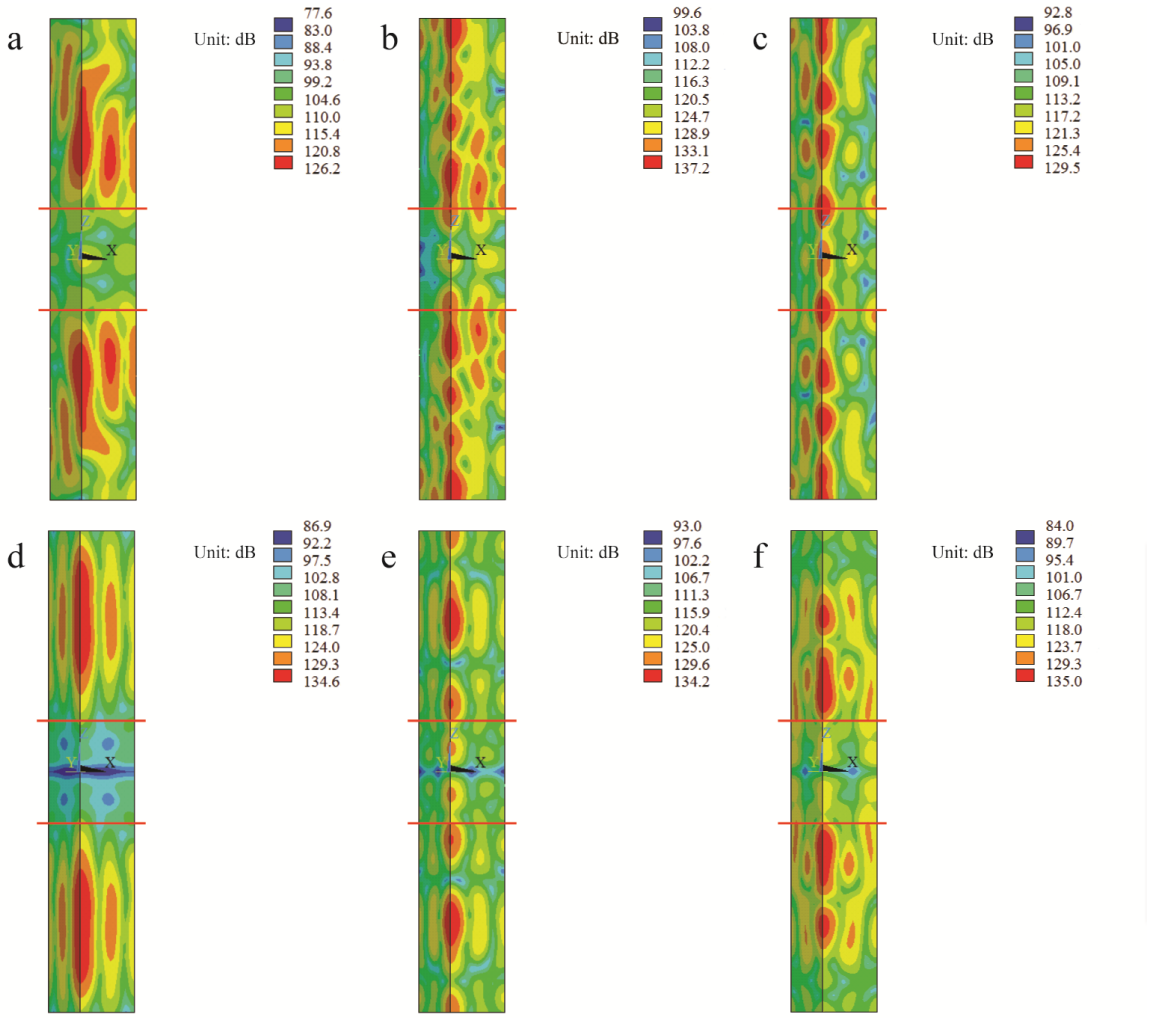

Fig. 5-7 Acoustic field distributions of the split MRI system. Only the acoustic field distributions in the central gap and the cylindrical tunnels are displayed here. (a, c and e) are the acoustic field distributions at frequencies 1200 Hz, 1300 Hz and 1400 Hz when the x coils were energized respectively; (b, d and f) are acoustic field distributions at frequencies 1200 Hz, 1300 Hz and 1400 Hz when the z coils were energized respectively. The regions between the two black lines in each subfigure are the central gaps and the regions outside the two black lines are the cylindrical tunnels.

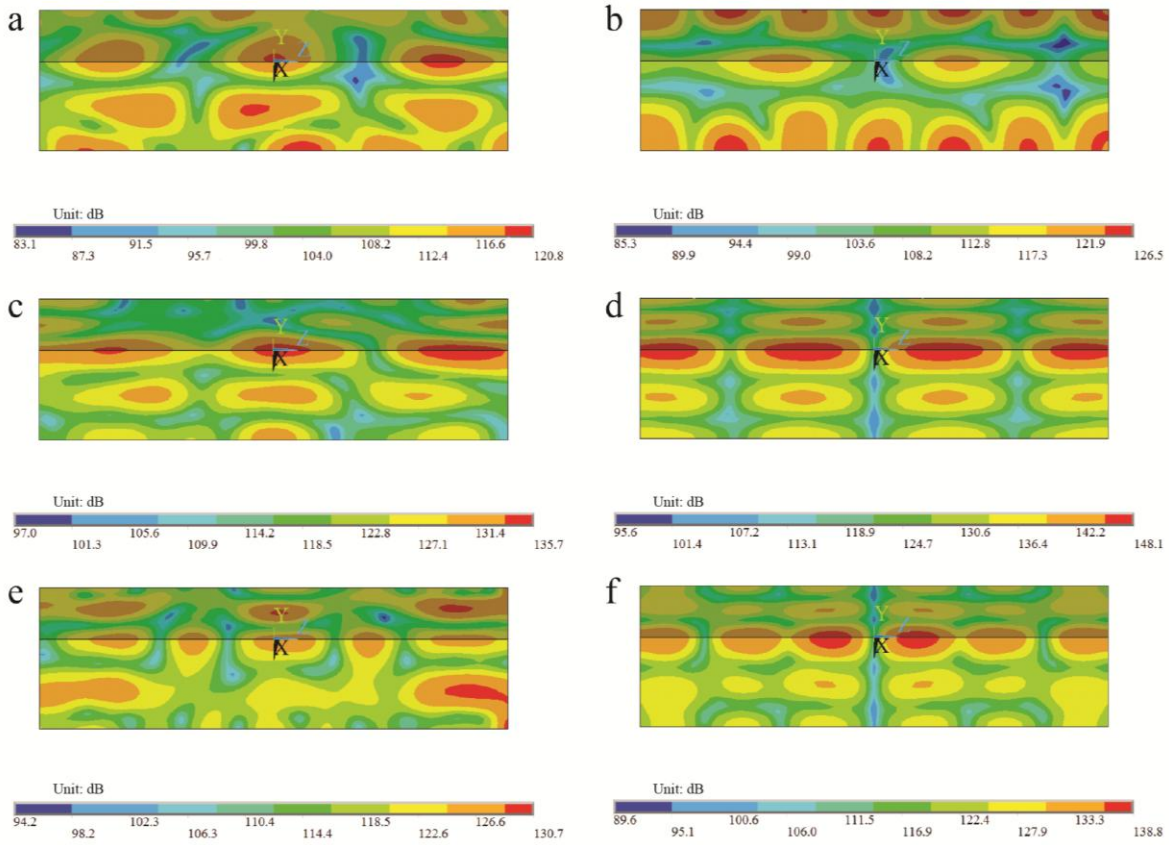

Fig. 5-8 Acoustic field distributions of the typical MRI system. Only the acoustic field distributions in the cylindrical tunnels are displayed here. (a, c and e) are the acoustic field distributions at frequencies 1200 Hz, 1300 Hz and 1400 Hz when the x coils were energized; (d-f) are acoustic field distributions at frequencies 1200 Hz, 1300 Hz and 1400 Hz when the z coils were energized.

Therefore, if the patient resides in the central gap perpendicular to the longitudinal axis of the split gradient system, it can relieve the patient's discomfort to some extent when doing non-brain imaging compared to lying along the axis. Actually, positioning the patient bed perpendicular to the axis of the split gradient system and mounting the LINAC parallel with the axis of the split gradient system has the potential to reduce the interference of the electron beam coming from the strong magnetic field of the main magnet.

As shown in Fig. 5-9, the average SPLs of both systems are frequency-dependent. Overall, the SPLs of both systems are of comparable levels at all frequencies. However, obvious differences of the two systems occur at a high frequency band, from 2450 Hz to 2950 Hz. When the x coils were energized in this frequency band, the average SPLs in the typical system cylindrical tunnel are approximately 20 dB lower than those in the central gap and the cylindrical tunnels of the split system. The opposite is true for the z-gradient coil. As listed in Table 5-4, the arithmetic mean values of the SPLs were then calculated to characterise the acoustic intensity of these two systems, where all the frequencies are independently and equally weighted. It can be seen that the x coils of

the split system produced slightly higher average SPLs than those in the typical system. The SPLs in the cylindrical tunnels of both systems, for the z coils, are almost identical. Comparatively, the central gap of the split system is about 6 dB quieter on average.

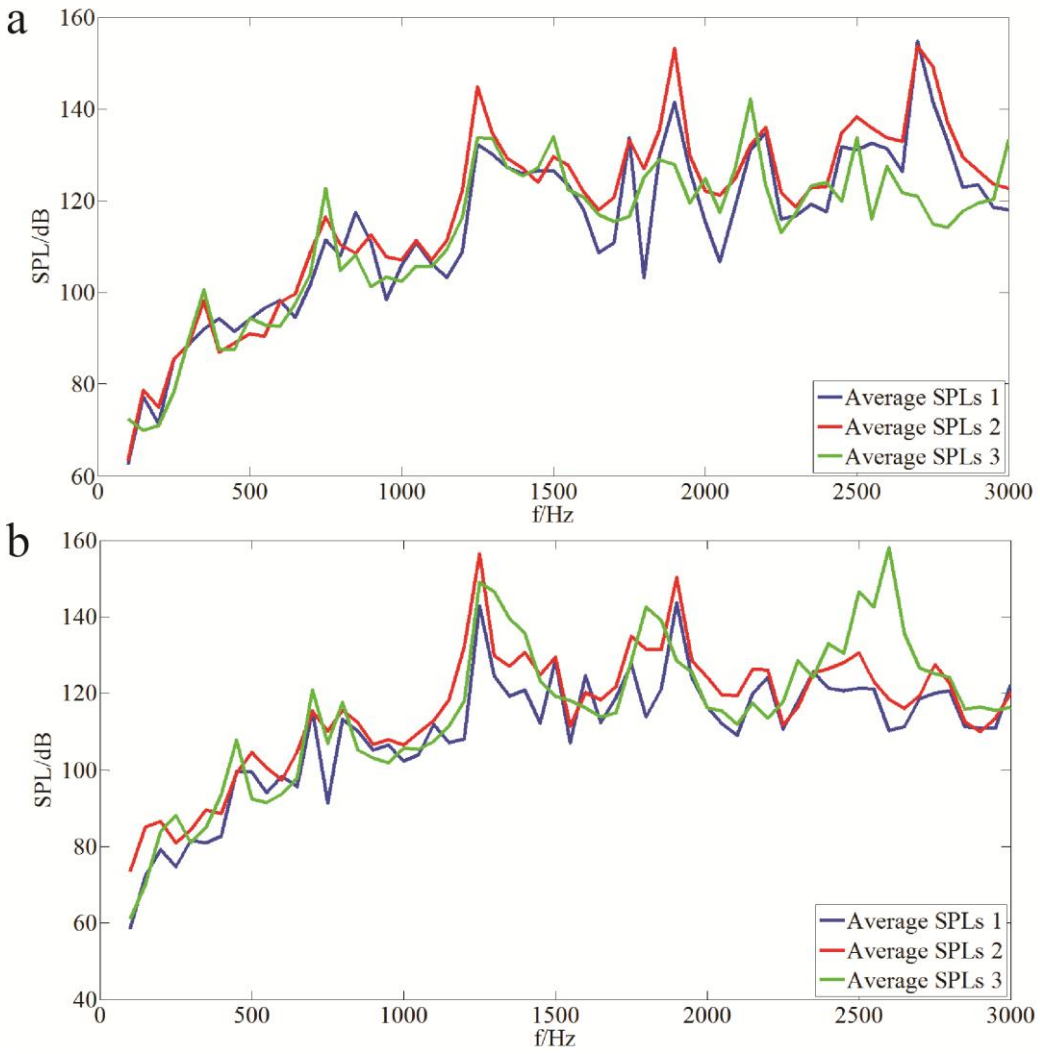

Fig. 5-9 Comparison of the average SPLs between the central gap, the cylindrical tunnels of the split MRI system and the cylindrical tunnel of its typical counterpart. (a) and (b) are the comparisons when the x coils and z coils were energized respectively. Average SPLs 1 represents the average SPLs of the central gap, Average SPLs 2 represents the average SPLs of the cylindrical tunnels of the split system and Average SPLs 3 represents the average SPLs of the cylindrical tunnel of the typical system.

Table 5-4 Average SPLs in specified regions of the split MRI system and its typical counterpart when x coils or z coils were energized

	Positions (Unit: dB)	Coils x	Coils z
Split MRI system	In the central gap	114.1	110.0
	In the cylindrical tunnels	118.0	115.7
Typical MRI system	In the cylindrical tunnel	113.0	115.6

When the patient resides in the central gap, the acoustic field will have direct influence on the patient's auditory system. Fig. 5-10 shows the acoustic field distribution of the central gap at frequencies 1200 Hz, 1300 Hz and 1400 Hz. Fig. 5-10 (a-c) display the acoustic field distributions of the x coils and Fig. 5-10 (d-f) display the acoustic field distributions of the z coils. It can be clearly seen that the x coils will create a regional loud area at the gap centre, while the z coils create a quite zone in the central gap. Similar phenomenon happens at other frequencies. Fig. 5-11 shows the average SPLs in the central gap when the x coils or z coils were energized. From Fig. 5-11 (a), when the x coils were energized, the average SPLs at the isocentre are higher than those in the central gap at most frequencies. Some obvious exceptions occur at frequencies 300 Hz, 400 Hz, 1650 Hz and 2950 Hz. From Fig. 5-11 (b), the z coils produced lower SPLs at the isocentre than in the central gap, at low- and medium-frequency band. From 1200 Hz onwards, the average SPLs at the isocentre are nearly the same as those in the central gap. Therefore, when the x coils were energized, a loud area will concentrate at the isocentre at most frequencies, whereas a quiet area will be produced by the z coils at low and medium-frequency band. In these investigations, the influence of the human body on the acoustic field distribution is not considered.

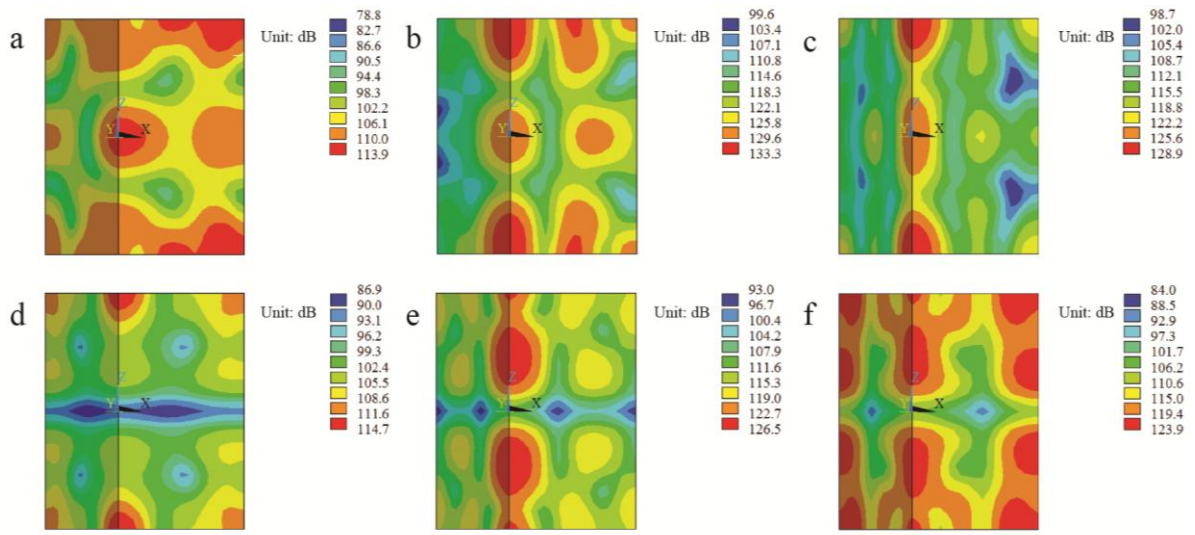

Fig. 5-10 Acoustic field distribution of the central gap at frequencies 1200 Hz, 1300 Hz and 1400 Hz. (a-c) are the acoustic field distributions when the x coils were energized and (d-f) are the acoustic field distributions when the z coils were energized.

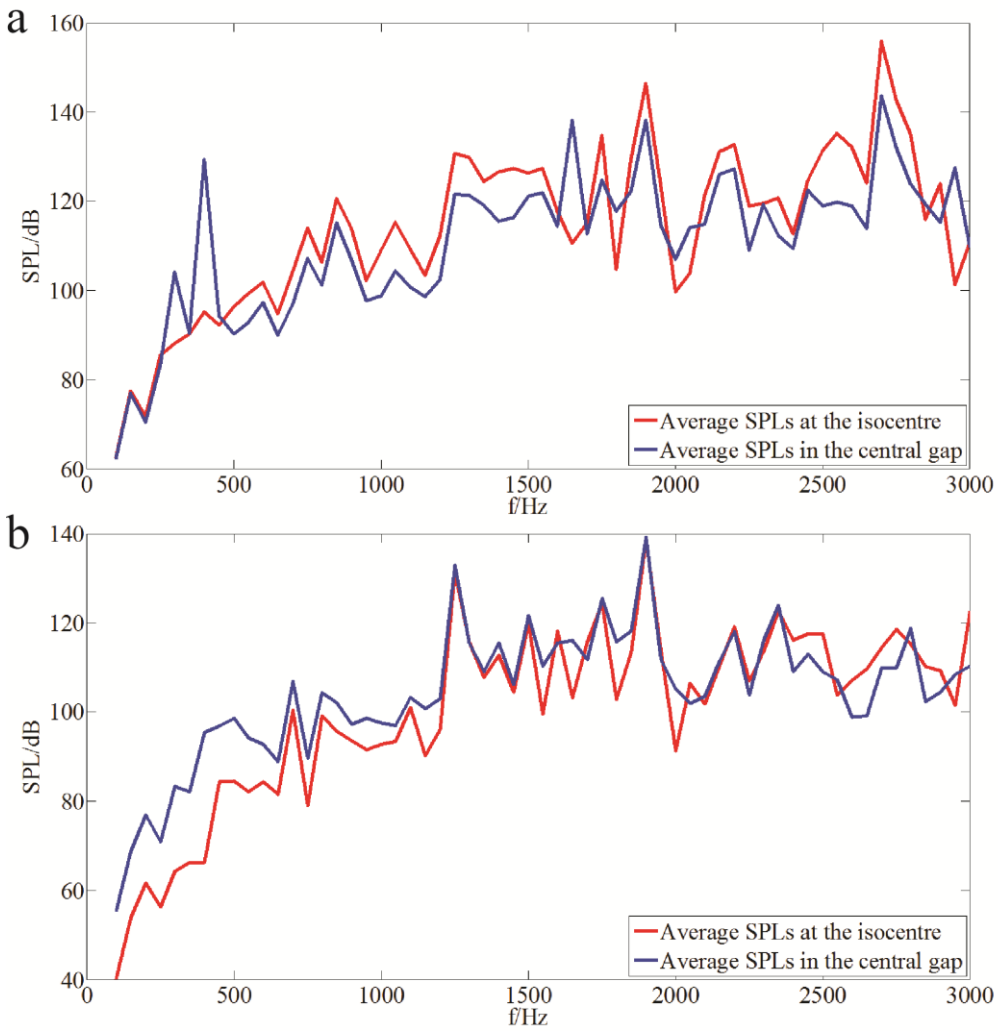

Fig. 5-11 Comparison of the average SPLs between the isocentre and the central gap. (a) Average SPLs when the x coils were energized and (b) average SPLs when the z coils were energized.

5.1.4 Conclusions

This study numerically analysed the acoustic characteristics of a split MRI system. From the harmonic analysis of the split MRI system, the dominant resonant frequencies were identified. It was found that the acoustic responses at low and medium-frequencies (no higher than 1200 Hz here) were distinctly lower than at high-frequencies (higher than 1200 Hz). Therefore, if the gradient pulse can avoid resonant frequencies and include more low and medium-frequency components, the SPL will be attenuated.

For the acoustic comparison between the split MRI system and the corresponding typical MRI system design, the average SPLs of the x coils of the split system were slightly higher than those in the typical system. For the z coils, the SPLs in the cylindrical tunnels of both systems were almost identical. Overall, the central gap of the split system was much quieter than the cylindrical tunnels

of the split system. Therefore, if the patient resides in the central gap perpendicular to the longitudinal axis of the split gradient system, it can relieve discomfort from noise levels to some extent compared to the patient lying along the longitudinal axis of the split gradient system. These findings will provide guidance for the reduction of acoustic noise in the future MRI-LINAC design.

5.2 Simulation study of noise reduction methods for a split MRI system using a finite element method

5.2.1 Introduction

For some approaches of an MRI-LINAC hybrid system, a cylindrical MRI scanner is designed to split into two halves to yield a central gap in which a LINAC, or similar device, can be inserted. However, splitting the MRI scanner into two halves brings about a range of engineering challenges. For instance, the Lorentz force distribution on the split gradient assembly may be not as balanced as conventional designs (conventional gradient coils are symmetrically distributed in an integral gradient assembly), thus resulting in more severe vibrations and louder noise levels than in the cylindrical tunnels [112]. In addition, similar to typical MRI systems, the faster the gradient current switches, the louder the noise will be [11, 52, 101, 130-133, 140].

Owing to the existence of the large central gap, it is anticipated that, in the hybrid MRI systems, the acoustic field distributions should be different from the conventional ones and may produce loud noises during operation [112]. In this situation, an efficient noise reduction method is necessary.

It is reported that damping structures can be used to attenuate the vibration of an MRI system [74, 141, 142]. When installed on a cryostat, gradient assembly and patient bore tube, these damping structures can effectively remove the mechanical resonances of the system to some extent [74]. Noise reductions of up to 10 dB have been achieved by placing damping inserts or wedges between the gradient assembly and the main magnet [141]. There is also an acoustically-damped gradient assembly designed by sandwiching damping layers between primary gradient coils and shielding gradient coils [142]. In this work, these damping methods will be applied to the split gradient assembly.

In addition, the proper arrangement of the mounting supports (see Fig. 5-12) between a split-gradient assembly and the main magnet may also help reduce acoustic noise level. This is because changing the positions of the supports will alter the vibration pattern of the split-gradient assembly; that is, the acoustic field distribution in the cylindrical tunnels and the central gap can be relocated.

Therefore, with the optimization of the positions of the supports, the loud areas in the cylindrical tunnels near the central gap can be attenuated, thus reducing the sound pressure level (SPL) in the central gap.

In this work, we developed a 3D (three-dimensional) Finite Element (FE) model of the split MRI system to investigate the noise reduction scheme. The acoustic field reallocation method was first studied through seeking optimal positions for the supports. To further attenuate the SPL, we also incorporated efficient damping treatments on the surfaces of the split gradient assembly for overall noise reduction.

5.2.2 Methods

5.2.2.1 Acoustic noise control simulation of a split MRI system using supports between the split gradient assembly and the main magnet

We propose using supports between the split gradient assembly and the main magnet to relocate the acoustic field distribution in a split MRI system with the aim of smoothing the acoustic frequency responses. This is predicted to alter where the largest acoustic emissions are in the split gradient assembly, away from the central imaging area, thus effectively reducing the noise level for patients. Fig. 5-12 shows a schematic diagram of a split gradient assembly in the MRI system. Here, eight supports are used between each gradient cylinder and the main magnet. Fig. 5-12 (a) shows the schematic diagram of the installation of these supports between the split-gradient assembly and the main magnet; Fig. 5-12 (b) shows the cross section of the new system. The supports at the ends closer to the central gap are fixed, while the supports at the far ends, away from the central gap, are adjustable. Using a diagonal plane to cross the split system (see Fig. 5-13 (a)), a beam model was built. As shown in Fig. 5-13 (b), there are four such beams in this plane; because these beams were symmetrical, only one of them was plotted, as shown in Fig. 5-13 (c), where a is the distance from the free end to the adjustable pin support and L is the length of the beam.

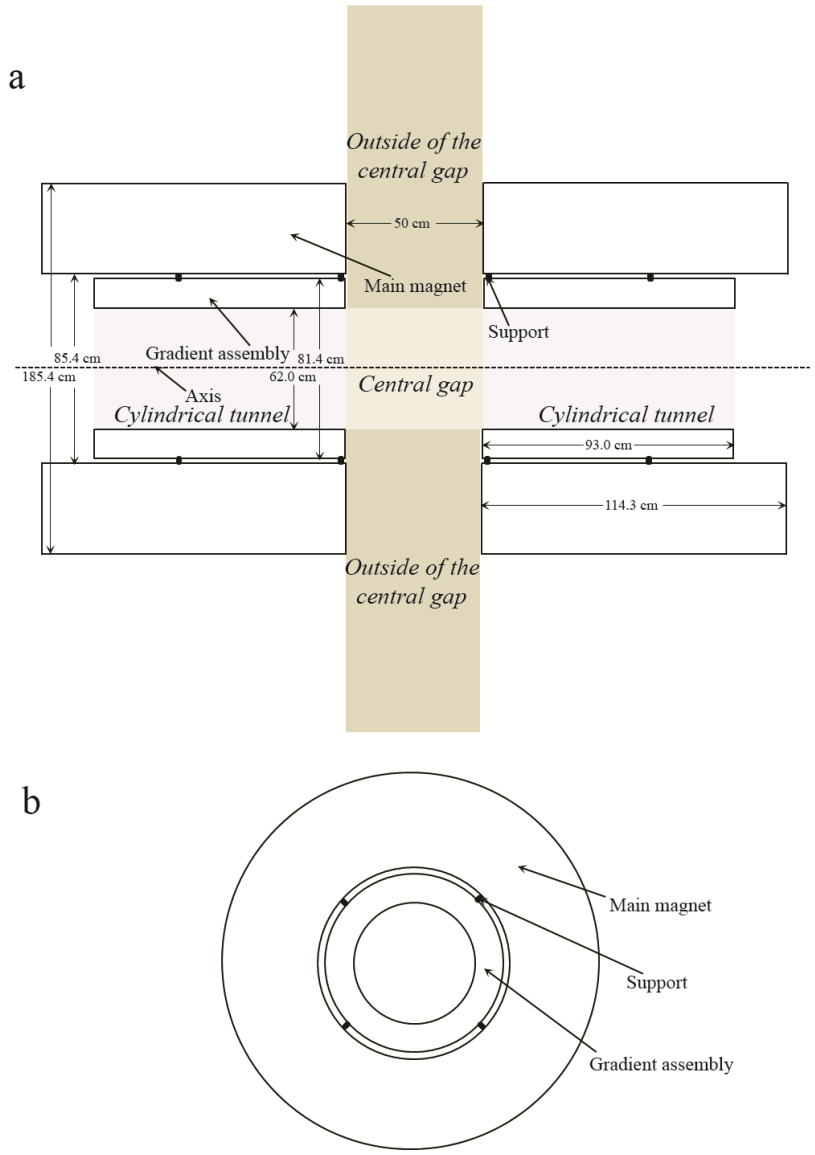

Fig. 5-12 Schematic diagram of a split gradient assembly in a split MRI system, (a) longitudinal cross section of the system and (b) transverse cross section of the system. The patient bed will be installed perpendicular to the axis of the cylindrical tunnels. The model dimensions are illustrated in (a). For the purpose of SPL evalutions, several regions were defined in and around the split scanner represented with different colours. The regions include the central gap (region I), cylindrical tunnels (region II) and outside of the central gap (z=-0.25m-0.25 m, r=0.31 m-1.8 m, region III).

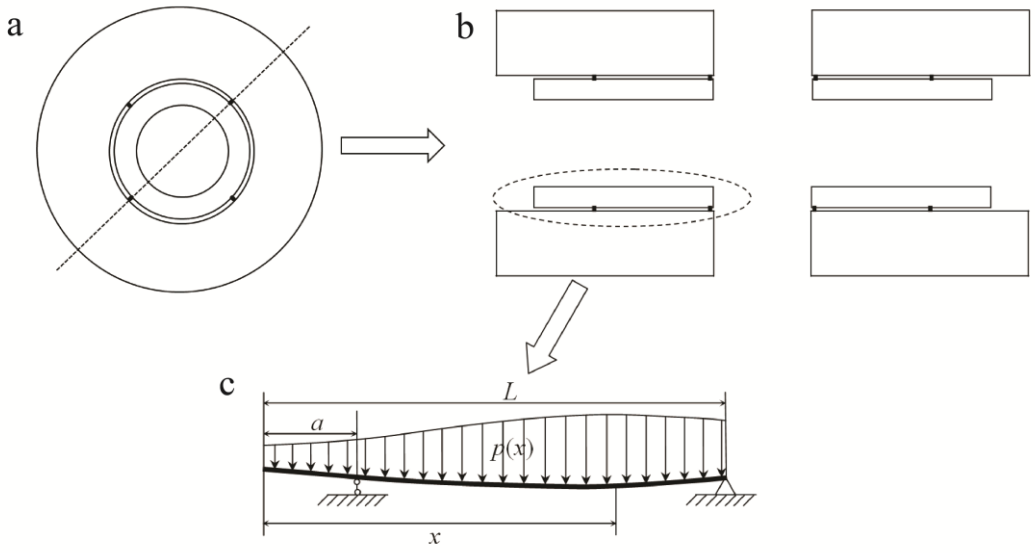

Fig. 5-13 Beam structure separated from the split gradient assembly, (a) cross section of the system with diagonal crossing plane (left view), (b) longitudinal section along the diagonal crossing plane (front view) and, (c) beam structure (one of the four beams).

Assuming there is a distributed load on the beam, as shown in Fig. 5-13 (b), the beam will have deflection from its original position. Using beam-deflection theory, we can obtain its deformation function, as expressed in Eq. (1) [114]

$$\frac{\mathrm{d}^2 y}{\mathrm{d}x^2} = \frac{M}{EI} \tag{5-1}$$

where y is the deflection of the beam, x is the distance between the free end of the beam and the position where the deflection occurs, M is the moment, E is Young's modulus and I is the moment of inertia. By adjusting the length of a, the beam deflection can be changed. Similarly, by adjusting the mounting supports between the split gradient assembly and the main magnet, the radial modes of the split gradient assembly can be altered. Thus, when the supports are at reasonable positions, a relatively quiet acoustic field may be acquired.

From the above assumption and analysis, a 3D split MRI acoustic model was established to investigate the noise control effects using supports. The model incorporated realistic coil tracks and was analysed using the commercial Finite Element Method (FEM) package ANSYS. It included a split gradient assembly, cryostat and main magnet coils. The supports between the split gradient assembly and the main magnet were simulated as aluminium blocks [112], and it was assumed that a vacuum was present between the different layers of the cryostat. The main magnet coils were immersed in liquid helium and the whole system was surrounded by air. Considering the symmetric

features of the split MRI system, only a quarter of the whole model was established. Fig. 5-14 shows the FE model and Table 5-5 records the mechanical properties of the components of the split MRI model.

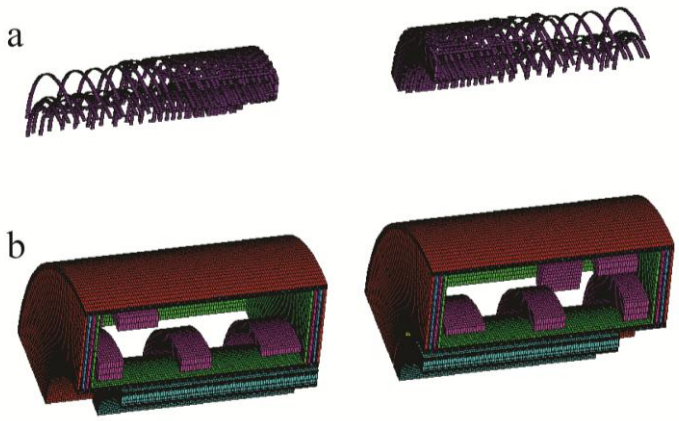

Fig. 5-14 FE model of the split MRI system (1/4 model), (a) split-gradient coils (including the x, y and z coils together), (b) split MRI system.

Table 5-5 Mechanical properties of the components of the split MRI model

	Item	E (Gpa)	μ	ρ (kg/m^3)	c (m/s)
Split MRI system	Gradient assembly (epoxy resin)	15.7	0.30	1835	
	Gradient coils (Copper)	117	0.34	8960	
	Support (Aluminium)	70	0.30	2700	
	Cryostat outer layer (steel)	210	0.30	7800	
	Cryostat shield 1 (Aluminium)	70	0.30	2700	
	Cryostat shield 2 (Aluminium)	70	0.30	2700	
	Liquid helium vessel (steel)	210	0.30	7800	
	Liquid helium			125	238
	Main magnet coils (copper)	117	0.34	8960	
	Main magnet coils cushion (steel)	210	0.30	7800	
	Surrounding air			1.225	340

E, μ and ρ are the Young's modulus, Poisson's ratio and density of the components of the split MRI model. c is the acoustic speed.

In the acoustic model, the near supports (relative to the central gap) were fixed and the adjustable supports were initially placed at the far ends (relative to the central gap) of the split gradient assembly. Then the adjustable supports were gradually moved towards the central gap by changing the length of a. The different lengths of a used in the acoustic noise control simulation are listed in

Table II. The average SPLs both in the central gap and outside of the central gap (see the regional divisions in Fig. 5-12 (a)) were calculated from 100 Hz to 3000 Hz. Harmonic analysis was used here. For every single-frequency response, the sound pressures of FE nodes (shown in Fig. 5-15) in and outside the central gap were extracted respectively and then the average SPLs were calculated by Eq. (5-2). The overall average SPL, considering all the investigated frequencies, was calculated using Eq. (5-3). Here, SPL_f is the frequency-dependent average sound pressure level, SPL_a is the overall average sound pressure level, N is the FE node number, M is the the number of sampling frequencies, p_i is the sound pressure and p_0 is the referential sound pressure (2×10^{-5} pa) [143]. The overall average SPL can be used to evaluate the total noise reduction. In the acoustic model of the split MRI system, the magnetic flux density of the main magnet was 1 T and the peak value of the sinusoidal gradient pulses was 600 A (producing a gradient strengh of 20 mT/m in the imaging area). This model has been previously validated [112].

$$SPL_f = 10\lg\left(\frac{\sum_{i=1}^{i=N} p_i^2}{Np_0^2}\right) \tag{5-2}$$

$$SPL_a = 10\lg\left(\frac{\sum_{f=100}^{f=3000}\sum_{i=1}^{i=N} p_i^2}{MNp_0^2}\right) \tag{5-3}$$

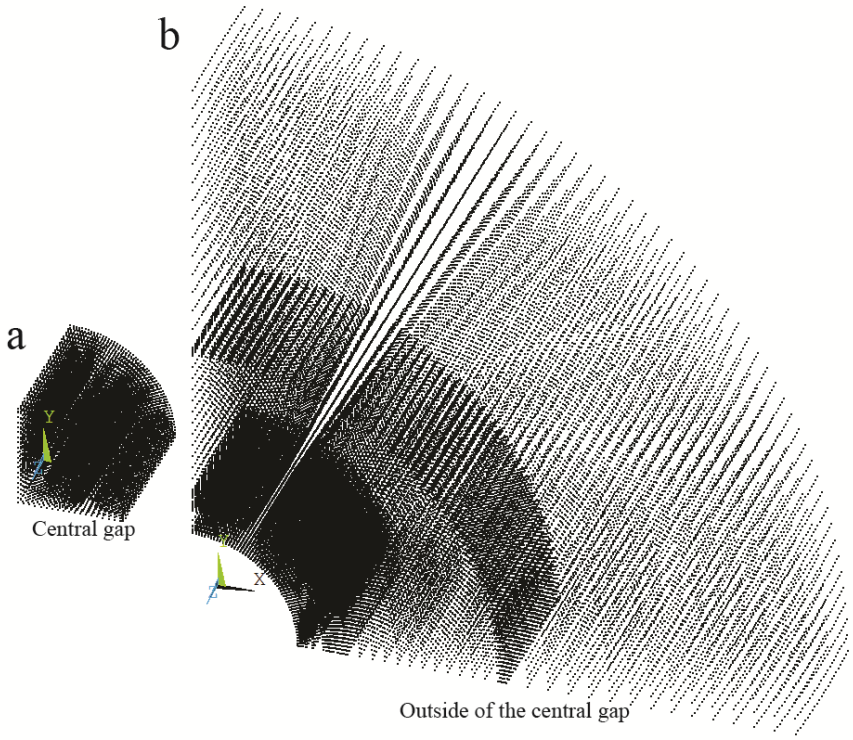

Fig. 5-15 The FE nodes used for the SPL calculation, (a) the FE nodes in the central gap and (b) the FE nodes outside the central gap (see the 2D plot in Figure 1(a) and also the dimensions).

Table 5-6 The different lengths of *a* used in the acoustic noise control simulation

Case # *n*	Length of *a* (cm)
1	0
2	5
3	10
4	15
5	20
6	25
7	30
8	35
9	40

For the nine cases in Table 5-6, the SPLs in the central gap of the sinusoidal gradient pulses were averaged. The average SPLs for these cases were compared and the optimal positions of the adjustable supports were assessed for their acoustic properties.

5.2.2.2 Acoustic noise control simulation in a split MRI system using damping materials

After finding the optimal positions of the supports and to further reduce the SPL, damping materials were laid on the outer surfaces of the split-gradient assembly first and later on the inner surfaces.

It is very common to use a damping loss factor (or simply a loss factor) to express the damping property of a material, namely hysteretic damping. The loss factor is the ratio of the energy dissipated per radian to the maximum strain energy in the system [144], which can be expressed by the following equation:

$$\eta_s = \frac{\Delta W_s}{2\pi W_s} \tag{5-4}$$

where η_s is the loss factor, ΔW_s is the energy dissipated per cycle and W_s is the total strain energy in the entire system at the maximum displacement. From Eq. (5-4), we can see that it is possible to significantly attenuate the structural vibration by applying damping materials with a large loss factor, thus reducing structural acoustic radiation.

The structural damping treatments essentially have two forms, a free-layer damping (FLD) and a constrained-layer damping (CLD). In this investigation, both FLD and CLD were simulated. Fig. 5-16 shows the two kinds of structural treatments on the split-gradient assembly. The damping material used here was a layer of viscoelastic damping polymer (3M ISD 130, Young's modulus 1.2

MPa, Poisson's ratio 0.49, density 0.95 g/cm^3 and material-dependent loss factor from 0.38 to 0.89 [145]). In ANSYS, it uses command MP, DAMP to specify damping as a material property [146]. The constraining layer used here was a layer of fiberglass (Young's modulus 40 GPa, Poisson's ratio 0.3 and density 2.55 g/cm^3). Four cases were investigated and compared in the simulation, using damping treatments on the outer surfaces of the split-gradient assembly that were listed in Table 5-7. The material loss factor was set at an intermediate value of 0.8 first. Harmonic analysis was also used from 100 Hz to 3000 Hz. The noise reduction effects of these four damping treatment cases were compared, and the best treatment was further applied on the inner surfaces of the split gradient assembly. Afterwards, the extreme conditions of the material loss factor at a minimum value 0.38 and a maximum 0.89 were investigated respectively.

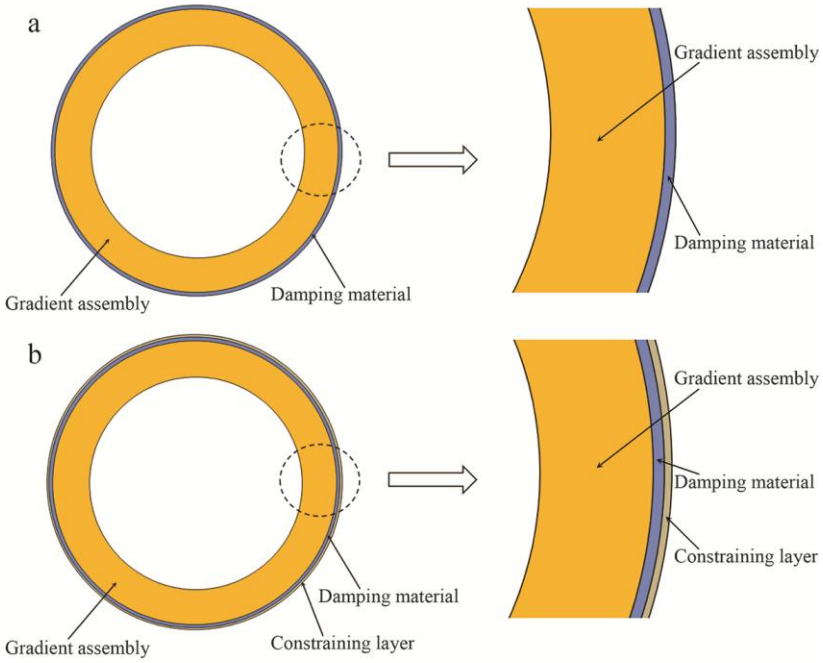

Fig. 5-16 Structural damping treatments on the split gradient assembly, (a) free-layer damping and, (b) constrained-layer damping.

Table 5-7 The structural damping treatments for a split gradient assembly

Case # *n*	Item	Thickness	
1	FLD	Damping material	
		1 cm	
2	CLD	Damping material	Constraining layer
		1 cm	0.3 cm
3		Damping material	Constraining layer
		0.7 cm	0.3 cm
4		Damping material	Constraining layer
		0.3 cm	0.7 cm

5.2.3 Results and discussion

5.2.3.1 Acoustic noise control effect in a split MRI system using supports between the split gradient assembly and main magnet

Fig. 5-17 shows the average SPLs in the central gap for the nine cases listed in Table 5-6 when the x coils were energized. The horizontal axis is the different lengths of *a*. The vertical axis is the overall average SPLs in the central gap considering the frequency from 100 Hz to 3000 Hz. The horizontal line is the overall average SPL when a=0, which is called the original average SPL here (131.5 dB). From Fig. 5-17, when $a \neq 0$, the far (relative to the central gap) supports are not placed at the free ends, the average-SPL reductions compared with the case when a=0 are very obvious. The lowest average SPL (121.6 dB) occurs at a=40 cm, and the corresponding average-SPL reduction amounts to 9.9 dB. However, there is an exceptional point where a=20 cm, at which the average SPL increases.

Fig. 5-18 (a) shows the average SPLs in the central gap at different frequencies when a=20 cm compared with when a=0 cm. Fig. 5-18 (b) shows the average SPLs in the central gap at different frequencies when a=40 cm compared with those when a=0 cm. The x coils were energized here. From Fig. 5-18 (a), there is a dominant resonant point at frequency 2800 Hz, which results in the increase of the average SPL in Fig. 5-17. However, in Fig. 5-18 (a), at frequencies 400 Hz, 1900 Hz, 2200 Hz and 2700 Hz, the average-SPL reductions are still very obvious. From Fig. 5-18 (b), the average-SPL reductions at frequencies 1900 Hz, 2200 Hz and 2700 Hz are considerable, amounting to 31.7 dB, 24.8 dB and 28.4 dB, respectively. In addition, obvious average-SPL reductions are also acquired at frequencies 150 Hz, 400 Hz, 2950 Hz, etc.

Fig. 5-18 (c) shows the average SPLs in the central gap at different frequencies when the z coils were energized. The average SPLs between a=0 cm and a=40 cm were compared. Similar to the x coils, the average-SPL reductions at some dominant resonant frequencies are quite a few, such as around 1900 Hz, 2200 Hz and 2350 Hz, which amounts to 32.4 dB and 18.9 dB and 9.8 dB, respectively. When a=0 cm, the overall average SPL considering the different frequencies is 126.5 dB and the corresponding overall average SPL when a=40 cm is 120.2 dB. Therefore, the average-SPL reduction for the z coils by moving supports towards to the central gap reaches 6.3 dB.

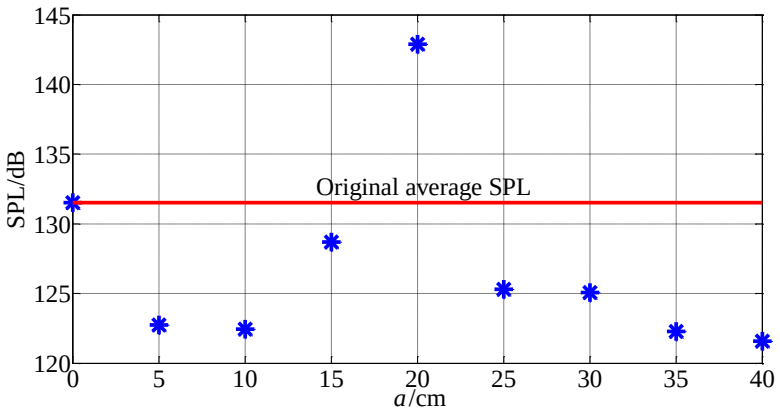

Fig. 5-17 Average SPLs in the central gap considering the frequencies from 100 Hz to 3000 Hz.

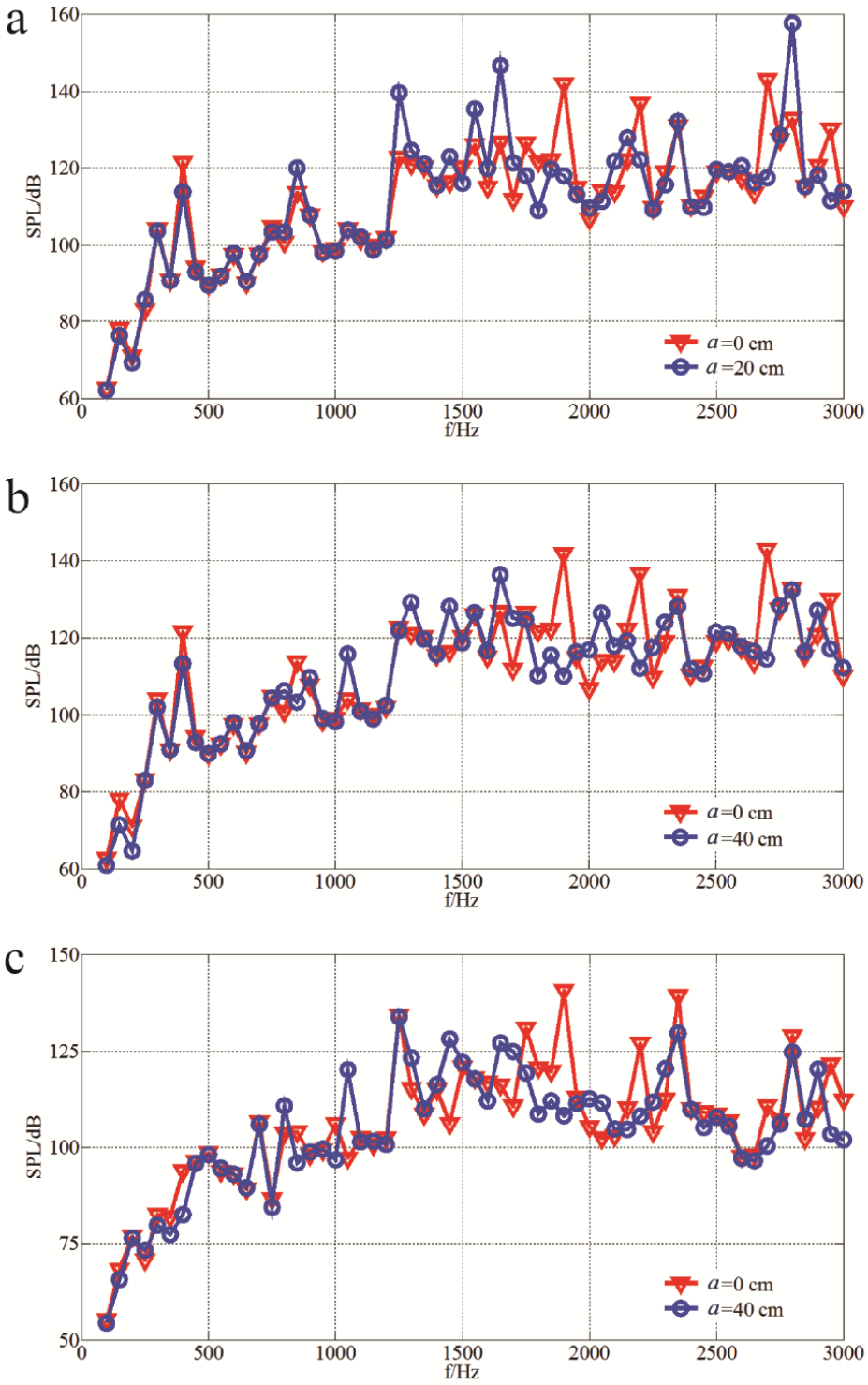

Fig. 5-18 Average SPLs in the central gap at different frequencies, (a) comparison between a=0 cm and a=20 cm when the x coils were energized, (b) comparison between a=0 cm and a=40 cm when the x coils were energized and, (c) comparison between a=0 cm and a=40 cm when the z coils were energized.

However, if the device is being used to treat/image the torso, pelvis or extremities, the patient's ears will be positioned in a much wider array of potential locations. Considering this, we also investigated the SPLs and acoustic field distribution properties outside the central gap. Fig. 5-19 (a) and (b) show the average-SPL comparisons outside the central gap when the x coils and z coils

were energized respectively. Similar to the situation in the central gap, the acoustic responses at the dominant frequencies 1900 Hz, 2200 Hz, 2700 Hz and also 2350 Hz were reduced considerably. Compared with that when a=0 cm, the average-SPL reductions when a=40 cm are 7.8 dB and 7.0 dB respectively for the x coils and z coils. However, there are also some frequencies where SPLs increase for both inside and outside the central gap, such as 1050 Hz and 1450 Hz when a=40 cm (see Fig. 5-18 and Fig. 5-19). This indicates that, while the dominant acoustic frequencies were attenuated by adjusting the positions of the supports, owing to the alterations of the boundary conditions (supports) of the split gradient assembly, some new vibration modes occur which may induce SPL splikes with lower levels at these frequencies. On the whole, both inside and outside the central gap, the direct effect after changing the positions of the supports is to adjust the vibration modes and smooth the acoustic frequency responses, thus reducing the overall average SPLs. The overall average-SPL reductions after adjusting the supports are summarized in Table 5-8.

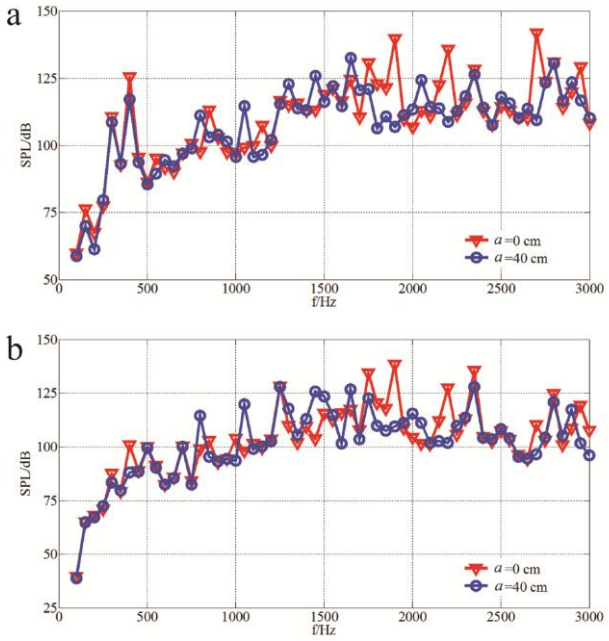

Fig. 5-19 Average SPLs outside the central gap at different frequencies, (a) comparison between a=0 cm and a=40 cm when the x coils were energized, (b) comparison between a=0 cm and a=40 cm when the z coils were energized.

Table 5-8 Overall average-SPL reductions in the specified regions of the split MRI system by using supports

Regions	Coils x (Unit: dB)	Coils z (Unit: dB)
In the central gap	9.9	6.3
Outside the central gap	7.8	7.0

Fig. 5-20 shows the acoustic field distributions in the cylindrical tunnels and the central gap for the x coils at frequencies 1900 Hz, 2200 Hz and 2700 Hz when a=0 cm and a=40 cm. The area between

the two black lines is the central gap and the areas beyond the two lines are the cylindrical tunnels. From the comparison between Fig. 5-20 (a–c) and Fig. 5-20 (d–f), the acoustic field intensities in the cylindrical tunnels reduce significantly when adjusting *a* from 0 cm to 40 cm. At 1900 Hz, the loud areas in the cylindrical tunnels seem to move to the far (relative to the central gap) ends. In the central gap, one obvious change is that the loud areas in the centre disappear or shrink. Also, the change of acoustic field intensities in the central gap is very obvious.

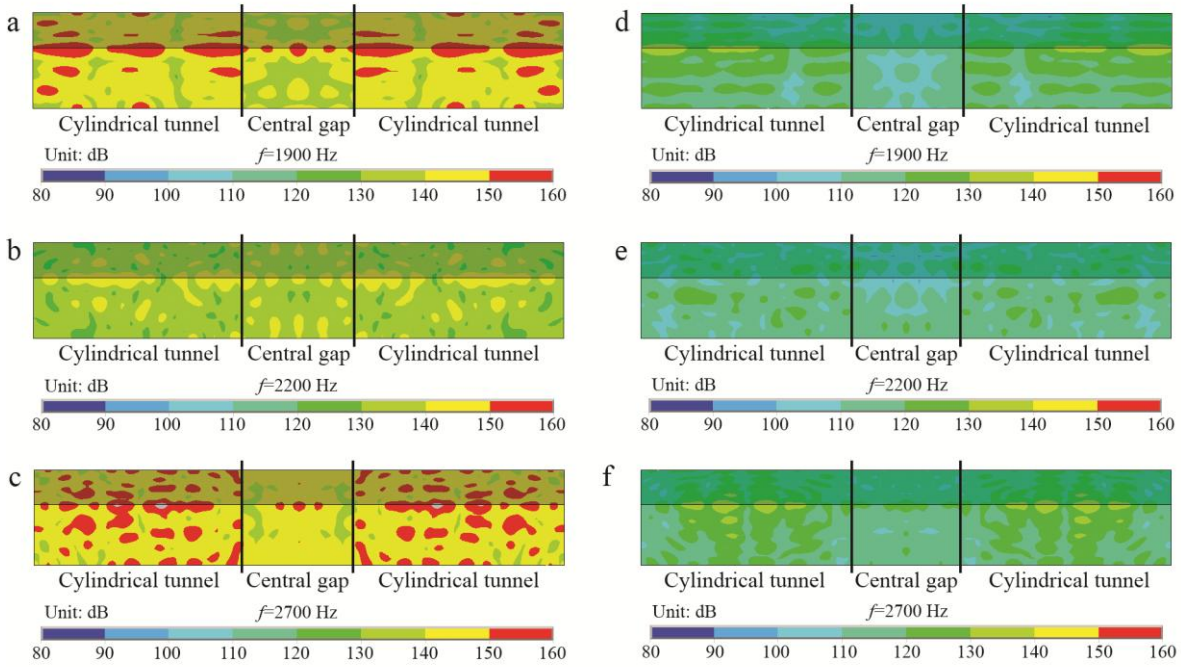

Fig. 5-20 Acoustic field distributions in the cylindrical tunnels and the central gap when the x coils were energized, (a-c) acoustic field distributions in the cylindrical tunnels and the central gap at frequencies 1900 Hz, 2200 Hz and 2700 Hz, respectively, when *a*=0 cm and (d-f) acoustic field distributions in the cylindrical tunnels and the central gap at frequencies 1900 Hz, 2200 Hz and 2700 Hz, respectively, when *a*=40 cm. The area between the two black lines is the central gap and the areas beyond the two black lines are the cylindrical tunnels.

Fig. 5-21 shows the acoustic field distributions outside the central gap for the x coils at frequencies 1900 Hz, 2200 Hz and 2700 Hz when *a*=0 cm and *a*=40 cm. From the comparison between Fig. 21 (a–c) and Fig. 5-21 (d–f), the acoustic field intensity variation outside the central gap, when adjusting *a* from 0 cm to 40 cm, is very obvious. Overall, the acoustic field intensity outside the central gap is much weaker than that in the cylindrical tunnels and also weaker than that in the central gap. From the central gap outwards, the acoustic field intensity tends to decrease gradually. It can be predicted that when doing the non-brain examination or treatment, the patient's ears will reside in a relatively quiet environment.

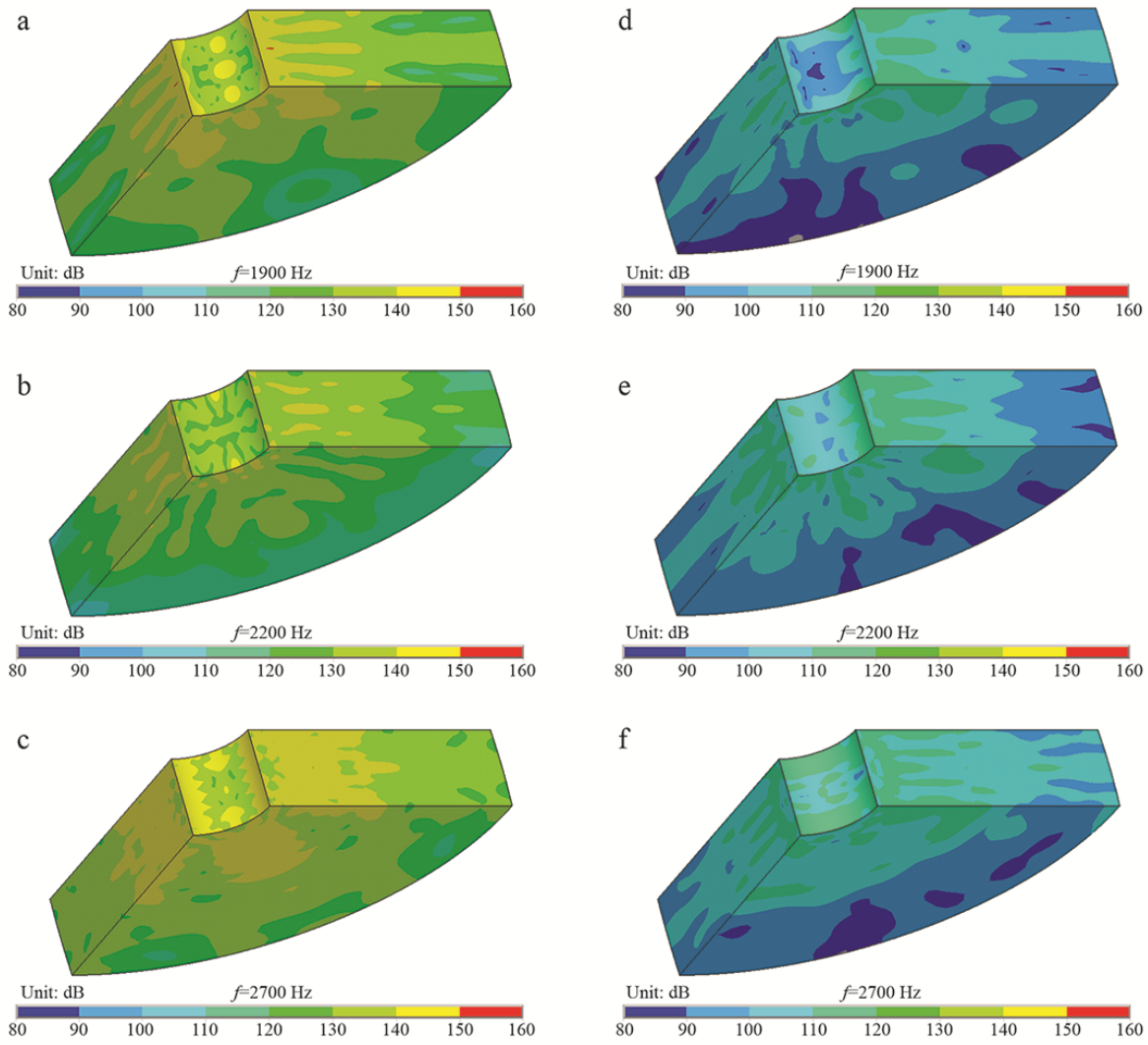

Fig. 5-21 Acoustic field distributions in the cylindrical tunnels and the central gap when the x coils were energized, (a–c) acoustic field distributions outside the central gap at frequencies 1900 Hz, 2200 Hz and 2700 Hz, respectively, when a=0 cm and (d-f) acoustic field distributions outside the central gap at frequencies 1900 Hz, 2200 Hz and 2700 Hz, respectively, when a=40 cm.

5.2.3.2 Acoustic noise control effect in a split MRI system using damping materials

After finding the optimal positions of the supports, damping materials were used to further reduce the SPL. All the damping treatments were applied on the outer surfaces of the split gradient assembly when a=40 cm and the material damping loss factor was set to be 0.8 first. Fig. 5-22 (a) shows the average SPLs in the central gap at different frequencies before and after applying FLD, as is the Case 1 in Table 5-7, when the x coils were energized. From Fig. 5-22 (a), it can be seen that the FLD has good noise reduction performances at high-frequency bands, such as from 1200 Hz to 3000 Hz. At low-frequency bands, it has significant noise reduction only at the frequencies of 300 Hz and 400 Hz. In particular, the FLD has greater noise reduction effects at resonant frequencies, for example, around 400 Hz, 1300 Hz, 1700 Hz, 2100 Hz, 2300 Hz, 2500 Hz and 2800

Hz, and so on. The largest noise reduction quantity occurs at 2800 Hz, which amounts to 30.2 dB. The average SPLs from 100 Hz to 3000 Hz before and after FLD was applied are 121.6 dB and 111.3 dB respectively. Therefore, after applying FLD on the outer surfaces of the split gradient assembly, the average SPL reduction is 10.3 dB.

Fig. 5-22 (b) displays the average SPLs in the central gap at different frequencies after applying FLD when the z coils were energized. Similar to the x coils, the FLD produces large SPL reductions at high-frequency bands, such as from 1300 Hz to 3000 Hz. At some resonant frequencies, the SPL reduction quantities are more than 10 dB. The average SPL was reduced from 116.4 dB to 109.1 dB, which created 7.3-dB SPL reduction.

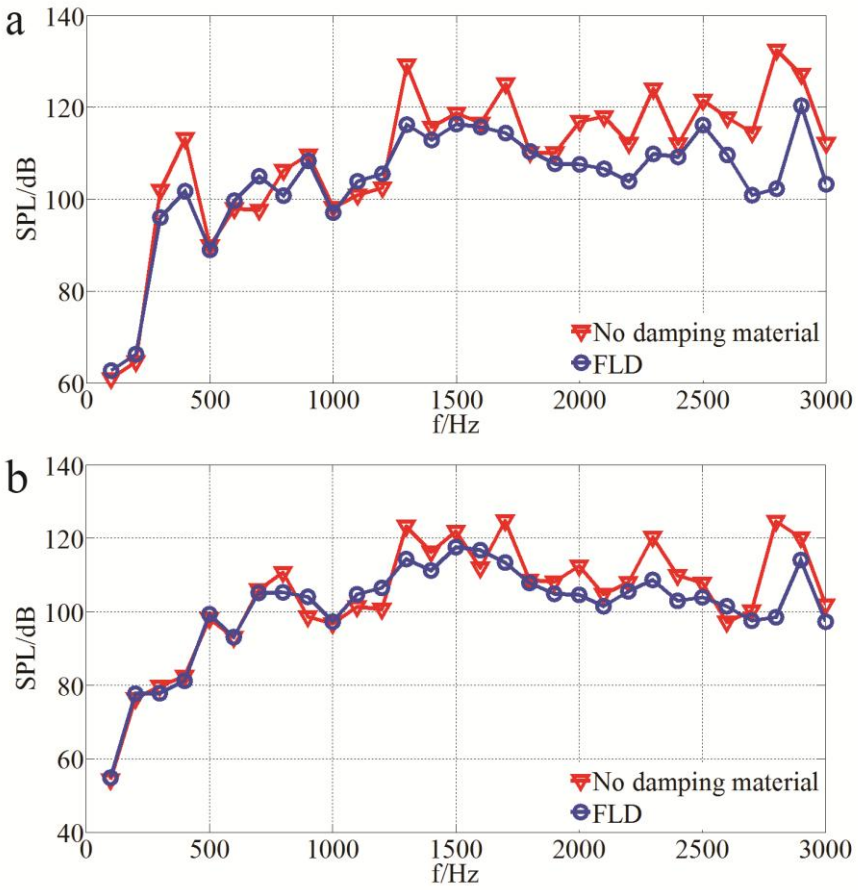

Fig. 5-22 Average SPLs in the central gap at different frequencies before and after applying FLD on the outer surfaces of the split gradient assembly, (a) the average SPLs in the central gap when the x coils were energized and, (b) the average SPLs in the central gap when the z coils were energized.

Fig. 5-23 shows the average SPLs in the central gap at different frequencies after applying the four kinds of damping treatments, listed in Table 5-8, on the outer surfaces of the split gradient assembly, when the x coils were energized. From Fig. 5-23, the SPLs at different frequencies all fall around or below 125 dB after these damping treatments. The damping materials, which are efficient at

attenuating structure's resonance [146-148], display good performance on the resonant frequencies, such as around 1300 Hz, 2300 Hz and 2800 Hz. However, for these damping treatments, obvious noise reduction differences occur at some frequencies. For example, damping treatment 4 (case 4) behaves better than damping treatment 1 (case 1) at lower-frequencies, such as 200 Hz, 400 Hz, but it tends to be ineffective at the high-frequencies. From 1400 Hz to 2400 Hz, nearly all the other three damping treatments show a better performance than the damping treatment 4. For damping treatments 1, 2 and 3, the SPLs in the central gap vary as the similar amplitude and trend, although the SPLs after applying damping treatment 3 are slightly higher than the other two treatments.

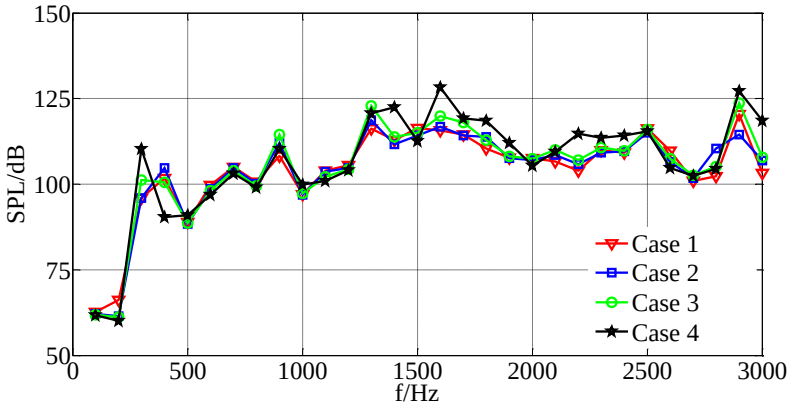

Fig. 5-23 The average SPLs in the central gap at different frequencies after applying the four kinds of damping treatments listed in Table II on the outer surfaces of the split gradient assembly when the x coils were energized. Cases 1, 2, 3 and 4 correspond to the order listed in Table 5-7.

After applying the four damping treatments, the SPLs in the central gap averaging from 100 Hz to 3000 Hz are 111.3 dB, 110.8 dB, 114.3 dB and 118.0 dB in order and the corresponding SPL reductions from 121.6 dB before applying these damping treatments are 10.3 dB, 10.8 dB, 7.3 dB and 3.6 dB, respectively. Therefore, the best damping treatment is Case 2, namely 1-cm damping material and 0.3-cm constraining layer. Compared with damping treatment 1 (1-cm damping material), the SPL reduction is a little bit larger, but adding the constraining layer increases the total thickness of the damping materials, which will be a challenge for the small space between the split gradient assembly and the main magnet. Damping treatments 3 and 4 are cases decreasing the thickness of the CLD in Case 2. However, the SPL reductions drop down to some extent. In addition, only from the comparison between damping treatment 3 (0.7-cm damping material and 0.3-cm constraining layer) and damping treatment 4 (0.3-cm damping material and 0.7-cm constraining layer), the selection of thicker damping material is clearly better than the selection of a thicker constraining layer. Because the split gradient assembly is made up of two thick hollow cylinders, they have a large bending stiffness. The shear action in the cylinder is not as significant

as a thin shell. Therefore, the advantage of CLD on a thick wall is not as obvious as a thin one. That is why damping treatment 2 does not behave much better than damping treatment 1 (only 0.5-dB more SPL reduction).

From the comparison of the four cases, the damping material plays a key role in the damping treatment for such thick hollow cylinders. That is, increasing the thickness of the damping material can increase the overall SPL attenuation effect. In addition, when the thicknesses of the FLD and CLD (including the thicknesses of both the damping material and the constraining layer) are the same, the CLD does not necessarily have a better performance than the FLD although it has a stiff constraining layer. Moreover, the FLD is easy to install on the surfaces of a structure. Therefore, our results show that the most appropriate damping treatment for the split gradient assembly should be FLD. After the damping process on the outer surfaces of the split gradient assembly, another 1-cm FLD was applied on the inner surfaces.

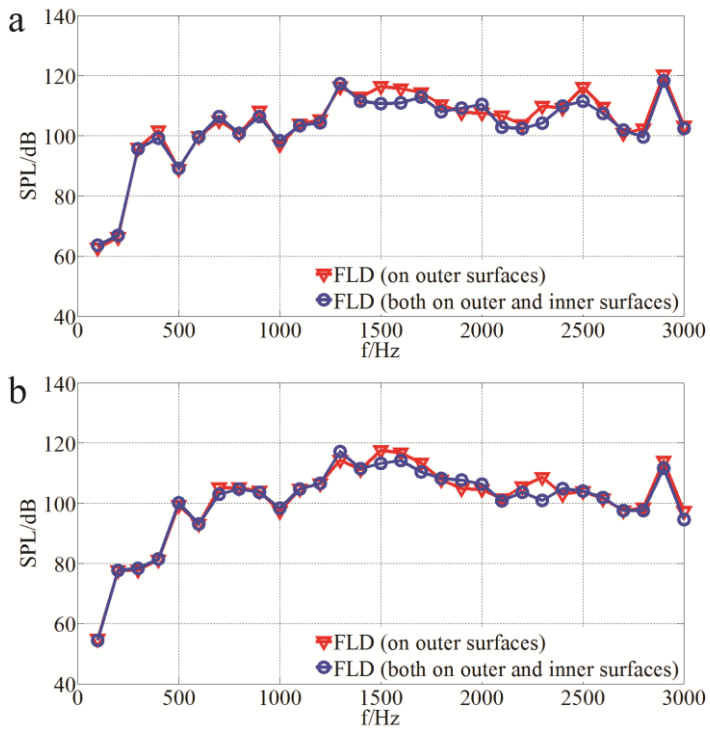

Fig. 5-24 The average SPLs in the central gap at different frequencies after applying 1-cm FLDs on the outer surfaces or on the outer and inner surfaces of the split gradient assembly, (a) the average SPLs in the central gap when the x coils were energized and, (b) the average SPLs in the central gap when the z coils were energized.

Fig. 5-24 (a) shows the average SPLs in the central gap at different frequencies after applying 1-cm FLDs on the outer surfaces or on both surfaces of the split-gradient assembly when the x coils were energized; Fig. 5-24 (b) displays the same application on the split gradient assembly when the z coils were energized. From Fig. 5-24, the average SPLs in the central gap were attenuated further at

some frequency bands, such as from 1500 Hz to 1700 Hz, from 2200 Hz to 2300 Hz. The further SPL reduction averaging all the frequencies for the x coils and z coils are 1.9 dB and 1.1 dB. Although the overall SPL reductions are minor, the SPL decreases at the resonant frequencies are obvious. Both for the x coils and z coils, the major SPL reductions amount to 5.6 dB and 5.7 dB, 4.2 dB and 7.8 dB at frequencies 1500 Hz and 2300 Hz, respectively.

We then investigated the extreme conditions of the material damping loss factor at a minimum value 0.38 and a maximum value 0.89. The damping materials were applied both on the outer and inner surfaces of the split gradient assembly and both the SPL properties in and outside the central gap were considered.

Fig. 5-25 shows the average-SPL comparisons at different frequencies between no damping treatment application and applying the FLDs on the surfaces of the split gradient assembly with a material damping loss factor 0.38. Fig. 5-26 shows the same situation but with a material damping loss factor 0.89. Here, the supports were placed at a=40 cm. In general, the damping material does not have an efficient low frequency attenuation performance. At some frequencies, the noise levels slightly increase. However, at the high-frequency band, the noise attenuation performance behaves much better, especially at some resonant frequencies such as around 400 Hz, 1300 Hz, 1700 Hz, 2300 Hz and 2800 Hz when the x coils were energized, or around 1500 Hz, 2000 Hz, 2300 Hz and 2800 Hz when the z coils were energized. Moreover, the damping treatment not only attenuates the noise level in the central gap but also outside the central gap, which results from abating the vibration of the split gradient assembly. The overall average-SPL reductions after damping processing are displayed in Table 5-9. From Table 5-9, the SPL reductions in the central gap are larger than those outside the central gap for both the two extreme loss factors of the damping material ISD 130. The SPL reduction quantities for the z coils are not as considerable as the x coils. Also, a larger loss factor can reduce noise levels. As a whole, the damping material ISD 130 can create 8.5-12.5 dB noise level reduction for the x coils and 6.3-8.8 dB noise reduction for the z coils.

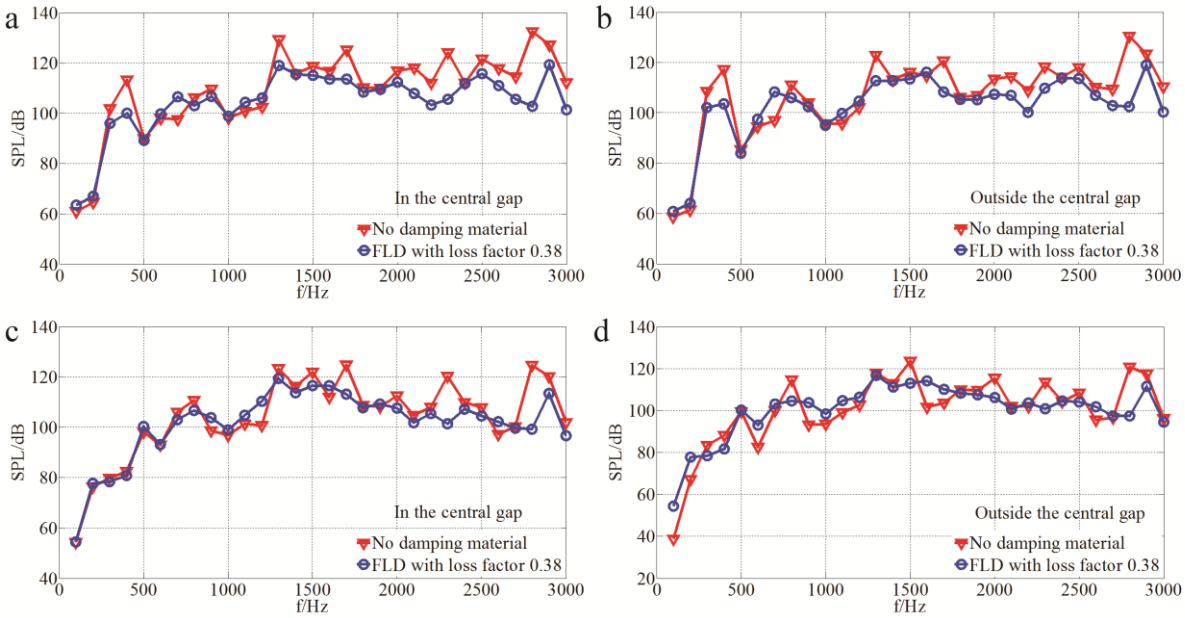

Fig. 5-25 The average-SPL comparisons at different frequencies between no damping treatment application and applying the FLDs on the surfaces of the split gradient assembly with a material damping loss factor 0.38, (a) the average-SPL comparison in the central gap when the x coils were energized and, (b) the average-SPL comparison outside the central gap when the x coils were energized, (c) the average-SPL comparison in the central gap when the z coils were energized and (d) the average-SPL comparison outside the central gap when the z coils were energized.

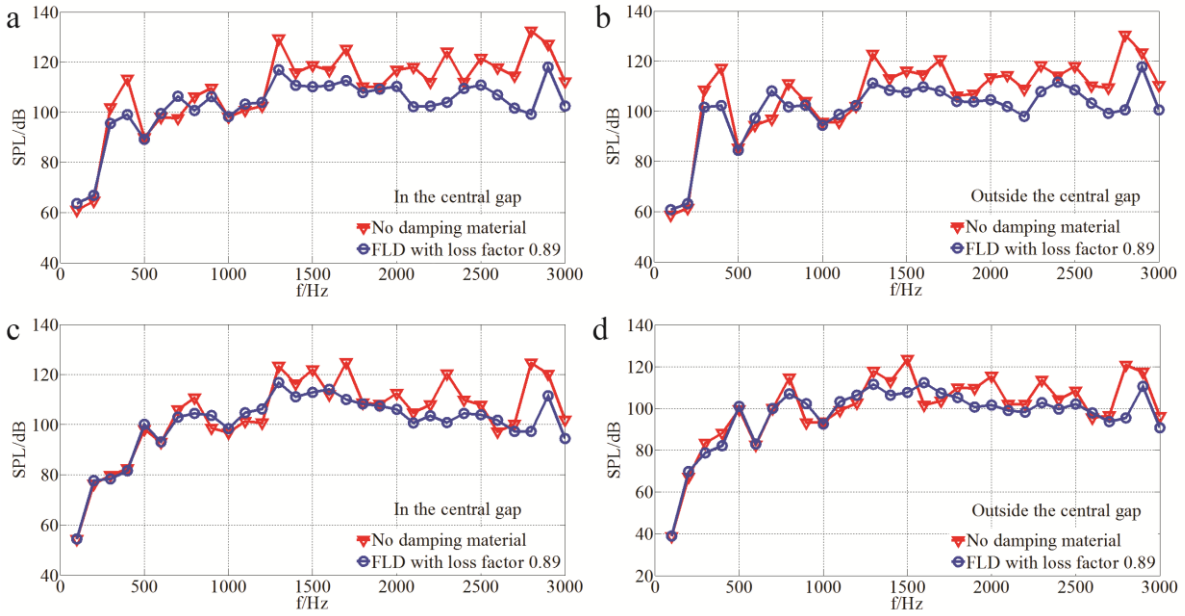

Fig. 5-26 The average-SPL comparisons at different frequencies between no damping treatment application and applying the FLDs on the surfaces of the split gradient assembly with a material damping loss factor 0.89, (a) the average-SPL comparison in the central gap when the x coils were energized and, (b) the-average SPL comparison outside the central gap when the x coils were energized, (c) the average-SPL comparison in the central gap when the z coils were energized and (d) the average-SPL comparison outside the central gap when the z coils were energized.

Table 5-9 Overall average-SPL reductions in the interested regions of the split MRI system after applying damping treatment

Loss factor	Regions	Coils x (Unit: dB)	Coils z (Unit: dB)
0.38	In the central gap	10.2	6.3
	Outside the central gap	8.5	6.8
0.89	In the central gap	12.5	8.8
	Outside the central gap	11.1	8.5

5.2.4 Conclusions

This study numerically investigates a scheme to attenuate the noise levels of a split MRI system. By adjusting the positions of the supports between the split gradient assembly and the main magnet, the vibration modes of the split gradient assembly can be altered and thus the acoustic field distribution can be relocated in the cylindrical tunnels and the central gap, which allows us to attenuate the sound level by about 6.3-9.9 dB inside and outside the central gap for both the x and z coils. With the application of damping materials on the surfaces of the split-gradient assembly, the acoustic noise can be further reduced. Different free-layer damping (FLD) and constrained-layer damping (CLD) treatments were investigated and compared. After applying the best damping treatment, the overall average SPL in and outside the central gap was further reduced by 8.5-12.5 dB for the x coils and 6.3-8.8 dB for the z coils, respectively. Future experimental validation will be performed to verify the proposed acoustic noise control method.

5.3 Theoretical investigation of gradient pulse alterations for acoustic noise reduction in an MRI-LINAC system

5.3.1 Methods

In an MRI scanner, if the main frequency of a gradient pulse is close to the natural frequency of the system, the gradient assembly will vibrate significantly and emit a loud noise. However, by avoiding the natural frequencies of the system through gradient pulse alterations, it is expected that the overall noise level will be attenuated [87]. Taking an echo planar imaging (EPI) sequence as an example, its basic pulse pattern is a trapezoidal form, as is shown in Fig. 5-27. Its time-domain periodic function can be expressed as a Fourier series shown in Eq. (5-5), where A is the plateau current value, t_1 is the rising or falling time and t_2 is the duration of the plateau. We investigated the acoustic responses of a simulated 2D simplified axisymmetric model of a split MRI scanner, an element of an MRI-LINAC system (only the split gradient assembly including the z coils were

simulated and the assembly ends were fixed). A series of sinusoidal gradient pulses were used to energize the z coils from 20 Hz to 20000 Hz and the average sound pressure levels (SPL) in the central gap were calculated to find the system's resonant frequencies. The peak current value of the sinusoidal pulses was 600 A and the static magnetic field strength was 1 T. The system is still currently being built. An acoustic model is shown in Fig. 5-28. After the resonant frequencies were identified, we removed the sinusoidal components of the pulse's Fourier series, which were identical or close to the system's resonant frequencies. During the removal process of the sinusoidal components, we set two principles, expressed as Eq. (5-6), where $SPL(f)$ is the acoustic response with respect to frequency, SPL_0 is a designated SPL value, $A_{\text{plateau-max}}$ is the maximum current value of the pulse plateau and $A_{\text{plateau-min}}$ is the minimum current value of the pulse plateau. Namely, we removed the sinusoidal components of those SPLs which were higher than a designated value and the pulse plateau part of the remaining sinusoidal components which had a deviation less than 3% [149, 150], which is an acceptably small deviation from a perfect plateau for an EPI pulse. The pulse alteration process balances these two principles in order to achieve an optimal pulse form. Assuming the system is linear, the sound pressure of the EPI pulse is a linear superposition of its sinusoidal components. The ultimate *SPL* can be easily acquired from Eq. (5-7), where p_n is the effective value of pressure and p_0 is the referential sound pressure. In Eq. (5-7), the cross terms were removed though orthogonality.

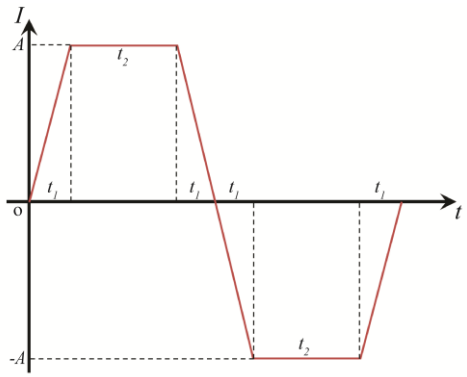

Fig. 5-27 Current form of an EPI gradient pulse.

$$\begin{cases} f(t)=\sum_{n=1}^{\infty} b_n \sin\dfrac{2\pi nt}{4t_1+2t_2} \\ b_n=\dfrac{A}{t_1}\dfrac{4t_1+2t_2}{\pi^2 n^2}\left[\sin\dfrac{2\pi nt_1}{4t_1+2t_2}+\sin\dfrac{2\pi n(t_1+t_2)}{4t_1+2t_2}\right] \end{cases} \tag{5-5}$$

$$\begin{cases} SPL(f)>SPL_0 \\ (A_{\text{plateau-max}}-A_{\text{plateau-min}})*0.5/A<3\% \end{cases} \tag{5-6}$$

$$SPL=10\lg\left(\sum_{n=1}^{\infty}\frac{b_n}{A}\cdot\frac{p_n}{p_0}\right)^2=10\lg\sum_{n=1}^{\infty}\left(\frac{b_n}{A}\cdot\frac{p_n}{p_0}\right)^2=10\lg\sum_{n=1}^{\infty}\left(\frac{b_n}{A}\right)^2\cdot10^{0.1*SPL\left(\frac{n}{4t_1+2t_2}\right)} \quad (5\text{-}7)$$

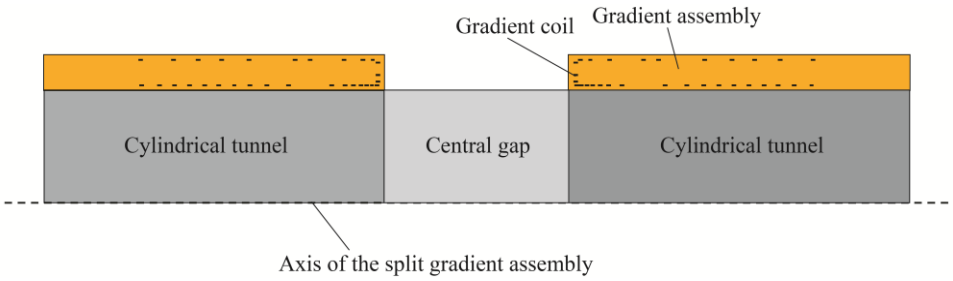

Fig. 5-28 Simplified 2D axisymmetric acoustic model of a split MRI scanner. The air in the space is not shown.

5.3.2 Results

The acoustic responses of the split MRI system were plotted and are shown in Fig. 5-29. Here t_1=237 μs, t_2=474 μs, the frequency components of the EPI pulse, its corresponding single-frequency (with current peak value 600 A) acoustic responses and amplitudes of its Fourier series are displayed in Table 5-10. Using the optimization procedures shown in Fig. 5-30, after a repeated comparison, SPL_0 was designated as 116 dB, and then the bold italic frequency components were removed from the Fourier series. The deviation of the pulse plateau with the remaining sinusoidal components is 1.6%. The standard trapezoidal pulse form and the altered one were plotted and are shown in Fig. 5-31, demonstrating similarity. After the alteration, the overall SPL of this EPI pulse was attenuated from 108.4 dB to 94.6 dB. Thus, a 13.8-dB SPL reduction was acquired. In reality, the effect of the proposed method depends on the frequency components of the pulse. The pulses with a higher energy level at the resonant frequency components experience greater noise reduction compared to those where the main energy is concentrated in a non-resonant frequency band.

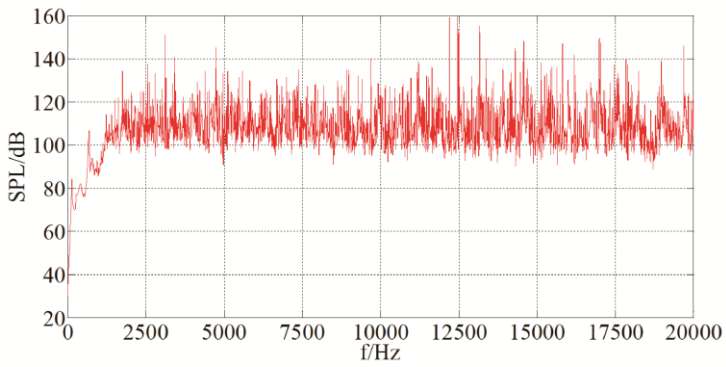

Fig. 5-29 Acoustic responses of the split MRI system.

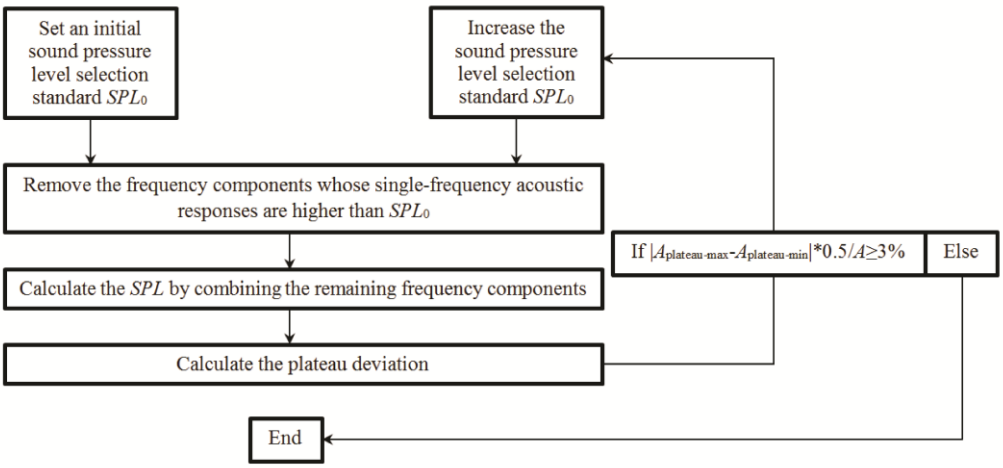

Fig. 5-30 Optimization procedures of the gradient pulse alterations for acoustic noise reduction in a split MRI system.

Table 5-10 Frequency components of an EPI pulse, its corresponding single-frequency acoustic response and amplitudes of its Fourier series

Frequency component *f* (Hz)	528	1583	2638	3694	***4749***	5804	6860	***7915***	8970	10026
Single-frequency response *SPL* (dB)	77.8	111.6	111.2	115.7	***145.2***	102.2	106.7	***116.8***	99.3	98.4
Fourier transform amplitude *I* (A)	687.8	76.4	-27.5	-14.0	***8.5***	5.7	-4.1	***-3.1***	2.4	1.9
Frequency component *f* (Hz)	11081	12136	***13192***	14247	***15302***	16358	17413	18468	19524	
Single-frequency response *SPL* (dB)	102.3	102.2	***116.3***	101.9	***116.6***	107.4	106.0	104.1	99.2	
Fourier transform amplitude *I* (A)	-1.6	-1.3	***1.1***	0.9	***-0.8***	-0.7	0.6	0.6	-0.5	

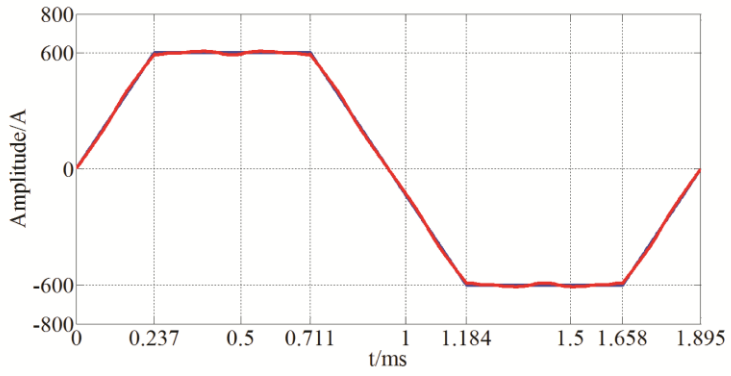

Fig. 5-31 Standard trapezoidal gradient pulse and the designed pulse.

5.3.3 Discussion

The gradient pulse alteration method is investigated theoretically on its ability to reduce the noise level of a split MRI system. This method is easily implemented without changing or reassembling the split MRI scanner. Future experimental measurements will be conducted to test the effect of this method and evaluate imaging quality.

5.3.4 Conclusion

The proposed gradient pulse alteration method can effectively attenuate the SPL of a split MRI system while keeping the pulse form. In the above case, an overall SPL reduction of 13.8dB was achieved when the proposed method was applied. It also kept the plateau deviation at 1.6%.

5.4 A numerical study of the acoustic radiation due to eddy current-cryostat interactions

5.4.1 Introduction

In most of these noise reduction methods described in Section 2.3.4, the assumption that the main noise source comes from the gradient coils was used. Other noises that could originate from the magnetic field induced eddy current and mechanical transmissions were not fully considered. Experimentally, noise arising from the eddy current induced vibrations of the inductive structures has been reported to be significant and it may account for the main noise source [9] if the gradient coils are not well-shielded. Compared to the noise issues related to the gradient coil assembly, the noise from the eddy current induced vibrations has so far largely been ignored and very little effort has been put into this area.

It is, therefore, with this in mind that the current theoretical work was carried out. In this work, we first improved the active shielding effect of the gradient coil and reduced the eddy current induced magnetic field insider the imaging volume, DSV. Then we took effort on modelling the eddy current-warm bore wall interaction, and finally performed a quantitative analysis on noise reduction under the condition of using damping materials.

5.4.2 Method

For the gradient coil design by constraint of the eddy current induced magnetic field, the current frequency was chosen as 1000 Hz. Two specific x coils with shielding ratio 2% (referred to as coil I)

and 0.5% (referred to as coil II) were considered in the present work. Here, 0.5% shielding ratio was selected for the consideration of a tradeoff between the eddy current control and coil performance, since stronger shielding would result in more coil turns on the shield, and therefore increased coil resistance and inductance. The gradient coil design method was based on a finite difference method presented in section 3.1.1. The noise originating from the gradient assembly alone and that from the warm bore wall was calculated and compared.

5.4.2.1 Acoustic model

The commercial FE package ANSYS was used here for modelling the acoustic properties. Fig. 5-32 shows the acoustic model considered in the present work. It includes the gradient coil set, the epoxy resin, the warm bore wall and air space. Because of the vacuum space between the warm bore wall and cold shield, the vibration from the warm bore wall outer surface did not have any acoustic radiation in the patient bore. Therefore, the outer space beyond the warm bore wall was not included in the acoustic model. Both the ends of the gradient assembly and the warm bore wall were clamped together to avoid any displacement. The dimensions of the gradient coil sets and other design parameters are listed in Table 5-11. The dimensions of the gradient assembly and the warm bore wall and other acoustic material parameters are given in Table 5-12 and illustrated in Fig. 5-33.

The mechanical parameters of the structural materials were taken from references [132, 151]. The damping loss factors of the materials themselves, which were omitted in a previous work [112], were included in the current model. The model was meshed with hexahedral elements with the element size less than 1/6 of the smallest wave length [112]. Two noise sources, one from the gradient assembly (due to the vibration of the gradient coils) and one from the warm bore wall (due to the induced eddy current by gradient coil switching) were modelled separately.

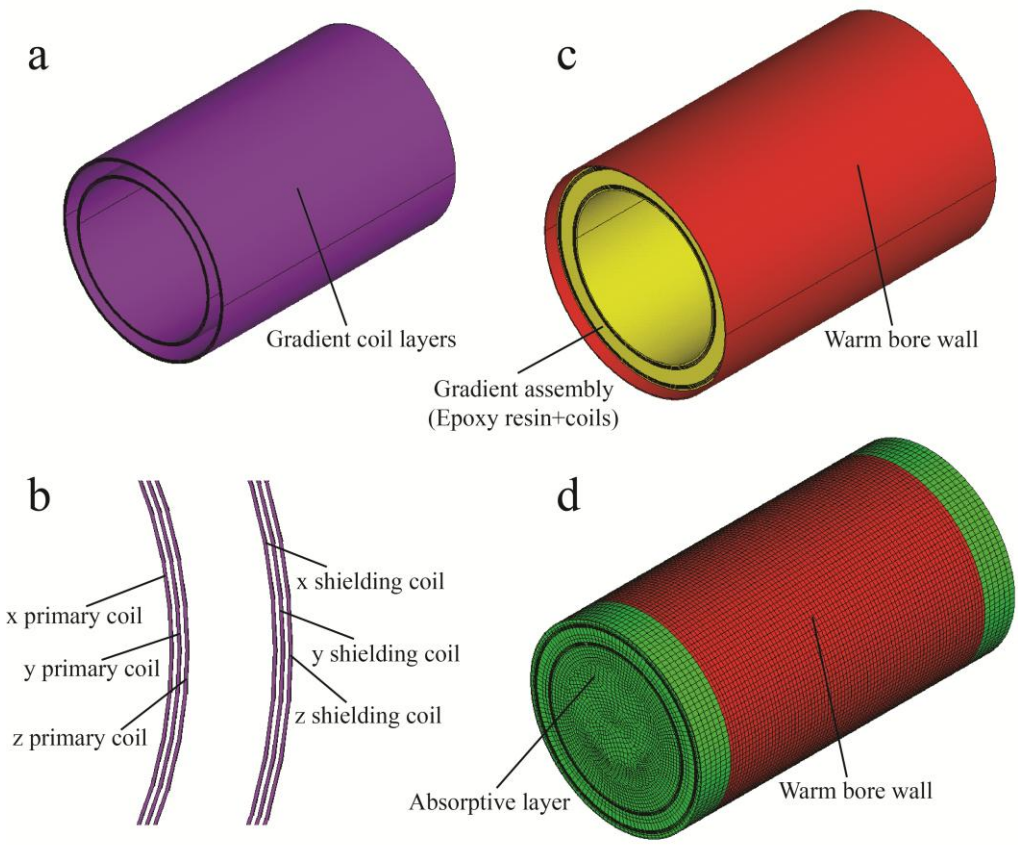

Fig. 5-32 The acoustic model that includes (a) gradient coil layers, (b) gradient coils layout, (c) entity components in the model and (d) meshed model. The gradient assembly including the gradient coil layers and epoxy resin, the warm bore wall and air space was modelled for the acoustic analysis. Absorptive air layers (green part in (d)) with sound absorptive coefficient 1 (no sound wave reflection there) were set to mimic free space.

Table 5-11 Dimensions and control parameters of the gradient coil design

Item		***r* (m)**	***l* (m)**
Gradient coils	**x primary coil**	0.374	1.24
	x shielding coil	0.454	1.30
Warm bore wall		0.486	1.46
Gradient strength		45 mT/m	
DSV (diameter)		0.5 m	
Linearity		5%	
Shielding ratio (coil I)		2%	
Shielding ratio (coil II)		0.5%	
Warm bore wall conductivity		1.1×10^6 S/m	

r is the radius of the coil layer and *l* is the length of the coil layer. The warm bore wall was used for the eddy current control.

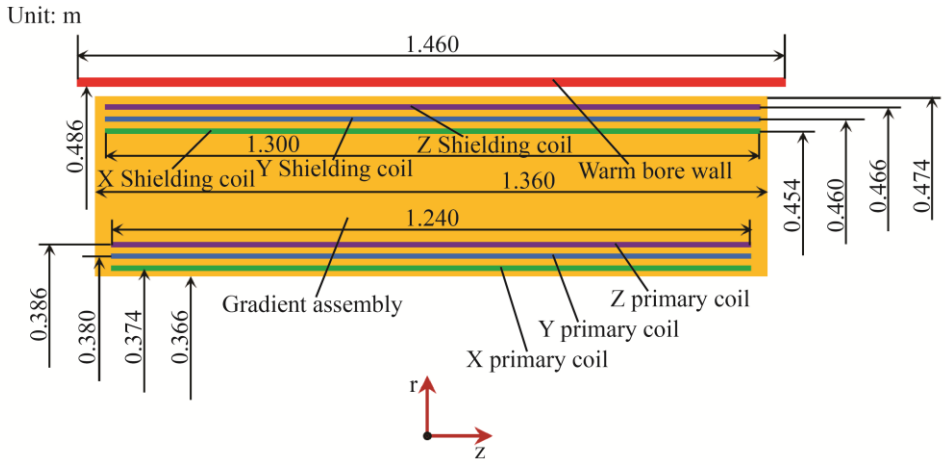

Fig. 5-33 Illustration of the model dimensions. Note that the y and z coils were also simulated in the acoustic model as copper layers.

Table 5-12 Dimensions and material parameters for the simulation of the acoustic model

Dimension							
Item		r_1 (m)	r_2 (m)	h (m)	l (m)		
Gradient assembly		0.366	0.474	0.108	1.36		
Warm bore wall		0.486	0.49075	0.00475	1.46		
Parameter							
Item		E (Gpa)	μ	ρ (kg/m^3)	σ	c (m/s)	α
Gradient assembly	**Epoxy resin**	15.7	0.32	1835	0.0360		
	Copper	117	0.34	8960	0.0030		
Warm bore wall	**Steel**	193	0.285	8000	0.0024		
Space	**Air I**			1.225		340	
	Air II			1.225		340	1

E, μ, ρ and σ are the Young's modulus, Poisson's ratio, material density and damping loss factor, where the damping loss factor $\sigma=2\zeta$ (damping ratio). c is the acoustic velocity and α is the sound absorptive coefficient. Air I is the air in the free space and Air II is the absorptive air layers at the surface of Air I with sound absorptive coefficient 1, namely no sound wave reflection. The gradient coils were simulated as copper layers in the gradient assembly with thickness 2.5 mm, as is shown in Fig. 5-32 (a) and (b) and Fig. 5-33.

The Lorentz force calculation was done for a 3T MRI system whose coil profile is shown in Fig. 5-34 and the distribution of the main magnet blocks are also illustrated. The Lorentz force on a discrete finite difference grid was calculated as

$$F=\left(J_x,J_y,J_z\right)\times\left(B_x,B_y,B_z\right)\cdot R\Delta\theta\Delta z \tag{5-8}$$

and

$$J_x = J_\theta \cos(\theta + \frac{\pi}{2})$$
$$J_y = J_\theta \sin(\theta + \frac{\pi}{2}) \tag{5-9}$$

where x, y and z represent the corresponding vector components in a Cartesian coordinate system, B is the main magnetic field, R is the radius of the gradient coil or the warm bore wall, Δz and $\Delta\theta$ are, respectively, the z and θ intervals of the finite difference grid.

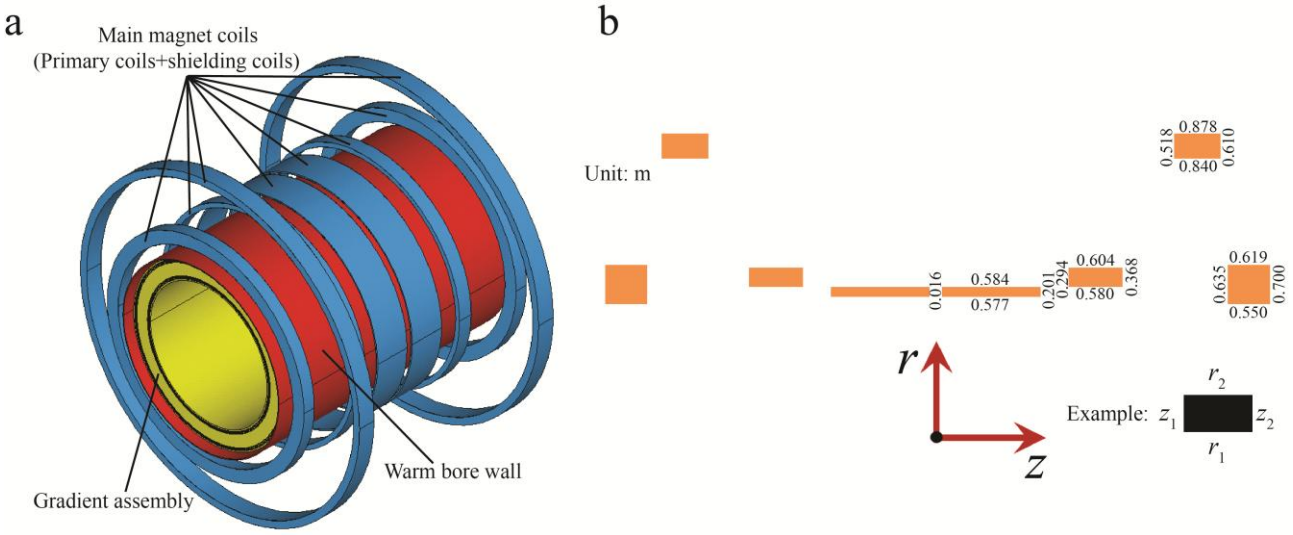

Fig. 5-34 Main magnetic field environment used for the acoustic model: (a) illustration of the gradient assembly and warm bore wall in a 3T main magnet and (b) illustration of the main magnet coil configuration.

Here the gradient strength was assumed to be 45 mT/m. The discrete Lorentz force was evaluated separately on the coil layers and on the warm bore wall, enabling the investigation of the acoustic radiation of the gradient assembly and from the warm bore wall separately.

The longitudinal component (Bz) and radial component (Br) of the 3T main magnetic field are plotted in Fig. 5-35 (a) and (b). It can be observed that although the main magnetic field is uniform within the DSV region, it fluctuates strongly in the stray field regions. The gradient coil and the warm bore wall actually reside in the stray field region. Thus, the Lorentz force calculation with a uniform main magnetic field without considering the real field profile may be inaccurate.

Harmonic analysis was used here to investigate the acoustic response of the model from 100 Hz to 3000 Hz, which covers the main frequencies of the gradient pulses. The acoustic response of a specific pulse can be approximately calculated by Fourier transform. The calculated results show that the current density distributions at the frequency band 100-3000 Hz are only slightly different (the amplitude difference is less than 10^{-4}). Fig. 5-35 (c) and (d) illustrate a Lorentz force

distribution example on the warm bore wall and gradient assembly. Here the Lorentz force was calculated under the Cartesian coordinate system. The clamped boundary constraints are shown at the ends of the warm bore wall and the gradient assembly.

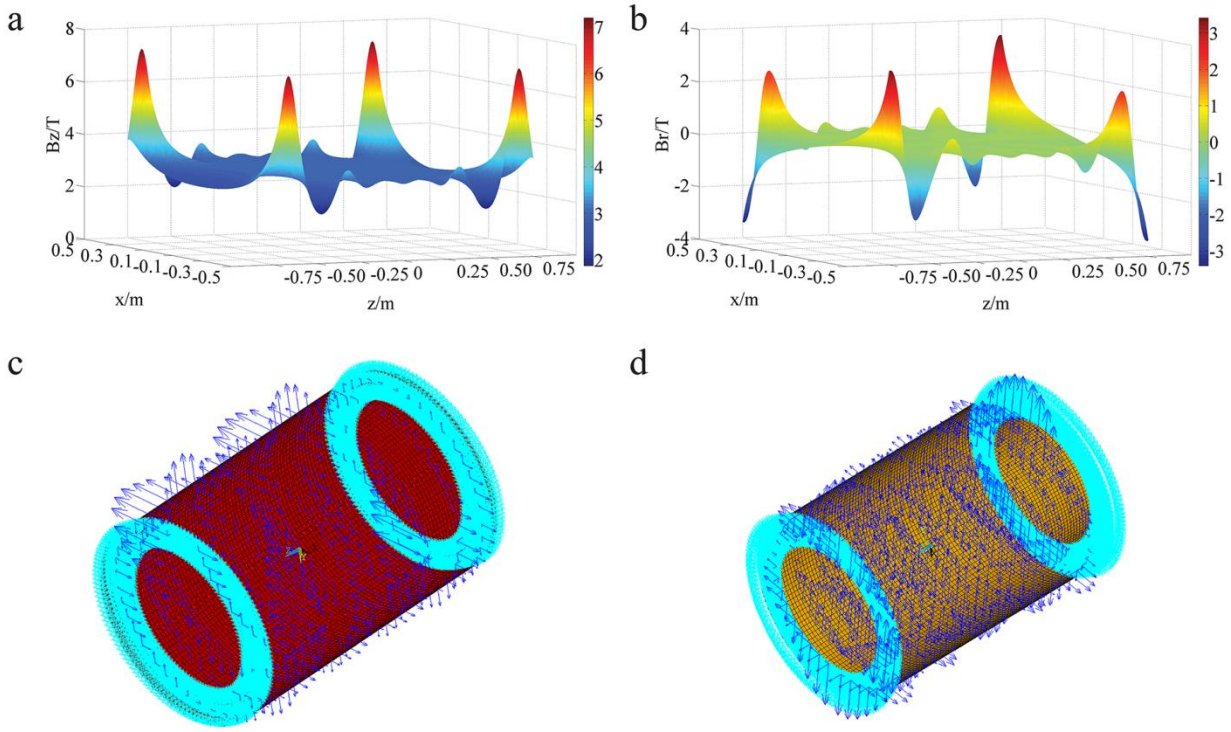

Fig. 5-35 Magnetic field and Lorentz force distributions within a 3T main magnetic field: (a) longitudinal component (Bz) of the main magnetic field, (b) radial component (Br) of the main magnetic field, (c) a Lorentz force distribution example on the warm bore wall and (d) a Lorentz force distribution example on the gradient assembly. The clamped boundary constraints are illustrated at the ends of the warm bore wall and the gradient assembly.

The acoustic response of coil I (shielding ratio 2%) was compared with coil II (shielding ratio 0.5%), including the warm bore walls, so as to determine the main noise source and evaluate the influence on acoustic noise reduction by eddy current control. Here the SPL for a specific frequency was averaged (logarithmic average) through the FE nodes in the patient bore by Eq. (5-2) and the overall averaged SPLs were calculated by Eq. (5-3).

5.4.3 Results and discussion

5.4.3.1 Coil configuration and current density distribution

The gradient coil loops of coil I (shielding ratio 2%) and coil II (shielding ratio 0.5%) are shown in Fig. 5-36 illustrating similar coil patterns (with different turns) between the two coils. It should be noted that coil I has an operating current of 641.9 A and coil II an operating current of 664.3 A.

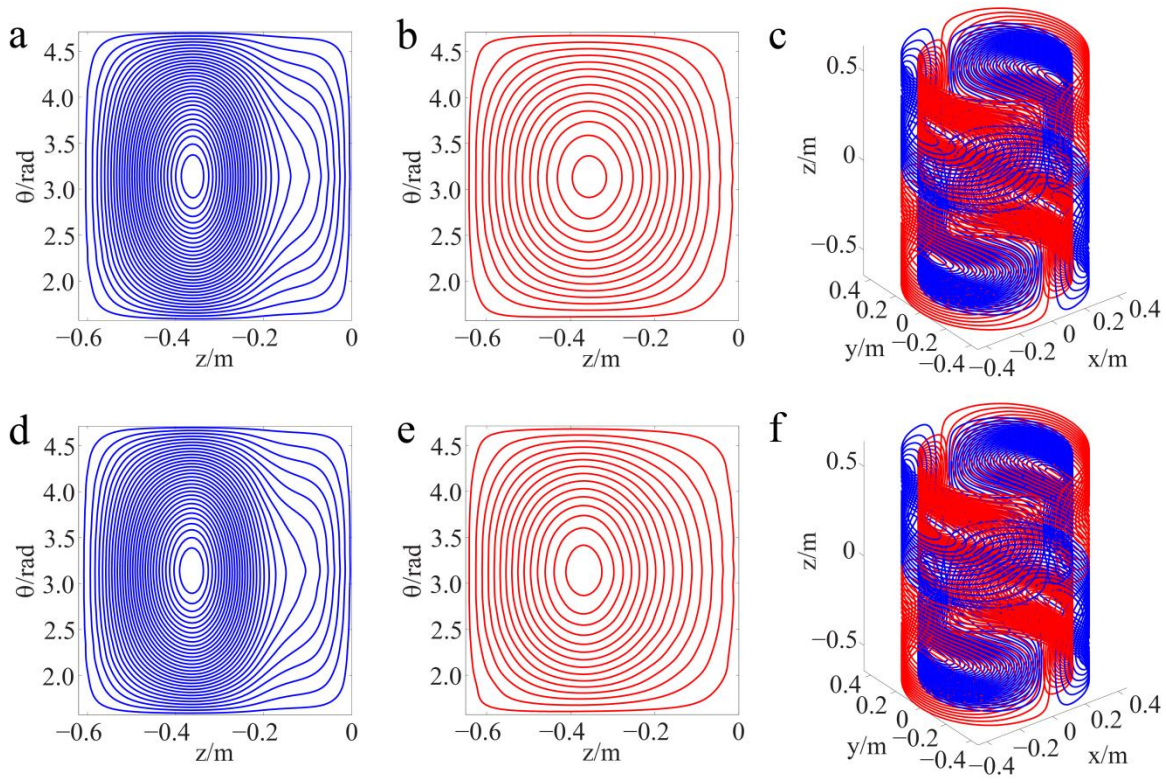

Fig. 5-36 Gradient coil patterns (only a quarter is displayed due to symmetry): ¼ of primary (a) and shield (b) coils (coil I); ¼ of primary (d) and shield (e) coils (coil II); 3D coil pattern of coil I (c) and coil II (f).

Fig. 5-37 shows the current density distributions on the primary coil, on the shielding coil and on the warm bore wall in coil I design, and Fig. 5-38 shows the corresponding current density distributions in coil II design. By comparison, the current density distribution of the coil I and coil II primary layers has little difference for both the circumferential component (J_θ) and longitudinal component (J_z) (comparing Fig 5-37 (a) and Fig.5-38 (a) and between Fig 5-37 (b) and Fig 5-38 (b)). For the shielding coil, some differences can be seen between coil I and coil II indicating coil II has a larger current density distribution on the shielding layer than coil I. The largest difference between coil I design and coil II design, however, is in the eddy current density distribution over the warm bore wall (comparing Fig. 5-37 (e) and Fig. 5-38 (e), and also Fig. 5-37 (f) and Fig. 5-38 (f)). It can be seen that the eddy current density on the warm bore wall was significantly attenuated with a smaller shielding ratio.

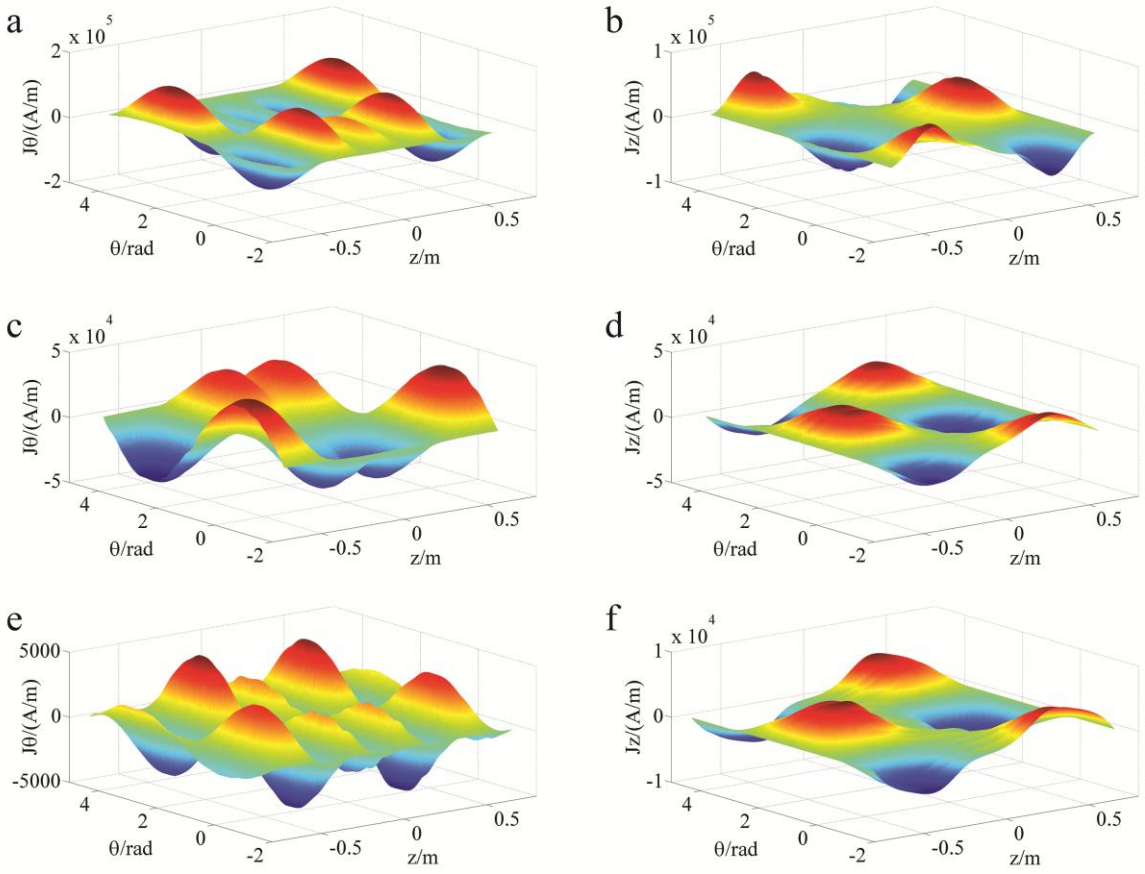

Fig. 5-37 Current density distributions in coil I design. The circumferential component (a) and longitudinal component (b) of the current density distribution on the primary coil only; the circumferential component (c) and longitudinal component (d) of the current density distribution on the shielding coil only; the circumferential component (e) and longitudinal component (f) of the current density distribution on the warm bore wall only.

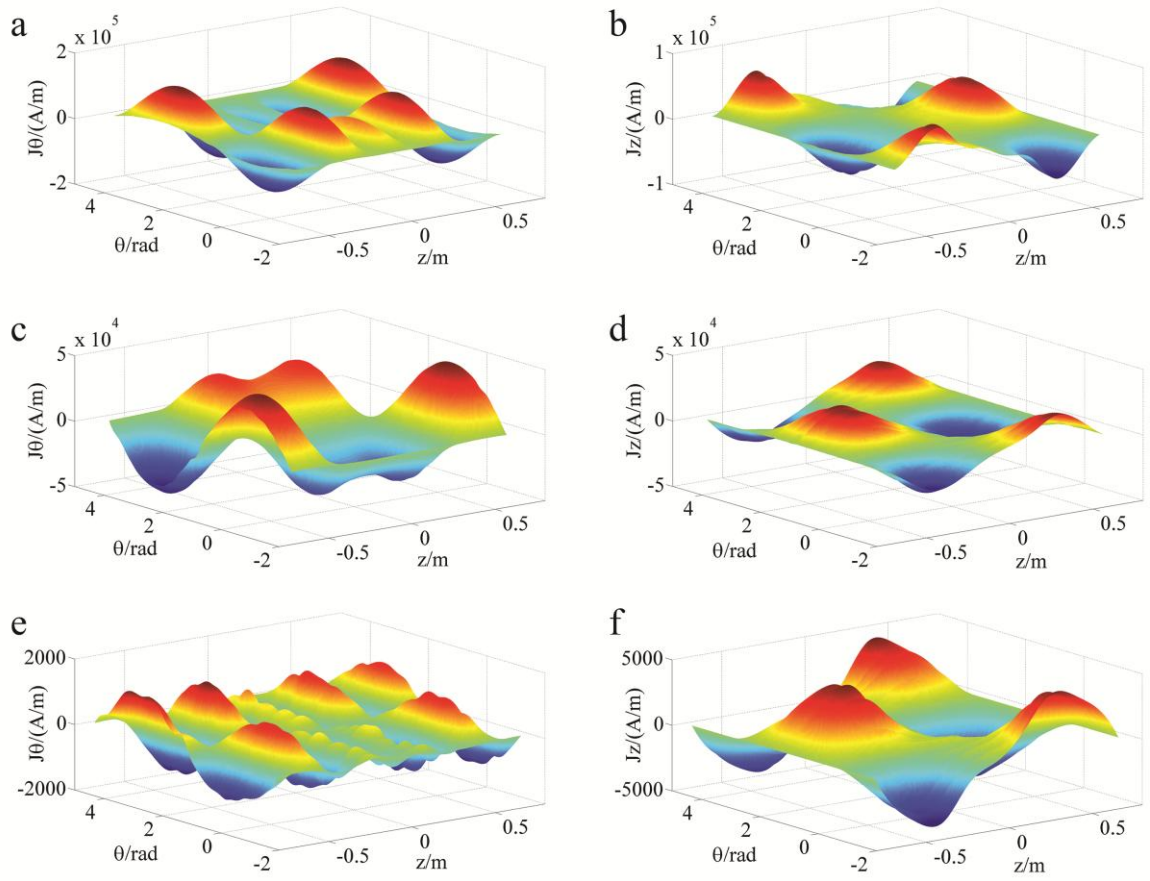

Fig. 5-38 Current density distributions in coil II design. The circumferential component (a) and longitudinal component (b) of the current density distribution on the primary coil only; the circumferential component (c) and longitudinal component (d) of the current density distribution on the shielding coil only; the circumferential component (e) and longitudinal component (f) of the current density distribution on the warm bore wall only.

5.4.3.2 SPL comparison between coil I and coil II

The acoustic responses of the warm bore wall and the gradient coils are plotted and compared in Fig. 5-39. The combined acoustic responses of the warm bore wall and gradient coils are also shown in Fig. 5-39 (a) and (b). From Fig. 5-39 (a), the warm bore wall accompanied with coil I (shielding ratio 2%), has stronger overall acoustic radiation than the gradient coil itself. The SPL for the warm bore wall is 102.6 dB (averaged over the frequency range) compared with the gradient coil of 97.9 dB. Specifically, in the frequency band 800-1250 Hz, the SPL of the warm bore wall is significantly higher than that of the gradient coil with the SPL difference peaked at 950 Hz, with a difference of 31.2 dB. Significant difference can also be seen in the frequency ranges of 500-700 Hz and 1500-1700 Hz. However, at high frequencies (1700-3000 Hz), the SPL of the warm bore wall is less at most frequencies. These results suggest that the previous acoustic control methods which only considered the gradient assembly may not work well, at least in some frequencies. For the combined acoustic fields of coil I, the global SPL reaches a level of 104.2 dB, which is close to that

generated by the warm bore wall only (102.6 dB). At those specific frequencies where the SPLs of the gradient coil are significantly higher than those of the warm bore wall (see around 1750 Hz and 2750 Hz), the combined SPL contour fits closer to the SPL contour of the gradient coil.

Fig. 5-39 (b) shows that the SPLs of the warm bore wall and the gradient coil accompanied with coil II design (shielding ratio 0.5%). At the frequency bands 100-800 Hz and 1550-2950 Hz, the SPL of the warm bore wall is on the whole controlled below that of the gradient coil. Although at the frequency band 800-1250 Hz, the SPL of the warm bore wall is higher than that of the gradient coil, the difference is smaller compared with that of coil I. For the combined acoustic response of coil II, at the frequency bands 100-800 Hz and 1550-2950 Hz, the SPL contour is mostly close to that of the gradient coil; however, at the frequency band 800-1250 Hz, the contour approximates that of the warm bore wall. The overall SPL of the combined acoustic response is 100.9 dB, which is comparable with that of the warm bore wall (98.7 dB) or gradient coil (97.5 dB). Compared with coil I, the overall SPL of coil II is reduced by 3.3 dB.

Fig. 5-39 (c) shows the SPLs of the warm bore wall accompanied with coil I design and coil II design. The averaged SPL of the warm bore wall for coil design I is102.6 dB and is reduced to 98.7 dB for coil II design. However, at certain frequency bands (100-700 Hz, 1500-2000, 2300-2850 Hz), higher reduction rates were found. For example, at the frequency band of 100-700 Hz, the averaged SPL was reduced from 89.6 dB to 69.8 dB.

Fig. 5-39 (d) shows the SPL comparison between the gradient coil I and the gradient coil II. Only slight difference can be observed between the SPLs of coil I and coil II, with only 0.5-dB noise difference in the averaged SPL. This is mainly due to the similar current density distributions and coil patterns of these two coils.

It is realized from Fig. 5-39 (c) that, in order to achieve significant noise reduction in the entire frequency range particularly in the frequency band 800-1250 Hz, some additional noise control methods needed to be applied. It is known that damping materials have the capability to tackle the structure vibration, especially at the resonant frequencies [74, 152]. Thus, further noise reduction by damping the warm bore wall was considered. Here the constrained damping treatment was applied on inner surface of the warm bore wall, since constrained damping treatment has obvious advantage than the free damping treatment on thin structure [144], which has smaller bending stiffness compared with a thick one.

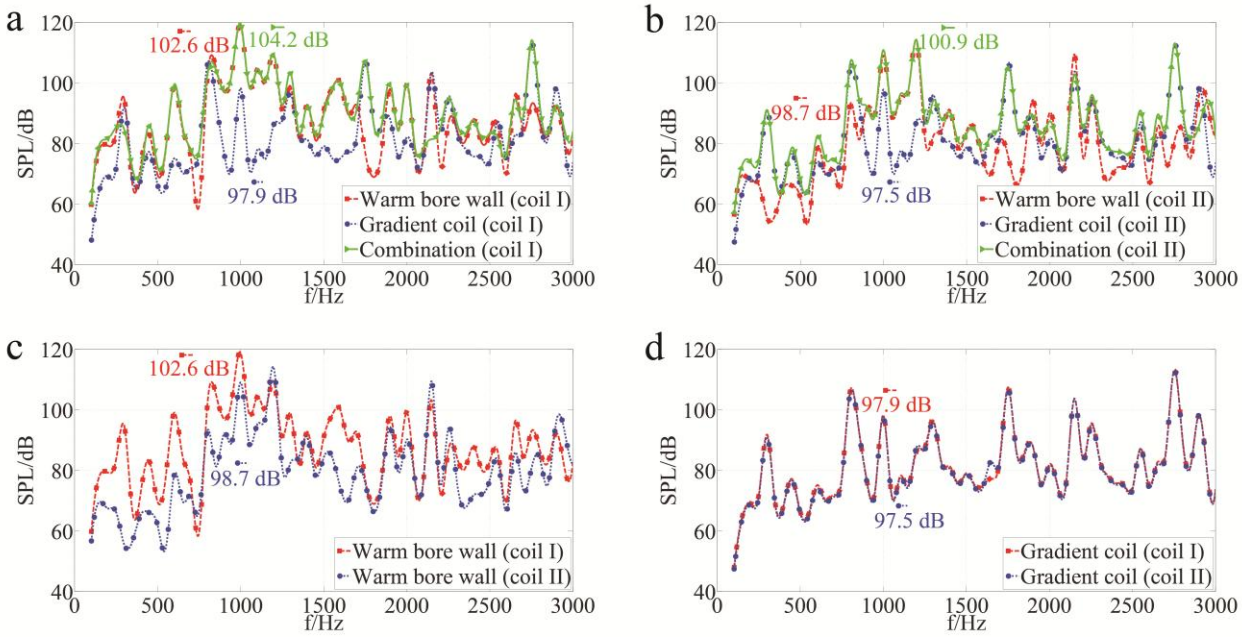

Fig. 5-39 Comparison of acoustic responses of the warm bore wall and gradient coil: (a) acoustic responses of the warm bore wall accompanied with coil I design, gradient coil I and combination of both, (b) acoustic responses of the warm bore wall accompanied with coil II design, gradient coil II and combination of both, (c) acoustic responses of the warm bore wall accompanied with coil I design, and with coil II design and (d) acoustic responses of gradient coil I and gradient coil II.

Fig. 5-40 shows the damping treatment installation on the warm bore wall with an enlarged view of a small section. The gradient coil was designed to leave some space for the installation of the damping materials. Here the thickness of the damping layer is 2 mm and the thickness of the constraining layer is 4 mm. The material parameters for the damping layer and constraining layer are listed in Table 5-13 [153].

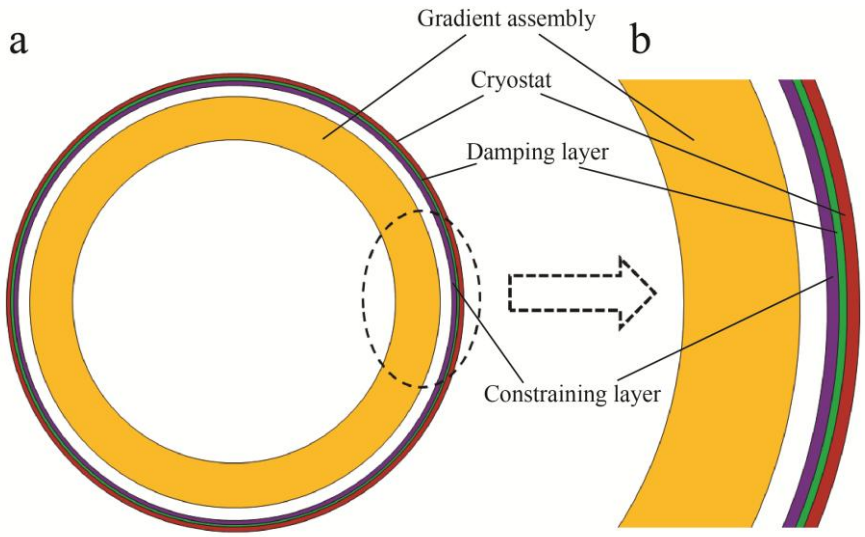

Fig. 5-40 Constrained damping treatment on the warm bore wall: an entire cross section view (a) and an expanded view (b).

Table 5-13 Material parameters for the constraining damping treatment

Item		***E* (Gpa)**	***μ***	***ρ* (kg/m^3)**	***σ***
Damping layer	**3M ISD 130**	0.0012	0.49	950	0.6
Constraining layer	**Fiberglass**	40	0.3	2550	0.01

The acoustic response of the warm bore wall for coil II design was calculated with the constrained damping layer applied. Fig. 5-41 shows the SPL comparison between the undamped and damped warm bore wall, and the combined SPL is also depicted. From Fig. 5-41 (a), it can be seen that for the main frequency band 800-1250 Hz, a significant reduction in SPL was observed, particularly at frequencies around 1000 Hz and 1200 Hz. For example, the SPL at 1000 Hz and 1200 Hz is reduced by 6.2 dB and 23.5 dB, respectively. In the entire frequency range, the averaged SPL is reduced from 98.7 dB to 93.0 dB by the damping treatment. When both the eddy current control and damping were taken into account, the average SPL is reduced from 102.6 dB to 93.0 dB, a reduction of 9.6 dB, as shown in Fig. 5-41 (b). For the frequency band 100-1700 Hz that covers the majority of frequencies for gradient pulses, the averaged SPL is reduced from 105.0 dB to 88.7 dB, a 16.3 dB reduction. From Fig. 5-41 (b), the overall SPL of the combined acoustic fields is reduced by 5.1 dB (from 104.2 dB to 99.1 dB).

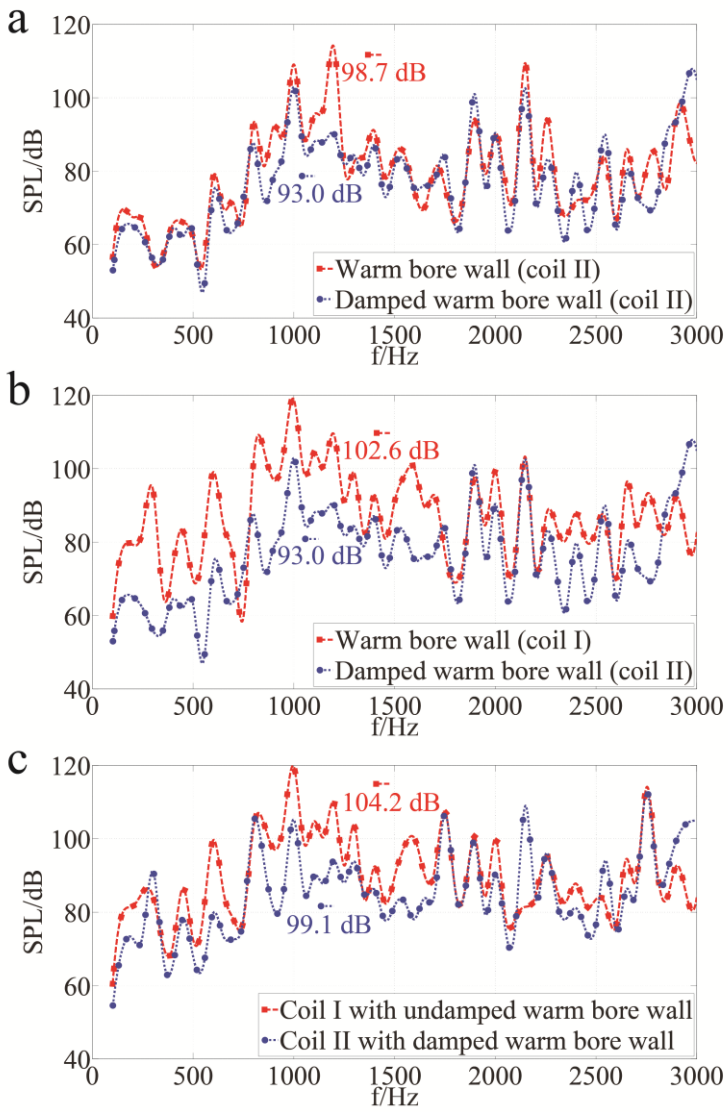

Fig. 5-41 Comparison of acoustic responses of the undamped warm bore wall, damped warm bore wall and combination of gradient coil and warm bore: (a) SPL comparison between the undamped warm bore wall and damped warm bore wall accompanied with coil II design, (b) SPL comparison between the undamped warm bore wall accompanied with coil I design and damped warm bore wall accompanied with coil II design and (c) SPL comparison between the combinations of coil I with undamped warm bore wall and coil II with damped warm bore wall.

Specific acoustic field distributions in the patient bore are plotted in Fig. 5-42. Here the responses of a 1000-Hz sinusoidal gradient pulse are illustrated. It can be seen that after the eddy current control and damping treatment, the acoustic field strength of the warm bore wall was reduced accordingly.

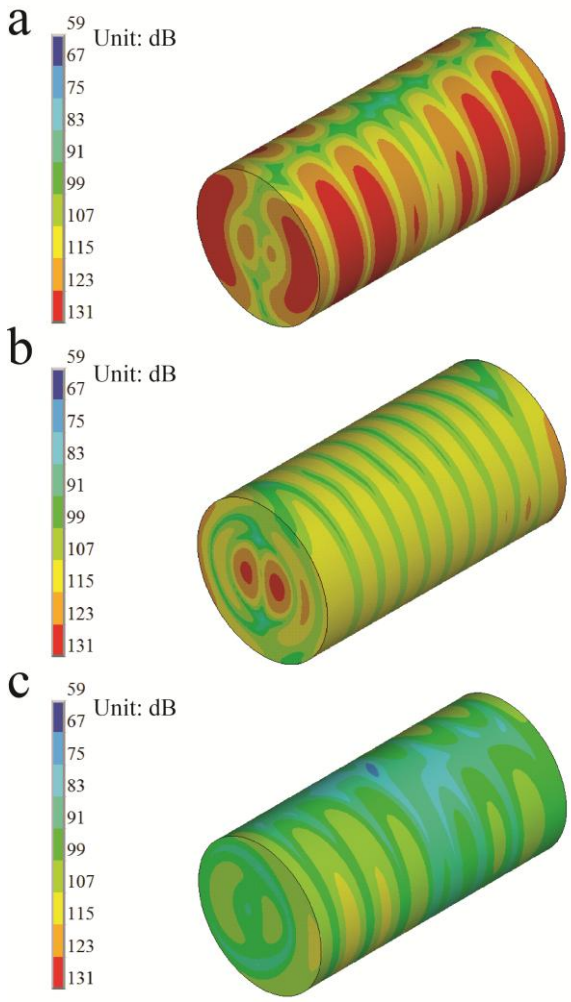

Fig. 5-42 Acoustic responses of the warm bore wall: acoustic field distribution of the warm bore wall accompanied with coil I design (a), acoustic field distribution of the warm bore wall accompanied with coil II design (b) and acoustic field distribution of the warm bore wall accompanied with coil II design after damping treatment (c). A 1000-Hz sinusoidal gradient pulse was used to energize the gradient coil.

5.4.4 Conclusion

This study theoretically investigated the eddy current-cryostat interaction in terms of acoustic response of an MRI system. A main magnet and two transverse gradient coils were designed and the corresponding eddy currents on the warm bore wall were calculated. The simulated results show that the averaged SPL of the warm bore wall is slightly higher than that of the gradient coil at a shielding ratio of 2%. However, at certain frequencies, the SPL of the warm bore wall was found to be much higher.

By constraining the shielding ratio from 2% to 0.5%, the eddy current density amplitude on the warm bore wall was significantly reduced. The acoustic radiation calculation shows that the

averaged SPL of the warm bore wall was reduced by 3.9 dB from 102.6 dB to 98.7 dB. For certain frequency bands, the SPL reduction was much higher. For example, for the 100-700 Hz frequency band, the SPL reduction is 19.8 dB. Although the eddy current control method can effectively reduce the SPL of the warm bore wall at certain frequencies, it performed rather poorly in the frequency band of 800-1250 Hz. Additional reduction was achieved by using a damping layer applied on the inner surface of the warm bore wall. It was found that after the suggested damping treatment, the averaged SPL of the warm bore wall was reduced to 93.0 dB, a further reduction of 5.7 dB. The use of the damping material worked extremely well at 1000 Hz and 1200 Hz with attenuation of 6.2 dB and 23.5 dB, respectively. For the combined acoustic fields of the warm bore wall and gradient coil, the overall SPL was reduced by 5.1 dB. Therefore, the combined eddy current control and suggested damping scheme can effectively reduce the noise level in a MRI system.

Chapter 6

Conclusions

This thesis is made up of two main sections, covering gradient coil design of MRI scanners and an acoustic investigation of MRI scanners. The first chapter introduced the topic and scope; the second chapter gave an overview of the function of gradient coils in MRI, gradient coil design methods, and existing acoustic noise control applications; the third chapter first described the proposed numerical methods for gradient coil designs in this thesis and then introduced the software operation process in the acoustic modelling; and the fourth and fifth chapter presented work published during the PhD candidature, based on gradient coil design and acoustic investigations of MRI scanners. This chapter concludes with the contributions made by this thesis, along with suggestions for future work.

6.1 Contributions

The contribution of this thesis can be divided into two parts, the first in the area of gradient coil design of MRI scanners and the second in the area of acoustic investigation of MRI scanners.

In regard to gradient coil design,

(a) An improved finite difference method was proposed. This finite difference method integrated the eddy current induced secondary magnetic field into the gradient coil design. Various designs and analyses have been undertaken in this thesis based on the finite difference method, for instance, the gradient coil design for identification of the main acoustic noise source, and eddy current control in the acoustic investigation section.

(b) An improved discrete wire method was proposed. A spiral gradient coil configuration, which includes both transverse coils and a longitudinal coil, was designed by using the discrete wire method. The spiral coils eliminated the cutting and reconnecting process required in the conventional gradient coil design, thus reducing the magnetic field performance loss, and the smooth coil pattern also enabled cooling water to be allowed to flow inside the hollow wire. The

discrete wire method was also used to design asymmetric head gradient coils with a layer-sharing scheme and the wire spacing can be easily controlled using this method.

In regard to acoustic investigation,

(c) An MRI scanner model was established, and the modelling method was experimentally validated by another feasible scanner. Based on this model, the acoustic properties of a split MRI system, which is the main part of a MRI-LINAC system, were concluded, and the SPL was compared with a typical counterpart. This acoustic model was coded by command flow from the modelling establishment to the post processing, and the model dimensions were parameterized, thus making it easy to alter the parameter values to test other similar modelling conditions.

(d) A support mounting and damping treatment scheme was proposed based on the established acoustic model. The numerical simulation result demonstrated the feasibility of this scheme. By mounting support between the gradient assembly and the main magnet, the acoustic field distribution was relocated and the resonance frequencies were altered, resulting in a relatively quieter acoustic field in the central gap, where the patient's head wound reside doing head imaging. The damping treatment further reduced the resonant amplitude and reduced the ultimate SPL.

(e) A software application scheme was also proposed by gradient pulse alternations, in addition to the new hardware assembly scheme. This method removed the resonant frequency components from the gradient pulse pattern, which resulted in significant acoustic noise reduction without changing the physical scanner structure.

(f) It was found that the main noise source might not be the gradient assembly if the gradient coil was not well shielded, by comparing SPLs radiated by the gradient coil and the warm bore wall. Thus, the eddy current induced vibration of the surrounding materials was found to be not negligible. By improving shielding of the gradient coil and installing a damping treatment, it was found that the eddy current induced SPL could be efficiently controlled.

6.2 Future work

Based on the research work done in this thesis, future work can be planned as follows.

In regard to gradient coil design,

(a) The spiral series gradient coil design could be fabricated and the actual performance experimentally checked. Furthermore, the 2D finite difference algorithm used in gradient coil

design can be extended to enable 3D design, and the grid meshing integrated with a professional meshing package. In addition, the discrete wire method can be further improved with more flexible geometry and a faster optimization algorithm.

In regard to acoustic investigation,

(b) A systematic acoustic investigation can be conducted on the MRI scanner. This will include the gradient coil vibration control, eddy current mitigation, mechanical transmission blocking and RF assembly barrier [75]. Furthermore, the integration of acoustic noise reduction into gradient coil design will be investigated.

On the whole in the future, acoustic noise control and gradient coil design will be more closely combined in MRI system design. It is expected that a novel electromagnetic design for an MRI scanner with a quiet acoustic environment will be developed.

References

[1] Z. A. Fayad, V. Fuster, K. Nikolaou, and C. Becker, "Computed tomography and magnetic resonance imaging for noninvasive coronary angiography and plaque imaging: current and potential future concepts," *Circulation*, vol. 106, pp. 2026-2034, Oct 2002.

[2] S. Bipat, A. S. Glas, J. van der Velden, A. H. Zwinderman, P. M. Bossuyt, and J. Stoker, "Computed tomography and magnetic resonance imaging in staging of uterine cervical carcinoma: a systematic review," *Gynecol Oncol*, vol. 91, pp. 59-66, Oct 2003.

[3] M. Arvanitakis, M. Delhaye, V. De Maertelaere, M. Bali, C. Winant, E. Coppens, *et al.*, "Computed tomography and magnetic resonance imaging in the assessment of acute pancreatitis," *Gastroenterology*, vol. 126, pp. 715-723, Mar 2004.

[4] I. L. Pykett, J. H. Newhouse, F. S. Buonanno, T. J. Brady, M. R. Goldman, J. P. Kistler, *et al.*, "Principles of nuclear magnetic resonance imaging," *Radiology*, vol. 143, pp. 157-168, Apr 1982.

[5] R. Turner, "Gradient coil design: A review of methods," *Magnetic Resonance Imaging*, vol. 11, pp. 903-920, 1993.

[6] M. Poole and R. Bowtell, "Novel gradient coils designed using a boundary element method," *Concepts in Magnetic Resonance Part B: Magnetic Resonance Engineering*, vol. 31B, pp. 162-175, 2007.

[7] X. F. You, W. H. Yang, T. Song, L. L. Hu, and H. X. Wang, "A novel approach of torque-balanced asymmetric gradient coil design for head imaging," in *Bioelectronics and Bioinformatics (ISBB), 2011 International Symposium on*, 2011, pp. 115-118.

[8] S. A. Counter, A. Olofsson, H. F. Grahn, and E. Borg, "MRI acoustic noise: sound pressure and frequency analysis," *J Magn Reson Imaging*, vol. 7, pp. 606-611, May 1997.

[9] W. A. Edelstein, R. A. Hedeen, R. P. Mallozzi, S.-A. El-Hamamsy, R. A. Ackermann, and T. J. Havens, "Making MRI Quieter," *Magnetic Resonance Imaging*, vol. 20, pp. 155-163, Feb 2002.

[10] W. A. Edelstein, T. K. Kidane, V. Taracila, T. N. Baig, T. P. Eagan, Y. C. Cheng, *et al.*, "Active-passive gradient shielding for MRI acoustic noise reduction," *Magn Reson Med*, vol. 53, pp. 1013-1017, May 2005.

[11] M. E. Ravicz, J. R. Melcher, and N. Y. S. Kiang, "Acoustic noise during functional magnetic resonance imaging," *The Journal of the Acoustical Society of America*, vol. 108, pp. 1683-1696, 2000.

[12] K. Takamori, H. Furukawa, Y. Morikawa, T. Katayama, and S. Watanabe, "Basic study on vibrations during tooth preparations caused by high-speed drilling and Er:YAG laser irradiation," *Lasers Surg Med,* vol. 32, pp. 25-31, 2003.

[13] Y. Boyle, D. E. Bentley, A. Watson, and A. K. Jones, "Acoustic noise in functional magnetic resonance imaging reduces pain unpleasantness ratings," *Neuroimage,* vol. 31, pp. 1278-1283, Jul 2006.

[14] J. R. Foster, D. A. Hall, A. Q. Summerfield, A. R. Palmer, and R. W. Bowtell, "Sound-level measurements and calculations of safe noise dosage during EPI at 3 T," *J Magn Reson Imaging,* vol. 12, pp. 157-163, Jul 2000.

[15] R. Govindaraju, R. Omar, R. Rajagopalan, R. Norlisah, and N. Kwan-Hoong, "Hearing loss after noise exposure," *Auris Nasus Larynx,* vol. 38, pp. 519-522, Aug 2011.

[16] P. Radomskij, M. A. Schmidt, C. W. Heron, and D. Prasher, "Effect of MRI noise on cochlear function," *Lancet,* vol. 359, p. 1485, Apr 2002.

[17] C. C. Sanchez, M. F. Pantoja, M. Poole, and A. R. Bretones, "Gradient-Coil Design: A Multi-Objective Problem," *IEEE Transactions on Magnetics,* vol. 48, pp. 1967-1975, 2012.

[18] J.-M. Jin, *Electromagnetic analysis and design in magnetic resonance imaging / Jianming Jin*. Boca Raton, Fla.: Boca Raton, Fla. : CRC Press, 1999.

[19] L. Saba, *Magnetic resonance imaging handbook / [edited by] Luca Saba*: Boca Raton : CRC Press, Taylor & Francis Group, 2017.

[20] R. Turner, "A target field approach to optimal coil design," *Journal of Physics D: Applied Physics,* vol. 19, p. L147, 1986.

[21] R. Turner, "Minimum inductance coils," *Journal of Physics E: Scientific Instruments,* vol. 21, p. 948, 1988.

[22] R. Turner and R. M. Bowley, "Passive screening of switched magnetic field gradients," *Journal of Physics E: Scientific Instruments,* vol. 19, p. 876, 1986.

[23] B. A. Chronik and B. K. Rutt, "Constrained length minimum inductance gradient coil design," *Magn Reson Med,* vol. 39, pp. 270-278, Feb 1998.

[24] K. F. Lawrence and C. Stuart, "A novel target-field method for finite-length magnetic resonance shim coils: I. Zonal shims," *Journal of Physics D: Applied Physics,* vol. 34, p. 3447, 2001.

[25] K. F. Lawrence and C. Stuart, "A novel target-field method for finite-length magnetic resonance shim coils: II. Tesseral shims," *Journal of Physics D: Applied Physics,* vol. 35, p. 839, 2002.

[26] K. F. Lawrence and C. Stuart, "A novel target-field method for magnetic resonance shim coils: III. Shielded zonal and tesseral coils," *Journal of Physics D: Applied Physics,* vol. 36, p. 68, 2003.

[27] J. W. Carlson, K. A. Derby, K. C. Hawryszko, and M. Weideman, "Design and evaluation of shielded gradient coils," *Magnetic Resonance in Medicine,* vol. 26, pp. 191-206, 1992.

[28] K. Yoda, "Analytical design method of self-shielded planar coils," *Journal of Applied Physics,* vol. 67, pp. 4349-4353, 1990.

[29] L. K. Forbes, M. A. Brideson, and S. Crozier, "A target-field method to design circular biplanar coils for asymmetric shim and gradient fields," *IEEE Transactions on Magnetics,* vol. 41, pp. 2134-2144, 2005.

[30] L. S. Petropoulos, "Finite size disc gradient coil set for open vertical field magnets," *Magnetic Resonance Imaging,* vol. 18, pp. 615-624, Jun 2000.

[31] Shou, "MRI coil design using boundary-element method with regularization technique: A numerical calculation study," *IEEE transactions on magnetics,* vol. 46, p. 1052, 2010.

[32] H. S. Lopez, F. Liu, M. Poole, and S. Crozier, "Equivalent Magnetization Current Method Applied to the Design of Gradient Coils for Magnetic Resonance Imaging," *Magnetics, IEEE Transactions on,* vol. 45, pp. 767-775, 2009.

[33] H. S. Lopez, M. Poole, and S. Crozier, "An improved equivalent magnetization current method applied to the design of local breast gradient coils," *Journal of Magnetic Resonance,* vol. 199, pp. 48-55, Jul 2009.

[34] M. Zhu, L. Xia, F. Liu, J. Zhu, L. Kang, and S. Crozier, "A finite difference method for the design of gradient coils in MRI--an initial framework," *IEEE Trans Biomed Eng,* vol. 59, pp. 2412-2421, Sep 2012.

[35] Y. Wang, F. Liu, X. Zhou, Y. Li, and S. Crozier, "A numerical study of the acoustic radiation owing to eddy current-cryostat interactions," *Medical Physics,* 10.1002/mp.12261, 2017.

[36] Y. Wang, F. Liu, X. Zhou, and S. Crozier, "Design of transverse head gradient coils using a layer-sharing scheme," *Journal of Magnetic Resonance,* vol.278, pp.88-95, 2017.

[37] G. N. Peeren, "Stream function approach for determining optimal surface currents," *Journal of Computational Physics,* vol. 191, pp. 305-321, Oct 2003.

[38] D. Tomasi, "Stream function optimization for gradient coil design," *Magn Reson Med,* vol. 45, pp. 505-512, Mar 2001.

[39] S. Crozier and D. M. Doddrell, "Gradient-Coil Design by Simulated Annealing," *Journal of Magnetic Resonance, Series A,* vol. 103, pp. 354-357, Jul 1993.

[40] E. C. Wong, A. Jesmanowicz, and J. S. Hyde, "Coil optimization for MRI by conjugate gradient descent," *Magnetic Resonance in Medicine*, vol. 21, pp. 39-48, 1991.

[41] S. Crozier, L. K. Forbes, and D. M. Doddrell, "The Design of Transverse Gradient Coils of Restricted Length by Simulated Annealing," *Journal of Magnetic Resonance, Series A*, vol. 107, pp. 126-128, Mar 1994.

[42] X. Du, Z. Zhu, L. Zhao, G. Zhang, F. Ning, Z. Liu, *et al.*, "Design of Cylindrical Transverse Gradient Coil for 1.5 T MRI System," *IEEE Transactions on Applied Superconductivity*, vol. 22, pp. 4402004-4402004, 2012.

[43] M. Stehling, R. Turner, and P. Mansfield, "Echo-planar imaging: magnetic resonance imaging in a fraction of a second," *Science*, vol. 254, pp. 43-50, Oct 1991.

[44] E. R. Andrew and E. Szczesniak, "Low inductance transverse gradient system of restricted length," *Magnetic Resonance Imaging*, vol. 13, pp. 607-613, Jan 1995.

[45] J. Leggett, S. Crozier, and R. W. Bowtell, "Actively shielded multi-layer gradient coil designs with improved cooling properties," *Journal of Magnetic Resonance*, vol. 165, pp. 196-207, Dec 2003.

[46] S. Pissanetzky, "Minimum energy MRI gradient coils of general geometry," *Measurement Science and Technology*, vol. 3, p. 667, 1992.

[47] A. M. Abduljalil, A. H. Aletras, and P.-M. Robitaille, "Torque free asymmetric gradient coils for echo planar imaging," *Magnetic Resonance in Medicine*, vol. 31, pp. 450-453, 1994.

[48] D. C. Alsop and T. J. Connick, "Optimization of torque-balanced asymmetric head gradient coils," *Magnetic Resonance in Medicine*, vol. 35, pp. 875-886, 1996.

[49] A. Trakic, F. Liu, H. S. Lopez, H. Wang, and S. Crozier, "Longitudinal gradient coil optimization in the presence of transient eddy currents," *Magnetic Resonance in Medicine*, vol. 57, pp. 1119-1130, 2007.

[50] H. Sanchez Lopez, F. Freschi, A. Trakic, E. Smith, J. Herbert, M. Fuentes, *et al.*, "Multilayer integral method for simulation of eddy currents in thin volumes of arbitrary geometry produced by MRI gradient coils," *Magn Reson Med*, vol. 71, pp. 1912-1922, May 2014.

[51] M. Poole, H. S. Lopez, O. Ozaki, H. Kitaguchi, I. Nakajima, S. i. Urayama, *et al.*, "Simulation of Gradient-Coil-Induced Eddy Currents and Their Effects on a Head-Only HTS MRI Magnet," *IEEE Transactions on Applied Superconductivity*, vol. 21, pp. 3592-3598, 2011.

[52] R. E. Brummett, J. M. Talbot, and P. Charuhas, "Potential hearing loss resulting from MR imaging," *Radiology*, vol. 169, pp. 539-540, Nov 1988.

[53] P. Mansfield, P. Glover, and R. Bowtell, "Active acoustic screening: design principles for quiet gradient coils in MRI," *Measurement Science and Technology,* vol. 5, p. 1021, 1994.

[54] P. Mansfield, B. L. W. Chapman, R. Bowtell, P. Glover, R. Coxon, and P. R. Harvey, "Active Acoustic Screening: Reduction of Noise in Gradient Coils by Lorentz Force Balancing," *Magnetic Resonance in Medicine,* vol. 33, pp. 276-281, 1995.

[55] B. L. W. Chapman and P. Mansfield, "Quiet gradient coils: active acoustically and magnetically screened distributed transverse gradient designs," *Measurement Science and Technology,* vol. 6, p. 349, 1995.

[56] L. K. Forbes, M. A. Brideson, S. Crozier, and P. T. While, "An analytical approach to the design of quiet cylindrical asymmetric gradient coils in MRI," *Concepts in Magnetic Resonance Part B: Magnetic Resonance Engineering,* vol. 31B, pp. 218-236, 2007.

[57] P. Mansfield, R. M. Bowley, and B. Haywood, "Controlled E-field gradient coils," *Magnetic Resonance Materials in Physics, Biology and Medicine,* vol. 16, pp. 113-120, 2003.

[58] R. A. Lemdiasov and R. Ludwig, "A stream function method for gradient coil design," *Concepts in Magnetic Resonance Part B: Magnetic Resonance Engineering,* vol. 26B, pp. 67-80, 2005.

[59] P. Michael, W. Pierre, L. Hector Sanchez, N. Michael, and C. Stuart, "Minimax current density coil design," *Journal of Physics D: Applied Physics,* vol. 43, p. 095001, 2010.

[60] M. S. Poole, P. T. While, H. S. Lopez, and S. Crozier, "Minimax current density gradient coils: Analysis of coil performance and heating," *Magnetic Resonance in Medicine,* vol. 68, pp. 639-648, 2012.

[61] P. T. While, M. S. Poole, L. K. Forbes, and S. Crozier, "Minimum maximum temperature gradient coil design," *Magnetic Resonance in Medicine,* vol. 70, pp. 584-594, 2013.

[62] G. Shou, L. Xia, F. Liu, M. Zhu, Y. Li, and S. Crozier, "MRI Coil Design Using Boundary-Element Method With Regularization Technique: A Numerical Calculation Study," *IEEE Transactions on Magnetics,* vol. 46, pp. 1052-1059, 2010.

[63] Y. Takano, M. Nagao, I. Sakaguchi, M. Tachiki, T. Hatano, K. Kobayashi, *et al.*, "Superconductivity in diamond thin films well above liquid helium temperature," *Applied Physics Letters,* vol. 85, pp. 2851-2853, 2004.

[64] D. L. Price, J. P. De Wilde, A. M. Papadaki, J. S. Curran, and R. I. Kitney, "Investigation of acoustic noise on 15 MRI scanners from 0.2 T to 3 T," *Journal of magnetic resonance imaging : JMRI,* vol. 13, pp. 288-293, Feb 2001.

[65] Y. Wu, B. A. Chronik, C. Bowen, C. K. Mechefske, and B. K. Rutt, "Gradient-induced acoustic and magnetic field fluctuations in a 4T whole-body MR imager," *Magn Reson Med,* vol. 44, pp. 532-536, Oct 2000.

[66] A. Katsunuma, H. Takamori, Y. Sakakura, Y. Hamamura, Y. Ogo, and R. Katayama, "Quiet MRI with novel acoustic noise reduction," *Magma,* vol. 13, pp. 139-144, Jan 2002.

[67] R. Hurwitz, S. R. Lane, R. A. Bell, and M. N. Brant-Zawadzki, "Acoustic analysis of gradient-coil noise in MR imaging," *Radiology,* vol. 173, pp. 545-548, Nov 1989.

[68] M. E. Ravicz and J. R. Melcher, "Isolating the auditory system from acoustic noise during functional magnetic resonance imaging: examination of noise conduction through the ear canal, head, and body," *J Acoust Soc Am,* vol. 109, pp. 216-31, Jan 2001.

[69] C. K. Mechefske, R. Geris, J. S. Gati, and B. K. Rutt, "Acoustic noise reduction in a 4 T MRI scanner," *Magma,* vol. 13, pp. 172-6, Jan 2002.

[70] W. A. Edelstein, R. A. Hedeen, R. P. Mallozzi, S. A. El-Hamamsy, R. A. Ackermann, and T. J. Havens, "Making MRI quieter," *Magn Reson Imaging,* vol. 20, pp. 155-163, Feb 2002.

[71] T. R. Lin, P. O'Shea, and C. Mechefske, "Reducing MRI gradient coil vibration with rib stiffeners," *Concepts in Magnetic Resonance Part B: Magnetic Resonance Engineering,* vol. 35B, pp. 198-209, 2009.

[72] Y. Wang, F. Liu, and S. Crozier, "Simulation study of noise reduction methods for a split MRI system using a finite element method," *Medical Physics,* vol. 42, pp. 7122-7131, 2015.

[73] H. Takamori, A. Katsunuma, Y. Uosaki, T. Toyoshima, K. Iinuma, H. Kawamoto, *et al.*, "Magnetic resonance imaging system having mechanically decoupled field generators to reduce ambient acoustic noise," U.S. patent US6043653 A, Mar 2000.

[74] W. A. Edelstein, R. P. Mallozzi, R. A. Hedeen, S. A. El-Hamamsy, M. L. Miller, P. S. Thompson, *et al.*, "Low noise MRI scanner," U.S. patent US6437568 B1, Aug 2002.

[75] C. M. Ireland, R. O. Giaquinto, W. Loew, J. A. Tkach, R. G. Pratt, B. M. Kline-Fath, *et al.*, "A novel acoustically quiet coil for neonatal MRI system," *Concepts in Magnetic Resonance Part B: Magnetic Resonance Engineering,* vol. 45, pp. 107-114, 2015.

[76] M. McJury, R. W. Stewart, D. Crawford, and E. Toma, "The use of active noise control (ANC) to reduce acoustic noise generated during MRI scanning: some initial results," *Magn Reson Imaging,* vol. 15, pp. 319-322, 1997.

[77] F. Baumgart, T. Kaulisch, C. Tempelmann, B. Gaschler-Markefski, C. Tegeler, F. Schindler, *et al.*, "Electrodynamic headphones and woofers for application in magnetic resonance imaging scanners," *Med Phys,* vol. 25, pp. 2068-2070, Oct 1998.

[78] C. K. Chen, T. D. Chiueh, and J. H. Chen, "Active cancellation system of acoustic noise in MR imaging," *IEEE Trans Biomed Eng,* vol. 46, pp. 186-191, Feb 1999.

[79] J. Chambers, M. A. Akeroyd, A. Q. Summerfield, and A. R. Palmer, "Active control of the volume acquisition noise in functional magnetic resonance imaging: method and psychoacoustical evaluation," *J Acoust Soc Am,* vol. 110, pp. 3041-3054, Dec 2001.

[80] J. Chambers, D. Bullock, Y. Kahana, A. Kots, and A. Palmer, "Developments in active noise control sound systems for magnetic resonance imaging," *Applied Acoustics,* vol. 68, pp. 281-295, Mar 2007.

[81] N. B. Roozen, A. H. Koevoets, and A. J. den Hamer, "Active Vibration Control of Gradient Coils to Reduce Acoustic Noise of MRI Systems," *Mechatronics, IEEE/ASME Transactions on,* vol. 13, pp. 325-334, 2008.

[82] P. Mansfield and B. Haywood, "Principles of active acoustic control in gradient coil design," *Magma,* vol. 10, pp. 147-151, Jun 2000.

[83] P. Mansfield, B. Haywood, and R. Coxon, "Active acoustic control in gradient coils for MRI," *Magn Reson Med,* vol. 46, pp. 807-818, Oct 2001.

[84] F. Hennel, F. Girard, and T. Loenneker, ""Silent" MRI with soft gradient pulses," *Magn Reson Med,* vol. 42, pp. 6-10, Jul 1999.

[85] Y. Wang, F. Liu, E. Weber, F. Tang, J. Jin, Y. Tesiram, and S. Crozier, "Acoustic analysis for a split MRI system using FE method," *Concepts in Magnetic Resonance Part B: Magnetic Resonance Engineering,* vol. 45, pp. 85-96, 2015.

[86] F. Hennel, "Fast spin echo and fast gradient echo MRI with low acoustic noise," *J Magn Reson Imaging,* vol. 13, pp. 960-966, Jun 2001.

[87] M. Segbers, C. V. Rizzo Sierra, H. Duifhuis, and J. M. Hoogduin, "Shaping and timing gradient pulses to reduce MRI acoustic noise," *Magn Reson Med,* vol. 64, pp. 546-553, Aug 2010.

[88] M. A. Baker, "Reduction of MRI acoustic noise achieved by manipulation of scan parameters – A study using veterinary MR sequences," *Radiography,* vol. 19, pp. 11-16, Feb 2013.

[89] J. M. Jackson, M. A. Brideson, L. K. Forbes, and S. Crozier, "Tikhonov regularization approach for acoustic noise reduction in an asymmetric, self-shielded MRI gradient coil," *Concepts in Magnetic Resonance Part B: Magnetic Resonance Engineering,* vol. 37B, pp. 167-179, 2010.

[90] J. M. Jackson, L. K. Forbes, P. T. While, and M. A. Brideson, "Could image processing enable reduced acoustic noise during MRI scans?," *Concepts in Magnetic Resonance Part B: Magnetic Resonance Engineering,* vol. 39B, pp. 191-205, 2011.

[91] C. Q. T. B. S. Howard, *Acoustic Analyses Using Matlab® and Ansys®*, 2015.

[92] X. Li, D. Xie, and J. Wang, "Design of Gradient Coil Set With Canceled Net Thrust Force for Fully Open MRI System," *IEEE Transactions on Magnetics,* vol. 45, pp. 1804-1807, 2009.

[93] F. Tang, H. S. Lopez, F. Freschi, E. Smith, Y. Li, M. Fuentes, *et al.*, "Skin and proximity effects in the conductors of split gradient coils for a hybrid Linac-MRI scanner," *Journal of Magnetic Resonance*, vol. 242, pp. 86-94, May 2014.

[94] H. Sanchez Lopez, M. Poole, and S. Crozier, "Eddy current simulation in thick cylinders of finite length induced by coils of arbitrary geometry," *J Magn Reson*, vol. 207, pp. 251-261, Dec 2010.

[95] A. Trakic, H. Wang, F. Liu, H. S. Lopez, and S. Crozier, "Analysis of Transient Eddy Currents in MRI Using a Cylindrical FDTD Method," *IEEE Transactions on Applied Superconductivity*, vol. 16, pp. 1924-1936, 2006.

[96] L. Liu, H. Sanchez-Lopez, F. Liu, and S. Crozier, "Flanged-edge transverse gradient coil design for a hybrid LINAC–MRI system," *Journal of Magnetic Resonance*, vol. 226, pp. 70-78, Jan 2013.

[97] M. A. Brideson, L. K. Forbes, and S. Crozier, "Determining complicated winding patterns for shim coils using stream functions and the target-field method," *Concepts in Magnetic Resonance*, vol. 14, pp. 9-18, 2002.

[98] F. D. Doty, "MRI Gradient Coil Optimization," in *Spatially Resolved Magnetic Resonance*, ed: Wiley-VCH Verlag GmbH, 2007, pp. 647-674.

[99] S. Adhikari, "*Damping models for structural vibration*," PhD thesis, University of Cambridge, 2001.

[100] L. E. Kinsler, *Fundamentals of acoustics / Lawrence E. Kinsler ... [et al.]*, 4th ed.. ed. New York: New York : Wiley, 2000.

[101] W. Shao and C. Mechefske, "Acoustic analysis of a gradient coil winding in an MRI scanner," *Concepts in Magnetic Resonance Part B: Magnetic Resonance Engineering*, vol. 24, pp. 15-27, 2005.

[102] Y. Wang, F. Liu, Y. Li, F. Tang, and S. Crozier, "Asymmetric gradient coil design for use in a short, open bore magnetic resonance imaging scanner," *Journal of Magnetic Resonance*, vol. 269, pp. 203-212, Aug 2016.

[103] G. DeMeester, M. Morich, A. Byrne, F. Davies, D. Melotte, and A. Thomas, "Challenges of short magnet design," *Magma*, vol. 13, pp. 193-198, Jan 2002.

[104] F. Liu, R. Wei, and S. Crozier, "Open-bore magnet for use in magnetic resonance imaging," U.S. patent US20120258862 A1, Oct 2012.

[105] H. Zhao, S. Crozier, and D. M. Doddrell, "Asymmetric MRI magnet design using a hybrid numerical method," *J Magn Reson*, vol. 141, pp. 340-346, Dec 1999.

[106] P. T. While, L. K. Forbes, and S. Crozier, "3-D gradient coil design--initial theoretical framework," *IEEE Trans Biomed Eng*, vol. 56, pp. 1169-1183, Apr 2009.

[107] Y. Boyle, D. E. Bentley, A. Watson, and A. K. P. Jones, "Acoustic noise in functional magnetic resonance imaging reduces pain unpleasantness ratings," *NeuroImage,* vol. 31, pp. 1278-1283, Jul 2006.

[108] H. Sanchez, F. Liu, A. Trakic, E. Weber, and S. Crozier, "Three-Dimensional Gradient Coil Structures for Magnetic Resonance Imaging Designed Using Fuzzy Membership Functions," *Magnetics, IEEE Transactions on,* vol. 43, pp. 3558-3566, 2007.

[109] F. Jia, Z. Liu, M. Zaitsev, J. Hennig, and J. G. Korvink, "Design multiple-layer gradient coils using least-squares finite element method," *Structural and Multidisciplinary Optimization,* vol. 49, pp. 523-535, 2013.

[110] S. Shvartsman, M. Morich, G. Demeester, and Z. Zhai, "Ultrashort shielded gradient coil design with 3D geometry," *Concepts in Magnetic Resonance Part B: Magnetic Resonance Engineering,* vol. 26B, pp. 1-15, 2005.

[111] W. Arz, M. Gebhardt, F. Schmitt, and J. Schuster, "Gradient coil arrangement for nuclear spin tomography apparatus," UK patent 2347505, 1999.

[112] Y. Wang, F. Liu, E. Weber, F. Tang, J. Jin, Y. Tesiram, *et al.*, "Acoustic analysis for a split MRI system using FE method," *Concepts in Magnetic Resonance Part B: Magnetic Resonance Engineering,* vol. 45, pp. 85-96, 2015.

[113] R. Temam, *Navier-Stokes equations: theory and numerical analysis* vol. 2. Amsterdam ; New York ; Oxford: North-Holland, 1984.

[114] F. P. Beer, *Mechanics of materials* vol. Seventhition. New York, NY: McGraw-Hill, 2015.

[115] G. Li and C. K. Mechefske, "Structural-acoustic modal analysis of cylindrical shells: application to MRI scanner systems," *Magma,* vol. 22, pp. 353-364, Dec 2009.

[116] C. K. Mechefske, Y. Wu, and B. K. Rutt, "MRI gradient coil cylinder sound field simulation and measurement," *J Biomech Eng,* vol. 124, pp. 450-455, Aug 2002.

[117] B. Chronik, A. Alejski, and B. K. Rutt, "Design and fabrication of a three-axis multilayer gradient coil for magnetic resonance microscopy of mice," *Magma,* vol. 10, pp. 131-146, Jun 2000.

[118] M. Kamon, M. J. Tsuk, and J. K. White, "FASTHENRY: a multipole-accelerated 3-D inductance extraction program," *IEEE Transactions on Microwave Theory and Techniques,* vol. 42, pp. 1750-1758, 1994.

[119] M. Poole, R. Bowtell, D. Green, S. Pittard, A. Lucas, R. Hawkes, *et al.*, "Split gradient coils for simultaneous PET-MRI," *Magnetic Resonance in Medicine,* vol. 62, pp. 1106-1111, 2009.

[120] K. C. Chu and B. K. Rutt, "MR gradient coil heat dissipation," *Magnetic Resonance in Medicine,* vol. 34, pp. 125-132, 1995.

[121] V. Vegh, H. Sanchez, I. M. Brereton, and S. Crozier, "Toward designing asymmetric head gradient coils for high-resolution imaging," *Concepts in Magnetic Resonance Part B: Magnetic Resonance Engineering,* vol. 31B, pp. 1-11, 2007.

[122] D. Tomasi, R. F. Xavier, B. Foerster, H. Panepucci, A. Tannús, and E. L. Vidoto, "Asymmetrical gradient coil for head imaging," *Magnetic Resonance in Medicine,* vol. 48, pp. 707-714, 2002.

[123] M. Zhu, L. Xia, F. Liu, and S. Crozier, "Deformation-space method for the design of biplanar transverse gradient coils in open MRI systems," *IEEE Transactions on Magnetics,* vol. 44, pp. 2035-2041, 2008.

[124] M. Poole, H. S. Lopez, and S. Crozier, "Adaptively regularized gradient coils for reduced local heating," *Concepts in Magnetic Resonance Part B: Magnetic Resonance Engineering,* vol. 33B, pp. 220-227, 2008.

[125] S. A. Counter, A. Olofsson, E. Borg, B. Bjelke, A. Haggstrom, and H. F. Grahn, "Analysis of magnetic resonance imaging acoustic noise generated by a 4.7 T experimental system," *Acta Otolaryngol,* vol. 120, pp. 739-743, Sep 2000.

[126] Z. H. Cho, S. H. Park, J. H. Kim, S. C. Chung, S. T. Chung, J. Y. Chung, *et al.*, "Analysis of acoustic noise in MRI," *Magn Reson Imaging,* vol. 15, pp. 815-822, 1997.

[127] R. A. Hedeen and W. A. Edelstein, "Characterization and prediction of gradient acoustic noise in MR imagers," *Magn Reson Med,* vol. 37, pp. 7-10, Jan 1997.

[128] F. G. Shellock, S. M. Morisoli, and M. Ziarati, "Measurement of acoustic noise during MR imaging: evaluation of six "worst-case" pulse sequences," *Radiology,* vol. 191, pp. 91-93, Apr 1994.

[129] D. Tomasi and T. Ernst, "A simple theory for vibration of MRI gradient coils," *Brazilian Journal of Physics,* vol. 36, pp. 34-39, 2006.

[130] M. Rausch, M. Gebhardt, M. Kaltenbacher, and H. Landes, "Computer-aided design of clinical magnetic resonance imaging scanners by coupled magnetomechanical-acoustic modeling," *IEEE Transactions on Magnetics,* vol. 41, pp. 72-81, 2005.

[131] G. Z. Yao, C. K. Mechefske, and B. K. Rutt, "Characterization of vibration and acoustic noise in a gradient-coil insert," *Magma,* vol. 17, pp. 12-27, Sep 2004.

[132] C. K. Mechefske, G. Yao, W. Li, C. Gazdzinski, and B. K. Rutt, "Modal analysis and acoustic noise characterization of a 4T MRI gradient coil insert," *Concepts in Magnetic Resonance Part B: Magnetic Resonance Engineering,* vol. 22B, pp. 37-49, 2004.

[133] F. Wang and C. K. Mechefske, "Modal analysis and testing of a thin-walled gradient coil cylinder model," *Concepts in Magnetic Resonance Part B: Magnetic Resonance Engineering,* vol. 27B, pp. 34-50, 2005.

[134] F. Wang and C. K. Mechefske, "Vibration analysis and testing of a thin-walled gradient coil model," *Journal of Sound and Vibration,* vol. 311, pp. 554-566, Mar 2008.

[135] L. Liu, H. Sanchez-Lopez, M. Poole, F. Liu, and S. Crozier, "Simulation and analysis of the interactions between split gradient coils and a split magnet cryostat in an MRI-PET system," *J Magn Reson,* vol. 222, pp. 8-15, Sep 2012.

[136] L. Liu, A. Trakic, H. Sanchez-Lopez, F. Liu, and S. Crozier, "An analysis of the gradient-induced electric fields and current densities in human models when situated in a hybrid MRI-LINAC system," *Phys Med Biol,* vol. 59, pp. 233-245, Jan 6 2014.

[137] A. Trakic, L. Limei, H. Sanchez Lopez, L. Zilberti, L. Feng, and S. Crozier, "Numerical safety study of currents induced in the patient during rotations in the static field produced by a hybrid MRI-LINAC system," *IEEE Trans Biomed Eng,* vol. 61, pp. 784-793, Mar 2014.

[138] F. Liu, A. Trakic, H. S. Lopez, Q. Wei, M. Fuentes, E. Weber, *et al.*, "Reverse-engineering of gradient coil designs based on experimentally measured magnetic fields and approximate knowledge of coil geometry-application in exposure evaluations," *Concepts in Magnetic Resonance Part B: Magnetic Resonance Engineering,* vol. 35B, pp. 32-43, 2009.

[139] M. Tao and L.-K. Zhuo, "Simulation and analysis for acoustic performance of a sound absorption coating using ANSYS software," *Zhendong yu Chongji(Journal of Vibration and Shock),* vol. 30, pp. 87-90, 2011.

[140] C. K. Mechefske, G. Yao, and F. Wang, "Vibration and acoustic noise characterization of a gradient coil insert in a 4 T MRI," *Journal of Vibration and Control,* vol. 10, pp. 861-880, 2004.

[141] M. Sellers, J. Schuster, T. Carlberger, F. Boemmel, H. Hentzelt, and L. Hartmann, "Noise reduction arrangement for a magnetic resonance tomography apparatus," U.S. patent US64107799 A, Aug 2000.

[142] M. B. Sellers, T. Duby, N. Clarke, and A. Mantone, "Acoustically damped gradient coil," U.S. patent US20050040825 A1, Feb 2005.

[143] M. Bruneau, *Fundamentals of Acoustics*: Wiley-ISTE, 2010.

[144] R. Plunkett and C. T. Lee, "Length Optimization for Constrained Viscoelastic Layer Damping," *The Journal of the Acoustical Society of America,* vol. 48, pp. 150-161, 1970.

[145] J. M. Biggerstaff, "Vibrational damping of composite materials," PhD thesis, University of California San Diego, 2006.

[146] C. Cai, H. Zheng, M. Khan, and K. Hung, "Modeling of material damping properties in ANSYS," in *CADFEM Users' Meeting & ANSYS Conference*, 2002, pp. 9-11.

[147] H. Zheng, C. Cai, G. Pau, and G. Liu, "Minimizing vibration response of cylindrical shells through layout optimization of passive constrained layer damping treatments," *Journal of Sound and Vibration*, vol. 279, pp. 739-756, 2005.

[148] H. Zheng, C. Cai, and X. Tan, "Optimization of partial constrained layer damping treatment for vibrational energy minimization of vibrating beams," *Computers & Structures*, vol. 82, pp. 2493-2507, 2004.

[149] B. L. Chapman, B. Haywood, and P. Mansfield, "Optimized gradient pulse for use with EPI employing active acoustic control," *Magn Reson Med*, vol. 50, pp. 931-5, Nov 2003.

[150] B. Haywood, B. Chapman, and P. Mansfield, "Model gradient coil employing active acoustic control for MRI," *Magma (New York, N.y.)*, vol. 20, pp. 223-231, 2015.

[151] V. Taracila, W. A. Edelstein, T. K. Kidane, T. P. Eagan, T. N. Baig, and R. W. Brown, "Analytical calculation of cylindrical shell modes: Implications for MRI acoustic noise," *Concepts in Magnetic Resonance Part B: Magnetic Resonance Engineering*, vol. 25B, pp. 60-64, 2005.

[152] M. D. Rao, "Recent applications of viscoelastic damping for noise control in automobiles and commercial airplanes," *Journal of Sound and Vibration*, vol. 262, pp. 457-474, May 2003.

[153] Y. Wang, F. Liu, and S. Crozier, "Simulation study of noise reduction methods for a split MRI system using a Finite Element Method," *Medical Physics*, vol. 42, pp. 7122-7131, 2015.